UNIVERSITY OF SOUTHAMPTON

FACULTY OF PHYSICAL SCIENCES AND ENGINEERING

Optoelectronics Research Centre

Ultra precision physical micro-machining for integrated optics

by

Peter Allen Cooper

Thesis for the degree of Doctor of Philosophy

October 2015

UNIVERSITY OF SOUTHAMPTON

ABSTRACT

OPTOELECTRONICS RESEARCH CENTRE

Optoelectronics

Thesis for the degree of Doctor of Philosophy

ULTRA PRECISION PHYSICAL MICRO-MACHINING FOR INTEGRATED OPTICS

Peter Allen Cooper

This study looks at the application of physical micromachining techniques to integrated optics. These physical micromachining techniques were used to make structures which would be difficult or impossible to produce using conventional cleanroom based technologies.

A tuneable Bragg grating was fabricated and characterized and was found to offer an enhanced power efficiency for tuning of 45 pm/mW for the transverse magnetic mode and 39 pm/mW for the transverse electric mode. This an improvement in the operating power efficiency of a factor of 90 over bulk thermally tuned Bragg gratings in silica.

A dual cantilever device has also been demonstrated which can operate as a force sensor or variable attenuator. The response of the device to mechanical actuation was measured, and shown to be very well described by conventional fibre optic angular misalignment theory. The device has the potential to be utilized within integrated optical components for sensors or attenuators. An array of devices was fabricated with potential for parallel operation. The fabrication work features the first use of a dicing saw in plunge cutting mode to rapidly produce grooves which were free of chipping.

A wire electro discharge unit was designed and built. This was retrofitted to a micromill to give capability to manufacture tools directly on machine. This work built upon previous machining research in the group to allow free form diamond tools to be fabricated. Tools formed by wire electro discharge machining of polycrystalline diamond were formed. A ring tool was created and proved to be able to machine ring structures in the ductile mode regime in germanium oxide glass with a surface roughness of Ra 4.9 nm. This is the first time that ductile mode machining has been achieved in glass with this type of tool. By using a XeF_2 etch this was shown to be able to create the stuctures necessary for whispering gallery mode resonators. A number of exemplar micro disk

structures have been researched in this work to test the concept and provide real examples. Firstly a phosphogermanate glass on silica resonator was fabricated. A germanium oxide glass disc was also fabricated using the silicon under-etch process.

These trial optical devices have shown that physical machining provides a viable route for fabricating integrated optical elements.

Contents

List of Tables

List of Figures

DECLARATION OF AUTHORSHIP

I,Peter Allen Cooper declare that this thesis and the work presented in it are my own and has been generated by me as the result of my own original research.

Ultra precision physical micro-machining for integrated opticsI confirm that:

1. This work was done wholly or mainly while in candidature for a research degree at this University;
2. Where any part of this thesis has previously been submitted for a degree or any other qualification at this University or any other institution, this has been clearly stated;
3. Where I have consulted the published work of others, this is always clearly attributed;
4. Where I have quoted from the work of others, the source is always given. With the exception of such quotations, this thesis is entirely my own work;
5. I have acknowledged all main sources of help;
6. Where the thesis is based on work done by myself jointly with others, I have made clear exactly what was done by others and what I have contributed myself;
7. Parts of this work have been published as: [please list references below]:

P.A. Cooper, L.G. Carpenter, P.L. Mennea, C. Holmes, J.C. Gates, P.G.R. Smith

Integrated optical dual-cantilever arrays in silica on silicon

Optics Express 2014 Vol.22(26) pp.31801–31813

P.A. Cooper, L.G. Carpenter, C. Holmes, C. Sima, J.C. Gates, P.G.R. Smith

Power efficiency enhanced thermally tunable Bragg grating for silica-on-silicon photonics

IEEE Photonics Journal. Submitted January 2015

Signed: .....

Date:.....

Acknowledgements

I am very grateful to other staff and students in the ORC who have doing this work far easier than it would otherwise have been. My supervisors Peter Smith and James Gates who have always been available and eager to pass on knowledge as well providing encouragement. To everyone in the group who make it a great place to work, especially to Chris Holmes and Lewis Carpenter who have provided plently of practical assistantance in the lab as well good company and an eclectic music selection played loudly.

All of the technical staff who provide the facilities on the which the equipment used for the research relies. Especially Paul Allwood who spent a lot of time teaching me on the workshop machines and Neil Sessions who did the same in the cleanroom.

The work would not have been possible without the support of David Richards Engineering Ltd and Element 6 . I'm very grateful to Element 6 for supplying a wafer polycrystalline diamond for research. Richard Cox at David Richards Eng provided a lot of time making tools for us as well as passing on very useful knowledge.

Finally thank you to my family; parents Andrew and Susan (who page 13 is dedicated to) and David and May who have always been supportive.

Definitions and Abbreviations

µEDM	Micro Electro Discharge Machining
ASE	Amplified Spontaneous Emission
BBO	beta Barium Borate Oxide
CBN	Cubic Boron Nitride
CCD	Charge Coupled Device
CNC	Computer Numerical Control
DI	Deionised Water
DWDM	Dense wavelength division multiplexing
EDM	Electro Discharge Machining
EDX	Electro Dispersive Spectroscopy
FEA	Finite Element Analysis
FEM	Finite Element Model
FFT	Fast Fourier Transform
FHD	Flame Hydrolysis Deposition
FP	Fabry Perot
FWHM	Full Width Half Maximum
HF	Hydrofluoric Acid
HNA	Hydrofluoric Acid, Nitric Acid, Acetic Acid
ICP	Inductively Coupled Plasma
InGas	Indium Gallium Arsenide
IP	Integrated Photonics
KOH	Potassium Hydroxide
LED	Light Emitting Diode

LN	Lithium Niobate
MEM	Microelectromechanical systems
MOEM	Microoptoelectromechanical systems
OSA	Optical Spectrum Analyser
OVD	Outside vapor deposition
PCD	Polycrystalline diamond
PSD	Power spectral density
PV	Peak to valley
RC	Resistor capacitor circuit
RIE	Reactive ion etching
RMS	Root mean square
SEM	Scanning electron microscope
SLED	Superluminescent light emitting diode
SMF	Single Mode Fibre
TE	Transverse Electric
TM	Transverse Magnetic
UV	Ultraviolet
WC	Tungsten Carbide
WDM	Wavelength division multiplexing
WEDG	Wire Electro Discharge Grinding

Chapter 1: Introduction

1.1 Motivation and aims

The drive for the adoption of integrated optics comes from the desire to achieve miniaturization, compactness and stable optical performance. So for example, semiconductor lasers use sophisticated integrated optics for tuning [1], while arrayed waveguide gratings allow for multi-channel add/drop functions in Wavelength Division Multiplexing (WDM) networks [2]. However, integrated optics also holds tremendous future promise, with opportunities in sensing, quantum optics, optical switching and metrology, etc. Some of these future devices can make use of current fabrication techniques, which are normally based on silicon processing, and use lithography, deposition and etching. However, the toolbox available from silicon cleanroom processing has some limitations, particularly in creating 3D devices (e.g. variable depth) as well as often limiting the choices of materials. Furthermore, silicon processing can be time consuming (e.g. for deep etching), and the inherent strengths and weakness of these cleanroom techniques have led to particular directions being favoured in integrated optics research. In the work reported in this thesis new approaches based on micro machining have been explored.

Integrated optics is often seen as being a logical extension to bulk optics, in the same way that microelectronics developed from discrete component electronics. However, integrated optics differs from integrated electronics in that optics is strongly geometrical and affected by surface quality (roughness) in a way that electronics is not. Thus any fabrication technique that is applied to integrated optics must be capable of meeting these twin requirements (precise geometrical control and low surface roughness). Physical machining is well known to meet these requirements in the production of bulk optics (e.g. in diamond turned freeform lenses), however, it is not widely used in integrated optics.

As will be seen later in this thesis, micromilling is a technique which shows promise for 3D flexible design, it offers low surface roughness, and has excellent geometric form accuracy in glass. Understanding how these two requirements can be simultaneously achieved requires an understanding of the removal processes as well as the machine dynamics and careful choice of machining parameters. Also in this thesis the technique of ultra-precision dicing is extended as another physical machining technique that has recently been adopted for integrated optics. Dicing has been shown to give extremely high throughputs when the geometric complexity is lower. Our group is also known for the fabrication of UV written planar waveguides and Bragg gratings and

these techniques have also been used heavily in this work, and in particular to allow precise optical characterisation.

1.1.1 Wire Electro Discharge Grinding (WEDG) process

Micromilling is a tool based process which is strongly dependent on the shape and properties of the tool. Commercial micromilling tools can be purchased but they are expensive and not always ideally suited to the task in hand. Recent research has highlighted the potential of on-machine creation of polycrystalline diamond (PCD) tools for smooth milling of glass, and in this study part of the goal is to apply this technique to fabricate a new range of devices. The freedom to choose tool geometry increases the range of freeform structures that can be fabricated. Diamond is chosen because it has the highest known hardness of any material and as such it is frequently employed in cutting tools, especially in glass.

1.1.2 Microstructures for sensors and actuators

The integrated platform lends itself for applications in sensing of physical parameters or actuation and manipulation of light. Often the basic chip form is not ideal for these functions and performance improvements can be made if the device is structured, for example a cantilever arm for displacement sensing. A device which includes electrical, optical and mechanical functions is known as a MOEM (micro-optical-electrical-mechanical) [3]. This is an extension of the MEM's device (micro-electrical-mechanical) which are very commonly used as sensors, for example in accelerometers [4].

1.2 Synopsis

The layout of the thesis is as follows. The first chapter will look at the optical theory behind the devices, covering basic theory of optical waveguides, Bragg gratings and resonator structures. These results will be used in the following chapters. The second chapter will explore the field of physical machining with an overview of the topic. Attention will be focused on micro milling and dicing however other techniques will also be summarized. Attempts to describe ductile machining theoretically in the literature will be covered. The fundamental concepts of a micro-milling machine will be discussed. This will include how the machine components and design can affect the finished optical surfaces. As the 'adage' goes "it's impossible to cut better than it is to measure" and so it is important to have accurate metrology to measure the cut surfaces. The equipment used to measure the surfaces will be described and explained. Chapter 4 will document the fabrication and characterization of a tunable Bragg grating device. This utilizes a

micromilling process. Chapter 5 will describe a related dual cantilever sensing device. The fabrication is based around a dicing process. Chapter 6 will cover the addition of a WEDG unit to the micromill for on-machine tool fabrication. The theory of EDM will also covered. The fabrication of different tool types will be demonstrated. Chapter 7 presents attempts to apply a WEDG fabricated ring tool to make a whispering gallery resonator. This device is then optically characterized.

1.3 References

[1] R. G. Hunsperger, *Integrated Optics: Theory and Technology*, 6th Ed. Springer, 2009.

[2] K. Okamoto, *Fundamentals of Optical Waveguides*, 2nd Ed. Academic Press, 2006.

[3] M. E. Motamedi, *MOEMS: Micro-opto-electro-mechanical Systems*. SPIE Press, 2005.

[4] N. Yazdi, F. Ayazi, and K. Najafi, "Micromachined inertial sensors," *Proc. IEEE*, vol. 86, no. 8, pp. 1640–1659, Aug. 1998.

Chapter 2: Precision machining of glass in photonics

2.1 Introduction

For millennia glass has been worked and machined into useful shapes[1]. The field of glass machining is a large one and attention will be focused on precision physical micromachining for deterministic smooth surfaces. The first optical elements to feature high-precision physical machining were optical lenses and mirrors [2]. Lens fabrication would typically consist of a rough machining step followed by successively finer polishing steps. Although the form errors in these components were extremely small, the accuracy of the machines was not required to match this level. Possibly the first example of micro machining was the ruling engine for producing diffraction gratings as the machine tolerances were as high as the period of the gratings produced [3]. Micro milling developed as a scaled down version of the traditional milling machine which had been a staple machine in machine shops for making metal components. With the proliferation of computer numerical controlled (CNC) machining from the 1960's and 70's the accuracy and throughput of machines greatly increased. Another important development was the air bearing spindle and air bearing stages which allowed far smoother operation than standard ball bearing contact systems. The ability to machine glass to a mirror finish without using a polishing step was first demonstrated by Bifano in 1991 by machining in a regime known as the ductile mode regime [4]. This opened the way for structures to be directly machined into glass without the need for costly and limiting polishing steps.

This chapter will survey different types of physical machining that can be applied to integrated optics. Special focus will be given to the techniques that are used to fabricate the devices in this thesis. This will include information such as the best achieved surface roughness to give an indication of the progress of the field and allow comparisons between processes. The concept of the ductile-brittle transition and its importance to glass machining will be discussed. Theories explaining this transition in the literature will be looked at. Competing and complementary glass manufacturing techniques to physical machining will also be explained. This will allow the pros and cons of physical machining to be better understood. A section on the metrology techniques used to measure surfaces and structures will also be included. This will outline the basic principles of the metrology equipment used in this work and the performance capabilities of each instrument.

2.2 Definition of surface features

The following section aims to explore some of the surface features that can occur following machining. No machined surface is perfect and the objective is to ensure that the machining techniques selected can allow the surfaces to meet the specifications required for their application.

2.2.1 Surface feature characterization

Overall shape deviations from the planned shape over an extended area are known as 'form errors'. Depending on the device some parts of the geometry may have more critical form requirements than others. Figure 1 shows an example of profile exhibiting form error around a notional design line at y=0.

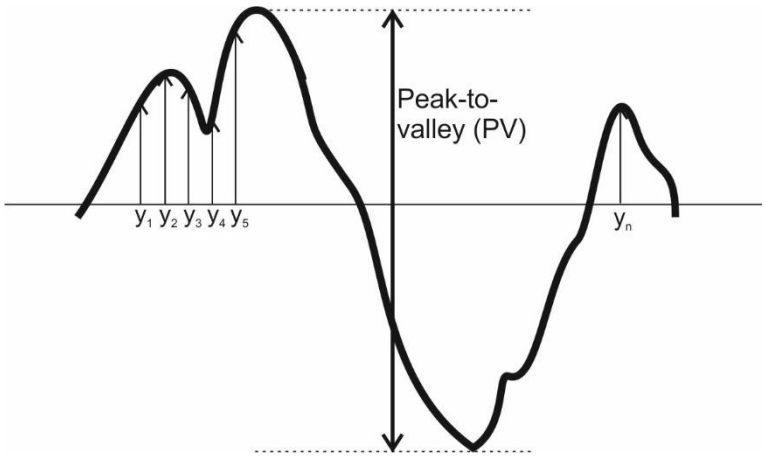

Figure 1. Surface profile illustrating how error parameters are calculated.

Errors in form are often expressed as the peak to valley (PV) error which is the distance between the highest and lowest point on the surface. The root mean square error (RMS) is another commonly used specification and is often expressed as S_q for 2D areal data and R_q for profile data. R_q is defined by equation (1) for a flat surface with a design shape of y_{design}.

$$R_q = \sqrt{\frac{1}{n}\sum_{i=1}^{n}(y_i - y_{design})^2} \qquad (1)$$

The arithmetic average R_a for a profile and S_a for a surface is another common specification defined by equation.

$$R_a = \frac{1}{n}\sum_{i=1}^{n}\left|y_i - y_{design}\right| \qquad (2)$$

Any device in the thesis which has a surface which interacts optically with light, such as the whispering gallery device in Chapter 7 requires careful attention to the machining in order to reduce surface roughness.

Form errors are more likely caused by machine performance rather than the nature of the machining process. Waviness describes elements of shape deviation with higher spatial frequency than form errors. The boundary between waviness and form is not well defined however waviness generally has a periodic nature and is often caused by machine oscillations such as 'chatter' [5].

Roughness describes the high spatial frequencies that are often a direct result of the microscopic nature of the machining process, whether mechanical, thermal or chemical. Rough surfaces are diffuse and will scatter light over wide angles. Rough surfaces may be either isotropic or anisotropic with a preferred direction. Chapter 3 will look at how surface roughness causes scattering and quantify the effect. The spatial frequency band that constitutes roughness may differ depending on the application. For optical applications a range of 10^1 to 10^6 mm^{-1} is often considered to be classified as roughness [6].

2.2.2 Chipping, scratching and cracking

While roughness is considered be fairly consistent over the optical surface, more irregular defects may be found. These are sometimes known as cosmetic defects but can cause poor optical performance. Chips are areas where a part of the material has broken off as a clump leaving a void behind. They may be caused by poor machining or defects in the workpiece material. Chips with dimensions larger than the size of a waveguide can cause serious losses in optical devices if they occur near the mode position. For this reason chipping in critical places must be controlled whilst in other places it can be tolerated. Chips may occur more often in certain areas. During dicing, chipping where the tool first contacts the surface (known as topside chipping) is common. Scratches are long surface features often found after abrasive machining. Standards exist to classify surfaces based on the size and density of scratches [7]. Cracks are volume features which are often present after aggressive machining. They may leave the optic vulnerable to mechanical stresses and chemical ingress.

2.2.3 Surface contamination

Many tool based machining methods have the possibility of leaving tool particles embedded in the surface. Tools which rely on ion bombardment of a surface may leave an implanted layer of

ions at some distance determined by the ion energy below the surface [8]. A targeted chemical etch may be able to remove the contamination from the surface.

2.2.4 Material movement

When machining a surface containing boundaries between materials it may be possible to move particles from one surface region to another. This is more likely in contact machining with large contact areas such as polishing. This type of contamination may be more difficult to remove chemically. This material movement or reflow is commonly exploited in polishing but degrades performance in optical devices.

2.3 Physical micromachining techniques for integrated optics

2.3.1 Grinding

Grinding is a high removal rate process making it popular for initial 'roughing' operations. Grinding uses a rapidly rotating tool with multiple small elements to remove material. Cup wheel tools are commonly used to shape spherical and planar optics prior to polishing [9]. This is shown in Figure 2.

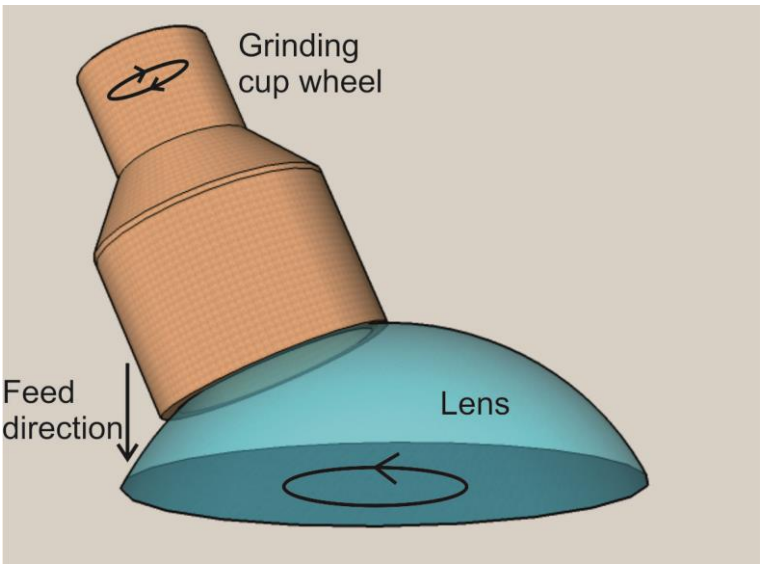

Figure 2. Schematic of grinding a convex lens with a diamond cup wheel tool.

Grinding can cause sub-surface damage whereby even a surface which appears smooth can have a damaged layer due to the machining forces involved [9]. This layer must then be removed, often with a polishing step which will be discussed in the next section.

2.3.2 Polishing

Chemical mechanical polishing of glass is a technique where a polishing pad is used in conjunction with slurry to remove material and generate smooth surfaces. It is both a chemical process and a mechanical process with removal requiring both speed and pressure. Polishing is the method used to fabricate bulk optics such as lenses and prisms, however it has found applications in waveguide facet and surface polishing. Traditionally polishing was done with a lapping plate larger than the optic to be polished. More recent technology uses a smaller tool which is able to fabricate aspheres and free form shapes [10]. Polishing is capable of generating very smooth surfaces however it is difficult to produce structures with small lateral dimensions. Polishing will also tend to change the form of a component unless feedback from metrology data is used.

2.3.3 Ultrasonic machining

Ultrasonic machining uses an abrasive slurry and ultrasonically actuated tool to remove material. Ideally there is no physical contact between the tool and workpiece [3]. Typically a shaped tool, known as a sonotrode is fed into the workpiece, either to produce a negative shape of the tool or to follow a contoured toolpath [11]. The vibration amplitude is typically around 25 µm and the transducer has a frequency of 0.1 to 40 kHz. The machining pressure is low which has made it popular for machining brittle materials including glass. While ultrasonic machining is the best technique for reducing surface damage it has not yet achieved very low surface roughness's with reports of an Ra of 300 nm achieved for a hole drilled in to glass [12]. Figure 3 shows the two modes of ultrasonic machining.

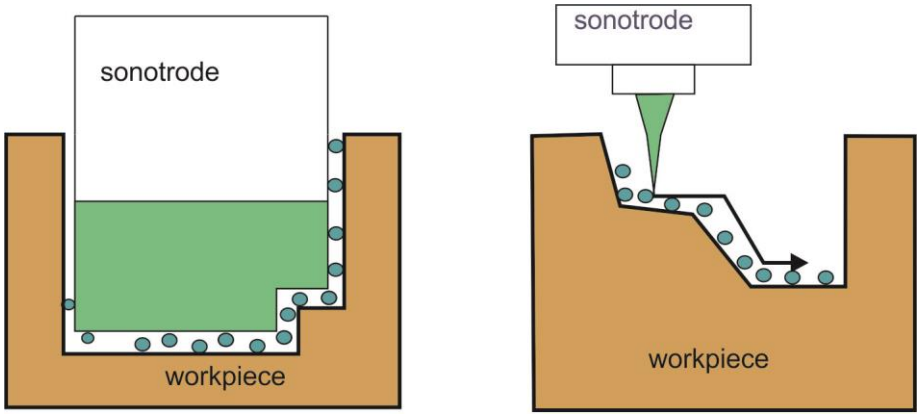

Figure 3. Diagram showing the two modes of ultrasonic machining.

Ultrasonic actuation can be used to assist other machining processes. This changes the dynamics of the cutting process and can also allow more lubricant to reach the cutting end. Moriwaki *et al.* reported an increase of a factor of 7 in the critical depth of cut when ultrasonic actuation was

used in combination with a diamond turning process [13]. Kuo found that when used to assist milling it improved the depth of cut at the expense of surface roughness [14].

2.3.4 Dicing

Dicing was adopted by the semiconductor industry as a technique to separate dies, however it can also be applied to glass to leave surfaces with surface quality approaching a polished surface. Dicing is similar to cutting with a circular saw in that a rapidly rotating blade is translated along a sample to produce a straight channel of a uniform depth. Figure 4 illustrates the principles of the dicing process.

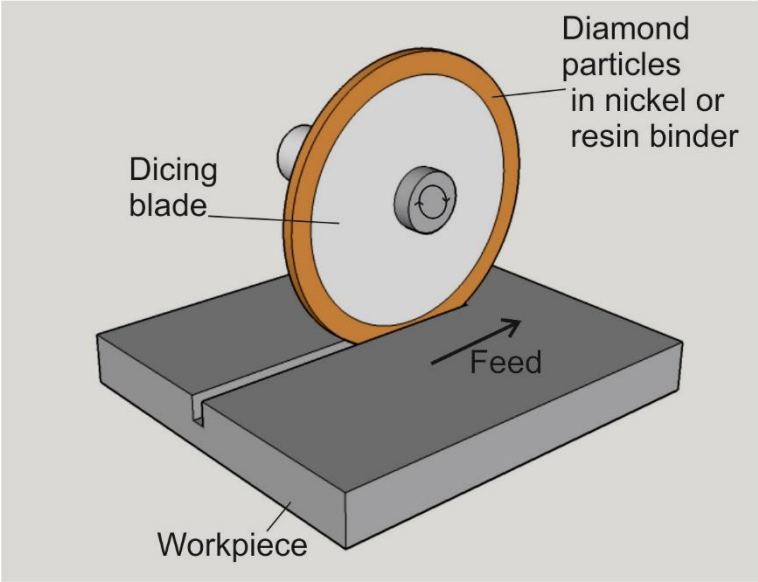

Figure 4. Schematic of dicing process.

Diamond particles are impregnated into a binder at the cutting edge of the dicing blade; the binder is usually nickel or resin. When a diamond particle becomes blunted, it is ripped out of the binder and in this way the blade is replenished. Plaza *et al.* showed the potential for producing high aspect ratio structures in glass [15]. Within our group Carpenter *et al*. showed that dicing could be adopted for dicing waveguide facets with surface roughness of Sa 4.9 nm [16]. This avoided a time consuming polishing process. Dicing is generally limited to fabricating straight channels which pass through the full length of the substrate although a 'plunge' mode can be used with careful parameter optimization to make structures in the centre of a workpiece. Dicing is utilized in the dual cantilever device described in Chapter 5. It is also used more generally during the work to dice chips out of the bulk wafer.

2.3.5 Diamond point turning

The fundamental concept of diamond turning is an extension of the 'turning' process on a lathe. A rotationally symmetric piece is fabricated by rotating and bringing it into contact to the tool. For ductile materials diamond turning has allowed components to be made deterministically with surface roughness as good as polished surfaces. With CNC control virtually any component shape is possible providing it has rotational symmetry. The machine must have ultraprecise translation stages to ensure that the depth of cut can be carefully controlled. Figure 5 shows a schematic of the diamond turning process.

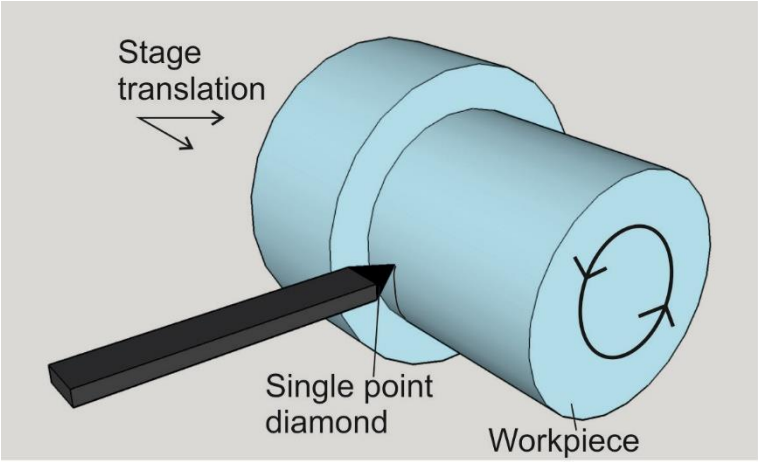

Figure 5. Diamond turning process.

Either single crystal diamond or PCD is used as the cutting tool [17]. Diamond turning is extremely common for metal fabrication but is difficult to apply successfully to glass [18]. Ravindra *et al.* turned quartz using diamond however the surface roughness of 45 nm did not approach that which can be achieved on metal materials [19]. Brehm *et al.* used substrate heating whilst turning to make the glass behave closer to a ductile material during machining. In a variety of glasses including BK7 (but not pure silica) they claimed to demonstrate surfaces with finishes approaching polished surfaces [20]. It is not known how this approach could be adapted for the higher softening point of silica or whether thermal expansion could be compensated for to allow micron precision. New machine control developments mean that non-axially symmetric components can be fabricated [21]. This is made possible by quickly moving the substrate multiple times per revolution of the tool.

2.3.6 Micromilling

Micromilling is a scaled down version of the common mill found in most machine shops. The tool axis is orientated perpendicular to the workpiece surface giving more geometric freedom than for dicing. Figure 6 shows a schematic of the milling process.

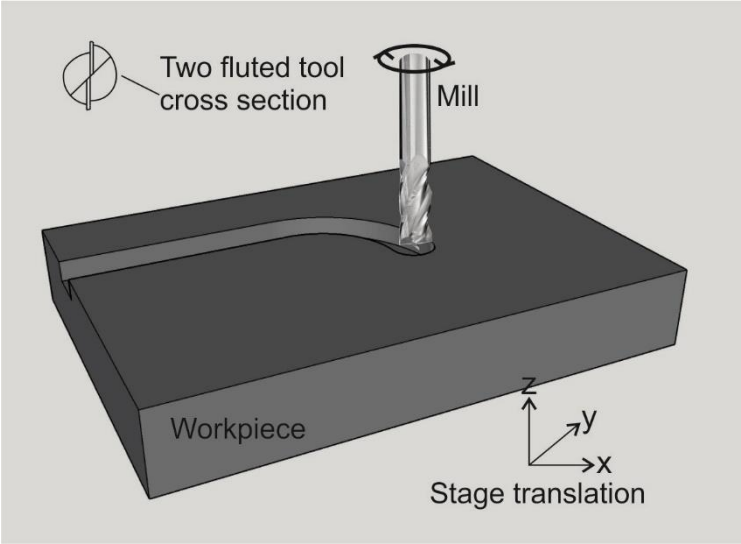

Figure 6. Schematic of micromilling.

Slotmills are milling tools capable of drilling vertically. These increase the variety of structures that can be fabricated. This extra freedom generally comes at the price of lower throughput and shorter tool life, when the process is compared to dicing. Fluted tools have sharp cutting edges and helical channels to help coolant reach the cutting zone and improve debris removal. Tools must be made from strong materials with good thermal conductivity to remove heat from the cutting zone. Tungsten carbide is one popular choice as it fulfils both of these criteria. The tool can also have an amorphous diamond cutting surface to improve cutting performance and extend tool life. Some newer milling processes use tools that are composed of diamond cutters in a binding material. Examples of this include PCD tools and bonded cubic boron nitride (CBN) tool which can be dressed to custom shapes [22]. The fabrication and milling with PCD tools will be demonstrated in a later chapter.

2.4 Principles of ductile mode machining

When light is required to interact optically with a surface this places requirements on the quality of the surface. As will be shown in Chapter 3 the root mean square error (RMS) of the surface roughness is an excellent indicator of the amount of scattering that can be expected, although the spatial frequency content and correlation length of the roughness are also important to consider. To understand how smooth surfaces are produced when machining it is necessary to understand

the physical material removal mechanisms. Glass, which is a brittle material will behave very differently during machining from ductile material such as metals [23]. During milling a cutting edge will continually remove chips from the material. This process is illustrated in Figure 7 The material will initially deform, as every substance is elastic to some extent. When the shear stress becomes too high material will be removed and energy dissipated. The dynamics of machining are complicated with variation in machine performance between studies making direct comparisons difficult.

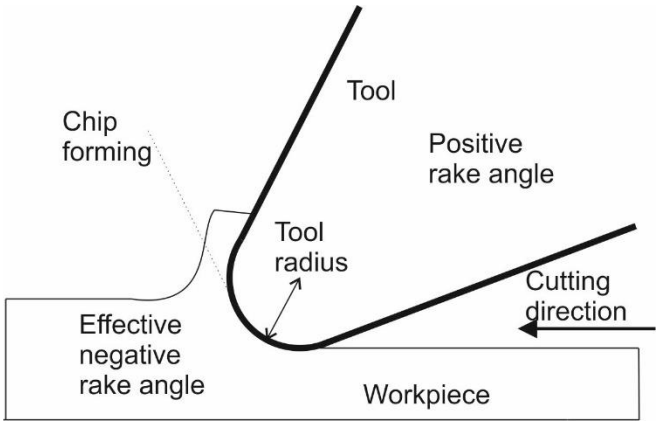

Figure 7. Diagram showing chip removal in brittle materials.

The first use of the term 'ductile machining' in the literature was by Bifano *et al*. [4]. They considered that in the ductile regime material removal occurred by a plastic flow effect, avoiding fracturing. Bifano employed a simple argument to explain the dependence of the ductile-brittle transition based on energetics. To plastically deform a surface the energy E_p is proportional to the volume deformed.

$$E_p = \sigma_y V_p \tag{3}$$

Here σ_y is the yield stress of the material. V_p is the volume of the material deformed. The energy to form a crack is given by

$$E_f = GA_f \tag{4}$$

A_f is the area of the new surface created by the crack propagation. G is the Griffith crack propagation parameter which is a measure of the resistance to fracture. As

$$V \propto d^3 \tag{5}$$

$$A_f \propto d^2 \tag{6}$$

Where d is the depth of cut, we can show that the ratio of energies between the two competing removal processes is

$$\frac{E_p}{E_f} \propto d \tag{7}$$

Thus, as the depth of cut increases it will cost relatively less energy for cracks to propagate. This can be used to explain why cracking becomes more common with greater depths of cut, or conversely why with sufficiently shallow removal it is possible to remain in the plastic removal regime.

2.5 Ductile mode micromilling

While much of the research into ductile mode machining has been conducted for diamond turning, however micromilling has received attention too. Arif *et al.* have produced an analytical result based on crack propagation that provides a critical feed rate per edge [24]. Figure 8 shows that for side milling the chip thickness changes from a minimum at the start of the cut moving towards a maximum at the end of the cut due to the feedrate of the tool. According to this notion brittle fracture can be tolerated as long as it is contained within the volume that will be removed anyway. If chips are allowed to propagate further they will result in chipping and roughness on the machined surface.

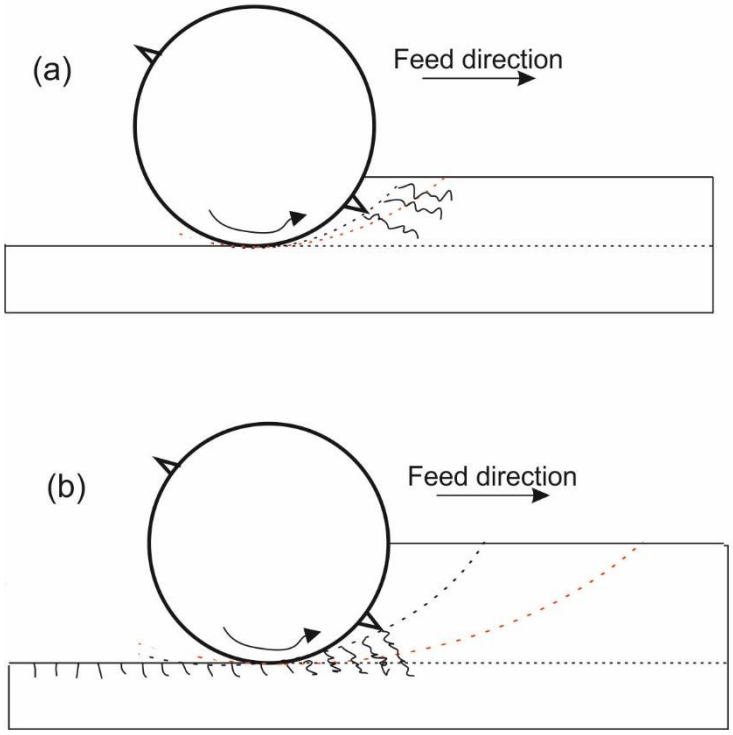

Figure 8. A two fluted tool cutting a chip (a) Shallow cuts avoid cracks in finished workpiece (b) When the chip thickness becomes too large cracks may propagate into the finished surface.

Arif *et al*. used information about the behaviour of materials from indenter experiments to develop the model of ductile machining. Indentation hardness tests are a common way of characterizing the hardness of materials by indenting them with a sharp tool tip shaped as a

pyramid or ball. The indentation is then measured. An indentation test will produce a plastic deformation for small loads. If the load is increased lateral and meridional cracks will form. As much data is available from indention tests for various materials this approach holds promise that initial machining parameters could be estimated from data available in the literature. Tapered cutting using a single point tool is slightly more realistic way of finding the ductile-glass transition than single point indenture tests. In these tests a tool is translated along a surface with gradually increasing depth. Fang *et al.* [25] found a critical depth of cut of 62 nm for BK7 glass which gives an indication that the chip size for ductile machining is small.

A typical milling tool has flutes to aid the cut and these can be characterized by a rake angle which is considered an important choice when selecting a cutting tool for a material. If the chip thickness is of the order of the cutting tool radius an effective negative rake angle is present [25]. Fang *et al.* claimed it is this effective negative rake angle that allows necessary hydrostatic pressure for plastic shear deformation to be the primary material removal mechanism.

While this analysis was derived for fluted tools, another class of tools exists where the tool is formed from many small cutting points. Polycrystalline diamond (PCD) and cubic boron nitride (CBN) are examples of materials from which this kind of tool is commonly made. This form of machining has elements of both traditional milling and grinding operations. The first work to apply PCD tools to glass was from Morgan *et al.* [26]. They formed tools using electrodischarge machining and subsequently used those tools to machine a groove in Ultra Low Expansion glass to a depth of 1.5 µm in the ductile regime. This approach had the additional advantage that the tool shape and dimension could be customized.

Most of the literature describes the ductile-transition critical-depth of cut for milling operation as being ~1 µm in glass materials [22]. More recent work by Carpenter *et al.* [27] has reported smooth surfaces for much deeper cuts. As discussed a best figure of 3 nm Sa with a 17 µm deep groove was achieved in FHD silica in our group. The ability to reach this depth in a single cut reduces the number of passes that must be made. These results were optimized by a feedrate of 5 nm/rev and a spindle speed of 40 krpm. They found a significant increase in roughness and brittle mode machining when the spindle speed was reduced to 10 krpm. This could have been because the chip size became larger and the critical depth of cut exceeded.

2.6 Microfabrication techniques

Physical machining is not the only way that glass can be machined. Many techniques have been adopted from the microelectronics industry based around photolithographic patterning. Due to the small scale of many integrated optic features and the desire for high throughput these

methods have become a popular choice. With photolithography there is usually no additional cost between processing a wafer or a single chip, meaning devices can be batch fabricated. Much of the equipment used in this type of processing requires cleanroom housing which can be expensive or difficult to access. As most of the removal processes remove a constant thickness of material it is difficult to make truly 3d shapes such as a channel with a variable depth.

2.6.1 Photolithography

Photolithography is a process by which a layer of photo sensitive polymer, known as photoresist, is patterned by exposure to light through a photo mask [3]. With positive photoresists, the exposed photoresist becomes soluble in an aqueous developer and is removed. When negative photoresists are used, unexposed portions are soluble in an organic developer. For further processing the patterned photoresist may be a sufficient mask. For other more aggressive processes another harder mask material, such as aluminium may be deposited and the photo resist removed. The pattern of the photoresist is then transferred to the substrate through a subtractive process. Common examples of this include wet and dry etching.

2.6.2 Dry etching

Reactive ion etching (RIE) is a subtractive technique in which a plasma is used to bombard a surface removing material [3]. The plasma is created from a high energy RF field and contains ions that are chemically reactive with the substrate. The substrate pattern will build up a negative charge due to absorption of electrons which have high mobility in the field. This will subsequently attract ions which will attack the surface and react. As the ion motion is directional in the electric field the etch profile tends to be anisotropic which is desirable for many applications. A variant of this technique with faster etching rates is called inductively coupled plasma (ICP) etching. In an ICP etcher a time varying magnetic field is used to generate an electric field in the gas. Dry etching can be controlled to give anisotropic etch profiles which are desirable for many applications. Li *et al*. optimized the plasma enhanced etching process to fabricate waveguides in silica with surface roughness of 10 nm [28]. Techniques for dry etching vertical sidewalls exist but often compromise the surface texture. A patented silicon etch known as the Bosch process alternates between an anisotropic plasma etch and deposition of a chemically inert passivation layer. As the plasma etch contains ions these attack the substrate from a vertical direction and erode the passivation layer at the bottom but not the sidewalls of the trench. With time, new unpassivated sidewalls will be created so the cycle must be repeated. This leads to a layered (or scalloped) structure to the sidewall which is not generally beneficial to optical applications [29]. Dry etching applies virtually no force to the substrate so can be to produce very high aspect ratio delicate structures. Dry

etching is a chemical process which means recipes must be designed based on the material to be etched. Some optically important materials such as lithium niobate suffer from material redeposition and non vertical sidewalls after dry etching [30]. There are non-chemical processes that etch using physical processes such as argon ion etching [3].

2.6.3 Wet etching

Wet etching consists of immersing a substrate in a chemical solution which reacts with exposed areas. Wet etching can be isotropic and etch with equal rates in all directions or be anisotropic. The type of etching which occurs is usually determined by crystalline properties of the material. Figure 9(a) shows the etch profile obtained after isotropic wet etching. In this case the etch distance from the mask opening is constant. This is the situation when etching most glasses with hydrofluoric acid. Figure 9(b) shows a possible anisotropic etch profile. This is the case with silicon etching with potassium hydroxide (KOH) when the mask is aligned with a certain crystallographic plane orientation. Tetramethylammonium hydroxide (TMAH) is another wet anistropic silicon etch which shows less etching of silica than KOH [3]. Anisotropic etching may limit the application of wet etching for certain crystalline materials such as lithium niobate.

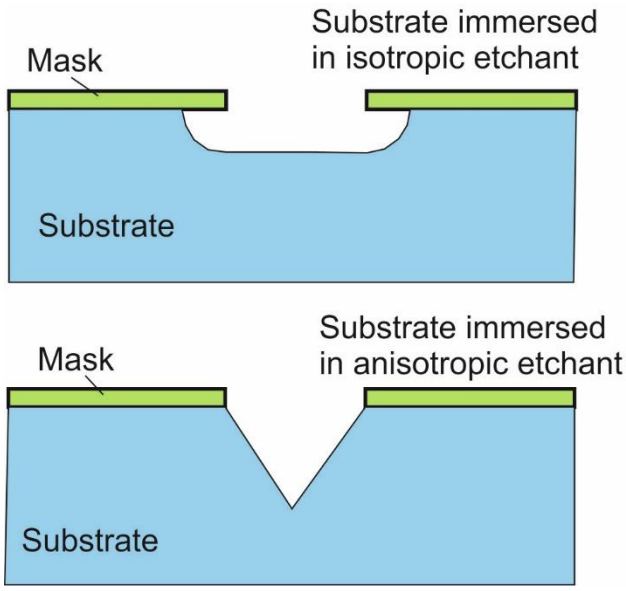

Figure 9. (a) Demonstration of isotropic etching (b) A possible etch profile following anisotropic etching.

Hydrofluoric acid is one of the few chemicals which will etch silicon dioxide. It also has the advantage of being substantially unreactive with silicon, meaning the etch will terminate once it reaches a silicon surface. Pure hydrofluoric acid is rarely used by itself to etch glass as the etch speed is too fast to control and the etched surfaces are rough. Typically the etchant is buffered by the addition of ammonium fluoride or hydrochloric acid. Buffered HF can produce extremely

smooth surfaces although accurate form control can be difficult [31]. One way of compensating for the lack of control over etch depth is to monitor the device optically whilst etching. Potassium hydroxide wet etching of silicon is used to etch the silicon substrate to release glass structures (described in the device fabrication Chapters 4 and 5). KOH will still etch silica at rate of ~100 nm/hour at 80°C so will affect glass surfaces, although it will etch silicon much faster (approximately 1 µm/min) [3].

2.6.4 Ion beam milling

Ion beam milling is a technique whereby ions from a source are focused and directed towards a sample. Gallium is a common choice of ion as it has a high mass which increases surface ablation and can also be readily ionized when heated to the liquid form. As the beam can be focused to a very small spot, ion beam milling is capable of very high resolution machining: structures with length scales 10-15 nm can be produced [11]. The machining rate is however slow and on the order of 1 µm/hr in silica glass [32]. Ion beam machining is often used as a final polishing process for optics and is capable of generating smooth surfaces with sub nanometer surface roughness when argon ions are used as the source.

2.6.5 Laser machining

Laser machining can be used to ablate or melt the surface of a substrate. For silicon dioxide machining it is necessary to use a wavelength at which the glass will absorb and for this reason carbon dioxide lasers with a wavelength of 10.6 µm are often used. Hunger *et al*. used CO_2 laser machining to machine concave lenses into silica [33] with an Ra of 0.2 nm. The low value of surface roughness is due to the laser energy causing reflow of glass, surface tension then creates a smooth surface. It is possible to machine glasses with wavelengths of light at which they are normally transparent using the nonlinear process of two photon absorption. Femtosecond lasers are commonly used for this application as they can generate the necessary intensities for the non-linear processes to occur. This form of laser machining has the advantage that the material modification will only occur at the focal point of the laser meaning that interior structures can be produced in glass. Femtosecond machining can be combined with wet etching to produce channels inside a glass substrate [34]. The laser writing will modify the glass increasing its chemical sensitivity to HF acid, so that the exposed glass can be etched away.

2.7 Metrology

When measuring surfaces it is important to understand the basic principles of the tools as these can affect the results obtained.

2.7.1 Scanning electron microscope

Scanning electron microscopy is a technique whereby electrons are used as a probe to measure the topography and composition of a surface. A focused beam of electrons is scanned across a surface by using magnetic coils in a 'raster' path. Figure 10 shows a schematic of the SEM.

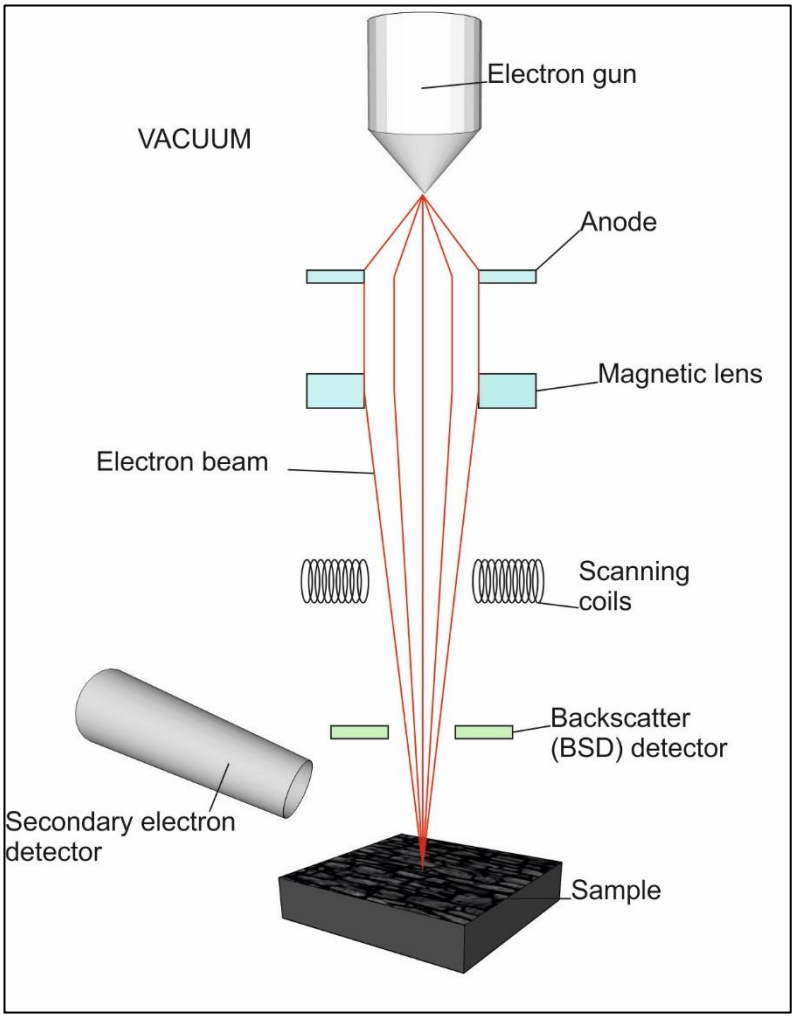

Figure 10. Diagram showing core elements of SEM.

The SEM is capable of generating images with spatial resolution of around 10 nm depending on the size of the spot used. Although the SEM can resolve surface roughness and features it is not easy to get a numerical estimate of the surface roughness data. The SEM can operate in two modes depending on whether the sample is conductive. If an electrically insulating sample is imaged it is necessary to have a gas present to help with removal of electrons from the substrate.

For a conducting sample high vacuum mode can be used which allows higher resolution imaging. For this reason insulating samples are often coated with a thin (~10 nm) layer of gold prior to imaging. Various detectors can be used which make use of the different signals given off by the sample.

1. The secondary electron detector has the highest spatial resolution and detects electrons knocked out of orbit by the incident beam.
2. The backscatter detector (BSD) which detects electrons scattered by atoms. This effect has a larger interaction volume but has a dependence on the atomic number, Z of the material meaning it can be used to give composition information about the sample.

X-ray emission. When an electronic transition is induced an x-ray can be emitted with energy corresponding to the difference in energy between the electron orbitals involved. The possible transitions can be combined to provide a unique 'fingerprint' for an element. This is known as EDX (electro dispersive spectroscopy) and can provide chemical analysis of the sample.

2.7.2 White light interferometer (Zemetrics Zescope)

The Zescope makes use optical interference to image and quantify a small area of a surface. It is especially useful for quantitative analysis of surface roughness. Figure 11 shows a diagram of the Zescope.

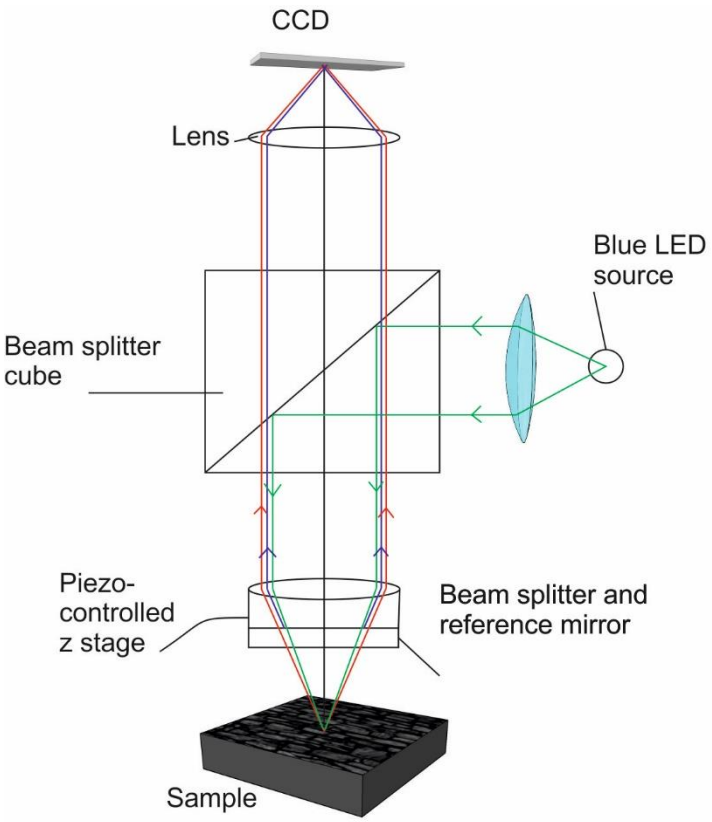

Figure 11. Schematic of a white light inteferometer. A white light source beam (green) is split into a reference beam (blue) and a test beam (red) by a reference mirror. The test beam reflects off the sample surface and interferes with the reference beam on the surface of the CCD. Colour is used for the diagram and has no relation to wavelength.

The light source for the Zescope has a short coherence length. A beam splitter is used to split the beam into a test beam and reference beam. The test beam is reflected onto the sample and recombined with the test beam at the CCD (charge coupled detector). When the optical path length between the beams is close fringes will be present. By translating the sample fully through the coherence length of the source the output will feature an envelope peak containing interference fringes. So long as the sample is translated through a distance greater than the peak to valley length of the surface then the intensity from each CCD pixel can be processed to give the surface height at that position. This is illustrated in Figure 12 which shows how the surface profile results in a signal envelope with a varying position.

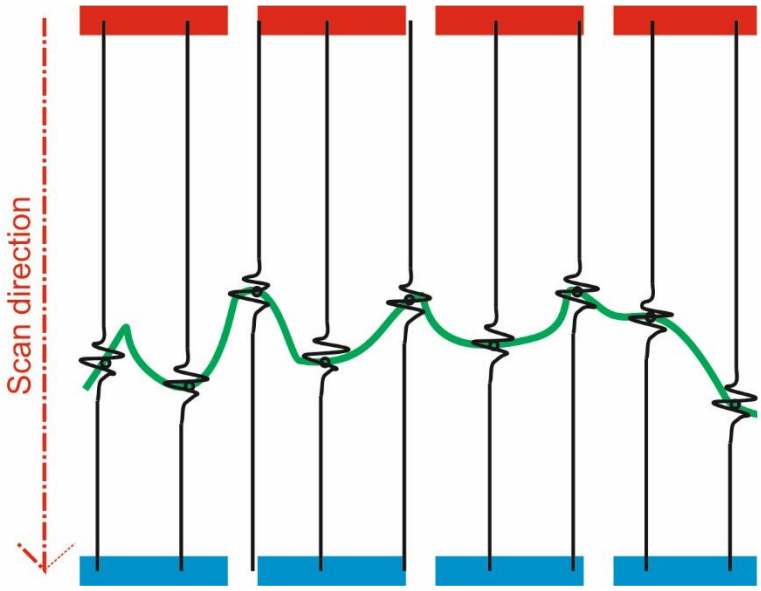

Figure 12. Output of pixel of CCD. By scanning over a distance greater than the peak to valley distance of the surface the interference fringes at each pixel can be used.

From a fit to the envelope in Figure 12, the height of the surface at a single point can be measured. When the x50 objective is used lateral resolution of ~ 600 nm is achievable allowing evaluation of the roughness at these high spatial frequencies [35]. At lower magnifications the tool is useful for measuring the shape of structures. A drawback of white light interferometry is that it can fail to return data when a surface is too rough or has too steep a gradient because the reflected beam is outside of the numerical aperture of the objective lens.

2.7.3 Profilometer (Tencor Alpha-Step)

The profilometer is an instrument which builds up a profile of a surface by dragging a probe across the surface. Deflections of the stylus are often measured electrically with a capacitance sensor [36]. Figure 13 shows the schematic of the profiler.

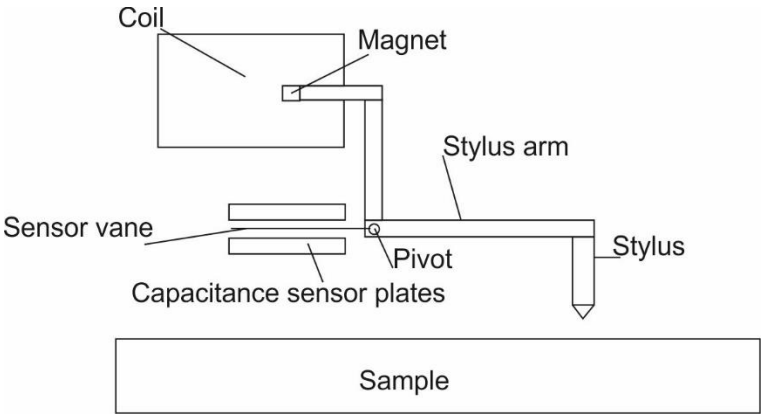

Figure 13. Schematic of stylus profiler.

The stylus tip which senses the surface is typically a conisphere as the shape allows the tip to smoothly ride the surface. The cone angle, which is often 60° sets a limit to the slope that the profilometer can measure. The instrument has a very high theoretical resolution however noise will limit this considerably. The radius of curvature of the stylus tip will cause some filtering of the high spatial frequency components of the surface. If the grooves in the surface are smaller than the stylus size, it will not be able to enter them which will limit the lateral resolution. Vertical resolution is limited by the mechanics and electronic readout including noise.

2.8 References

[1] J. Henderson, “Glass, and the Manufacture of Prehistoric and Other Early Glass Beads. Part I: Technical Background and Theory,” *Irish Archaeol. Res. Forum*, pp. 55–62, Jan. 1978.

[2] M. Daumas, *Scientific Instruments of the Seventeenth and Eighteenth Centuries*. Praeger Publishers, 1972.

[3] M. J. Madou, *Fundamentals of Microfabrication and Nanotechnology*, 2nd ed. CRC Press Ltd, 2011.

[4] T. Bifano, TG Dow and R. Scattergood, “Ductile-regime Grinding - A New Technology For Machining Brittle Materials,” *J. Eng. Ind. Asme*, vol. 113, no. 2, pp. 184–189, May. 1991.

[5] B. Braunecker, R. Hentschel, and H. J. Tiziani, *Advanced Optics Using Aspherical Elements*. SPIE Press, 2008.

[6] J. M. Bennett and L. Mattsson, *Introduction to surface roughness and scattering*, 2nd Ed. Optical Society of America, 1989.

[7] J. H. Mcleod and W. T. Sherwood, “A Proposed Method of Specifying Appearance Defects of Optical Parts,” *J. Opt. Soc. Am.*, vol. 35, no. 2, p. 136, Feb. 1945.

[8] C. Lehrer, L. Frey, S. Petersen, M. Mizutani, M. Takai, and H. Ryssel, “Defects and gallium contamination during focused ion beam micro machining,” in *International Conference on Ion Implantation Technology*, pp. 695–698, Sept. 2000.

[9] S. Li, Z. Wang, and Y. Wu, “Relationship between subsurface damage and surface roughness of optical materials in grinding and lapping processes,” *J. Mater. Process. Technol.*, vol. 205, no. 1–3, pp. 34–41, Aug. 2008.

[10] D. D. Walker, R. Freeman, G. McCavana, R. Morton, D. Riley, J. Simms, D. Brooks, E. Kim, and A. King, "Zeeko/UCL process for polishing large lenses and prisms," in *Large Lenses and Prisms*, pp. 106–111, Feb. 2002.

[11] J. A. McGeough, *Micromachining of Engineering Materials*, 1st ed. New York/Basel: CRC Press, 2002.

[12] D. Kremer, S. M. Saleh, and S. R. Ghabrial, "The state of the art of ultrasonic machining," *CIRP Ann. - Manuf. Technol.*, vol. 30, no. 1, pp. 107–10, 1981.

[13] T. Moriwaki, E. Shamoto, and K. Inoue, "Ultraprecision Ductile Cutting of Glass by Applying Ultrasonic Vibration," *CIRP Ann. - Manuf. Technol.*, vol. 41, no. 1, pp. 141–144, Jan. 1992.

[14] C. Kuo, K; Tsao, "Rotary ultrasonic-assisted milling of brittle materials," *Trans. Nonferrous Met. Soc. China*, vol. 22, no. 3, pp. 793–800, Dec. 2012.

[15] J. Plaza, M. Lopez, and A. Moreno, "Definition of high aspect ratio glass columns," *Sensors Actuators A Phys.*, vol. 105, no. 3, pp. 305–310, Aug. 2003.

[16] L. G. Carpenter, H. L. Rogers, P. A. Cooper, C. Holmes, J. C. Gates, and P. G. R. Smith, "Low optical-loss facet preparation for silica-on-silicon photonics using the ductile dicing regime," *J Phys D Appl Phys*, vol. 46, no. 47, p. 475103, Nov. 2013.

[17] W. B. Lee and B. C. F. Cheung, *Surface Generation in Ultra-precision Diamond Turning: Modelling and Practices*, 1st ed. John Wiley & Sons, 2003.

[18] A. E. Gee, R. C. Spragg, K. E. Puttick, and M. R. Rudman, "Single-point diamond form-finishing of glasses and other macroscopically brittle materials," in *Commercial Applications of Precision Manufacturing at the Sub-Micron Level*, pp. 39–48, Apr. 1992.

[19] D. Ravindra and J. Patten, "Ductile regime single point diamond turning of quartz resulting in an improved and damage-free surface," *Mach. Sci. Technol.*, vol. 15, no. 4, pp. 357–375, Oct. 2011.

[20] R. Brehm and J. Haisma, "Turning of transparent optical-glass with a single-point tool," *J. Opt. Soc. Am.*, vol. 70, no. 12, p. 1608, 1980.

[21] S. R. Patterson and E. B. Magrab, "Design and testing of a fast tool servo for diamond turning," *Precis. Eng.*, vol. 7, no. 3, pp. 123–128, Jul. 1985.

[22] C. J. Morgan, R. R. Vallance, and E. R. Marsh, “Micro machining glass with polycrystalline diamond tools shaped by micro electro discharge machining,” *J Micromech Microeng*, vol. 14, no. 12, pp. 1687–1692, Dec. 2004.

[23] B. K. A. Ngoi and P. S. Sreejith, “Ductile Regime Finish Machining - A Review,” *Int. J. Adv. Manuf. Technol.*, vol. 16, no. 8, pp. 547–550, Jul. 2000.

[24] M. Arif, M. Rahman, and W. Yoke San, “Analytical model to determine the critical feed per edge for ductile–brittle transition in milling process of brittle materials,” *Int. J. Mach. Tools Manuf.*, vol. 51, no. 3, pp. 170–181, Mar. 2011.

[25] F. Z. Fang and G. X. Zhang, “An experimental study of optical glass machining,” *Int. J. Adv. Manuf. Technol.*, vol. 23, no. 3–4, pp. 155–160, Feb. 2004.

[26] C. J. Morgan, R. R. Vallance, and E. R. Marsh, “Micro-machining and micro-grinding with tools fabricated by micro electro-discharge machining,” *Int. J. Nanomanuf.*, vol. 1, no. 2, pp. 242–258, 2006.

[27] L. G. Carpenter, P. A. Cooper, C. Holmes, C. B. E. Gawith, J. C. Gates, and P. G. R. Smith, “Nanoscale roughness micromilled silica evanescent refractometer,” *Opt Express*, vol. 23, no. 2, p. 1005, Jan. 2015.

[28] W. T. Li, D. A. P. Bulla, J. Love, B. Luther-Davies, C. Charles, and R. Boswell, “Deep dry-etch of silica in a helicon plasma etcher for optical waveguide fabrication,” *J. Vac. Sci. Technol. A Vacuum, Surfaces, Film.*, vol. 23, no. 1, p. 146, Dec. 2005.

[29] S. Franssila, *Introduction to Microfabrication*. John Wiley & Sons, 2010.

[30] K. Shima, N. Mitsugi, and H. Nagata, “Surface precipitates on single crystal $LiNbO_3$ after dry-etching by CHF_3 plasma,” *J. Mater. Res.*, vol. 13, no. 03, pp. 527–529, Jan. 2011.

[31] H. Lee, T. Chen, J. Li, O. Painter, and K. J. Vahala, “Ultra-low-loss optical delay line on a silicon chip.,” *Nat. Commun.*, vol. 3, p. 867, Jan. 2012.

[32] A. A. Tseng, “Recent developments in micromilling using focused ion beam technology,” *J Micromech Microeng*, vol. 14, no. 4, pp. 15–34, Apr. 2004.

[33] D. Hunger, C. Deutsch, R. J. Barbour, R. J. Warburton, and J. Reichel, “Laser micro-fabrication of concave, low-roughness features in silica,” *AIP Adv.*, vol. 2, no. 1, p. 012119, Jan. 2012.

[34] A. Marcinkevičius, S. Juodkazis, M. Watanabe, M. Miwa, S. Matsuo, H. Misawa, and J. Nishii, “Femtosecond laser-assisted three-dimensional microfabrication in silica,” *Opt Lett*, vol. 26, no. 5, p. 277, Mar. 2001.

[35] “Zemetrics, Zescope Specification.” 2010.

[36] “KLA-Tencor, "P-16 Specification,” 2007.

Chapter 3: Integrated photonics

3.1 Introduction

Integrated photonics (IP) is concerned with the integration of multiple optical elements in a single planar platform. The fundamental element in integrated optics is the waveguide as this allows light to be directed between other components, ideally with a low level of energy loss.

The motivation for moving from free space optics with bulk components such as lenses, beamsplitters and diffraction gratings to integrated optics is that it can offer a number of benefits both in device performance and in cost/size and environmental stability. For example a laser beam moving through the air can be affected by changes in the position of optics caused by vibration and temperature variation [1]. A free space setup will often be large and bulky and may need to be mounted on an anti-vibration table. By contrast an integrated optical device can be very small and not require any special mounting requirements.

This chapter will begin with the theoretical explanation of how waveguides guide light based upon Maxwell's equations of electromagnetism. This theory is built up in degrees of complexity by first looking at a symmetric slab waveguide, then showing how this is used to find the modes of the channel waveguide. Bragg gratings, which form a key part of the devices made, are then studied. A discussion of how the IP devices are used as sensors, actuators and in wavelength division multiplexing (WDM) systems follows. The key fabrication steps towards fabricating waveguides are discussed. Flame hydrolysis deposition (FHD) which is used to form the glass layers in this work is reviewed in terms of the equipment and process. The UV writing process used to define the channel waveguides is also covered.

3.2 Waveguide theory

3.2.1 Fresnel equations and Snell's law

When light travelling from a region of one refractive index to another encounters a boundary the fractions of light reflected and transmitted can be described by the Fresnel equations. Figure 14 shows the geometry of a plane wave encountering an interface between dielectric media. The plane containing the incident, reflected and transmitted rays defines the plane of incidence.

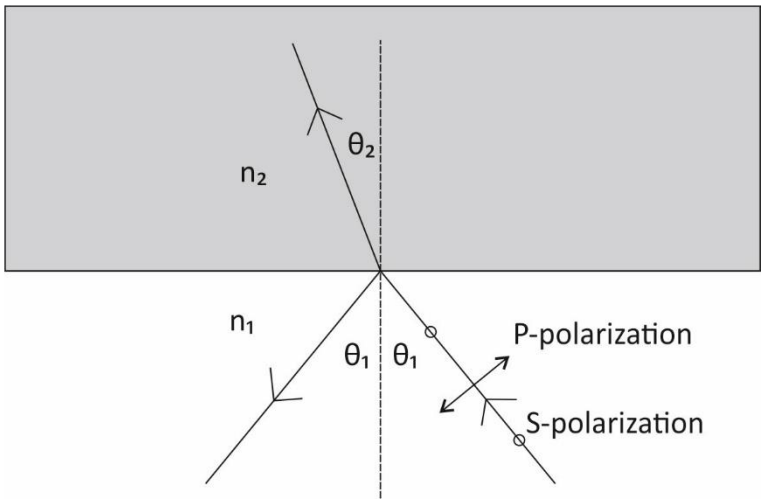

Figure 14. Reflection and transmission of light at an interface between dielectric media. P-polarized light has its E-field vector in the plane of incidence whilst the S-polarization is perpendicular to this.

Any plane wave can be decomposed into a superposition of linearly polarized plane waves and this is a necessary step to fully calculate the reflection and transmission coefficients. These results will be important in the analysis of the devices described throughout the thesis. The component of the light with its E-field parallel to the plane of the incidence is known as the P-polarization and the S-polarization is perpendicular to this. Using the Fresnel equations the reflectivity and transmitivity can be found for both polarizations as in equations (8) and (9) [2].

$$R_s = \left| \frac{n_1 \cos\theta_1 - n_2 \sqrt{1 - \left(\frac{n_1}{n_2} \sin\theta_1 \right)^2}}{n_1 \cos\theta_i + n_2 \sqrt{1 - \left(\frac{n_1}{n_2} \sin\theta_1 \right)^2}} \right|^2 \tag{8}$$

$$R_p = \left| \frac{n_1 \sqrt{1 - \left(\frac{n_1}{n_2} \sin\theta_1 \right)^2} - n_2 \cos\theta_1}{n_1 \sqrt{1 - \left(\frac{n_1}{n_2} \sin\theta_i \right)^2} + n_2 \cos\theta_1} \right|^2 \tag{9}$$

Where the angle of transmittance is related to the incident angle by Snell's law.

$$n_1 \sin\theta_1 = n_2 \sin\theta_2 \tag{10}$$

Figure 15 shows a plot of the Fresnel equations for light passing from a lower to higher refractive index. It shows that for a certain angle (55.3° for an air-silica interface) all of the 'p' polarization light is transmitted. This is known as Brewster's angle. Again, for silica at close to 0°, 3.7% of the

light is reflected for both polarizations. This is the common situation when light encounters a surface at normal incidence without any form of coating.

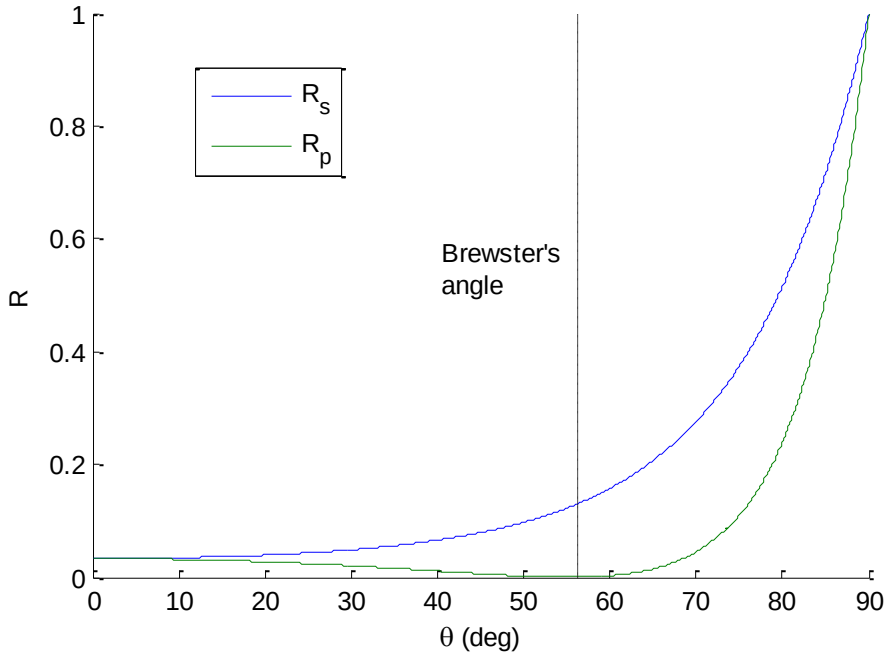

Figure 15. A plot of Fresnel's law for n_1 = 1 and n_2 = 1.445, light propagates from the lower refractive index to higher refractive index medium.

For light passing from higher refractive index to lower refractive a plot of the reflectance is shown in Figure 16 This is the situation when guiding light in an optical waveguide.

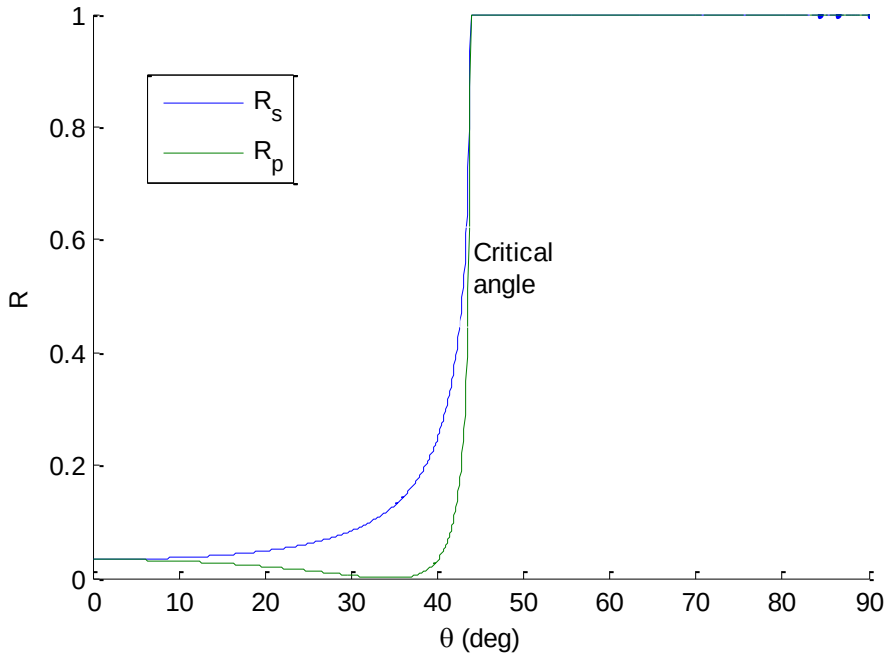

Figure 16. Fresnel equation for n_1 = 1.445 and n_2 = 1 light propagates from the higher refractive index to the lower refractive index.

For the case where $n_1 > n_2$ it can be seen that there is an angle above which no light is transmitted. Total internal reflection will begin when $\theta_2 = 90°$. The input angle for which this occurs is given by equation (11).

$$\sin\theta_1 = \frac{n_2}{n_1} \tag{11}$$

This provides the basis to how waveguides can in principle be used to propagate light from point to point as above this critical angle 100% of light will be reflected.

3.2.2 Maxwell's equations

The propagation of light can be explained using Maxwell's equations (12) - (15) first reported in 1861 [3]. They describe the dependence of the electric field $\underline{E}$ and magnetic field $\underline{B}$ on the sources; electrical charge density ρ and electrical current density $\underline{J_f}$.

$$\nabla.\underline{D} = \rho_{free} \tag{12}$$

$$\nabla.\underline{B} = 0 \tag{13}$$

$$\nabla \times \underline{E} = -\frac{\partial \underline{B}}{\partial t} \tag{14}$$

$$\nabla \times \underline{H} = \underline{J}_f + \frac{\partial \underline{D}}{\partial t} \tag{15}$$

The auxiliary fields $\underline{D}$ and $\underline{H}$ can be expressed in terms of $\underline{E}$ and $\underline{B}$.

$$\underline{D} = \varepsilon_0 \underline{E} + \underline{P} \tag{16}$$

$$\underline{H} = \frac{1}{\mu_0} \underline{B} - \underline{M} \tag{17}$$

$\underline{P}$ is the polarization field caused by the application of an electric field to molecules in the material, which act like dipoles. For a linear, homogeneous isotropic which is a good approximation for most glasses when low powers are used, $\underline{P}$ depends linearly on the electric field.

$$\underline{P} = \varepsilon_0 \chi_E \underline{E} \tag{18}$$

X_E is the electric susceptibility of the medium and ε_0 is the permittivity of free space. For linear dielectric materials we may put

$$\underline{D} = \varepsilon_0 \varepsilon_r \underline{E} \tag{19}$$

$\underline{M}$ is the magnetization which is the response of the material to an applied magnetic field. Again for most glasses $\underline{M}$ is linear in $\underline{H}$

$$\underline{M} = \chi_m \underline{H} \tag{20}$$

χ_m is the magnetic susceptibility. Similarly, we can write

$$\underline{B} = \mu_0 \mu_r \underline{H} \tag{21}$$

where $\mu_r = 1$ for most dielectric materials.

3.2.3 Types of waveguide

A planar channel waveguide guides light by having a higher refractive index than its surroundings, allowing total internal reflection. Other types of waveguide use antiresonant optical coatings (ARROW) [4] or photonic crystal structures to give guidance [5] but these are not used in this work. The type of waveguide chosen for a device will depend on factors such as the material, waveguide specifications and the available fabrication capabilities. Three of the most common geometries are shown in Figure 17.

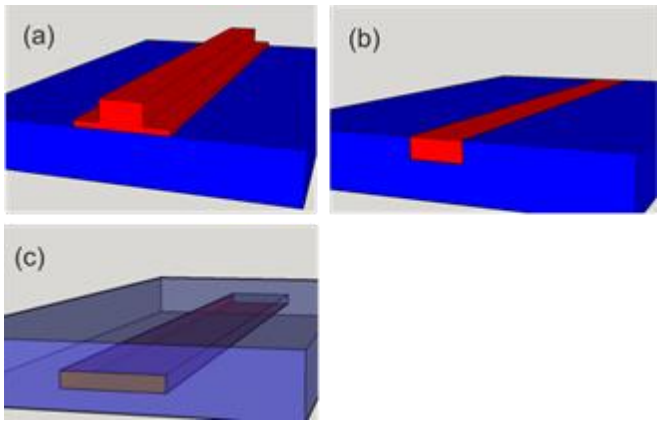

Figure 17. Different geometries of waveguide (a) ridge (b) diffused (c) buried.

Both the ridge and diffused waveguides are inherently sensitive to the environment because the guiding construct is exposed, however the buried waveguide is not. UV written waveguides are largely buried structures, however they can also be partially exposed when a substrate without a cladding layer is used. This feature is exploited in evanescent field sensing devices [6].

3.2.4 Symmetric slab waveguides

The symmetric slab waveguide is the simplest waveguide to analyse and model the silica-on-silicon device structure before a UV written waveguide is fabricated.

Figure 18 shows the structure of the slab waveguide and the coordinate system used for the analysis. In this case $n_2 > n_1$. The slab waveguide only provides guidance in one dimension.

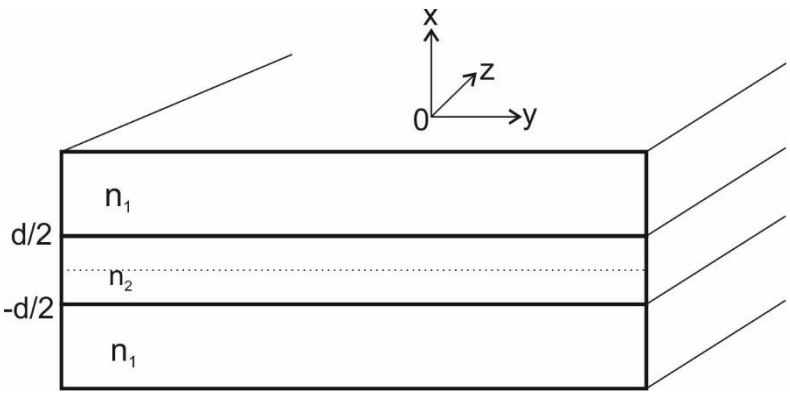

Figure 18. Diagram of slab waveguide structure.

To begin we take the curl of eq (14)and substituting in eq (8).

$$\underline{\nabla} \times (\underline{\nabla} \times \underline{E}) = -\mu_0 \varepsilon_0 n^2 \frac{\partial^2 \underline{E}}{\partial t^2} \tag{22}$$

From equation (12) and the definition of $\underline{D}$ we can obtain

$$\nabla^2 \underline{E} = -\left(\frac{1}{n^2}\right) n^2 \underline{\nabla}.\underline{E} \tag{23}$$

Substituting this into equation (22) we obtain

$$\nabla^2 \underline{E} + \nabla\left(\left(\frac{1}{n^2}\right)\nabla n^2 \underline{E}\right) - \varepsilon\mu n^2 \frac{\partial^2 \underline{E}}{\partial t^2} = 0 \tag{24}$$

Equation (24) applies to propagation in an inhomogeneous medium. However if the medium is homogenous the 2nd term in the left hand side can be neglected. This allows the 3 electric field components to be decoupled. In the case of the slab the material is homogenous in each layer with abrupt boundaries that can be dealt with using boundary conditions.

A similar expression can be derived for the magnetic field.

$$\nabla^2 \underline{H} + \frac{1}{n^2}\underline{\nabla} n^2 \times \left(\underline{\nabla} \times \underline{H}\right) - \varepsilon_0 \mu_0 n^2 \frac{\partial^2 \underline{H}}{\partial t^2} = 0 \tag{25}$$

It is possible to factorize $\underline{E}$ and $\underline{H}$ in equations (24) and (25) into the transverse spatially dependent part and an exponential part that depends on *t* and *z*.

$$\underline{E} = \underline{E}(x,y)e^{i(\omega t - \beta z)} \tag{26}$$

$$\underline{H} = \underline{H}(x,y)e^{i(\omega t - \beta z)} \tag{27}$$

β is an important quantity known as the propagation constant of the mode, and in this case propagation is assumed to be along z.

For the slab symmetric waveguide the problem can be simplified by taking *n* to be a function of *x*. This simplification assumes an infinitely wide slab, but assuming the slab is wide enough the solutions at the centre will still be valid.

When these expressions are reinserted into Maxwell's equations (14) and (15) a set of 6 equations is obtained.

Importantly the first three equations only contain E_y, H_x and H_z whilst the last three contain E_x, E_z and H_y. This means we reduce this to two independent sets of equations and they form the TE and TM modes respectively. Focusing on the TE modes in which the electric field only has a transverse component.

$$\frac{d^2 E_y}{d^2 x} + \left[k_0^2 n^2(x) - \beta^2\right] E_y = 0 \tag{28}$$

The refractive index profile of the slab can be applied. We must solve the boundary conditions at the interfaces, namely that E_y and H_z are continuous across the boundary where x = ±d/2.

We can apply the actual refractive index profile of the slab to (28) to get the two equations

$$\frac{d^2E_y}{d^2x}+\left[k_0^2n_1^2-\beta^2\right]E_y=0 \tag{29}$$

For the core and

$$\frac{d^2E_y}{d^2x}+\left[k_0^2n_2^2-\beta^2\right]E_y=0 \tag{30}$$

For the cladding. The nature of the solution will depend on the sign of the expression $k_0^2n_2^2-\beta^2$. Guided modes will have a field intensity that exponentially decays in the cladding which implies that

$$\beta^2>k_0^2n_2^2 \tag{31}$$

To satisfy the boundary conditions we must have

$$\beta^2<k_0^2n_1^2 \tag{32}$$

This puts a limit on allowable values of β

$$n_2^2<\frac{\beta^2}{k_0^2}<n_1^2 \tag{33}$$

In the core region the solution of (29) is

$$E_y\left(x\right)=A\cos\kappa x+B\sin\kappa x \tag{34}$$

For $x < d/2$

For the clad region

$$E_y\left(x\right)=\begin{cases}Ce^{\gamma x};x<-d/2\\De^{\gamma x};x>d/2\end{cases} \tag{35}$$

For symmetric modes

$$E_y\left(x\right)=\begin{cases}A\cos\kappa x;\left|x\right|<-d/2\\Ce^{-\gamma\left|x\right|};\left|x\right|>d/2\end{cases} \tag{36}$$

For the antisymmetric modes

$$E_y(x) = \begin{cases} B\sin\kappa x; |x| < -d/2 \\ De^{-\gamma|x|}; |x| > d/2 \end{cases} \tag{37}$$

Now applying the boundary condition of E_y and its derivative being continuous at the interface eventually lead to eq's (38) and (39).

$$\xi \tan\xi = \left[\left(\frac{V}{2}\right)^2 - \xi^2\right]^{1/2} \tag{38}$$

$$-\xi \cot\xi = \left[\left(\frac{V}{2}\right)^2 - \xi^2\right]^{1/2} \tag{39}$$

where

$$\xi = \frac{\kappa d}{2} = \left(k_0^2 n_1^2 - \beta^2\right)^{1/2} \frac{d}{2} \tag{40}$$

$$V = k_0 d\left(n_1^2 - n_2^2\right)^{1/2} \tag{41}$$

If we let

$$\eta = \sqrt{\left(\frac{V}{2}\right)^2 - \xi^2} \tag{42}$$

Equations (38) and (39) have no analytical solution but solutions can found graphically by plotting both sides and finding the intersection points.

Figure 19 shows plots of the left and hand and right sides of eq (38) and eq (39). To model the silica-on-silica devices, $\Delta n = 1\times10^{-3}$ and $\lambda_0 = 1550$ nm.

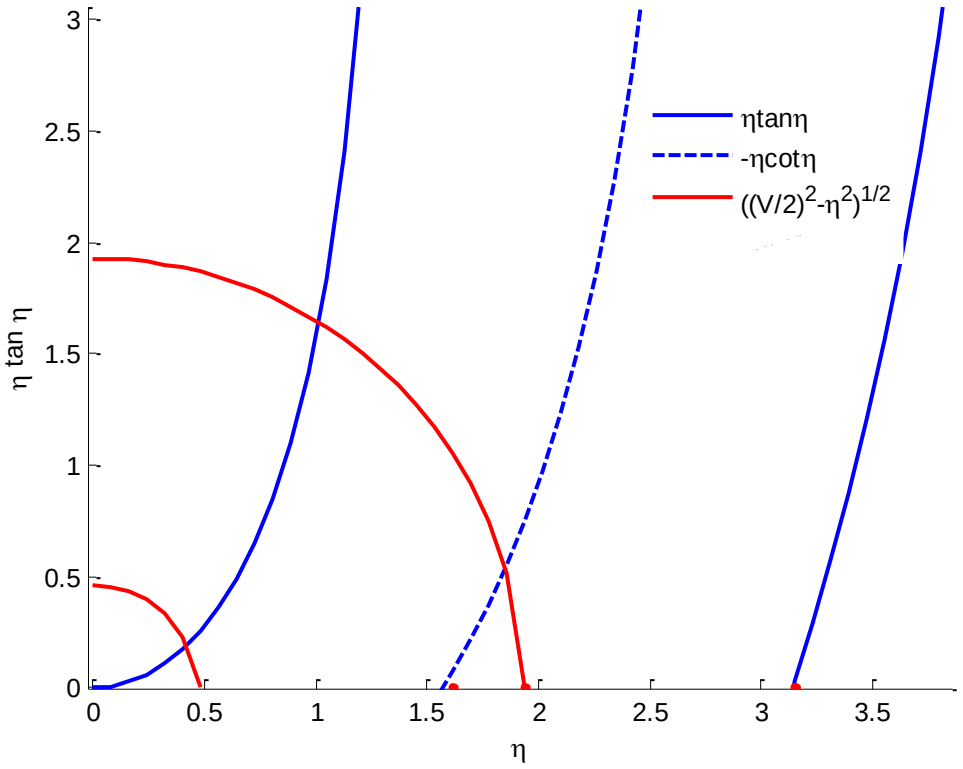

Figure 19. Plots of the left and right hand sides of equations (37) and (38) Allowed values of β can be found by looking for the intersection points.

For the thinner core (d = 6 μm) it can be seen there is only intersection point indicating that for this waveguide geometry only a single symmetric mode would be supported. For the larger core (d = 25 μm) there is one symmetric mode and one antisymmetric mode.

The cut off value of V for various modes is given by

$$V_c = m\pi \tag{43}$$

This implies for the slab waveguide that there will always be at least one mode.

A similar analysis for transverse magnetic modes gives the transcendental equations

$$\xi \tan\xi = \left(\frac{n_1}{n_2}\right)^2 \left[\left(\frac{V}{2}\right)^2 - \xi^2\right]^{1/2} \tag{44}$$

For symmetric TM modes and

$$-\xi \cot\xi = \left(\frac{n_1}{n_2}\right)^2 \left[\left(\frac{V}{2}\right)^2 - \xi^2\right]^{1/2} \tag{45}$$

for antisymmetric modes.

Maxwell's equations can be rearranged to express the electric field. For weakly guiding waveguides, typical for silica photonics, there will very little amplitude for the field components in the direction of propagation.

For a channel waveguide where light is guided in 3 dimensions a method of finding solutions based upon the slab waveguide solution was developed by Okamoto [7]. In this analysis the channel waveguide is first considered to be a slab waveguide running in a x-z plane. The effective index is found for this waveguide. This effective index is then used for the core index of a slab waveguide in the y-z plane.

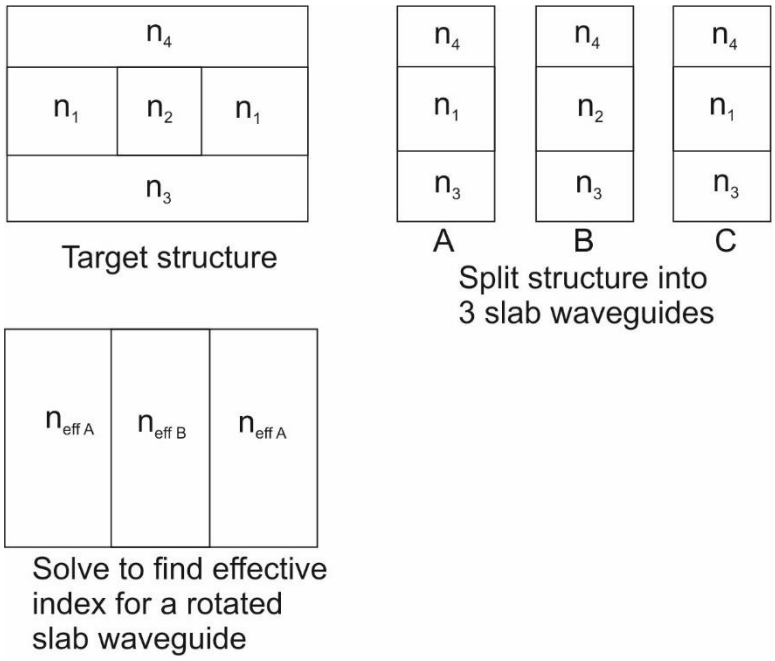

Figure 20. Method of finding effective index of channel waveguide.

The effective index makes the assumption that the electromagnetic fields can be expressed with the separation variables methods as

1. $$H_y(x,y) = X(x)Y(y) \tag{46}$$

This may not be a valid approximation depending on the geometry or wavelength, in which case computational methods such as the finite element or finite difference methods must be used.

3.2.5 Waveguide loss mechanisms

An ideal waveguide will guide light with no loss of optical power however in reality losses are present due to fabrication imperfections, waveguide geometry and material absorption characteristics. In many devices it is necessary to couple light out of the waveguide and this will have an associated loss. More details about the loss mechanism are discussed in the following sections.

1) **Absorption**

Materials absorb when the wavelength of light corresponds to a particular resonance of the bonds in the materials. In silica most of the chemical bond resonant frequencies are outside of the visible and near infrared which is why the glass appears transparent. Intrinsic loss is considered to be loss from the material the light is propagating in and is unavoidable. For silica at near IR wavelength the main cause of this loss is from the infrared absorption tail [8]. However certain impurities or dopants can increase loss and this is known as extrinsic absorption. Water absorption via O-H bond resonances is a common source of loss as it is common contaminant with a peak at 1.38 μm.

2) **Radiative loss**

When the guided mode gets coupled to lossy modes in the cladding this is known as radiative loss. Inhomogeneities in the fibre can cause scattering of the guided light in a phenomenon known as Rayleigh scattering. This scales as $1/\lambda^4$ so can be mitigated by moving to longer wavelengths. Dopants can also increase the level of scattering.

3) **Surface Scattering**

Scattering can be considered either in the bulk of the material or at an interface. Rough sidewalls will diffusely scatter light and cause radiation to scatter out of the waveguide. Insight can be gained as to the nature of scattering by considering reflection from a smooth sinusoidal surface with spatial frequency comparable to the wavelength of light. This surface will act as a diffraction grating with defined diffraction orders either side of the specular reflection. A more realistic surface topography such as cusps can be considered to be composed from sinusoids and the scatter pattern will show discrete spots with position corresponding to the frequencies present [9]. Analytical expressions have been derived for the scattering loss by Payne *et al.* [10]. The derived analytical solution for α based on the assumption that the auto correlation (a measure of the distance after which the periodicity drops away) followed an exponential function.

$$\alpha = \frac{\sigma^2}{\sqrt{2}k_0 d^4 n_1} g(V) f_c(x,\gamma) \tag{47}$$

Here d is half the thickness of the waveguide. σ is the RMS surface roughness of the sidewalls. k_0 is the free space wavenumber, n_1 is the refractive index of the core, g is given by

$$g(V) = \frac{U^2 V^2}{(1+W)} \tag{48}$$

U,V and W are normalized waveguide parameters

$$\begin{aligned} U &= d\sqrt{n_1^2 k_0^2 - \beta^2} \\ V &= k_0 d\sqrt{n_1^2 - n_2^2} \\ W &= d\sqrt{\beta^2 - n_2^2 k_0^2} \end{aligned} \tag{49}$$

$$f(x,\gamma) = \frac{x\left\{\left[\left(1+x^2\right)^2 + 2x^2\gamma^2\right]^{1/2} + 1 - x^2\right\}^{1/2}}{\left[\left(1+x^2\right)^2 + 2x^2\gamma^2\right]^{1/2}} \tag{50}$$

x is the normalized correlation length, and Υ measures how weakly guiding the waveguide is. The waveguides used in this work have refractive index contrast of between 10^{-4} and 10^{-3} so fall into the category of weakly guiding and have Υ >>1.

f_e will always have a maximum for some normalised autocorrelation length, x. Based on this the authors derived an upper limit for the waveguide loss for weakly guiding waveguides.

$$\alpha \le \frac{\sigma^2}{2k_0 d^4 n_1} g(V) \tag{51}$$

This result can be understood as when correlation length is infinite this implies that the surface would have no surface roughness. However a very short correlation length would only be measureable at distances below the wavelength of light and scattering losses would be low. As the loss depends on the square of the RMS surface roughness this emphasizes the requirement to fabricate smooth surfaces as well as the suitability of the RMS metric as an indicator of the loss that a surface will cause. As the waveguides are fabricated using direct UV writing sidewall roughness is expected to be low, however any machined surface that interacts with the guided mode will need to be smooth to reduce loss. To estimate the waveguide loss that surface roughness can cause the loss was calculated for values typical for the silica waveguides used in this report but with surface roughness typical of a machined surface (σ = 10 nm). This would be the situation for a UV written waveguide with a machined surface to allow for evanescent

coupling. In this case, an upper limit on the loss can be calculated using equation (51) to be 0.28 dB/cm. This emphasizes how not requiring directly machined surfaces is an advantage of the direct UV writing process.

4) **Coupling losses**

It is common to require a method for getting light in and out of a waveguide device. Common methods are butt-coupling with an optical fibre, end-fire focusing and prism coupling. For the devices described in this thesis the butt-coupling method was used. This involves pressing or gluing an optical fibre to the end facet of the waveguide (often incorporating additional components). Optical glue is available with the same refractive index as glass to minimize Fresnel reflections. The waveguides used in this work are designed to have dimensions which give a similar mode size to single mode optical fibre (SMF 28). The planar waveguides are approximately square so there will be some modal mismatch between the waveguide and fibre causing loss. In practice additional strain relieving elements are used with butt coupling to ensure a robust attachment.

3.3 Bragg gratings

Bragg gratings are wavelength dependent mirrors which can be written into the waveguide. A region with a periodically modulated refractive index will reflect light which interferes constructively after small reflections from each individual interface.

3.3.1 Coupled mode theory

It is useful to a have theoretical way of deriving the spectral response of Bragg gratings with different index modulations. Coupled mode theory provides a way of calculating how the distribution of energy between two modes of system changes due to some perturbation. This analysis is based on that by Ghatak and Thyagarajan [8]. Figure 21 shows the situation of Bragg grating coupling forward propagating light backwards.

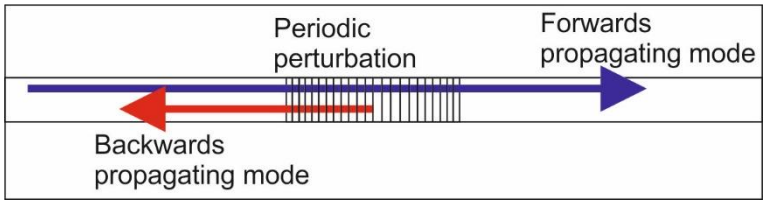

Figure 21. Contradirectional coupling where a periodic perturbation the refractive index causes coupling from a forward propagating mode into a backwards propagating mode.

If we assume the light in the waveguide can be expressed as the superposition of a forward and backward propagating mode, which is the case for a straight waveguide with a Bragg grating.

$$E(x,y,t) = [A(z)E_1(x)e^{-i\beta_1 z} + B(z)E_2(x)e^{i\beta_2 z}]e^{i\omega t} \tag{52}$$

The position dependent coefficients *A* and *B* are linked through the following relationships.

$$\frac{dA}{dz} = \kappa B e^{i\Gamma z} \tag{53}$$

$$\frac{dB}{dz} = \kappa A e^{-i\Gamma z} \tag{54}$$

Where

$$\Gamma = \beta_1 + \beta_2 - K \tag{55}$$

κ is a constant which depends on waveguide parameters, operation wavelength and the amplitude of the Bragg grating refractive index modulation.

For the phase matching condition Γ = 0.

If the coupling is occurring between identical modes travelling in opposite directions then

$$\beta_1 = \beta_2 = \frac{2\pi}{\lambda_0} n_{eff} \tag{56}$$

As *K* is related to the perturbation wavelength we can write

$$\Lambda = \frac{\lambda_0}{2n_{eff}} \tag{57}$$

This is known as the Bragg condition.

Another important feature of a Bragg grating is its reflectivity, or what fraction of the incident power it reflects into the backward propagating mode.

By differentiating equation (54) with respect to z and substituting in (53)

$$\frac{d^2B}{dz^2} = \kappa^2 B \tag{58}$$

The solution to this is

$$B(z) = b_1 e^{\kappa z} + b_2 e^{-\kappa z} \tag{59}$$

If a unit power is incident upon a Bragg grating of length L $A(z=0)=1$. In addition there is no back coupled wave at $z = L$ and $B(z=L)=0$

These expressions allow the amplitudes to be expressed as

$$B(z) = \frac{\sinh \kappa (z-L)}{\cosh \kappa L} \tag{60}$$

$$A(z) = \frac{\cosh \kappa (z-L)}{\cosh \kappa L} \tag{61}$$

The reflectivity of the grating is given by

$$R = \frac{B(z=0)^2}{A(z=0)^2} = \tanh^2 \kappa L \tag{62}$$

κ is given by

$$\kappa = \frac{\pi \Delta n}{\lambda_0} \tag{63}$$

For the UV written waveguides and Bragg gratings considered in this report $\Delta n \approx 0.5\times10^{-3}$ and λ_0 =1550 nm giving $\kappa \approx 811$ m^{-1}.

To illustrate how the power changes between the modes plotting the power in the forward and backwards propagating modes in Figure 22 shows that for a input power of 1 W at the length of the Bragg grating (L = 2 mm) there is almost no light in a backward propagating mode. P_1 and P_2 refer to the power in the forward and backwards propagating modes respectively.

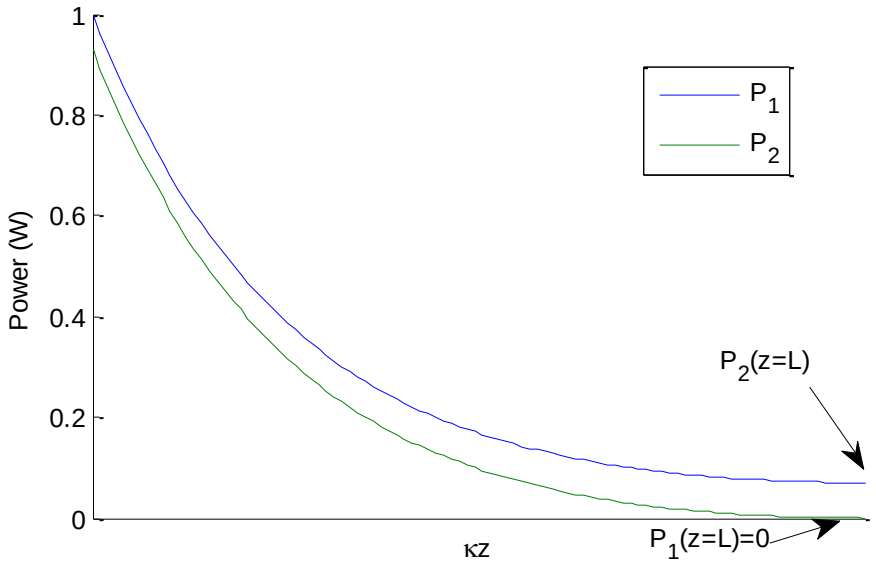

Figure 22. Powers in forward propagating (P_1) and backwards propagating modes (P_2) along the Bragg grating.

To show how long a grating would need to be to reflect 100 % of the light at the phase matching condition Figure 23 plots *R* against *L* for parameters typical of a UV written waveguide and Bragg grating resonant at 1550 nm.

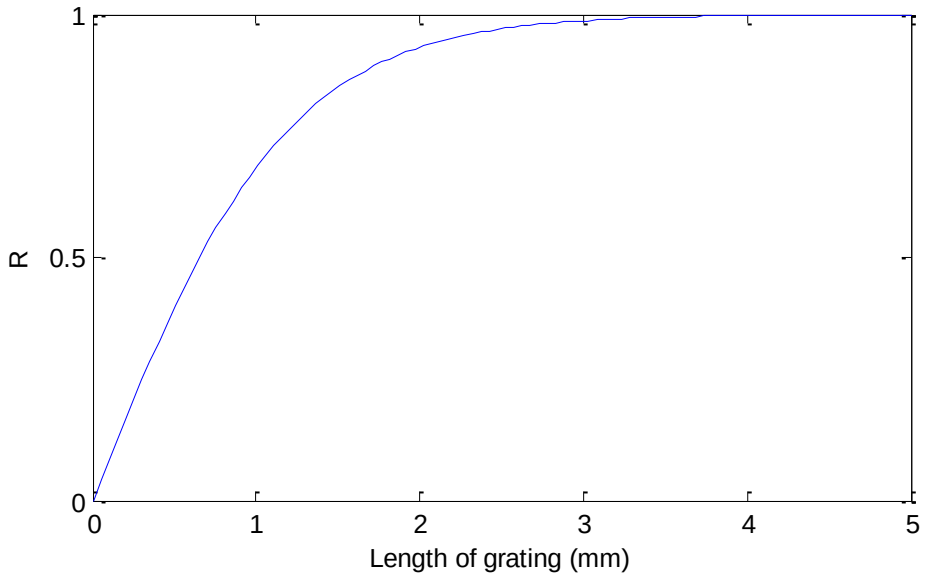

Figure 23. Reflectivity of uniform grating verses length. The refractive index modulation of the grating, $\Delta n = 0.5 \times 10^{-3}$ which is typical of a UV written waveguide.

This shows that if a uniform grating is required to reflect all of the light at a specific wavelength a length of ~4 mm is required. A grating of this strength is known as saturated and can be useful for calibration purposes.

A grating with a uniform modulation of refractive index along its profile will produce a spectral response with sidebands in addition to the main peak. These can be detrimental when an automated fit is made to the grating, for example in sensing applications. For low reflectivity gratings it is possible to engineer a Gaussian response by giving the refractive index a Gaussian envelope. Figure 24 shows a comparison of the spectra for the two types of grating. These graphs are derived on coupled mode theory code written by Lewis Carpenter.

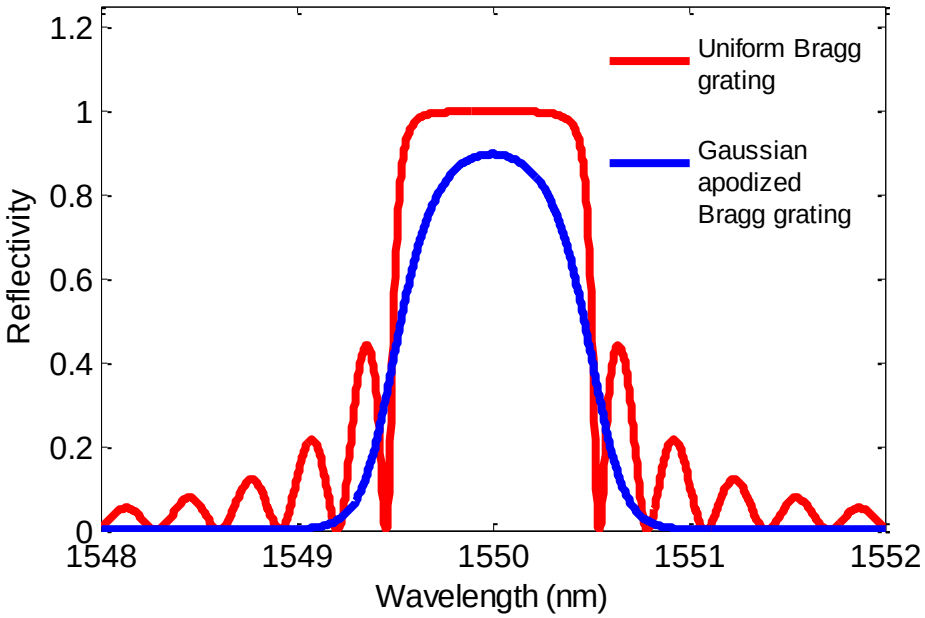

Figure 24. Spectrum of a Gaussian apodized Bragg grating obtained from coupled mode theory.

These plots were calculated from gratings of length 2.5 mm and refractive index contrasts of 0.8 $\times 10^{-4}$. It can be seen that the Gaussian apodized grating also has a Gaussian spectral response and lacks the side lobes of the uniform grating.

3.3.2 Sensors/ actuators

Bragg technology has found applications in sensing technology, both in the planar and fibre platforms. Fibre sensors are well suited to applications where distributed sensing over long lengths is required. Fibre Bragg gratings are currently widely deployed for strain and temperature sensing [11]. Planar Bragg grating sensors have found applications for chemical and biological sensing [12]. If the biological or chemical process causes a refractive index change, this can be sensed indirectly using the Bragg grating. The ability to fit a Gaussian function to the Bragg peak increases insensitivity to noise compared with measuring intensity at a single wavelength. As the Bragg grating period is fixed, the central reflected wavelength is only dependent on n_{eff} of the waveguide (assuming the waveguide is not subject to mechanical or thermal strain). An evanescent sensor has a cladding thin enough that the guided mode has a proportion of field

intensity exposed to the external environment. This type of device will naturally be sensitive to the environment. An embedded Bragg grating will also be sensitive to temperature as n_{eff} and grating pitch Λ are a function of temperature. A benefit of using grating structures for sensing is that multiple Bragg gratings with different reflection wavelengths can be used to sense different parameters. This is known as spectral multiplexing. For example an evanescent Bragg grating could be combined with an embedded grating for temperature compensation [13].

Bragg gratings can also be combined with microstructures for sensing applications. For example cantilevers can be used for displacement sensing [14][15]. This requires micromachining of the bulk chip to create the cantilever structure. An actuator changes the Bragg condition to give a tuneable Bragg grating. The fabrication and characterization of a tuneable Bragg grating are discussed in Chapter 4.

Bragg gratings are also commonly used in communication networks for wavelength division multiplexing; this enables multiple communication channels to be placed into different parts of a spectral band.

3.4 Waveguide fabrication

The techniques used to fabricate waveguides will very much depend on the material of construction, geometries and optical elements to which the waveguide must connect. The ability to define optical elements (for example Bragg gratings or couplers) in the same fabrication steps as forming the waveguide has advantages of writing speed and alignment. Usually it is required to couple light into and out of the waveguide. Butt-coupling to an optical fibre is a common approach and for this to have high efficiency the mode size and geometry must be close to that of the fibre.

3.4.1 Flame hydrolysis deposition

For optical waveguides to be high performance devices they need be low loss and have dimensions appropriate for the application, and wavelength of operation. For many applications single mode operation is also required. The approach adopted in this work follows on from previous work within the research group. The first work was carried out by Sam Watts, however the system used in that work was destroyed in the 2005 fire and the current system was supplied by CIP and SG controls. Flame hydrolysis deposition was researched by Maxwell [16].

Flame hydrolysis deposition (FHD) is used to deposit a core and an upper cladding layer, then ultraviolet laser writing is used to define a waveguide in the core layer. FHD is a technique for

depositing very pure layers of glass from gas precursors. Because of the initial purity of the gases the levels of contaminants is low. A range of dopants can also be added allowing engineering of the refractive index and control of the consolidation temperature. The machine is setup as shown in Figure 25.

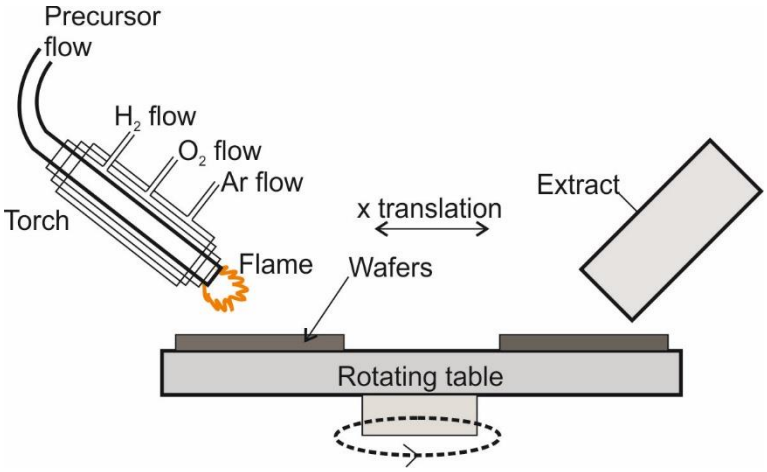

Figure 25. FHD system. A silicon carbide table rotates holding the wafers. The torch passes radially across the table ensuring uniform coverage. An extract removes toxic fumes.

The torch delivers the chloride-based precursor (GeCl4, PCl3, SiCl4, BCl3) via an oxyhydrogen flame. Within the flame hydrolysis and oxidation reactions occur [17]. The key reactions for $SiCl_4$ are given by equations (64) and (65). Direct oxidation occurs between silicon tetrachloride and oxygen gas

$$SiCl_4 + O_2 \rightarrow SiO_2 + 2Cl_2 \tag{64}$$

Hydrolysis also occurs between silicon tetrachloride and water vapour

$$SiCl_4 + H_2O \rightarrow SiO_2 + 4HCl \tag{65}$$

A rotating silicon carbide turntable holds up to 6 wafers. The torch is mounted on a motorized linear stage and passes across the wafer. When the glass is deposited, it is in the form of a porous low density soot. This must be consolidated in a furnace to form a uniform glass layer. The furnace is used to consolidate the layer with a controllable temperature profile with time. Typical chloride based precursors that are used at Southampton include boron, phosphorous and germanium. The effects of these dopants on photosensitivity, consolidation temperature and refractive index, with respect to pure silica are summarized in Table 1 [18].

Table 1. Effect of dopants on glass properties relative to pure silicon dioxide.

Dopant	**Effect on photosensitivity**	**Effect on refractive index**	**Effect on consolidation temperature**
Germanium	Increases	increases	reduces
Boron	Enhances Ge photosensitivity	reduces	reduces
Phosphorous	none	increases	reduces

A typical planar structure consists of a substrate of silicon with a pure thermally grown silicon oxide layer upon it. The thermal oxide is typically thick enough to act as an undercladding. Then the core layer of silica is deposited using FHD; germanium and boron are added to give photosensitivity to UV light. Then an overclad of silica will be deposited with added phosphorous and boron to reduce the consolidation temperature to allow consolidation without remelting of the core layer. A typical germanium doped silica core layer for single mode operation will have a refractive index contrast of 0.1% relative to the underclad and a thickness of ~ 5 μm after deposition.

3.4.2 UV writing

The germanium doped silica core in our devices is designed to be photosensitive to ultraviolet light. When an intense UV beam is focused into the layer a modification of the layer raises the refractive index. To increase the photosensitivity to UV light the sample is hydrogen loaded at high pressure prior to UV writing. This process was originally shown to enhance photosensitivity when writing Bragg gratings into optical fibre [19]. This effect is used to write waveguides into the core. Figure 26 shows a schematic of the UV writing process.

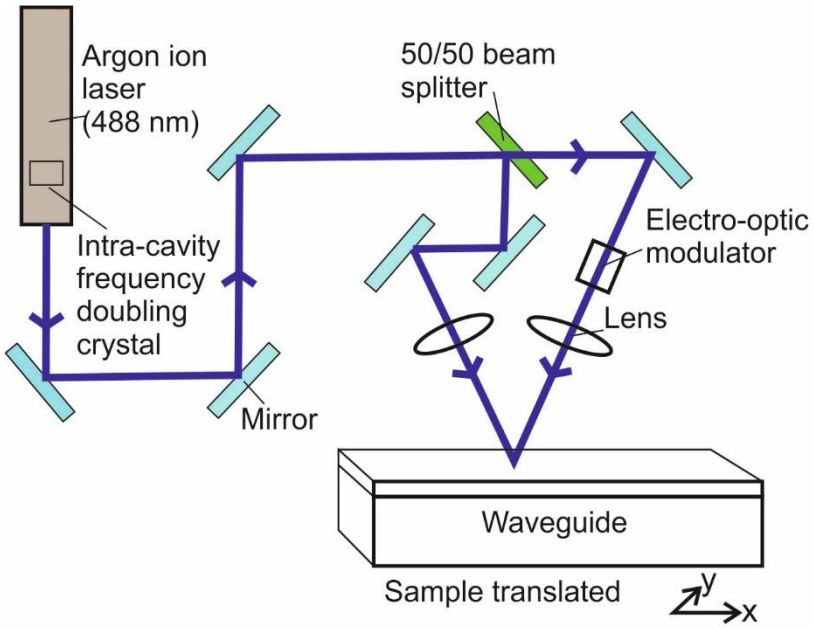

Figure 26. Experimental setup for UV writing.

In our system, an argon ion laser is frequency doubled by second harmonic generation using a beta barium borate (BBO) crystal to output continuous wave light at 244 nm. This beam is then split with a beam splitter. Two focusing lenses are aligned to overlap the two beams at the sample core height. The advantage of using two beams is that this method can also simultaneously produce the Bragg gratings [20]. As the two beams are formed from the initial coherent beam they will have a constant phase relationship meaning interference fringes are generated at the point at which they overlap. This is shown in Figure 27. This is used to define the Bragg grating. The beams are typically focused to spots of ~ 5 µm which is the dimension of a single mode waveguide. An electro-optic modulator modulates one of the beam's phases and the phase synchronisation is matched with the respective translation of the sample. Intensity of exposure can be varied through velocity control. When the sample is translated at a constant speed and the light is not phase modulated a normal waveguide is written (i.e. not containing a grating structure).

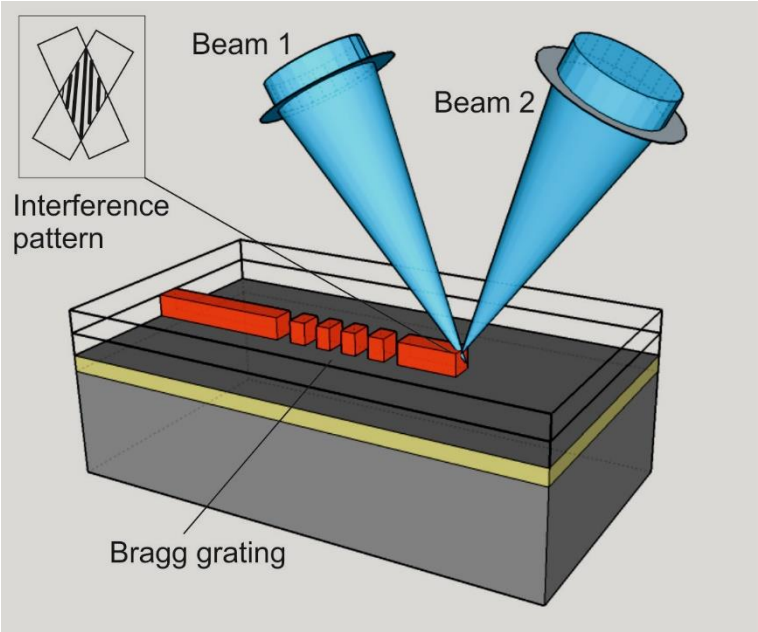

Figure 27. UV writing process. Two overlapping beams are used to define the waveguide.

The fluence of the focused spot is the amount of energy delivered per unit area. This quantity can be controlled independently of the laser by changing the translation speed of the sample. The fluence will affect the refractive index change and its effect needs to be understood if single mode operation is achieved. The focus of the spot into the core is also critical for repeatable waveguide writing and this can be checked by looking for the fluorescence given off when the correctly aligned beams hit the core.

UV writing has the benefit that losses due to sidewall roughness are low as the sidewalls are formed optically. So long as the core material is homogeneous it is unlikely the writing process will generate roughness causing scatter.

3.4.3 Alternative techniques for silica waveguides

While UV writing is used in our research it is more common in industry to use etch processes to define waveguides. One reason for this is it allows parallel processing of wafers to fabricate multiple chips at one time. Photolithographic waveguides use a mask based approach to form the waveguide structure. An etching process (usually a dry process such as ICP) is used to remove material as described in more detail in Chapter 2. A cladding is then deposited with lower refractive index. This technique benefits from the parallel processing, however the surface roughness of the etch step must be controlled to minimize scattering losses. A good description of conventional etched devices may be found in Calvo [21].

Another direct writing process is possible using femtosecond lasers. This process can produce waveguides in pure materials such as fused silica without the need for photosensitivity [22]. As

the fabrication mechanism is based on non-linear effects, it also potentially allows creation of three-dimensional waveguides as the focal point can be translated vertically. Currently femtosecond waveguides exhibit higher losses (0.5 dB/cm) [23] than UV written waveguides (0.2 dB/cm) [24].

3.5 Characterization

Once fabricated the optical devices are generally characterized to determine whether the performance matches what is required. For devices such as Bragg gratings it is important to know at which wavelengths the device reflects and the detailed spectrum of the reflected light. For this a suitable broadband source (e.g. amplified spontaneous emission (ASE), superluminescent diode(SLED)) can be used in combination with an optical spectrum analyser (OSA). Figure 28 shows an optical setup that is commonly used.

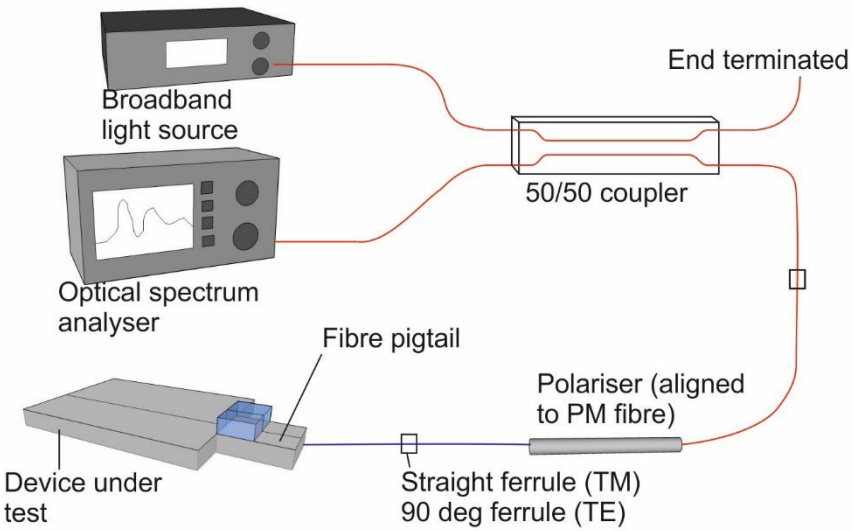

Figure 28. Broadband optical characterization setup. Non-polarization maintaining fibre is shown in red while polarizing maintaining is shown in blue.

Broadband light is input through a polarizer into the device under test. Reflected light from the device is sent back and 50 % of it will be guided to the optical spectrum analyser through the 50/50 coupler (sometimes an optical circulator is used). Often it is necessary to the test the device with a single wavelength or with higher wavelength resolution than the OSA can resolve. In this case, a tuneable laser and suitable photodiode detector are used as illustrated in Figure 29. This setup can also be used to measure gratings that change in time (response time) as used in Chapter 4.

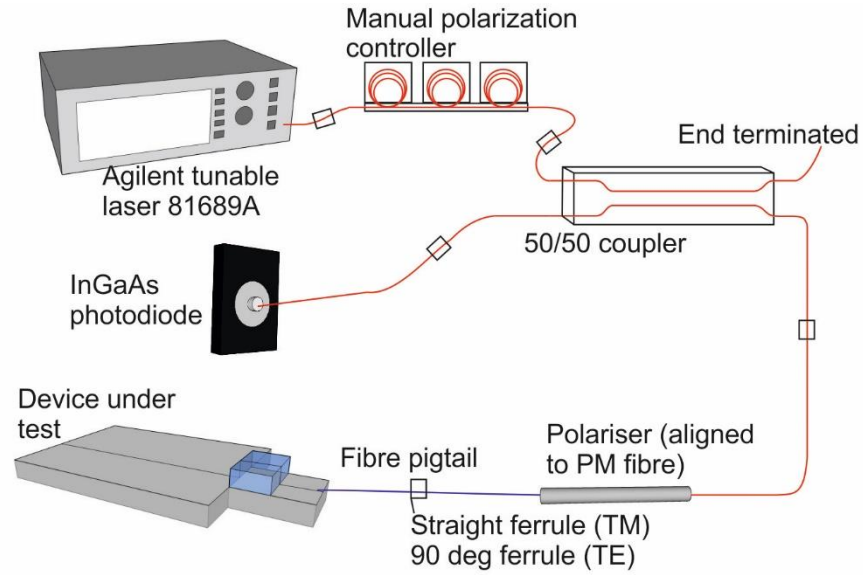

Figure 29. Optical setup for measuring the response time. Non-polarization maintaining fibre is shown in red while polarizing maintaining fibre is shown in blue.

When this setup is used additional care must be taken to ensure that the single mode fibre does not lose the linearly polarized state output by the laser. For that reason, a manual polarization controller (or paddles) is used to optimize power output through the non-polarizing maintaining section of the fibre before the device is characterized. Any non-polarization maintaining fibre must be secured to reduce vibration as this will change the polarization state of the guided light.

3.6 References

[1] L. S. Grattan and B. T. Meggitt, *Optical Fiber Sensor Technology*. Springer Science & Business Media, 2012.

[2] E. Hecht, *Optics*. San Francisco: Addison Wesley, 2002.

[3] D. J. Griffiths, *Introduction to Electrodynamics*, 3rd ed. Addison Wesley, 1998.

[4] D. Yin, H. Schmidt, J. P. Barber, and A. R. Hawkins, “Integrated ARROW waveguides with hollow cores,” *Opt Express*, vol. 12, no. 12, p. 2710, Jun. 2004.

[5] S. Y. Lin, E. Chow, S. G. Johnson, and J. D. Joannopoulos, “Demonstration of highly efficient waveguiding in a photonic crystal slab at the 1.5-µm wavelength,” *Opt Lett*, vol. 25, no. 17, p. 1297, Sep. 2000.

[6] J. Fluitman and T. Popma, “Optical waveguide sensors,” *Sensors and Actuators*, vol. 10, no. 1–2, pp. 25–46, Sep. 1986.

[7] K. Okamoto, *Fundamentals of Optical Waveguides*, 2nd Ed. Academic Press, 2006.

[8] A. Ghatak and K. Thyagarajan, *An Introduction to Fiber Optics*. Cambridge University Press, 1998.

[9] J. C. Stover, *SPIE Optical Scattering: Measurement and Analysis*, 2nd ed. SPIE Press, 1999.

[10] F. P. Payne and J. P. R. Lacey, "A theoretical analysis of scattering loss from planar optical waveguides," *Opt. Quantum Electron.*, vol. 26, no. 10, pp. 977–986, Oct. 1994.

[11] Y.-J. Rao, "In-fibre Bragg grating sensors," *Meas. Sci. Technol.*, vol. 8, no. 4, pp. 355–375, Apr. 1997.

[12] I. J. G. Sparrow, P. G. R. Smith, and G. D. Emmerson, "Planar Bragg grating sensors - Fabrication and Applications: A Review," *J. Sensors*, vol. 2009, 12 pages, 2009.

[13] I. J. G. Sparrow, G. D. Emmerson, C. B. E. Gawith, and P. G. R. Smith, "Planar waveguide hygrometer and state sensor demonstrating supercooled water recognition," *Sensors Actuators B Chem.*, vol. 107, no. 2, pp. 856–860, Jun. 2005.

[14] C. Holmes, L. G. Carpenter, H. L. Rogers, J. C. Gates, and P. G. R. Smith, "Quantifying the optical sensitivity of planar Bragg gratings in glass micro-cantilevers to physical deflection," *J Micromech Microeng*, vol. 21, no. 3, p. 035014, Mar. 2011.

[15] L. G. Carpenter, C. Holmes, H. L. Rogers, P. G. R. Smith, and J. C. Gates, "Integrated optic glass microcantilevers with Bragg grating interrogation.," *Opt Express*, vol. 18, no. 22, pp. 23296–23301, Oct. 2010.

[16] G. D. Maxwell, "Optical waveguide fabrication in silica using flame hydrolysis," University of Glasgow, 1990.

[17] X. C. Tong, *Advanced Materials for Integrated Optical Waveguides*. Springer Science & Business Media, 2013.

[18] A. K. Varshneya, *Fundamentals of Inorganic Glasses*. Gulf Professional Publishing, 1994.

[19] R. Kashyap, *Fiber Bragg Gratings*. San Diego: Academic Press, 1999.

[20] G. D. Emmerson, S. P. Watts, C. B. E. Gawith, V. Albanis, M. Ibsen, R. B. Williams, and P. G. R. Smith, "Fabrication of directly UV-written channel waveguides with simultaneously defined integral Bragg gratings," *Electron. Lett.*, vol. 38, no. 24, pp. 1531–1532, Nov. 2002.

[21] M. L. Calvo and V. Lakshminarayanan, *Optical Waveguides: From Theory to Applied Technologies*. CRC Press, 2007.

[22] R. R. Gattass and E. Mazur, "Femtosecond laser micromachining in transparent materials," *Nat. Photonics*, vol. 2, no. 4, pp. 219–225, Apr. 2008.

[23] L. Tong, R. R. Gattass, I. Maxwell, J. B. Ashcom, and E. Mazur, "Optical loss measurements in femtosecond laser written waveguides in glass," *Opt. Commun.*, vol. 259, no. 2, pp. 626–630, Mar. 2006.

[24] H. L. Rogers, S. Ambran, C. Holmes, P. G. R. Smith, and J. C. Gates, "In situ loss measurement of direct UV-written waveguides using integrated Bragg gratings," *Opt Lett*, vol. 35, no. 17, pp. 2849–2851, 2010.

Chapter 4: Power-efficiency enhanced thermally tunable Bragg grating device

4.1 Introduction

Microbeams are a common structure in Micro-Opto-Electro-Mechanical (MOEM) devices. In their most basic form they consist of a beam clamped at both ends suspended over a substrate. A variety of applications that take advantage of the special properties of microbeams can be found in the literature; Guckel *et al.* [1] fabricated microbeams to measure the stress in a deposited polysilicon film. A thermally driven microvalve was fabricated by Lisec *et al.* [2]. Joe *et al.* used the resonant frequency behaviour of microbeams for gas sensing applications [3]. Optical applications include a bridge suspended thermo-optic phase shifter [4] in silica-on-silicon and a tuneable Bragg grating in a silicon waveguide [5].

Bragg gratings in silica waveguides have already been proven in fields such as telecoms, sensing and quantum information experiments [6]. The ability to control either the reflected wavelength or the spectral shape of the Bragg grating can lead to new types of device. Wavelength tuning can be used in add/drop multiplexers for Dense Wavelength Division Multiplexing (DWDM) [7]. Tuning the chirp or non-linearity of a grating has applications in active dispersion control for communications systems [8]. For many applications it is desirable to reduce the power consumption of the performance of the tunable device and this is the motivation for researching the integration of a tuneable Bragg grating within a microbeam structure. The approach of undercutting a laser written microstructure has been used previously to demonstrate microcantilevers, clamped only at a single end [9], and membranes [10]. This new device allows for transmission operation and simplifies the placement of the heating element.

The microbeam geometry is expected to give enhanced thermal tuning efficiency performance due to its thermal isolation from the environment and the extremely low heat capacity of the microbeam. Having two clamped ends allows the device to used in transmission as well as making the operation of the heating element simpler. As the silicon substrate is an excellent conductor of heat, it efficiently sinks heat away from the waveguide, thereby increasing the thermal load and decreasing the energy efficiency when tuning in a bulk substrate. In a microbeam device the air gap around the microbeam provides effective thermal isolation. The current interest in fabricating optical waveguide chips for quantum information processing requires large numbers of heating elements for optical phase tuning, resulting in the chip having to dissipate large amounts of power

to remain at stable temperature [11]. Incorporating microbeam structures at heating points could drastically reduce the amount of bulk heating and cross-talk between phase shifters.

Various methods of optical tuning have been reported in the literature for integrated planar devices; piezoelectric actuation was used in a phase shifting device by Donati *et al.* [12] and liquid crystal tuning was demonstrated by Adikan *et al.* [13]. The ideal method of tuning will depend on different factors including device format, tuning range required and response time. Thermal tuning is a proven method of tuning for integrated optics and was selected for this work due to the reliability and relative simplicity of fabrication.

In this chapter a thermally tuneable Bragg grating is fabricated in the silica on silicon platform. This is the first device of this nature to published in a journal [14]. Figure 30 shows a photograph of the completed device.

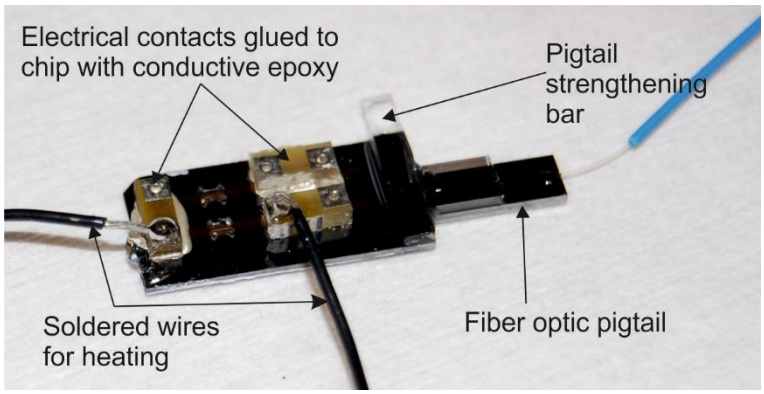

Figure 30. Photograph of completed device showing location of microbeam, fiber optic pigtail and electrical contacts.

The fabrication procedure includes a milling process, wet etching and metal deposition. Using a physical milling process is unusual for MOEM device fabrication. The milling process is developed to eliminate cracking which would result in microbeam fracture. The relevant thermooptic and optomechanical theory behind the device is explained. The theoretical tuning is presented. A finite element model is built in Comsol to estimate the tuning efficiency compared to a bulk device. The finished device is first characterized optically during fabrication to study how the undercut changes the optical response. The response of the device to electrical current is reported and the power efficiency obtained for tuning. The device is characterized mechanically which provides insight into how the structure deforms during tuning. Another important characteristic, the response time is found by measuring the response to a step change in current applied to the device. A 4-point-probe measurement uses the temperature dependence of resistivity to find the temperature reached during tuning and this is used to find the temperature tuning curve.

4.2 Thermal tuning theory

In our device we thermo-optically tune a Bragg grating, located in a microbeam, and also demonstrate control of the optical path length of a Fabry-Pérot cavity defined across the microbeam. The graphic in Figure 31 shows how the structure of the microbeam is created through a combination of micromilling and wet etching as well as the location of the optical elements in relation to the physical structure.

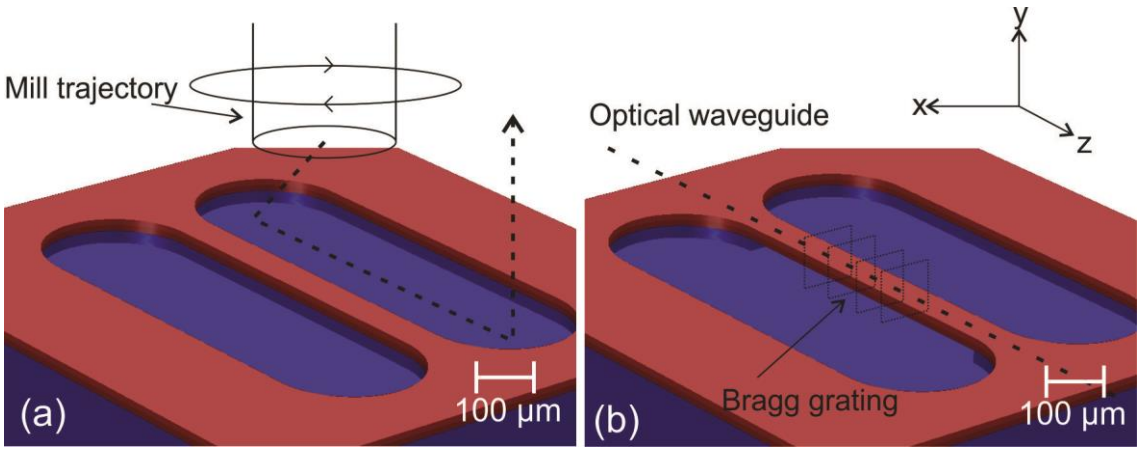

Figure 31. (a) Structure geometry following milling. The glass layers are shown in red while the silicon is coloured blue. The trajectory of the milling cutter is shown. (b) Structure after KOH wet etching showing how the silicon underneath the microbeam has been removed. The locations of the optical waveguide and Bragg grating are also shown with dotted lines. For simplicity the 'run-up' section described later are not included in this schematic diagram.

4.2.1 Bragg grating structure

A Bragg grating is a region of periodically modulated refractive index that reflects light resonantly at wavelengths given by the Bragg condition. As derived in Chapter 3 the Bragg condition gives the centre wavelength λ_B reflected by a Bragg grating and is given by equation (66).

$$\lambda_B = 2n_{eff}\Lambda \tag{66}$$

where Λ is the pitch of the Bragg grating and n_{eff} is the effective refractive index of the waveguide mode. A simple mathematical model can be developed to model the efficiency of thermal tuning by considering how the variables in equation (66) are affected by temperature and the associated changes in the waveguide. Thermal tuning can change the Bragg condition in three ways; firstly via thermo-optic effect, secondly through stress-optic and thirdly by grating pitch expansion, which in our device is modified due to the mechanical anchoring at either end of the

beam. The shift in Bragg peak wavelength can be expressed by the change in refractive index with equation (67).

$$\Delta\lambda_B = \frac{\Delta n}{n_{eff}}\lambda \tag{67}$$

Firstly, due to the thermo-optic effect in most materials n is a function of temperature. For small temperature changes the relationship is linear, given by equation (68).

$$\Delta n = \xi \Delta T \tag{68}$$

Here ξ is the thermo-optic coefficient and has a value of 1×10^{-5} K^{-1} for pure silica glass [15]. The core material of the waveguide is doped with germanium and boron and this will affect the thermo-optic coefficient. As the doping levels are low approximating the thermos-optic coefficient as that of pure silica should be acceptable to estimate the magnitude of the effect of the tuning.

For our device, we know that the modal refractive index $n_{eff} = 1.448$ for wavelengths around 1550 nm. By combining equations (67) and (68) the theoretical tuning sensitivity of the device due to the thermo-optic effect is 10.7 pm/°C and this is consistent with the values of standard non-MOEM type devices [16].

Secondly, the stress-optic effect, also referred to as photoelasticity, describes the effect of stress on the refractive index. In a constrained system heating will lead to thermal stress developing as the material is not free to expand. As stress is a tensor it is necessary to consider the change in refractive index along three orthogonal axes. The three components of refractive index are given by equations (69)-(71). The coordinate system used is as shown in Figure 31. A plane-polarized plane wave propagating in the z direction with electric field in the x direction will see a refractive index of n_x.

$$n_x = n - pS_x - q\left(S_y + S_z\right) \tag{69}$$

$$n_y = n - pS_y - q\left(S_x + S_z\right) \tag{70}$$

$$n_z = n - pS_z - q\left(S_x + S_y\right) \tag{71}$$

Where S_x, S_y and S_z are the normal components of the stress tensor and the stress optic coefficients p = 6.5×10^{-13} Pa^{-1} and q = 4.2×10^{-12} Pa^{-1} for pure silica glass [17]. If a normal stress is applied along the microbeam axis, this causes stresses in the orthogonal directions with a magnitude determined by Poisson's ratio.

$$S_x = -\nu S_z \tag{72}$$

$$S_y = -\nu S_z \tag{73}$$

Here ν is Poisson's ratio with a value of 0.17 for silica glass [18]. When equations (72) and (73) are substituted into equations (69) and (70), the refractive index change as a function of S_z is obtained.

$$\Delta n_{x,y} = S_z\left(p\nu - q(1-\nu)\right) \tag{74}$$

If the stress is caused by constrained thermal expansion it will be proportional to the temperature change.

$$S_z = E\alpha\Delta T \tag{75}$$

Here *E* is the Young's modulus of silica, taken to be 73.1 GPa, α is the coefficient of thermal expansion which was taken to be 0.55 x 10^{-7} [19]. This results in a negative tuning sensitivity due to the stress-optic effect of -0.12 pm/°C. This simple analysis is not capable of distinguishing any potential birefringence caused by the stress-optic effect.

Thirdly in addition to the stress induced by thermal changes, the microbeam will also tend to expand, altering the period of the grating. In an unconstrained system thermal expansion will cause an increase in the pitch of the Bragg grating.

$$\Delta\Lambda = \alpha\Delta T\Lambda \tag{76}$$

$\Delta\Lambda$ is the increase in pitch of the Bragg grating. For the device described the thermo-optic effect will always be contributing during the tuning. A further complication is that a stressed beam can undergo buckling to release stress which will affect how subsequent strains develop. If a microbeam is in the buckled state thermal strain will be only partially constrained and some grating pitch expansion will occur. If it is unbuckled, thermal stresses will occur but the grating pitch will not change appreciably. From examining the various contributions to the tuning it can ber seen that the thermo-optic effect is expected to be the dominant contributor to thermal tuning.

As mentioned, it is possible for an axially stressed beam to undergo buckling if its length exceeds a critical length. Buckling is a sudden, discontinuous change of beam shape in a response to a critical applied axial load in a beam. In a symmetric beam with uniform load there is a bifurcation and buckling in any direction is possible. However if the beam has shape imperfections or cross-sectionally varying stresses these may help to define the preferred buckling direction. A slightly bent beam under increasing stress will deflect continuously however it will not buckle until the critical load level is reached. The buckled beam has a characteristic shape known as the buckled

mode and will generally have its maximum displacement at the centre of the beam. The stress, *S*, required to cause buckling in a beam with length L_c is given by the Euler-Bernoulli equation [20].

$$S = \frac{\pi^2 E h^2}{3L_c^2} \tag{77}$$

L_c is the critical length of the microbeam beyond which buckling occurs. *h* is the thickness of beam. Figure 32 illustrates how an initially straight microbeam buckles to a lower energy configuration with the characteristic shape of the 1st buckling mode.

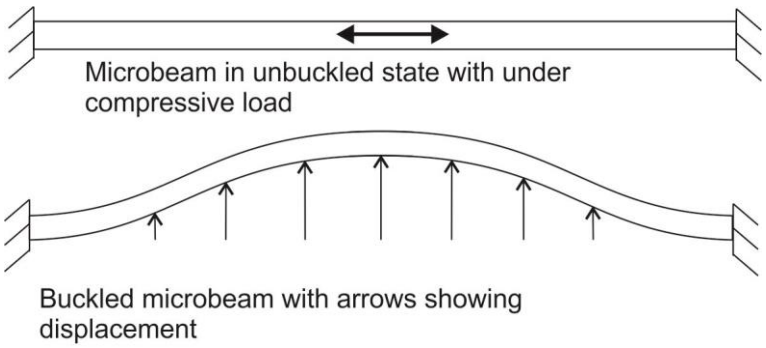

Figure 32. Graphic showing how a microbeam will eventually buckle to relieve compressive stress when mechanically anchored at both ends.

For the silica microbeams found in this work, the thermally grown silica has a lower coefficient of thermal expansion than the FHD deposited clad and core layers. This leads to the thermally grown silica having the highest compressive stress.

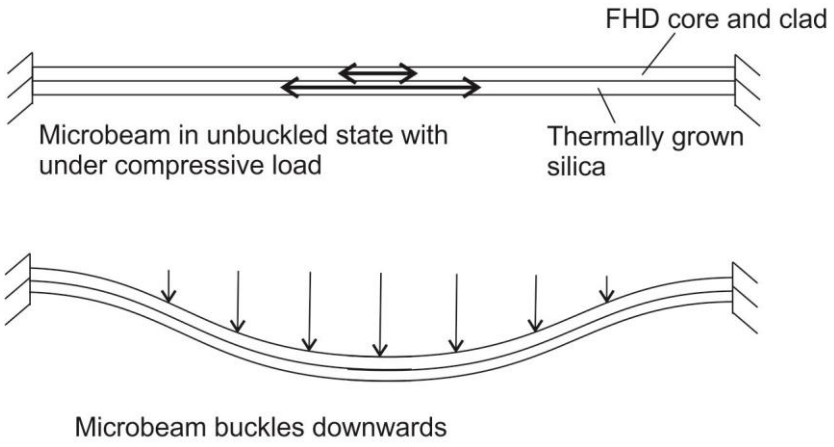

Figure 33. Graphic showing how in a 2 layer system the thermally grown silica layer can relieve more stress when the whole microbeam buckles downwards

4.3 Finite element modelling

4.3.1 Comsol modelling of heat diffusion

As part of the investigation into the potential benefits of the tunable microbeam device COMSOL Finite Element (FEA) modelling was undertaken to determine the power efficiency gain that could be expected. This analysis will consider the stationary condition which considers that the heat source is constant and enough time has passed for the system to reach thermal equilibrium. The spatial distribution of temperature does not change and is determined by the heat source and boundary conditions. The heat conduction equation is given by

$$\nabla.(k\nabla T)+Q=0 \tag{78}$$

k is the thermal conductivity, *Q* is the heat produced and *T* is the temperature [21].

The boundary conditions for the model set the surfaces for which heat is allowed to flow out. For this model the top layer was set as an insulator as it was assumed that heat transfer to the air would be small compared to transfer through the silica and silicon. Mathematically the insulating boundary is defined by

$$-\underline{n}.(-k\underline{\nabla}T)=0 \tag{79}$$

Where $\underline{n}$ is the normal vector to the surface. The boundary condition for the boundary of the silicon block used in the simulation was

$$T=T_0 \tag{80}$$

Where T_0 is chosen to be room temperature. While convective cooling by the air and radiative emission would be present in reality it was decided not to include them in the model as they required an estimate of the convective cooling heat transfer coefficient. When the microbeam geometry is considered this becomes complicated and a fluid mechanics simulation would be required. This would be undertaken if further optimization of microbeam geometry was to be undertaken but the purpose of this simulation was to improve understanding of the increase in efficiency that could be expected with the microbeam device.

4.3.2 Simulation of heat diffusion in a bulk device

A bulk device is first investigated which simulates a typical Bragg grating with a heater element defined over the grating. A volume of interest is chosen which represents where the Bragg grating would be located. This volume is considered a heat source and the resulting temperatures

are calculated. The base of the silicon is considered to be a heat sink at room temperature. Figure 34 shows a cross section of the modelled temperature due to localized tuning in a bulk device.

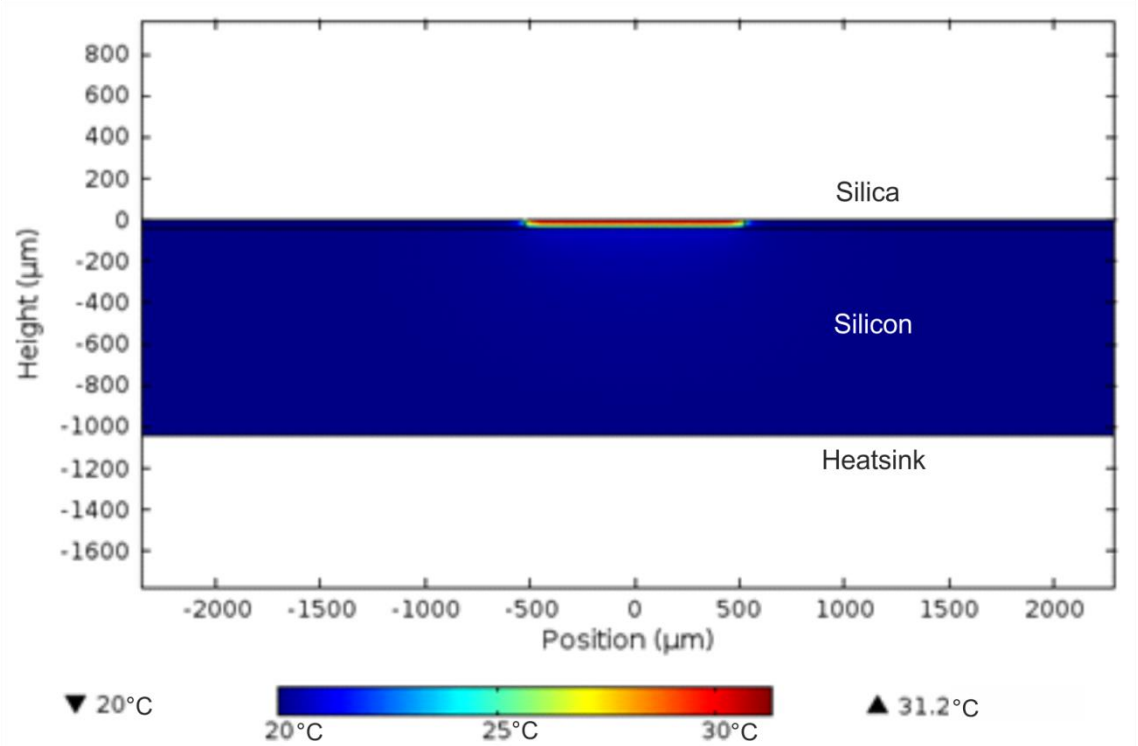

Figure 34. Modelled temperature fields due to locally heating a small volume of silica glass in a bulk substrate. Temperature is in °C.

If the colourmap is altered to exclude the higher temperatures, the direction of the heat flow is clearer. Figure 35 shows that heat flux down into the silicon substrate is stronger than through the silica layer.

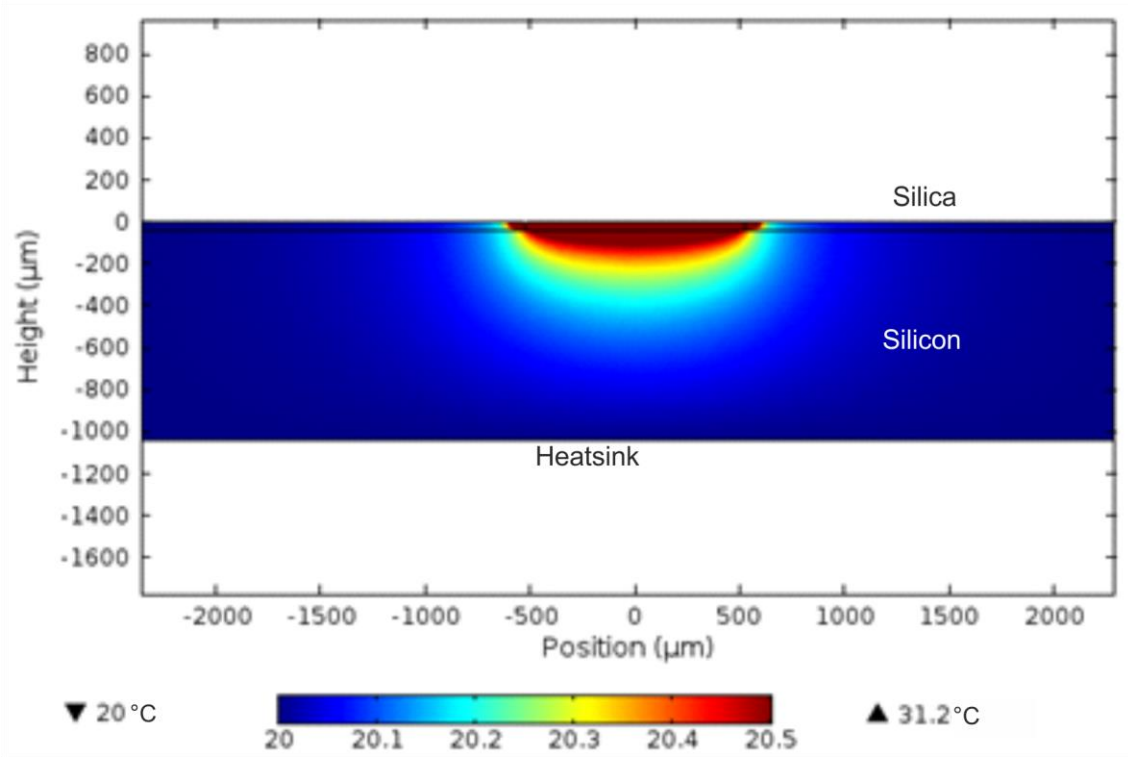

Figure 35. Modelled temperature due to heating in bulk substrate. This figure plots exactly the same simulation as Figure 34 but the colourmap has been changed to highlight heat flow through the silicon substrate. Temperature is in °C.

For an applied power of 100 mW, the average temperature of the volume of interest was 26.5 °C.

4.3.3 Simulation of heat diffusion in a microbeam device

A similar simulation but with the microbeam geometry was then modelled. By considering a volume of interest of the same dimensions but free from the substrate the 3-dimensional temperature field was simulated. Figure 36 shows the temperature field from the simulation of the microbeam geometry.

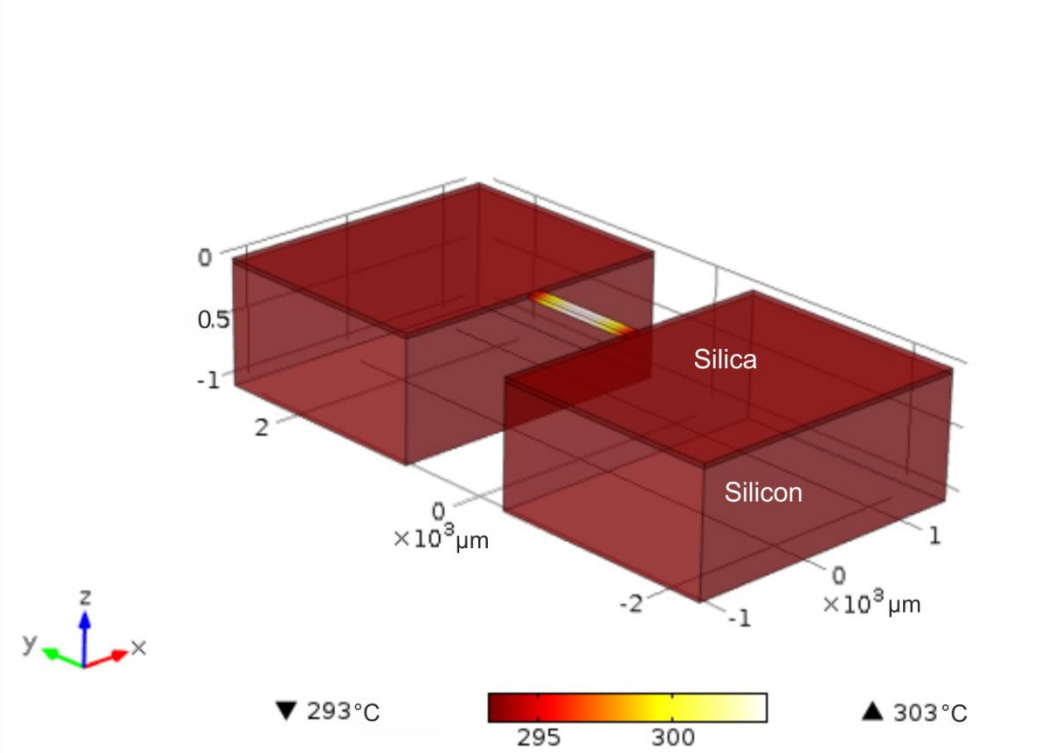

Figure 36. 3D temperature map of heating in the micro beam device. Temperature is in °C.

A 2d slice of this model was taken and is shown in Figure 37.

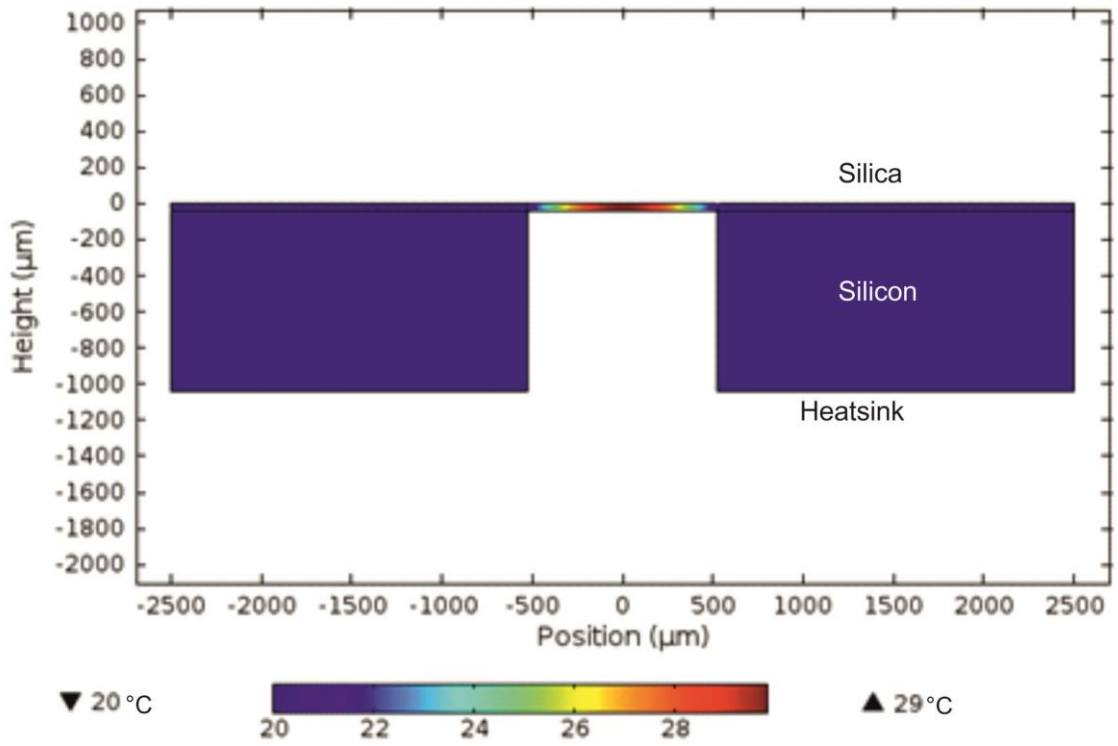

Figure 37. Modelled temperature field due to heating in microbeam. Temperature is in °C.

Figure 37 shows how the centre of the microbeam reaches the highest temperature as it is the most thermally isolated point. A heating power of 0.45mW produced an average temperature of

26.5 °C in the region of interest. The efficiency has increased by a factor of ~220 compared to the bulk device. As will been shown, the dominant tuning effect in silica is the thermo-optic effect. Due to this, the refractive index and hence Bragg wavelength shift will be proportional to the temperature change. This strongly suggests that a tunable microbeam device could give major improvements in efficiency. It is also possible to incorporate the stress-optic and thermo-mechanical effects into the COMSOL simulation. This is an option for future work to build an understanding of how the birefringence is affected by tuning.

4.4 Fabrication

The fabrication process for our tunable Bragg grating device includes physical micromachining, wet etching and metal deposition. The initial substrate consists of 2 layers of FHD deposited glass on a silicon wafer with a 15 µm thermally grown layer to act as an underclad. The core layer is doped with germanium to increase photosensitivity. The wafer is diced with a commercial dicing saw to produce device sized chips or die. In this work microbeams of two lengths were fabricated. A 1 mm long microbeam contained optical elements and was characterized both optically and mechanically whilst a 1.5 mm microbeam didn't contain any optical elements and was only characterized mechanically in Section 4.5.2.

4.4.1 Micromilling

For the wet etch to fully undercut the microbeam, two deep trenches must be machined through the silica exposing the silicon. The grooves must be sufficiently deep to prevent premature formation of slow etching <100> etch planes, which drastically reduce the etch rate. Reactive ion etching (RIE) and inductively coupled etching (ICP) would have required very long process times to reach this depth of groove. For this reason physical micromachining was selected as the machining time was shorter and fabrication of lithographic masks was not required, and in addition is capable of yielding very smooth surfaces [22]. A micro-mill was used to fabricate two grooves to a depth of 80 µm (and will be discussed in full detail in Chapter 6). The micro-mill has a Loadpoint Bearings air-bearing spindle with dynamic runout better than 1 µm. The workpiece is translated on an air-bearing Aerotech X,Y translation stage with nanometer level resolution. Table 2. shows the processing parameters used during the milling operation. These parameters have previously been used to successfully mill deep grooves in silica by Carpenter *et al.* [22].

Table 2. Machining parameters used for micromilling of grooves

Tool diameter	0.5 mm
Mill type	UKAM 500 µm diameter diamond microdrill
Spindle speed	60,000 rpm
Linear feed rate	0.1 mm/min

It was essential to minimise edge chipping and cracks in the silica as these could cause failure of the microbeam at the etch stage. Figure 38 shows the result of the first milling run.

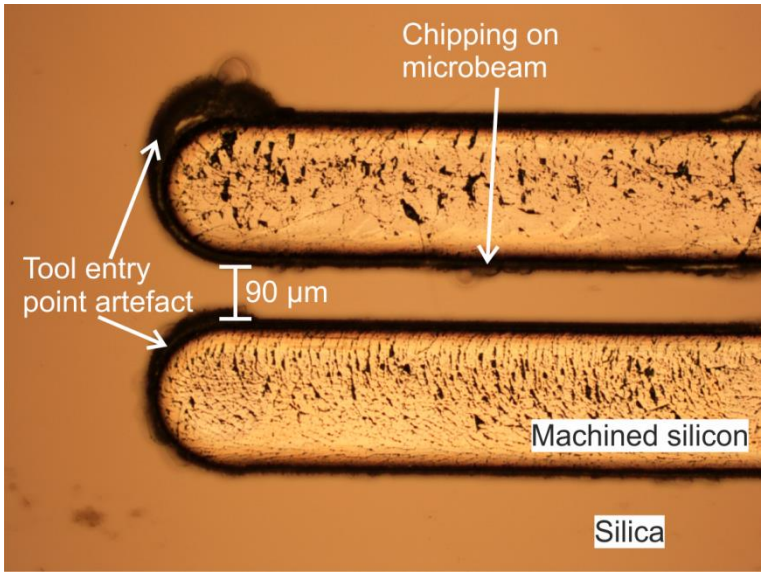

Figure 38. Microscope image (x10) after milling process.

It can be seen that there is evidence of chipping along the central ridge between the grooves. Based on experience from dressing dicing blades it was decided to dress the tools deeper than the specified cut depth to ensure that a slight variation in cut depth did not result in the undressed tool causing top side chipping.

It can also been seen that large chips are more prevalent at the start and end of grooves where the tool was either engaging or disengaging the surface. For this reason, 'run-up' sections at 90º to the main grooves were introduced and can be seen in Figure 39. The purpose of these was to keep initial edge chipping out the way without affecting the function of the device. Each 'run-up' was 0.5mm in length and the tool took a linear descent to the cut-depth of 80 microns.

The milling run was repeated with the same parameters as Table 1. but with the addition of 'runup' sections and deeper tool dressing. Figure 39 shows the two milled grooves and

demonstrates that the edge chipping has been kept to a low level. The reduction in the chipping and depth of cut to allow undercutting were the crucial features that could affect the function of the device.

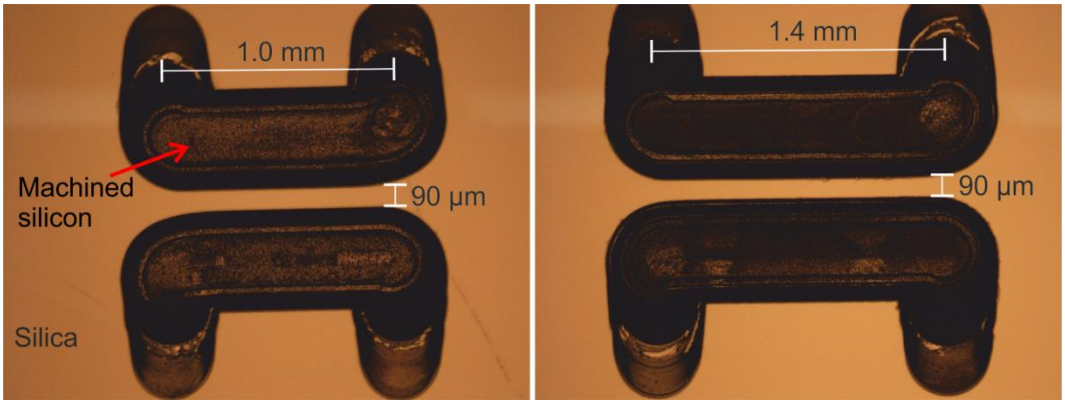

Figure 39. Optical microscope images of milled grooves prior to UV writing and etching. (a) 1mm (b) 1.5mm. Run up grooves are used to provide entry and exit points away from the microbeams to reduce chipping.

Figure 40 shows a magnified image of the groove showing significant reduction in the level of chipping.

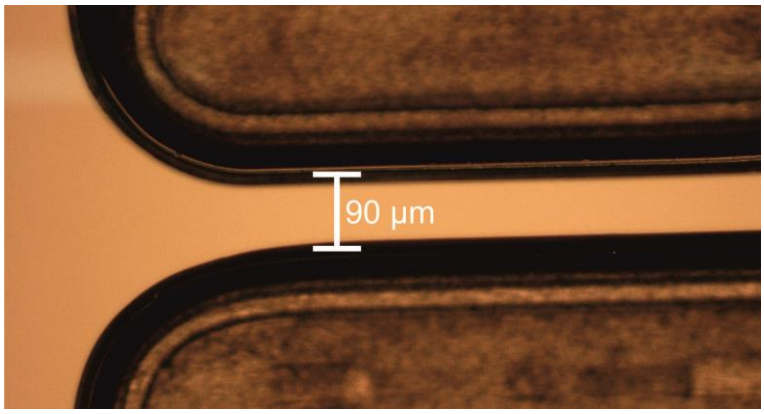

Figure 40. x10 optical microscope image of milled device in Figure 39(a) allowing for comparison with Figure 38.

4.4.2 UV writing of waveguide and Bragg gratings

The chip is loaded under high-pressure hydrogen to give increased photosensitivity. Single mode waveguides and Bragg gratings are written into the glass layer using the direct UV writing process which is described in more detail in Chapter 3. Figure 41 shows the layout of the optical elements in the device. A Gaussian apodized Bragg grating with central reflection wavelength of 1565 nm is located in the microbeam whilst two Bragg gratings with a peak reflection wavelength of 1550 nm are written either side to form a Fabry-Pérot cavity. As the Fabry-Pérot cavity is formed with two

Gaussian apodized Bragg gratings, spectrally it consists of sharp fringes with periodicity determined by the cavity length with a Gaussian function envelope. The cavity was used to determine the response time of the microbeam to applied heating due to sensitivity of fringe position to changes in the optical path length.

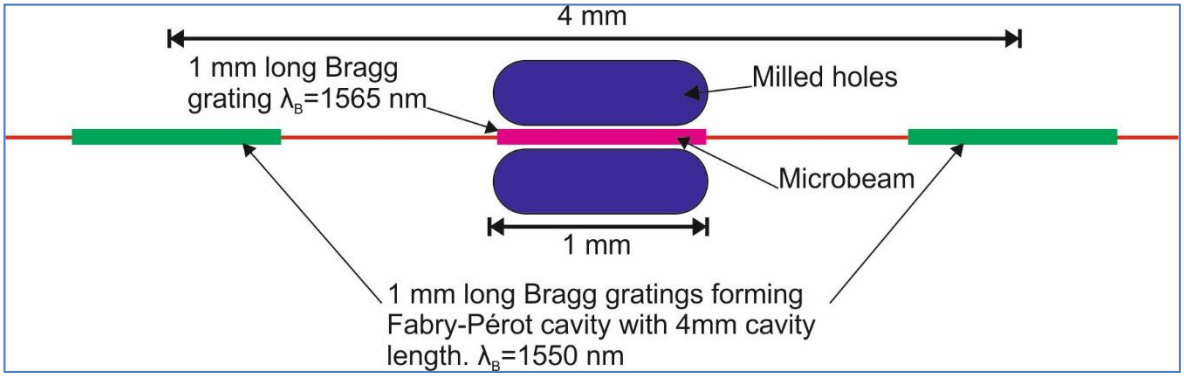

Figure 41. Schematic showing layout of microbeam and Bragg gratings.

4.4.3 KOH under-etching

A potassium hydroxide wet etch was used to remove the exposed silicon releasing the microbeam. The chip was immersed in 4.5 mol/l solution at 75 ºC for 5 hours. Figure 42 shows microscope images of the released microbeams. The glass microbeam is almost transparent but can be seen above the silicon floor in the microscope image. The irregular silicon etch features are a result of anisotropic etching of the groove bases due to the crystalline planes of the <100> substrate.

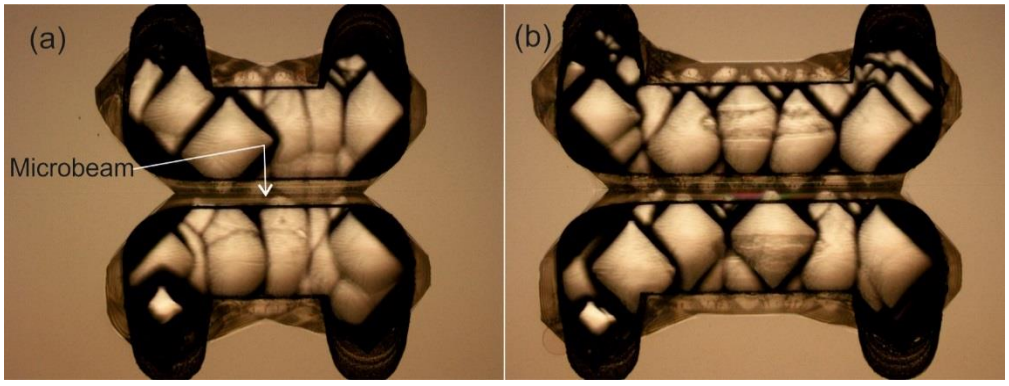

Figure 42. Microscope images of the microbeams following KOH wet etch (a) 1mm (b) 1.5mm. The arrow locates the glass microbeam separated from the underlying silicon floor.

The reflection spectrum of the device was characterized optically before and after etching. Figure 43 shows a comparison of the spectra before and after etching. The data is normalized to the source power so that 0 dB is full reflection. The Bragg grating in the microbeam is shown at

around 1566 nm whilst the Fabry-Pérot cavity peak location is at approximately 1552 nm. A zoomed-in section of the spectra is plotted to show the Fabry-Pérot fringes more clearly.

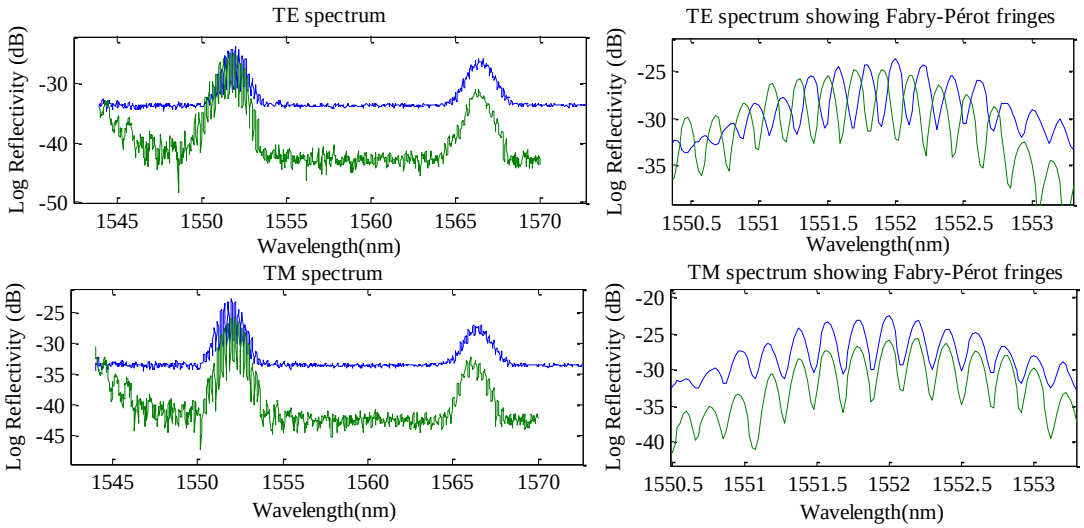

Figure 43. Comparison of spectra before (blue line) and after etching (green line) for the TE and TM modes.

It can be seen that the background level is lower for the measurement after etching and this is believed to be due to improved optical coupling in this characterization measurement.

4.4.4 Deposition of metal heating element

A gold heating strip is deposited using evaporative deposition. A 5 nm seed layer of chromium is first deposited to improve adhesion between the gold and silica glass. The thickness of the gold layer is 25 nm. Polyimide tape was used as a rough mask for the heating strip. A microscope image following this step is shown in Figure 44. The reduction in width across the microbeam ensures that the majority of Joule heating will occur in this region. The metallic heater element is separated by 17 µm of cladding glass from the core of the waveguide, thus ensuring that the optical field does not suffer attenuation due to the metal.

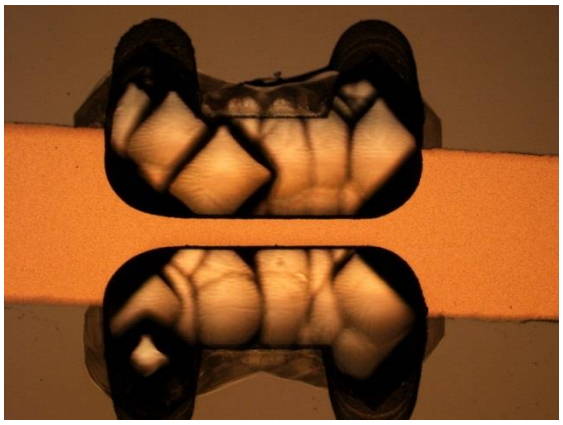

Figure 44. Optical microscope image of microbeam following the chromium and gold deposition

A scanning electron microscope was used to image the device to confirm it had been fully undercut. Figure 45 shows two shows SEM images for two different lengths of microbeam.

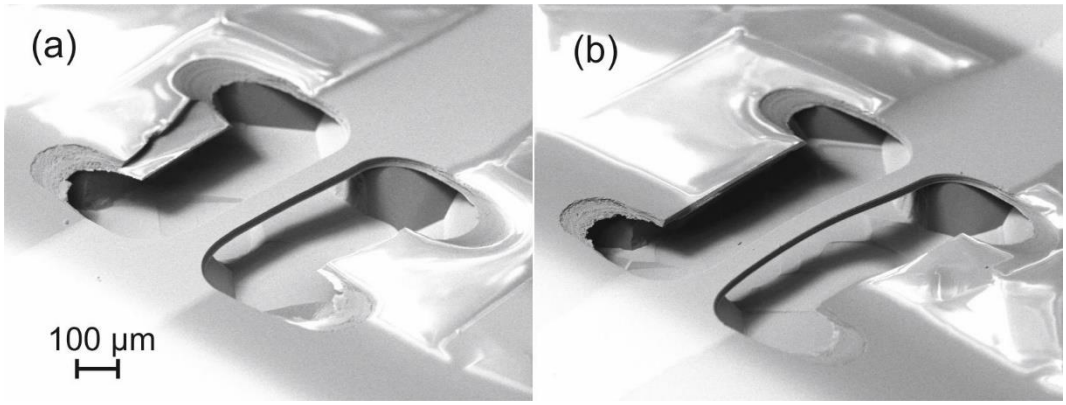

Figure 45. SEM images showing released microbeams.(a) 1mm (b) 1.5mm.

These images confirm the device is fully undercut and free of obvious defects. The bright regions either side of the structure are due to charging as they did not have the gold coating to remove electrons.

4.5 Characterisation

4.5.1 Thermo-optical characterization

With the heating element deposited the tuning of each Bragg grating's reflection wavelength with heating power was studied. An Optical Spectrum Analyser (OSA) was used to measure the reflection spectrum of the device for a range of heating powers. Gaussian fitting to the Bragg peak allows the peak Bragg wavelength to be plotted as a function of heating power. The optical setup includes a polariser which allows the TM and TE modes to be studied independently. The measurement setup for broadband characterization is described in more detail in Chapter 3.

Figure 46 shows the shift in central Bragg peak wavelength with electrical heating power. Also shown is the average temperature of the microbeam during tuning. This was measured using a 4-point-probe method which will be described later in the report.

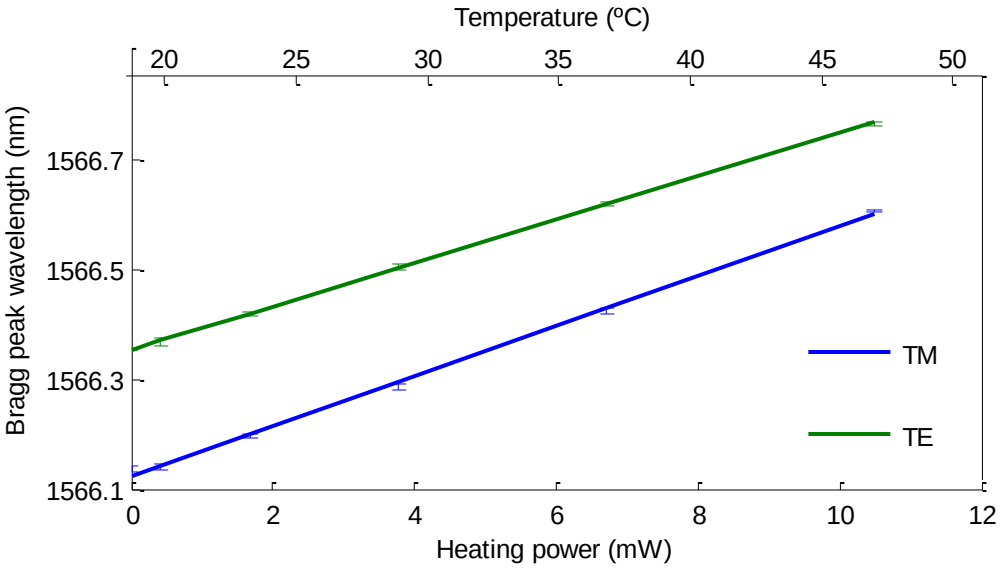

Figure 46. Shift in central Bragg peak wavelength with electrical heating power. The top axis also shows the temperature reached by the microbeam as measured by a 4-point-probe technique. The error bars are calculated from the error in the mean of 5 measurements taken for each data point.

It can be seen that the tuning efficiency is slightly higher for the TM mode at 45±2 pm/mW verses 39±1 pm/mW for the TE mode. This is believed to be due to the inherent in-plane fabrication stress in the silica which means the material behaves anisotropically when heated. The Bragg peak shift is linear in power for both modes and this is an indication that the microbeam remains in the unbuckled mode during tuning. For a tuneable reflector device it is desirable that the spectral shape of the Bragg peak is maintained during tuning. Figure 47. shows that this is the case over the tuning range studied. The fringes in Figure 47 result from interference between the Bragg grating response and imperfectly terminated end-facets and this is confirmed by the period of the fringes. The gratings in this device were Gaussian apodised, but can in principle, be designed to offer more advanced functionality as commonly used in laser written Bragg gratings [23].

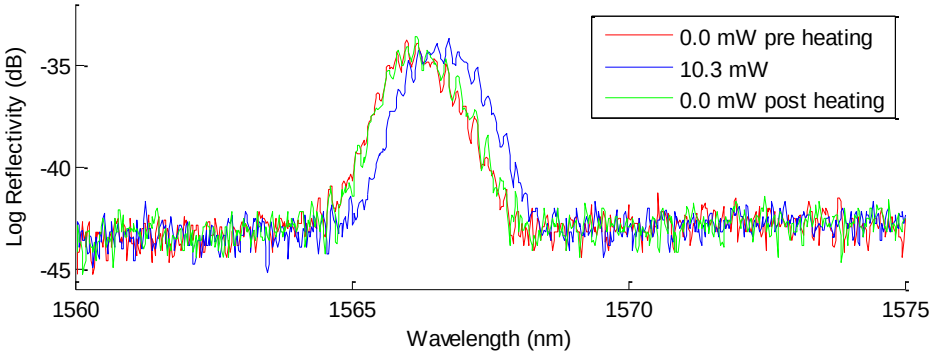

Figure 47. Spectra showing Bragg peak during tuning.The spectrum at maximum heating is shown in blue and indicates that the spectral shape and height are preserved during tuning.

A four-point probe measurement was conducted to find the temperature reached by the microbeam. During tuning the current supplied to the heating element was measured using an Agilent U1253A multimeter and the voltage drop across the element was measured using a Keithley 2100 multimeter. From this data the I-V relationship for the thin film heating element was established. The temperature dependent coefficient of resistance was determined by bulk heating of the device and performing the 4-point probe measurement at low current to reduce extra heating. The experimentally determined temperature coefficient of resistance was determined to be 0.00230(6) $°C^{-1}$. It has previously been reported that in thin metallic gold films the temperature coefficient of resistance is lower than for the bulk material [24]. The data in Figure 46 includes the inferred temperatures reached during Bragg peak tuning. It can be seen an average temperature of 47 °C is reached at the maximum of the tuning. The tuning efficiency of this device is approximately a factor of 90 better than a thermally tuneable Bragg grating in a bulk silica device [16]. The limiting factor to the tuning range is expected to be either the erasure of the Bragg grating at high temperatures or the fracture of the microbeam due to additional mechanical stress during tuning.

4.5.2 Thermo-mechanical characterization

Following the optical characterisation the mechanical behaviour of the microbeam during tuning/heating was also investigated. Localised heating causes a thermal deformation of the microbeam. The microbeams were characterized mechanically using a Zemetrics Zescope optical profiler. The Zescope records 3 dimensional surface plots from which line slices of height can

extracted. Figure 48 shows the measured microbeam profiles without any applied heating. The sign convention is with positive deflection being upward out of the plane of the device.

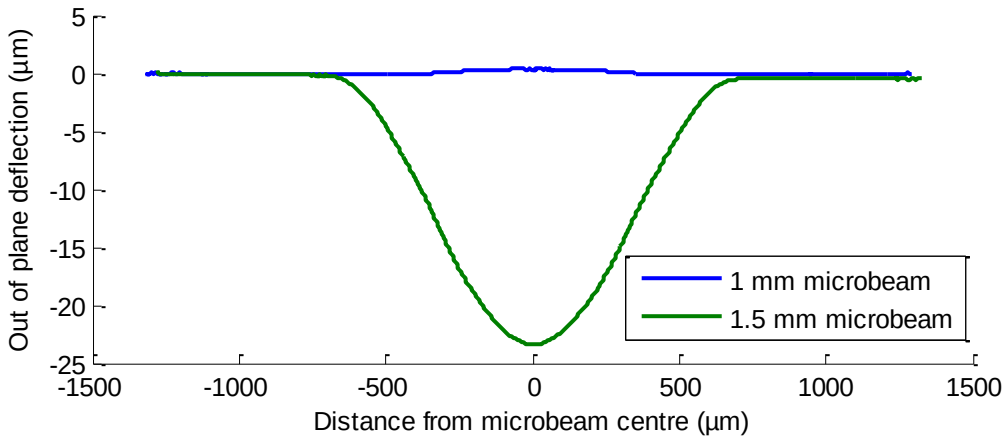

Figure 48. Deflection of microbeams following etch release. The shorter microbeam shows slight upward out-of-plane deflection whilst the longer 1.5 mm microbeam has undergone buckling downward.

It can be seen that for the 1 mm long microbeam there is a small positive deflection of 0.4 µm. The 1.5 mm microbeam has deflected downwards by 23.3 µm. This strongly suggests only the 1.5 mm microbeam has buckled. The direction of buckling is downwards, towards the silicon substrate. This direction offers greater strain relief to the thermal oxide underclad, which has higher initial compressive stress than the FHD overclad. The effect of heating on the deflection was also investigated for both the buckled and unbuckled microbeams. Figure 49 shows how the centre points of the microbeams moved under increasing heating.

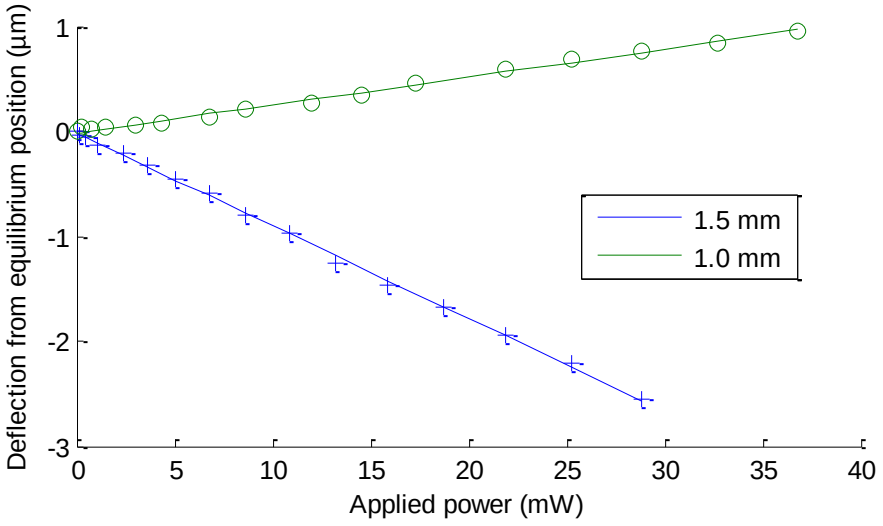

Figure 49. Effect of heating on microbeam deflection. The buckled microbeam shows greater out-of-plane growth for the same applied heating power than the unbuckled microbeam.

This data shows that the buckled microbeam deflects further out of the plane for a given heating power than the unbuckled microbeam. This is expected as the buckled microbeam is less constrained to deflect out of plane. The direction of the heating induced deflections follow the direction of initial movement following etch release which is expected as this reduces the thermal stress by lengthening the microbeam. For the unbuckled there will be a point at which the compressive stress exceeds the critical stress and after this point the device will initiate the buckling. For the unbuckled microbeam further heating would lead to breakage of the microbeam.

4.5.3 Response time

The increased energy efficiency of this device comes at penalty of a slower time response. The response time to a switch-on voltage of 0.5 V was measured using an optical setup consisting of a tuneable laser tuned to wavelength which coincides with a spectrally narrow Fabry-Pérot fringe. From the tuning efficiency results obtained this is equivalent to a peak shift of 0.43 nm for the TM mode.

The tunable laser was tuned to 1552.13 nm which was found to be between a maxima and minima on the Fabry-Pérot pattern. When heated the optical path length of the microbeam increased changing the cavity length of the Fabry-Pérot cavity. The heating power only increased the cavity length by a fraction of one wavelength and so the response from the photodiode was approximated to be linear with heating. Figure 50 and Figure 51 show the optical output for the switch-on and switch-off of the voltage respectively.

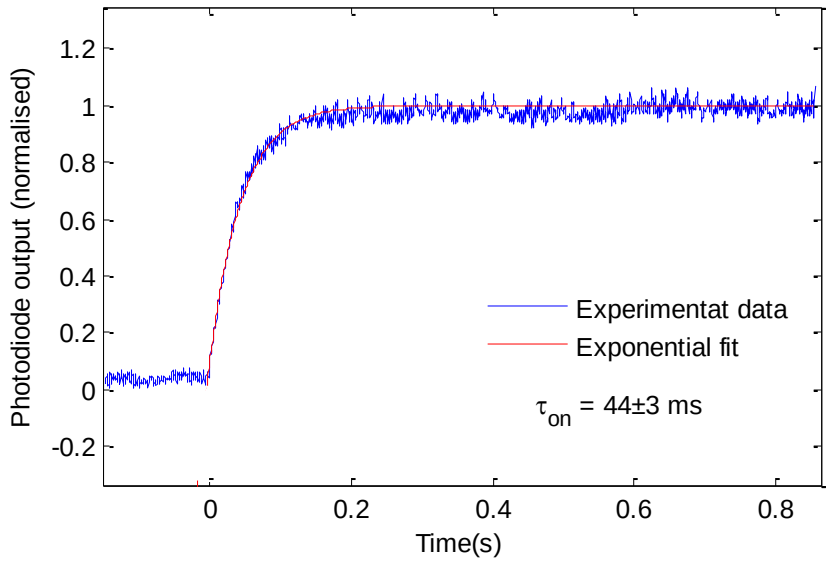

Figure 50. Switch on response time.

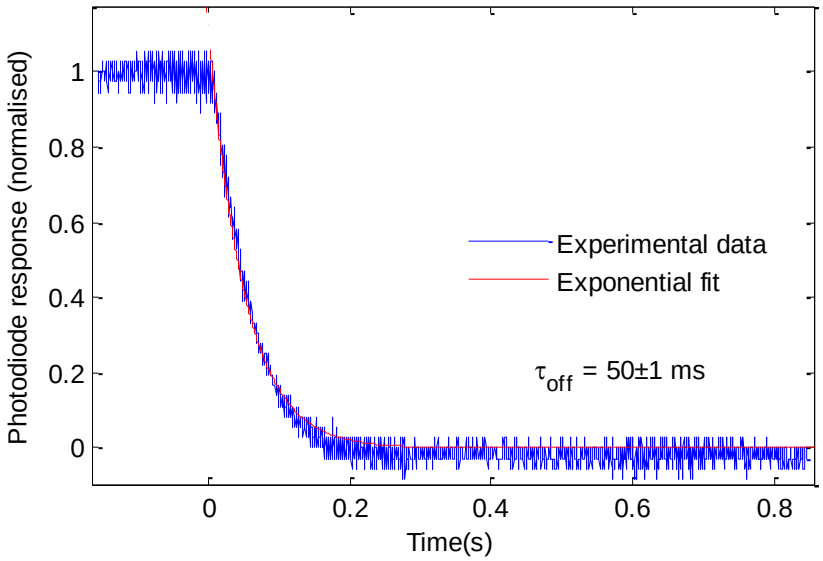

Figure 51. Switch off response time.

It can be seen that the response curve is closely modelled by an exponential function for both situations. For the switch-on a 1/e time of 44±3 ms was obtained and for the switch-off 50±1 ms was measured. This is a factor of ~50 slower than the tuning response times reported for Bragg gratings in bulk silica substrates and confirms that the trade-off for the device is between greater power efficiency and response time [16]. For applications in data-center switching or dispersion compensation our response times are sufficient, while for other applications devices with greater power consumption and high switching speeds may be preferable.

4.5.4 Loss measurement of microbeam

If the light passing through the microbeam interacts with the sidewalls or with the metal heating element this could cause loss. Although the device was designed to avoid this by having thick enough cladding that the mode should not interact with the walls of the microbeam it was tested optically to check this. A grating based method [25] was used to determine loss between two points in a waveguide. This method involves characterizing the waveguide from both ends and taking the ratio of the peak reflectivity's of Bragg gratings as seen from either end of the device.

$$\ln\frac{R_i'}{R_i''} = \ln\eta - 4\alpha x_i \tag{81}$$

Where R_i' is the reflectivity of grating '*i*'th when characterized from the first direction. R_i'' is the reflectivity of the '*i*'th grating when characterized from the second direction. x_1 is the position of the '*i*'th grating. The propagation loss α is then obtained from the gradient. More detail can be found about the derivation of this method in reference [25].

Figure 52 shows that loss is calculated from grating strengths after characterization from both ends of the device.

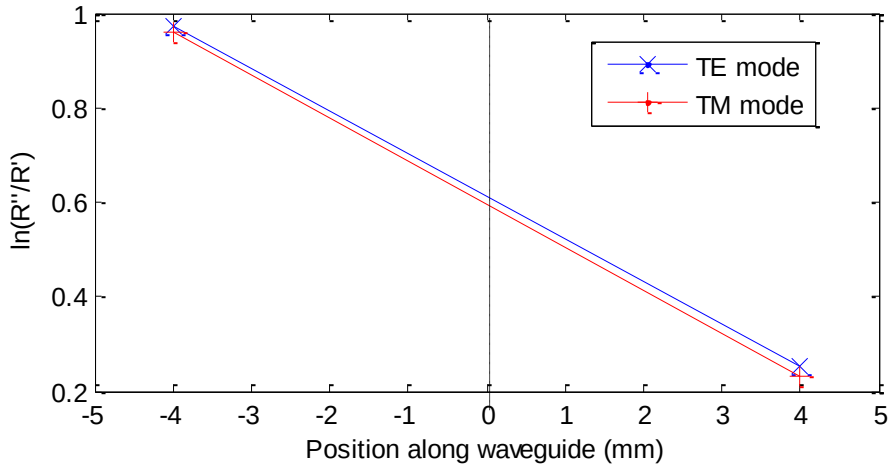

Figure 52. Grating based loss calculation method.

The loss, α is obtained by using equation (81) to give 0.18 dB for this 8 mm section. The propagation losses for FHD waveguides have been found by other work to be 0.16 dB for this length indicating the additional loss caused by the microbeam is small within experimental error.

4.6 Summary

The first tuneable Bragg grating in a microbeam structure in silica on silicon photonics has been demonstrated and shown to have a efficiency of tuning 45±2 pm/mW for the TM mode and 39±1 pm/mW for the TE mode. This is a factor of ~90 times better than achievable with a similar bulk silica device. The performance trade-off is with response time which is approximately 50 times lower than a comparable bulk device.

4.7 References

[1] H. Guckel, T. Randazzo, and D. W. Burns, “A simple technique for the determination of mechanical strain in thin films with applications to polysilicon,” *J. Appl. Phys.*, vol. 57, no. 5, p. 1671, Nov. 1984.

[2] T. Lisec, S. Hoerschelmann, H. J. Quenzer, B. Wagner, and W. Benecke, “Thermally driven microvalve with buckling behaviour for pneumatic applications,” in *Proceedings IEEE Micro Electro Mechanical Systems An Investigation of Micro Structures, Sensors, Actuators, Machines and Robotic Systems*, 1994, pp. 13–17.

[3] D. J. Joe, Y. Linzon, V. P. Adiga, R. a. Barton, M. Kim, B. Ilic, S. Krylov, J. M. Parpia, and H. G. Craighead, "Stress-based resonant volatile gas microsensor operated near the critically buckled state," *J. Appl. Phys.*, vol. 111, p. 104517, May 2012.

[4] A. Sugita, "Bridge-suspended silica-waveguide thermo-optic phase shifter and its application to Mach-Zehnder type optical switch," in *International Conference on Integrated Optics and Optical Fiber Communication*, 1990, pp. 105–109.

[5] C. R. Raum, R. N. Tait, and R. C. Gauthier, "Fabrication and characterization of a thermo-mechanically tunable grating-assisted suspended waveguide filter," Proc. SPIE 6898, Silicon Photonics III, 68981E, 13 Feb. 2008.

[6] B. Calkins, P. L. Mennea, A. E. Lita, B. J. Metcalf, W. S. Kolthammer, A. Lamas-Linares, J. B. Spring, P. C. Humphreys, R. P. Mirin, J. C. Gates, P. G. R. Smith, I. A. Walmsley, T. Gerrits, and S. W. Nam, "High quantum-efficiency photon-number-resolving detector for photonic on-chip information processing.," *Opt Express*, vol. 21, no. 19, pp. 22657–70, Sep. 2013.

[7] A. Iocco, H. G. Limberger, R. P. Salathe, L. A. Everall, K. E. Chisholm, J. A. R. Williams, and I. Bennion, "Bragg grating fast tunable filter for wavelength division multiplexing," *J Lightwave Technol*, vol. 17, no. 7, pp. 1217–1221, Jul. 1999.

[8] B. J. Eggleton, A. Ahuja, P. S. Westbrook, J. A. Rogers, P. Kuo, T. N. Nielsen, and B. Mikkelsen, "Integrated Tunable Fiber Gratings for Dispersion Management in High-Bit Rate Systems," *J Lightwave Technol*, vol. 18, no. 10, pp. 1418–1432, Oct. 2000.

[9] L. G. Carpenter, C. Holmes, H. L. Rogers, P. G. R. Smith, and J. C. Gates, "Integrated optic glass microcantilevers with Bragg grating interrogation.," *Opt Express*, vol. 18, no. 22, pp. 23296–23301, Oct. 2010.

[10] C. Holmes, L. G. Carpenter, J. C. Gates, and P. G. R. Smith, "Miniaturization of Bragg-multiplexed membrane transducers," *J Micromech Microeng*, vol. 22, p. 025017, Feb. 2012.

[11] B. J. Metcalf, J. B. Spring, P. C. Humphreys, N. Thomas-Peter, M. Barbieri, W. S. Kolthammer, X.-M. Jin, N. K. Langford, D. Kundys, J. C. Gates, B. J. Smith, P. G. R. Smith, and I. A. Walmsley, "Quantum teleportation on a photonic chip," *Nat. Photonics*, vol. 8, pp. 770–774, Sep. 2014.

[12] S. Donati, S. Barbieri, and G. Martini, "Piezoelectric actuation of silica-on-silicon waveguide devices," *Ieee Photonic Tech L*, vol. 10, pp. 1428 – 1430, Oct. 1998.

[13] F. R. Mahamd Adikan, J. C. Gates, A. Dyadyusha, H. E. Major, C. B. E. Gawith, I. J. G. Sparrow, G. D. Emmerson, M. Kaczmarek, and P. G. R. Smith, "Demonstration of 100 GHz electrically tunable liquid-crystal Bragg gratings for application in dynamic optical networks," *Opt Lett*, vol. 32, no. 11, pp. 1542-1544, Jun. 2007.

[14] P. A. Cooper, L. G. Carpenter, C. Holmes, C. Sima, J. C. Gates, and P. G. R. Smith, "Power-Efficiency Enhanced Thermally Tunable Bragg Grating for Silica-on-Silicon Photonics," *IEEE Photonics J.*, vol. 7, no. 2, Apr. 2015.

[15] J. H. Wray and J. T. Neu, "Refractive Index of Several Glasses as a Function of Wavelength and Temperature," *J. Opt. Soc. Am.*, vol. 59, no. 6, pp. 774-776, Jun. 1969.

[16] C. Holmes, D. O. Kundys, and J. C. Gates, "150 GHz of thermo-optic tuning in direct UV written silica-on-silicon planar Bragg grating," *Electron. Lett.*, vol. 45, no. 18, pp. 954–955, Aug. 2009.

[17] A. Barlow and D. Payne, "The stress-optic effect in optical fibers," *IEEE J. Quantum Electron.*, vol. 19, no. 5, pp. 834–839, May 1983.

[18] B. G. Aitken and R. E. Youngman, "Borophosphosilicate glasses: properties and structure," *Phys Chem Glasses*, vol. 47, no. 4, pp. 381–387, Aug. 2006.

[19] N. P. Bansal and R. H. Doremus, *Handbook of Glass Properties*. Elsevier, 2013.

[20] J. M. Gere and S. P. Timoshenko, *Mechanics of Materials*, Fourth. Stanley Thornes, 1999.

[21] T. L. Bergman and F. P. Incropera, *Fundamentals of Heat and Mass Transfer*. John Wiley & Sons, 2011.

[22] L. G. Carpenter, P. A. Cooper, C. Holmes, C. B. E. Gawith, J. C. Gates, and P. G. R. Smith, "Nanoscale roughness micromilled silica evanescent refractometer," *Opt Express*, vol. 23, no. 2, p. 1005-1014, Jan. 2015.

[23] R. Kashyap, *Fiber Bragg Gratings*. San Diego: Academic Press, 1999.

[24] F. Avilés, O. Ceh, and A. I. Oliva, "Physical Properties Of Au And Al Thin Films Measured By Resistive Heating," *Surf. Rev. Lett.*, vol. 12, no. 1, pp. 101–106, Jan. 2005.

[25] H. L. Rogers, S. Ambran, C. Holmes, P. G. R. Smith, and J. C. Gates, "In situ loss measurement of direct UV-written waveguides using integrated Bragg gratings," *Opt Lett*, vol. 35, no. 17, pp. 2849–2851, 2010.

Chapter 5: Integrated optical dual-cantilever arrays in silica on silicon

5.1 Introduction

The cantilever is common structure in MOEM devices. Its geometry makes it flexible and especially well-suited to function as a sensor or actuator [1]. MOEM devices using a single cantilever have been demonstrated previously, for example, where a moveable waveguide is displaced relative to a fixed waveguide. Ollier *et al.* fabricated an optical switch based on silica-on-silicon technology that used electrostatic switching to function as a switch between channel waveguides [2]. While single cantilevers provide a way to create devices, the use of dual cantilevers has been pioneered by Park *et al.* as a way of attracting cells to adhere to a cantilever, whereon they can be cultured and weighed using a resonance frequency method [3]. In another example of this geometry Xu *et al.* fabricated dual cantilevers in polymer, which also served as waveguides, in a device that functioned as an acoustic sensor [4].

Various schemes are well known for transducing mechanical motion onto an optical signal. For example, a small mirror mounted on the cantilever will deflect a laser beam, an approach widely deployed together with quadrant detectors in atomic force microscopy. However, all free space optics are susceptible to their local environment, for example temperature, airflow, vibration, shock, *etc.*, and a well-known advantage of integrated optics, beyond the simple factor of compactness, is robustness and reduced cross-sensitivity. Thus, if the components for optical sensing can be integrated into the cantilever then this can have benefits for the performance and compactness of the device. The integration of optical components into a glass cantilever for force sensing has already been demonstrated by Zinoviev *et al.* [5]. Carpenter *et al.* [6] incorporated two Bragg reflectors into a glass cantilever to create a cavity. In that work deflection of the cantilever caused a change in the optical path length of the cavity thereby modifying the optical spectrum which was used to determine the deformation.

Beyond sensing, fibre based variable optical attenuators have been demonstrated by Barber *et al*. [7]. They used a voltage-controlled moving mirror MEMS device to achieve up to 50dB of attenuation. Ford *et al*. fabricated a MEMS device which used a silicon nitride quarter wave plate to realize a variable reflective mirror [8]. Their device exhibited 25 dB of dynamic range with an insertion loss of 3 dB. Another area where the dual-cantilever geometry is employed is in the domain of particle trapping. Constable *et al*. first demonstrated an optical light trap configuration

comprising of only two optical fibres avoiding the use of any other optical elements [9]. They indicated that angular displacement of the fibres allows the trap position to be moved. Black *et al*. [10] further showed that translational displacement could be used to give controlled rotation of smooth muscle cells. As well as applications in biological science, Succo *et al*. demonstrated a monolithic implantation of a cold atom trap [11] using dual waveguides. A dual-cantilever version of this device could be used to provide better physical access for probing of the atom, and offers potential for microscopic adjustment of trap parameters. In this report, we describe a dual-cantilever device, fabricated and characterized for the first time in silica-on-silicon. The new devices in this work are larger in cross-section than conventional MEMS leading to greater bending stiffness and high resonant frequencies. While high stiffness requires greater force to actuate, it can be advantageous in providing better immunity to acoustic noise or vibration and thus can be desirable for attenuator, switching or trapping applications. Furthermore, in some MEMs applications in harsh environments, e.g. projectiles, accelerations of up 100,000g occur and more robust MEMs structures may have advantages [12]. The lack of free space optics combined with the potential for multiplexed sensing could make possible the use of this type of device in field applications.

As described in Chapter 2 dicing is a relatively new technique to be applied to integrated optics. Dicing is the core technique in the fabrication of the dual cantilever device and is used to machine grooves in a similar way to the fabrication of the microbeam in the previous chapter. As the volume of material to remove is larger, it is well suited to the task.

In this chapter the design of the dual cantilever device will be explained and applications examined. The work has already been reported as a journal paper [13]. The novel fabrication process involving the dicing and KOH etching is described in detail, with parameters given for the machining and etch. The bend of the cantilevers due to deposition stress in the glass is modelled using COMSOL software and by treating cantilevers as a two layer glass structure with varying physical and deposition parameters. The response of the cantilevers to mechanical actuation is found by deflecting them with an optical fibre and measuring the transmission using a grating based method. This is done for both simultaneous deflection of the cantilevers and single deflection. This data is compared with theory by using fibre-optic misalignment theory and considering rotation, translation and offset. The effect of adding index matching oil into the gap between cantilevers is also reported.

5.2 Fabrication of dual cantilever device

Figure 53. Shows a 3D visualization showing the concept of dual opposing cantilevers machined into silica-on-silicon. Each cantilever contains an optical waveguide. The cantilevers are produced using dicing technology and etching away silicon to release the silica structures.

The dual cantilever arrangement shown in Figure 53 consists of a neighbouring pair of cantilevers with each cantilever containing a waveguide. The devices are fabricated in silica-on-silicon and the details of the fabrication will be described in detail later. When both cantilevers are deflected, this changes the relative angle between them and hence the coupling of light between the launching waveguide and the receiving waveguide. This section will describe the fabrication steps, as well as design considerations that affect the performance of the device. The underlying substrate is a silicon wafer of <100> orientation of 1mm thickness, providing a robust starting platform. The key techniques in the fabrication of the cantilevers are a micromachining process using a dicing approach and wet etch with potassium hydroxide. The initial substrate is the same as used for the microbeam device in Chapter 4. A core layer doped with germanium is deposited with the FHD process onto a 17 µm thermally deposited silica layer on silicon. A clad is deposited onto the core layer. Although high temperatures are required during the fabrication of the substrate, other devices, such as MEMS, could be integrated upon the substrate but only post consolidation. The high processing temperatures result in a very physically and chemically robust platform.

5.2.1 Dicing in plunge cut mode

To create the cantilevers a Loadpoint Microace dicing saw was used to define 7 grooves through the silica and into the silicon. A plunge-cut mode was used which consists of the blade coming vertically downwards onto the workpiece without any translation. The parameters selected are

shown in Table 3. These parameters were obtained after work to find parameters would not cause blade breakage or excessive chipping.

Table 3. Dicing parameters for plunge cut mode.

Blade type	100 µm nickel bonded diamond (ZH05-SD4000-N1-50 KK)
Spindle speed	20 krpm
Plunge speed	5 µm/s
Depth of cut	45 µm

As plunge-cutting is more susceptible to blade breakage and top-edge chipping, optimization was required to avoid these issues. Figure 54(a) shows the structure after the dicing steps.

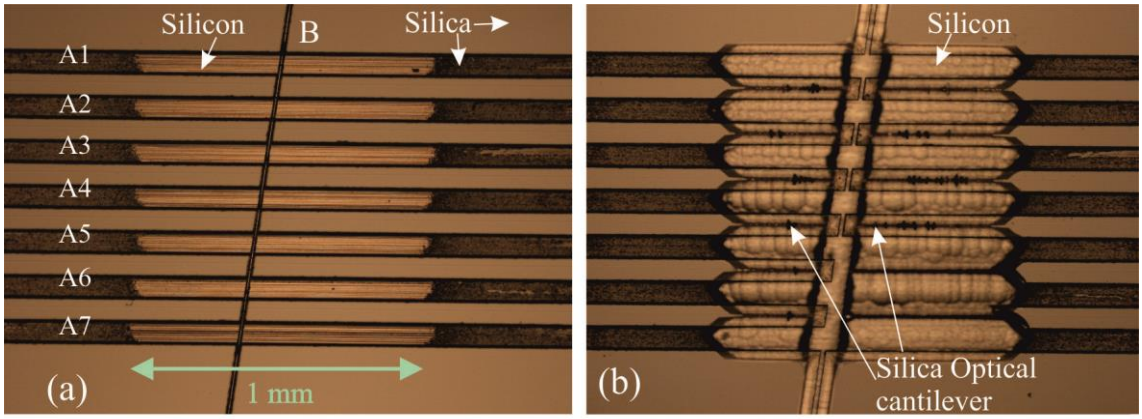

Figure 54. The image shows an optical microscope (top-side) image of the glass cantilevers before etching. 7 parallel grooves are diced using a plunge method technique (labelled as A1-A7 on the image). The silicon substrate is observed in the middle of the grooves and highlights the crescent shape. A second channel (B) is diced at an angle of 8° from perpendicular to the previous grooves which was in a conventional non-plunge mode. Fig 2b shows the glass cantilevers after etching. The regions of exposed silicon are removed by the KOH etchant, resulting in the lighter coloured central regions. The overlaying optical cantilevers are essentially transparent but can be seen most clearly in the region of the central channel.

As seen in the image the exposed silicon at the centre shows higher reflectivity than the exposed silica due to lower surface roughness and increased Fresnel reflection. Due to the circular blade shape, the resultant grooves are crescent shaped with the silicon only being exposed at the centre where the grooves are deepest as shown in the graphic Figure 55.

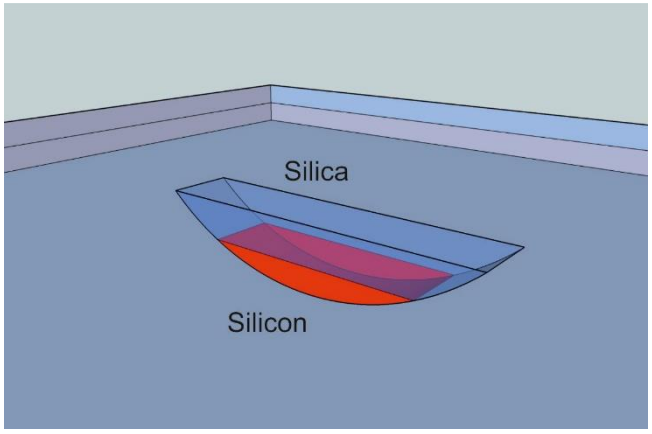

Figure 55. Image shows a 3D visualization of the crescent shaped plunge-cut illustrating that the silicon becomes exposed only in the central region of each cut. This is important as the silicon etches much faster with KOH, so it is this exposed region that undercuts the overlying adjacent silica to create the cantilevers.

To create the dual cantilevers a second groove (B) is diced with a 15 µm width blade at an angle of 8 degrees from perpendicular to the previous grooves. Having the end facets of the cantilevers at this angle ensures that the reflected light exceeds the numerical aperture of the guide, which could lead to fringes in the measured spectrum.

5.2.2 UV writing of waveguide and Bragg gratings

The previously reported direct UV writing process [14] is used to simultaneously define the waveguides and Bragg gratings. 9 Bragg gratings are written along the waveguide with various periods which will be used for characterization. The waveguides were written after the dicing but before the wet-etch described in the next section. Using the UV fluorescence from the sample, the waveguides and Bragg gratings were precisely aligned to the diced grooves. The location and wavelengths of the Bragg gratings are shown in Figure 56.

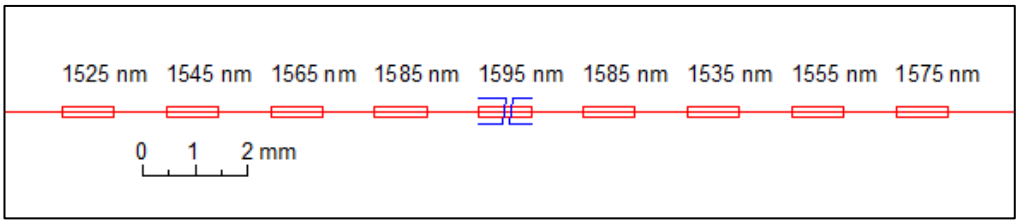

Figure 56. A schematic showing the locations of the waveguide and Bragg gratings in relation to the cantilevers. Red: Bragg gratings and waveguide. Blue: Cantilevers. The gratings are 1mm in length and separated by 1mm. The total cantilever section length is also approximately 1mm and only affects the 1595 nm grating. The total device size is 10mm × 20mm.

The thickness of the core FHD layer was measured using a Metricon prism coupling system to be 5.4 µm. This defines the vertical dimension of the waveguide core. The horizontal dimension is controlled by the UV writing spot size and the applied fluence. These parameters have been adjusted to match the mode size to standard single mode optical fibre and hence the mode field diameter at 1550nm is ~10um in the vertical and horizontal directions. The resulting waveguide is single mode which is confirmed by the single Bragg peaks observed during spectral characterization. This data also confirms that the waveguides have little birefringence and indicates that the two polarization modes have similar modal dimensions. This is also confirmed by modelling with a commercial modelling program Fimmwave (Photon Design Ltd). More details of this modelling and optical mode measurements can be found elsewhere [17,18]. The dimensions of the cantilevers were designed such that the core mode was more than 17 µm away from any lateral surfaces to ensure that the mode was not affected by the external environment. Finally, the chip was wet-etched in 25% potassium hydroxide solution at 75°C for 5 hours to preferentially remove the silicon and release the glass cantilevers from the substrate. A comparison of the device pre and post etching can be seen in Figure 54.

The cross-sectional area of the cantilever is 100µm × 40µm. The channel waveguide runs through the cantilever such that it is centered about the vertical and horizontal neutral axis. This minimizes strain induced refractive index and physical length variations upon actuation [17].

Figure 57 shows a Scanning Electron Microscope (SEM) image of the released cantilevers after etching. At the stage of wafer fabrication the glass layers are all under compressive stress due to the lower coefficient of thermal expansion of the glass compared to the silicon. In addition, stress in each layer of the glass differs due to the different doping levels and also their consolidation temperatures. For example the thermal expansion coefficients vary between ~5.5×10^{-7} K^{-1} for pure silica, representative of thermal oxide, and up to 4.3×10^{-6} K^{-1} for borophosphosilicate [18]. This differential is evident in Figure 57. where upon release the micro-cantilevers deflect out of plane. Thus cantilever curvature can be controlled through a combination of layer thicknesses, cross-sectional form, or directly manipulating stress in the layers through changing dopant concentrations and consolidation temperature of the FHD process.

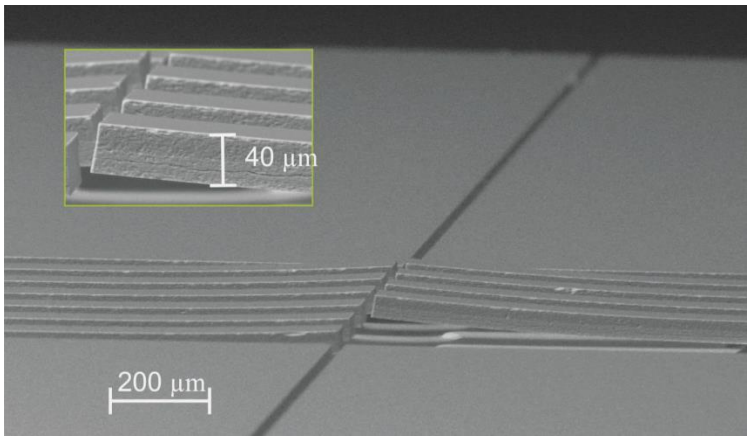

Figure 57. SEM image of the etched cantilever device. Note that first two cantilevers at the right side of the image sustained damage during the etching / drying process, however, this enables a clear visualization of the side walls of the third cantilever (shown in the inset image). The deflection out of the plane occurs because of stress inherent in the layers due to their high consolidation temperature.

The inset of Figure 57 shows a side wall image of one of the cantilevers. The device was further characterized with a Zemetrics Zescope optical profiler and results are shown in Figure 58.

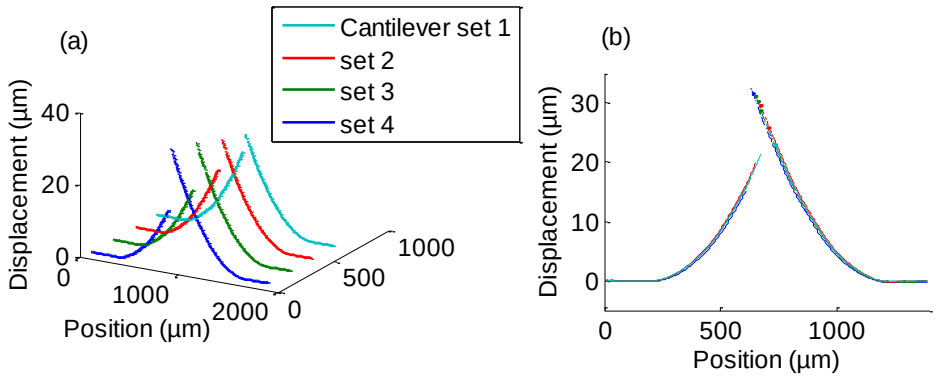

Figure 58. Profiles of cantilevers showing out-of-plane displacement without load (due to the release of intrinsic stress) (a) shows deflection of each cantilever measured with the Zescope optical profiler. The length mismatch results in differing maximum displacements. (b) shows the same data but with the curves overlapped, effectively an isometric view of (a). The shapes are very consistent with only a difference in final height between the curves.

These measurements show that the form of the intrinsic displacement was essentially the same for each cantilever. For the set of cantilevers the resultant intrinsic displacement after fabrication ranged from 5 µm to 17 µm for the shortest and longest devices respectively. The curvature of the cantilevers is due to the thermal oxide having higher compressive stress than the core and cladding. Due to the 8° crosscut used to form the dual cantilevers, the cantilever pairs have varying levels of length mismatch. The main cause of variation in the form, is due to the position

of the root which is affected by the KOH etching conditions. The limiting factors for the size of cantilever that could be produced by this method are the lateral positional accuracy of the dicing saw used and the physical strength of the machined ridge. Were the width of the cantilever to become too narrow the interaction between the optical mode and the sides of the cantilever would increase, risking additional loss.

5.3 Finite element modelling of deflection

A finite element simulation (FEM) model was run using COMSOL Multiphysics 4.3 software to investigate the nature of the bending of the cantilevers following etch release. This bending is a result of stresses in the thermally grown and FHD deposited glass layers. The first stage of the simulation is to simulate the stress profile through the layers of the substrate following deposition. The second stage is to model the dicing and etch release by using the stress and strain values obtained as input to a cantilever structure anchored at one end.

5.3.1 Simulation of deposition stresses

The Structural Mechanics module of COMSOL is used to simulate the stresses that develop when the glass layers and silicon are cooled from down to room temperature. The core layer is not included as it is thin relative to the under and overclad and the bending is expected to be dominated by these layers. The thermomechanical properties of the core layer are also not currently well known. A reference temperature is input to the model to mark the point when the glass layer solidifies and thermal stresses are built up. This approach closely follows the consolidation of FHD layers where the glass is reflowed in a furnace to consolidate the deposited soot layer. While the glass is molten it is able to relieve stress by flow, however as it cools it will pass through the glass transition temperature and further cooling will result in the build-up of thermal stresses. The situation for the thermally grown silica layer is different as the glass layer is grown beneath the melting point of pure silica. For this reason the reference temperature for the thermal silica growth is taken to be the temperature at which it is grown which is taken as 1300 °C. The model also requires thermal expansion coefficients which are well known for pure silica and silicon but known with less certainty for the clad. The following values were used for the thermal expansion coefficients. Silicon: 2.5×10^{-6}. Thermal oxide silica: 0.55×10^{-6} K^{-1}. Cladding layer glass (borophosphosilicate): 4.3×10^{-6} K^{-1}. Figure 59 shows the stress profile varies through the substrate.

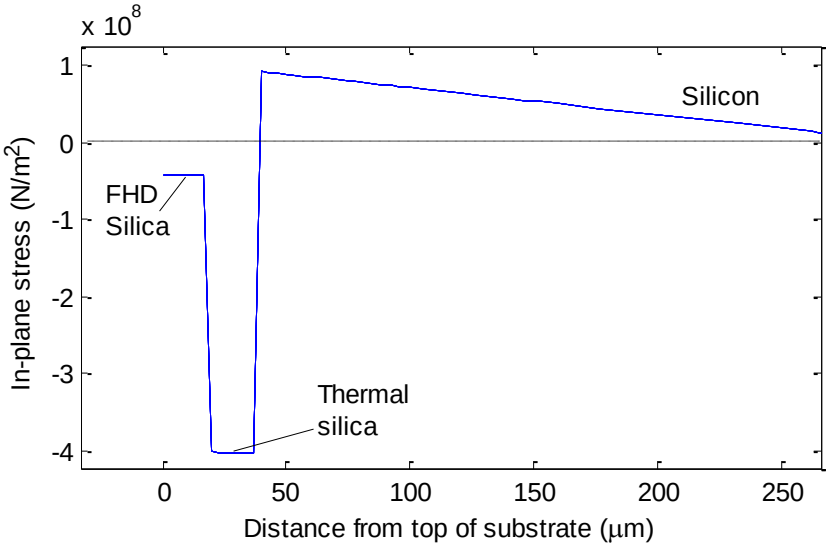

Figure 59. Simulation of stress through deposited layers.

According to the simulation the thermally grown silica layer has compressive stress of almost 400 MPa while clad has compressive stress of 50 MPa. The silicon is under tensile stress which decreases with the distance from the glass layers.

5.3.2 Modelling out of plane deflection

The 3rd stage was to model the out of plane deflections once the cantilevers are freed from the silicon substrate. This is done by passing the stress and strain values obtained from the previous study to the cantilever geometries which have one end set to be a fixed constraint. The results from the COMSOL simulation are shown in Figure 60.

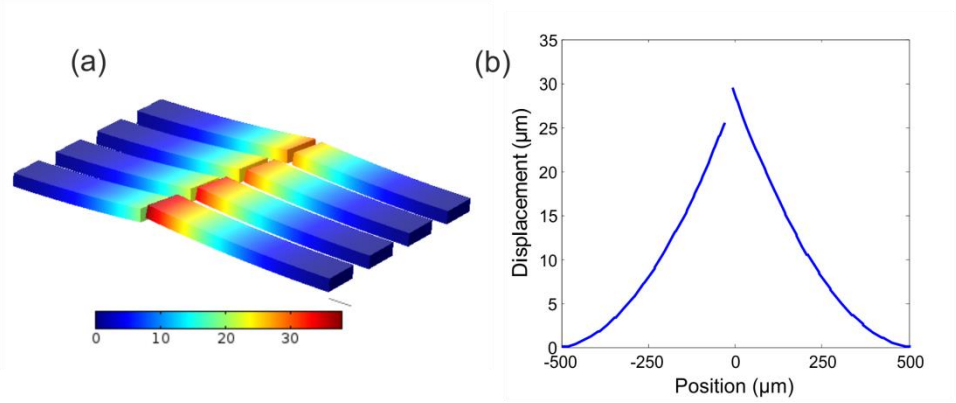

Figure 60. (a) Comsol simulation showing out-of-plane displacement following etch release (in microns). (b) The displacement cross-section through the pair of cantilevers most equal in length. The parameters of the simulation are listed in the text.

To compare the model with the experimental data the out-of-plane deflection of cantilevers in set 1 was studied. The model predicted 25 and 29 µm for the two cantilevers, while for the real device the deflections were 19 and 26 µm. This difference is believed to arise because the true coefficient of thermal expansion of the cladding layer is not known with high accuracy. However the reasonable accuracy of the model suggests that the biggest contribution to the bending is the higher thermal coefficient of expansion of the FHD cladding glass compared to the thermal oxide.

5.3.3 Actuation of cantilevers

The COMSOL model can also be used to determine what force is required to bring the cantilevers back into the plane of the glass layers. This can be simulated with COMSOL by running a sweep over a range of point loads on the end of the cantilever and measuring for the subsequent displacement. The simulation is carried out on one of cantilevers in Set 1. Figure 61 shows a plot of the displacement of the cantilever when a variable edge load is applied.

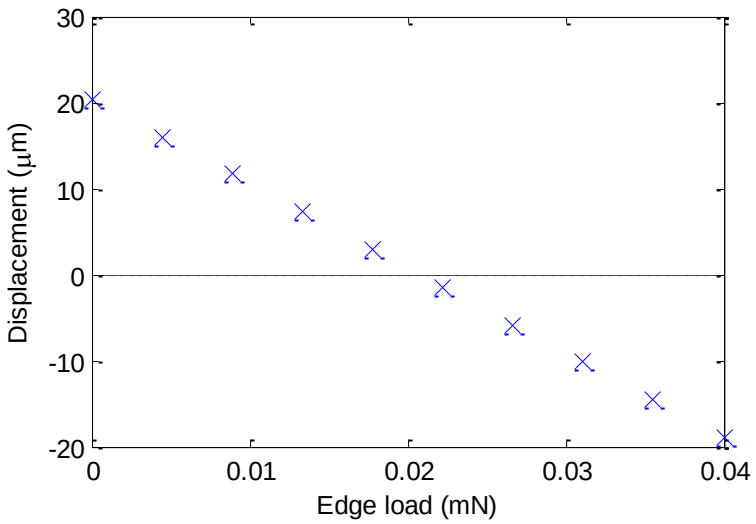

Figure 61. COMSOL simulation of displacement of the end of cantilever verses force on edge

The model shows a linear relationship between load and displacement. The simulation predicts a force of 0.2 mN to bring the cantilever into the plane of the glass layers. To actuate both cantilevers in the set to this level would then require double this force.

Figure 62 shows a 3d image of the displacement following actuation.

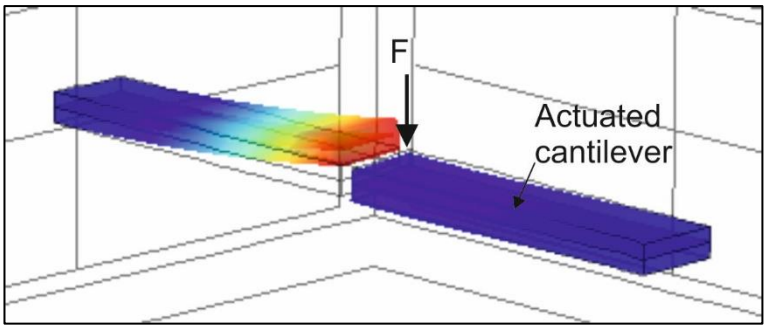

Figure 62. COMSOL 3d simulation of cantilevers showing how actuated cantilever is pushed back into plane of glass layers

By comparing the actuated cantilever to the untouched one it can be seen that the effect of a load at the tip is to push it back into plane.

It has shown that COMSOL is useful aid when investigating deflections of microstructures due to deposition stresses and for simulating the force required to actuate a cantilever. COMSOL can also be used to model stress optical effects such as stress-induced birefringence. This could be a route for further study but would require careful meshing processes to adequately cover the small core.

5.4 Results and discussion

Having fabricated the dual cantilever containing waveguides and Bragg gratings, the loss was measured using an approximation of the grating based method [19]. The optical setup for the broadband characterization is as described in Chapter 3.

Polarization maintaining optical fibre components and a polarizer are used so that the two orthogonal polarization modes can be measured separately. Figure 63 shows the spectra for the TE and TM modes. The reflectivity is normalized to the source power and includes the coupling loss due to the fibre-optic pigtailing. There is a loss between the cantilevers due to the Fresnel reflections at the two interfaces (calculated to be ~0.3dB). There is also loss from the lateral misalignment caused by the 8° interface and is calculated to be ~0.6 dB. The two gratings at 1585nm form a Fabry-Pérot cavity. The fringes from this are clearly visible in Figure 63. but will not be used in this work. The effective indexes of the TE and TM modes at 1550 nm are 1.44823 and 1.44847 respectively. This birefringence is due to in-plane thin film stress caused by the mismatch in thermal expansion coefficients between the silica and silicon. This corresponds to birefringence of 2.36×10^{-4}. This effect is due to the stress-optic effect creating anisotropic refractive index, with the TM mode exhibiting a higher refractive index.

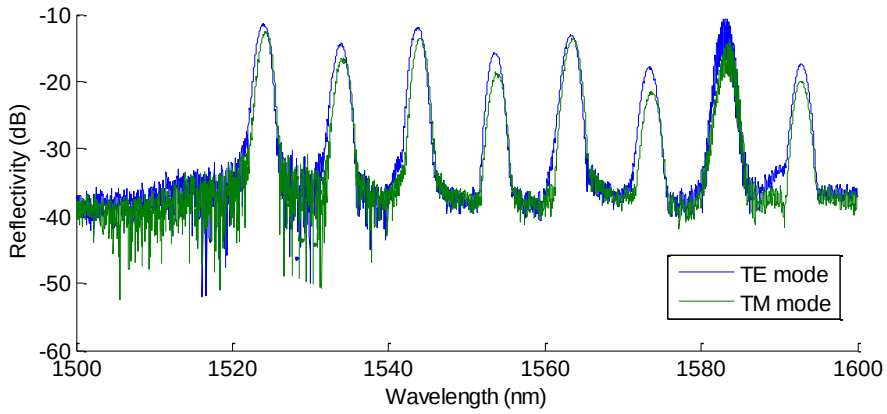

Figure 63. Reflection spectra taken after dicing but before etching. The data shows the absolute reflectivity calibrated against a known fibre end reflection. Analysis of the peaks shows a wavelength shift due to birefringence of 0.28 nm.

After etching the cantilevers are released, without load the misalignment becomes large and effectively zero signal is seen from the gratings beyond the diced groove. This is to be expected as the dual cantilevers were all asymmetric in length and so without load sit at different heights. The robustness of the cantilevers allows them to be deflected using an external load thereby bringing the waveguides into alignment. In the next section measurements will be presented demonstrating this operation.

5.4.1 Double cantilever actuation

To test the optical response of the cantilevers to actuation, an optical fibre was used to deflect the cantilevers as it could be easily cleaved to give a perpendicular end facet, as well as benefitting from having a small diameter which restricts the contact area to be close to the ends of the cantilevers. The device was mounted on a flexure translation stage (Thorlabs 3-Axis NanoMax Stage) which allowed X, Y and Z positioning with sub-micron precision. Two modes of actuation are possible: to push a single cantilever or to deflect both simultaneously as shown in Figure 64(a) & (b) respectively. In this paper a positive displacement corresponds to the cantilevers being pushed into the plane of the device. Figure 65 shows camera images of the device taken during the experiment.

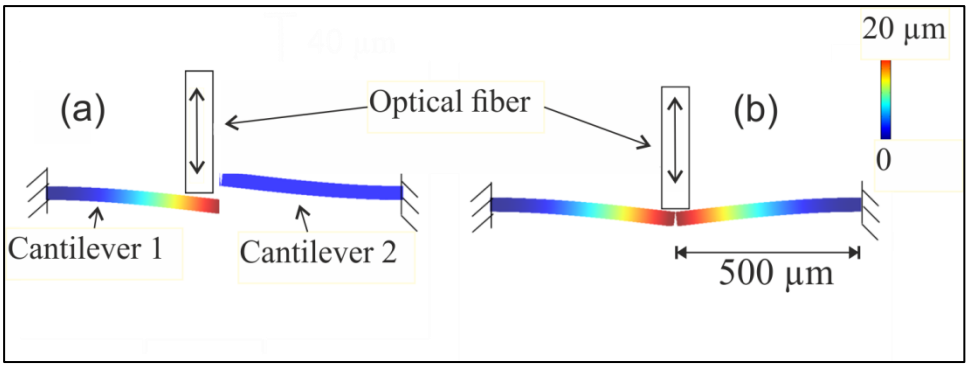

Figure 64. Showing the two possible types of actuation. The colour maps calculated in Comsol indicate the displacement of the cantilever from its rest state. The colour bar shows the displacement in microns.

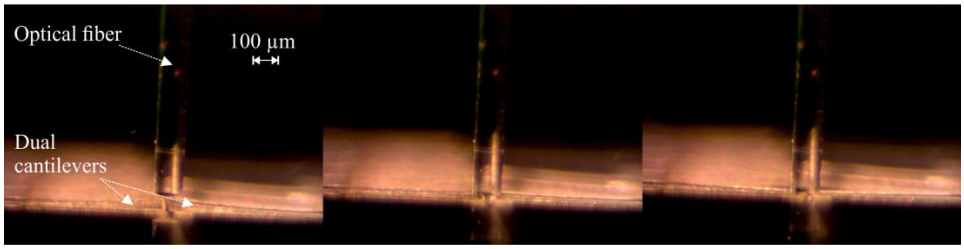

Figure 65. Camera images showing physical actuation of the cantilevers with an optical fibre pushing down on the cantilever with different heights of actuation. An optical fibre was used as it is only 125 micron in diameter and provides a stiff small cross-section rod.

Figure 66 shows a comparison of the TE spectra for the actuated and rest states. Upon actuation the two cantilevers can be aligned, such that light couples between them. This is observed when on actuation the Bragg reflections from both cantilevers can be seen. Those marked with the label ‘A’ are on the side of the device coupled to the optical fibre while those labeled ‘B’ are on the other side. This means the ‘A’ peaks in the spectrum are always visible while the ‘B’ peaks only become visible when the device is actuated. The peak labeled ‘C’ is from the Fabry-Perot cavity whilst the grating giving peak ‘D’ is located in the cantilevers. There is also an increase of approximately 10 dB in the background level due to increased broadband Fresnel reflection from the facet of the second cantilever.

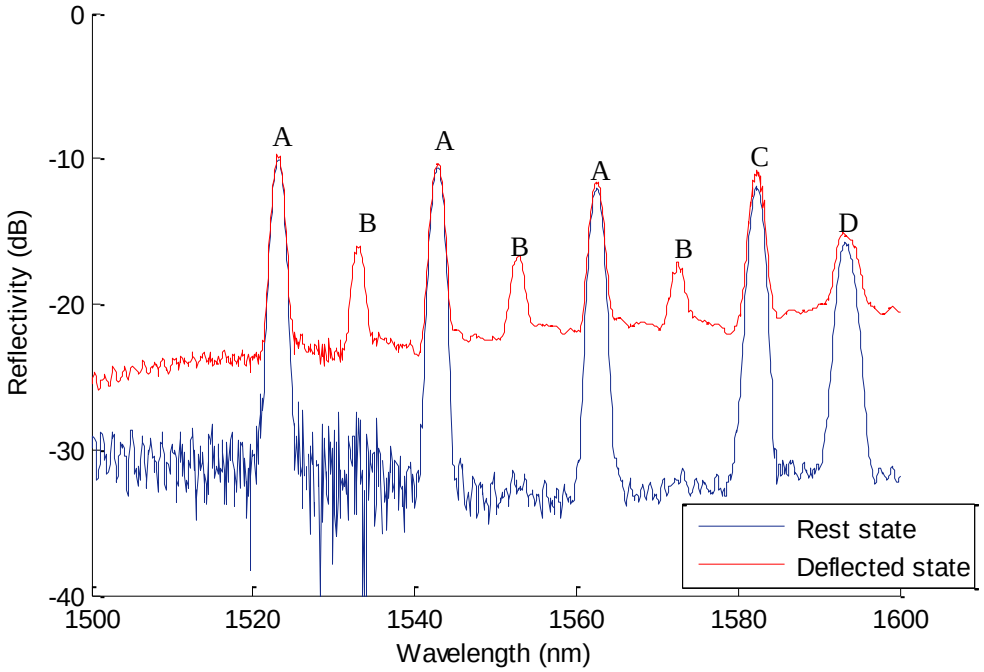

Figure 66. The measured TE spectra of the device in the rest state (blue), and a deflected state (red). Actuating the devices increases the reflectivity of Bragg gratings opposite to the coupling side. As can be seen it also increases the background level by approximately 10 dB. The Bragg gratings labelled with 'A' are on the side of the device coupled to the optical fibre while those labelled 'B' are on the other side.

The optical coupling between the cantilevers is determined by the angle between them. By measuring the transmitted intensity it is possible to measure the coupling. However by using the reflectivities of the Bragg gratings it is also possible to measure them in a way which is insensitive to fluctuations in source power and requires only coupling to one waveguide facet. Peak intensities are fitted to Gaussian apodized Bragg gratings (1555nm and 1565nm) on each side of the central cavity and used to give a relative reflectivity which is only dependent on the optical coupling between the cantilevers. The insertion loss at the maximum coupling point can be obtained by measuring the spectrum from both ends of the device [19]. The measured minimum coupling losses were 2.4±0.1 dB for the TM mode and 2.8±0.2 dB for the TE mode. The data suggests that there may be a greater loss for the TE mode, but as the difference is only 1.7σ this may not be statistically significant. The slightly greater numerical aperture of the TM mode, due to birefringence, may contribute to this difference.

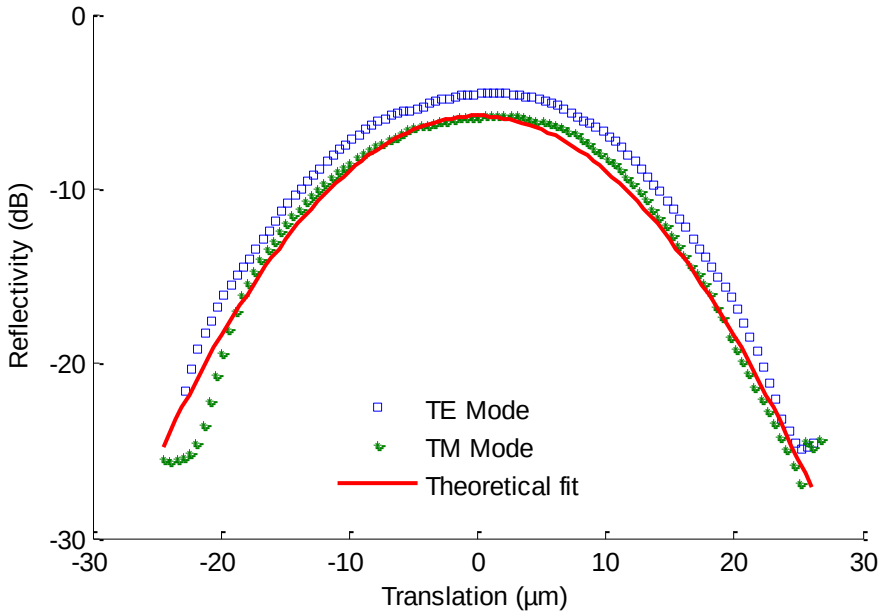

Figure 67. Plot showing the ratio of reflectivity from Bragg gratings on opposing sides of the dual cantilevers (relative reflectivity) versus the displacement of both cantilevers. The theoretical fit is included.

Figure 67 shows the coupling as both cantilevers are pushed simultaneously. The zero value for translation is obtained by fitting the quadratic misalignment loss curve after the experiment. It can be seen that the optical coupling goes through a maximum which occurs for a certain angle between the cantilevers. This is expected to be 0°, however error in the angle of the facets from the fabrication processes may give an offset. The geometry is related to the problem of loss due to angular misalignment between two fibres [20]. Here the misalignment angle is taken to be twice the angle of rotation of a single cantilever. The loss in dB is given by eq (82).

$$\alpha_a(dB) = 4.34\left(\frac{\pi n_l w\theta}{\lambda_0}\right)^2 \qquad (82)$$

Here α_a is the loss in decibels, n_l is the refractive index of the medium between the fibre ends, θ is the angle of misalignment, λ_0 is free space wavelength and w is the spot size of the mode. This loss figure (given in dB) is derived from the overlap integral of the mode exiting a first fibre being coupled into the input mode of a second fibre. The mode size w of the UV written waveguide, is approximated as 5 µm which is similar to SMF28 single mode optical fibre.

5.4.2 Single cantilever actuation

Actuating a single cantilever was also accomplished, and similarly, shows a coupling peak as seen in Figure 68. The peak is asymmetric once the actuated cantilever moves below the second cantilever, which suggests coupling from cladding modes back into the core mode. This is thought

to be as a result of the curvature of the cantilevers and the angled interface of the receiving cantilever which remains deflected due to the intrinsic stress. Once the deflected cantilever is below the receiving cantilever coupling is still possible due to refraction and scattering resulting in an asymmetric peak. The sensitivity of relative reflectivity to translation over the central 10 µm of the fitted model is 0.16 dB/µm.

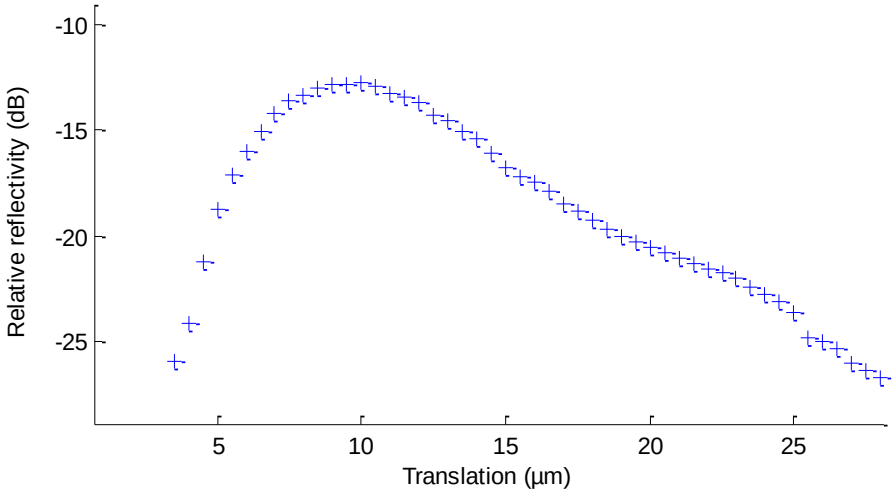

Figure 68. The relative reflectivity response of a single cantilever translation also showing a point of maximum coupling for the TE mode. It is however less symmetric which suggests that there is coupling to the fundamental mode through cladding modes and due to the lack of verticality of the receiving cantilever end facet. Scatter may also contribute to this asymmetry.

5.4.3 Transmitted intensity with refractive index oils

The experiment was also carried out using the transmitted intensity. For this experiment the device was pigtailed with optical fibres at both ends of the waveguide using UV curing glue. The spectra are shown in Figure 69 and again show good agreement to the theoretical coupling efficiency. This experiment was then repeated with the device covered with refractive index oil of n = 1.46. This modifies the gap refractive index and shows the expected change of making the peak narrower with a higher transmission (1.13 dB) as the Fresnel reflection is reduced. Furthermore, diffraction is reduced in the higher index oil leading to a narrower width. In addition the higher refractive index of the oil will tend to strip cladding modes reducing excitations at larger displacement. The deviation of the experimental data from the model is observed at larger displacements corresponding to lower light levels at 15 dB below the peak transmitted signal due to both background scatter and excitation of cladding modes. This effect was not observed in the reflection data of Figure 69 due to the high return loss of the device.

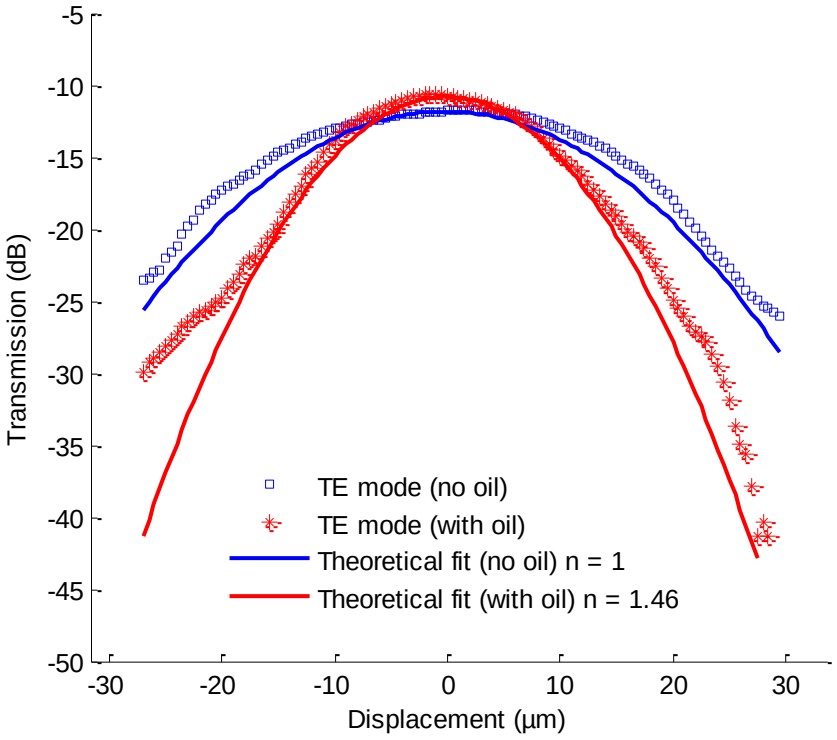

Figure 69. Transmission during double push actuation showing effect of immersion in oil n = 1.46. The total transmission is improved with oil as would be expected from reducing off scatter and Fresnel loss. The peak narrows because the output beam does not diffract as rapidly so the receiving fibre position becomes more critical.

5.5 Conclusion

A novel dual cantilever device has been constructed which can function as a sensor or actuator. The physical dicing process is used along with wet etching to form the cantilevers. A Comsol model was done to simulate the bending due to deposition stresses. The response to actuation of both a single and a double cantilever is presented and modelled by comparing it to fibre optic misalignment theory.

5.6 References

[1] A. Boisen, S. Dohn, S. S. Keller, S. Schmid, and M. Tenje, “Cantilever-like micromechanical sensors,” *Rep Prog Phys*, vol. 74, no. 3, p. 036101, Mar. 2011.

[2] E. Ollier, “Optical MEMS devices based on moving waveguides,” *IEEE J Sel Top Quant*, vol. 8, no. 1, pp. 155–162, 2002.

[3] K. Park, J. Jang, D. Irimia, J. Sturgis, J. Lee, J. Robinson, M. Toner, and R. Bashir, "'Living cantilever arrays' for characterization of mass of single live cells in fluids.," *Lab Chip*, vol. 8, no. 7, pp. 1034–41, Jul. 2008.

[4] T. Xu, M. Bachman, F.-G. Zeng, and G.-P. Li, "Polymeric micro-cantilever array for auditory front-end processing," *Sensors Actuators A Phys.*, vol. 114, no. 2–3, pp. 176–182, Sep. 2004.

[5] K. Zinoviev, C. Dominguez, J. A. Plaza, V. J. C. Busto, and L. M. Lechuga, "A novel optical waveguide microcantilever sensor for the detection of nanomechanical forces," *J Lightwave Technol*, vol. 24, no. 5, pp. 2132–2138, May 2006.

[6] L. G. Carpenter, C. Holmes, H. L. Rogers, P. G. R. Smith, and J. C. Gates, "Integrated optic glass microcantilevers with Bragg grating interrogation.," *Opt Express*, vol. 18, no. 22, pp. 23296–23301, Oct. 2010.

[7] B. Barber, C. R. Giles, V. Askyuk, R. Ruel, L. Stulz, and D. Bishop, "A fiber connectorized MEMS variable optical attenuator," *IEEE Photonic Tech L*, vol. 10, no. 9, pp. 1262–1264, Sep. 1998.

[8] J. E. Ford, J. A. Walker, D. S. Greywall, and K. W. Goossen, "Micromechanical fiber-optic attenuator with 3 µs response," *J Lightwave Technol*, vol. 16, no. 9, pp. 1663–1670, 1998.

[9] A. Constable, J. Kim, J. Mervis, F. Zarinetchi, and M. Prentiss, "Demonstration of a fiber-optical light-force trap," *Opt Lett*, vol. 18, no. 21, pp. 1867-1869, Nov. 1993.

[10] B. J. Black and S. K. Mohanty, "Fiber-optic spanner," *Opt Lett*, vol. 37, no. 24, pp. 5030–5032, 2012.

[11] M. Succo, "An Integrated Optical-Waveguide Chip for Measurement of Cold-Atom Clouds," Imperial College London, 2011.

[12] T. Brown, "Harsh military environments and microelectromechanical (MEMS) devices," in *Sensors, 2003. Proceedings of IEEE (Volume:2)*, 2003, pp. 753–760.

[13] P. A. Cooper, L. G. Carpenter, C. Holmes, C. Sima, J. C. Gates, and P. G. R. Smith, "Power-Efficiency Enhanced Thermally Tunable Bragg Grating for Silica-on-Silicon Photonics," *IEEE Photonics J.*, vol. 7, no. 2, Apr. 2015.

[14] G. D. Emmerson, S. P. Watts, C. B. E. Gawith, V. Albanis, M. Ibsen, R. B. Williams, and P. G. R. Smith, “Fabrication of directly UV-written channel waveguides with simultaneously defined integral Bragg gratings,” *Electron. Lett.*, vol. 38, no. 24, pp. 1531–1532, Nov. 2002.

[15] R. M. Parker, “Optofluidic Bragg Grating Sensors For Chemical Detection,” University of Southampton, 2010.

[16] R. M. Parker, J. C. Gates, M. C. Grossel, and P. G. R. Smith, “A temperature-insensitive Bragg grating sensor-Using orthogonal polarisation modes for in situ temperature compensation,” *Sensor Actuat B-Chem*, vol. 145, no. 1, pp. 428–432, 2010.

[17] C. Holmes, L. G. Carpenter, H. L. Rogers, J. C. Gates, and P. G. R. Smith, “Quantifying the optical sensitivity of planar Bragg gratings in glass micro-cantilevers to physical deflection,” *J Micromech Microeng*, vol. 21, no. 3, p. 035014, Mar. 2011.

[18] B. G. Aitken and R. E. Youngman, “Borophosphosilicate glasses: properties and structure,” *Phys Chem Glasses*, vol. 47, no. 4, pp. 381–387, Aug. 2006.

[19] H. L. Rogers, S. Ambran, C. Holmes, P. G. R. Smith, and J. C. Gates, “In situ loss measurement of direct UV-written waveguides using integrated Bragg gratings,” *Opt Lett*, vol. 35, no. 17, pp. 2849–2851, 2010.

[20] A. Ghatak and K. Thyagarajan, *An Introduction to Fiber Optics*. Cambridge University Press, 1998.

Chapter 6: WEDG Micromilling

6.1 Introduction

In this chapter, micromilling with on-machine fabricated diamond tools will be reported. The Wire-electro-discharge-machining (WEDG) process is used to form tools out of polycrystalline diamond (PCD).

The ability to fabricate truly 3 dimensional structures into optical materials greatly increases the range of devices that can be made. Existing fabrication techniques are limited in the way that they generate certain structures such as channels of variable depth and high depths of cut. Micromilling has already been shown to be a promising machining technique when used in the ductile mode of machining [1]. When the tool shape and dimensions can be customized this greatly expands the range of devices that can be fabricated. Currently it is difficult to find suitable commercial tools smaller than 0.25 mm in diameter, and off-the-shelf tools often do not have the optimum shapes for micromilling leaving them vulnerable to breaking. Previous work in the group had shown that dicing with diamond blades was a promising technique for integrated optics and the motivation behind this work was to apply to these techniques to milling to allow greater geometrical freedom. From a literature study it was decided that using polycrystalline diamond as a tool material was a promising option. The technique of using an electrically generated spark between an electrode and work piece to erode the work piece is known as electro discharge machining. Any conductive material or composite can be machined with this method and it has found a niche for cutting hard conductive materials that are difficult to machine by other means. WEDG with PCD tools offers a promising route for making custom tools in a hard material, well suited to glass machining. Harder tools minimise tool wear and the loss of form that results.

A micromill developed by a previous PhD student (Lewis Carpenter) was retro-fitted with the components to enable on machine fabrication of tools with the WEDG technique. Carpenter had built the micromill system for existing components during his PhD and used the system to demonstrate ductile dicing in silica at greater depths-of-cut than any previously published work [2]. The main components built and tested during the PhD were a precision wire feed system and a power supply circuit. The common design types of these components are reviewed and reasons for the selection of the components that were built are given. Iterations in the design of the wire feed unit are explained and the power supply circuit is characterized. Once a viable process was found for machining the polycrystalline diamond tools, the main tools fabricated were a 50 µm diameter micro-milling tool, a 100 µm diameter micromilling tool with teeth and a ring tool. The

fabrication steps involved in producing the tools are described in detail. The tool geometries are studied using the SEM to compare them to the target design and analyse the nature of the cutting surface. Electro dispersive spectroscopy (EDX) techniques are used to determine the PCD composition and elemental distribution in an electrodischarge machined (EDM) produced surface. These tools are used for the machining in Chapter 7.

6.2 Overview/Background

6.2.1 Overview

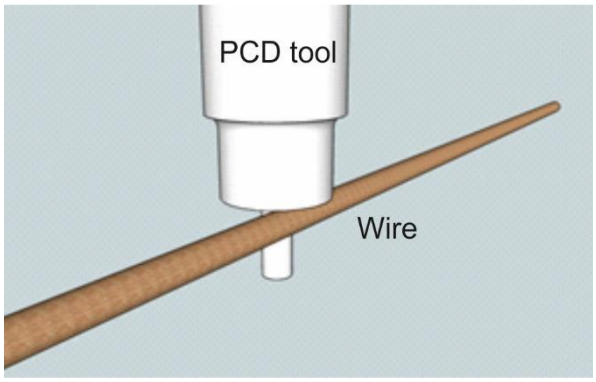

Figure 70. Schematic of wire electro-discharge grinding.

Wire electro discharge grinding (WEDG) uses a continuously fed wire as the electrode to create electrical discharges which erode the workpiece. This ensures that the electrode is continuously replenished which is important for form accuracy and when cutting materials with low ablation rates. Figure 70 shows how the wire is used to form the spinning tool.

6.2.2 PCD Background

Diamond has long been considered a material of choice for machining due to it having the highest Mohs hardness (10) of all known materials [3]. This means that it will scratch any other material while resistant to being scratched itself. The disadvantages are the high price, difficulty in machining ferrous materials and being difficult to form due to its hardness. First reported in 1953 the advent of synthetic diamond allowed a cheaper supply for use as tooling. Polycrystalline diamond is a form of synthetic diamond with microscopic diamond crystals bonded together with a nickel binder. Although the diamond particles are electrically insulating the nickel binder ensures that the material is sufficiently conductive to machine with the WEDG process. PCD tools thus have a hardness approaching single crystal diamond but with the benefit of having a ready technique for shaping them. PCD is available from 3 suppliers worldwide and is available in a range of grades corresponding to the average diamond size. Element 6 manufacture a grade with

sub-micron diamond size called CMX850 and were able supply a wafer for the research in this thesis. A local toolmaker, Dave Richards Engineering Ltd assisted with the research by cutting the tool blanks out of the wafer and brazing them to tungsten carbide shanks.

6.2.3 WEDG Background

The first use of an electrical spark as a tool for material removal occurred in the 1940's when Russian scientists were looking for a way of reducing erosion of tungsten contacts due to sparking [4]. They found that the erosion was more controllable when carried out in a dielectric fluid which has been used in EDM machining since. Simultaneously an American team produced an EDM machine for removing broken taps from aluminium components [5]. The first commercially available wire machine became available in the 1960's and since then has established itself as an unconventional technique for machining materials that would be difficult to cut by other methods. What could be considered the first true micro electrodischarge machining (µEDM) work was the fabrication of 6 µm holes in cemented carbide [6]. The first application of the EDM process to PCD was by Kozak *et al*. [7]. This proved to be a more economical way of cutting tool blanks out of the PCD wafer than grinding. Masuzawa *et al.* reported development of the WEDG geometry for fabricating rotationally symmetric components [8]. The on-machine creation of PCD diamond tools was first accomplished by Morgan *et al*. [9] to produce simple D-shaped tools with diameters of 50 µm and single point scratch tools. They used these tools to machine channels into ULE glass (product of Corning Inc) and Pyrex with low surface roughness. Since then other groups have fabricated more complicated geometries of tool. Cheng *et al.* used a 6 axis machine to make a fluted tool [10]. Rees *et al*. have investigated aspects relating to the creation of micro electrodes such as the effect of electrode material on surface roughness and contamination of the workpiece by the electrode material [11].

6.2.4 Theory

The fundamental action of ablation during the EDM process is caused by a spark being created between the tool and the workpiece. While this could be initiated in air it has been found that the repeatability of the discharge is higher with a dielectric fluid between the electrodes. In the past paraffin was used however, dielectric oils with lower flammability risks have replaced it. Deionised (DI) water can also be used so long as the resistivity is low enough. The theory behind the erosion can be broken into four key phases [12].

2. **Build up phase**: With the application of the electric field existing free charges in the fluid will begin to accelerate towards the electrodes. The electric field will also cause the cathode to emit electrons in a process known as field emission.

3. **Ignition phase**: The accelerated electrons impact on neutral particles causing additional ionisation greatly increasing the number of charge carriers
4. **Discharge phase**: The charge carriers impact on the electrode surfaces converting their energy into heat
5. **Breakdown phase**: When the discharge channel is switched off this results in ejection of the electrode material into the fluid

These stages are illustrated in Figure 71.

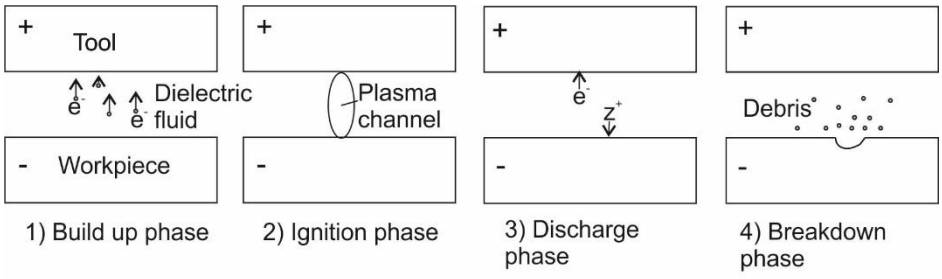

Figure 71. Stages during the spark erosion process.

The relative wear rates of the tool and workpiece depend on the polarities and duration of the discharge. For the short discharge times commonly encountered in micro EDM (10 ns to 1 µs) erosion will occur preferentially on the workpiece (which is the desirable situation) providing the tool is charged as the cathode (with positive polarity). Once the discharge current is switched off, this results in the collapse of the plasma channel. The effect of this is to cause a region of low pressure that will reduce the boiling point of the workpiece material. This will cause a small region of the workpiece to be ejected into the fluid. The fluid will also help clear this eroded material from the breakdown zone and prevent redeposition. The dielectric breakdown will be initiated once the electric field in the gap exceeds the critical breakdown voltage for the dielectric used. This distance will be determined by the voltage, electrode geometry and dielectric constant of the dielectric liquid. One of the features that makes EDM attractive for machining is that the highest points on the surface will be preferentially eroded, naturally leading to the flat surfaces. The surface roughness of the finished surface will depend on the size of the craters left from spark erosion process and can generally be reduced by using lower energy discharges. The tool electrode, regardless of the geometry, will always undergo erosion. This has been studied by various researchers [13][14]. Electrode wear will result in geometry errors in the finished workpiece if not controlled. This is the prime motivation for using a continuously fed wire as the tool electrode as it ensures fresh electrode material is constantly available.

6.3 Components of the WEDG system

A WEDG machine maybe thought of as having components common to any CNC such as stages for movement and control and spindles for tool rotation. It also has the components specific to WEDG such as a wire feed system and power supply. The critical components and important features about them are listed here.

6.3.1 Power circuit

The power circuit provides the voltage between the workpiece and wire. Two principle design types exist which are the RC (resistor capacitor) circuit and the pulsed transistor circuit. The RC circuit works by charging a capacitor. When the electric field between the tool and the workpiece increases above the breakdown value for the dielectric fluid an electrical discharge will occur and the capacitor will recharge. The pulsed transistor circuit supplies a pulse of current with the frequency supplied to the transistor. For this work the RC circuit was selected as it was simpler to design and construct; high removal rates given by a transistor style circuit were not required. The power supply was constructed with off the shelf electronic components. The diagram of the circuit designed and built is shown in Figure 72.

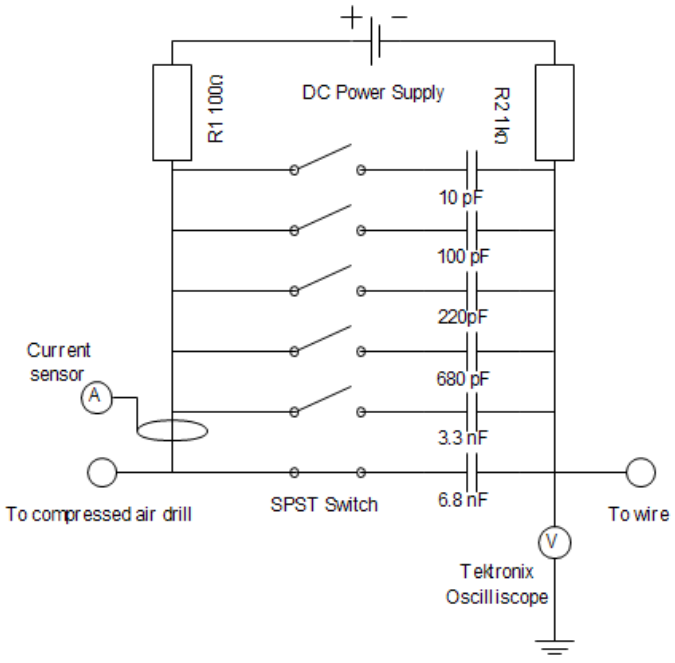

Figure 72. Circuit diagram for WEDG experiment.

Polystyrene capacitors were used as these have low equivalent series resistance. Switches are used to select from between 4 values of capacitance. The total energy released in a discharge is given by

$$E = \frac{1}{2}CV^2 \tag{83}$$

The discharge energy can both be changed by controlling voltage or capacitance providing the opportunity to optimize the process for both surface finish and speed. Parameter optimization for EDM has been demonstrated by Fonda *et al*. [15]. Wong *et al.* developed a generator for applying a single spark to study the single discharge for a RC type circuit [16]. As the surface roughness is limited by the size of a single discharge this provided connection between the theoretical and experimental models of the erosion process.

6.3.2 Wire feed unit

As the WEDG system uses an electrical discharge between the tool and the workpiece there will also be some unavoidable erosion of the tool. With the correct choice of polarity this is reduced however additional steps are required to minimise tool wear. The strategies to reduce tool electrode wear are shown in Figure 73. A spinning disc will offer more fresh electrode surface although will eventually be consumed. A block will also give greater surface area for dressing. A continuously fed wire continuously presents fresh electrode meaning the geometric accuracy of the finished workpiece is higher. It is the most technically demanding solution and wire vibration and breakage must to be taken into account.

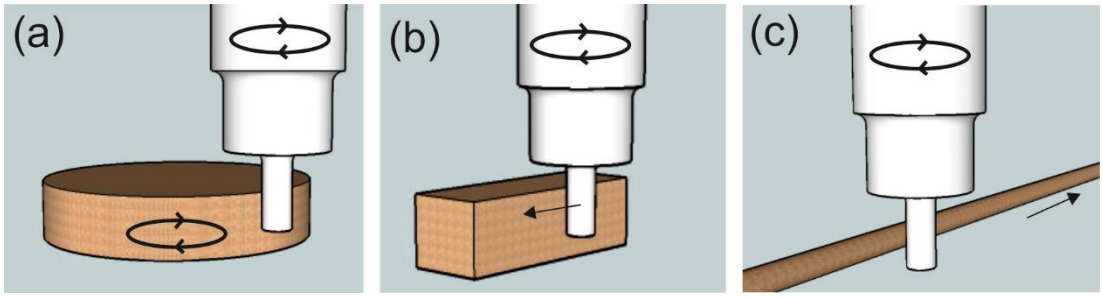

Figure 73. Types of EDM tool forming.

The first wire feed unit made is shown in Figure 74.

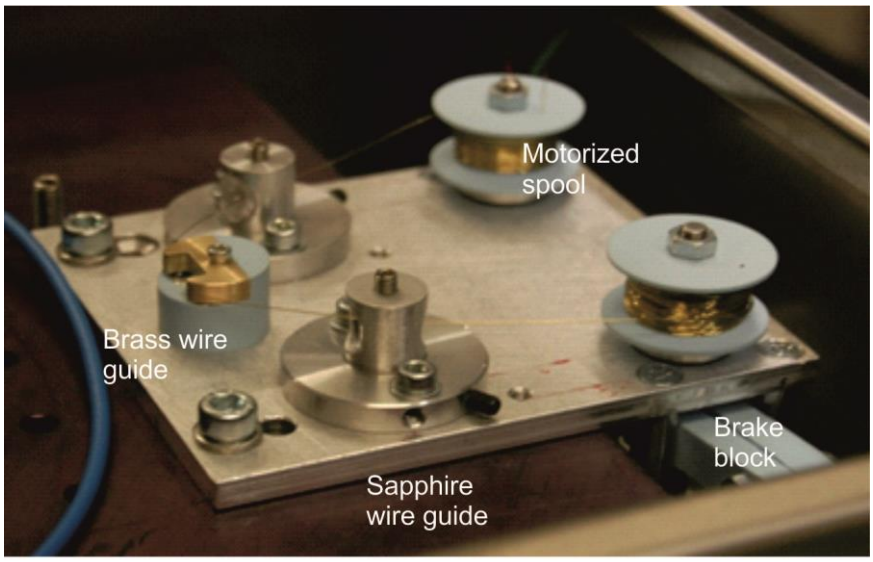

Figure 74. First wire feed system. A motor driven take up spool pulls wire from the supply spool around a front block with groove which is electrically live. A brake block around the supply spool shaft can be adjusted to give varying amounts of friction which controls the wire tension.

The spools and front guide post are made from Tuffset plastic which provides electrical insulation between the live wire and ground base plate. It is also stiff and easily machinable. Sapphire wire guides are also insulating and due to their hardness are resistant to wear from the wire.

6.3.3 Stage system

The machine must have some way of moving the wire around the part to create the necessary geometries and this is the role of the 'axis' or stage system. A WEDG machine may have anything from 2 axis to 5 axis depending on the complexity of parts that are needed to fabricate. As EDM is essentially a non-contact process the machining forces will be far smaller than generated during milling operation. However if the machine is to be used for hybrid operation the stages will need to have the necessary stiffness to cope with machining forces. A stage can be specified by key parameters which indicate how it can be expected to perform.

1. **Accuracy**: The accuracy of a stage is the degree to which a stage moves to a commanded position.
2. **Repeatability**: The repeatability is a measure as to the spread of positions when a position is approached multiple times. Approaching a point from different directions may yield poorer results due to features of the stage system such as backlash and and thus repeatability is usually specified as uni directional or bi directional.
3. **Resolution**: The resolution is smallest movement that can be distinguished. It is important to state whether this is the resolution of the encoders used to measure the

position of the stage, or the real motion of the machine as determined at the point of use as these can be different.

4. **Loop stiffness**: This is the stiffness of the loop formed from the tool around from the tool to the workpiece. When the tool engages the workpiece there will be some deflection due to machining forces. High loop stiffness will reduce this. The stage system will be a contributor to the loop stiffness of the machine.

6.3.4 Glass encoders

Stage systems work with a servo system arrangement whereby the control signal is determined by the current position of the stage and desired position. The measuring system for an axis is known as an encoder and this will be a limiting factor in the performance of the stage. Optical encoders give the highest resolution. These can work by different principles however a common method involves moving two blocks with gratings over the top of each other and measuring the optical transmission.

6.3.5 Air bearing spindle

As tools fabricated using the WEDG process would be used for milling operation it was necessary to use a spindle that would perform well for milling. This means it is not necessary to transfer the tool between spindles after WEDG forming which can cause misalignment errors. 'Runout' describes lateral rotation from the rotation axis of a spindle. The ideal spindle will have low runout- both dynamic and static as well low vibration and high stiffness. Airbearing spindles excel in all of these respects however are more expensive than ball bearing spindles which limits their use to high-end applications. A difficulty of using an airbearing spindle for EDM is that typically airbearing spindles have no physical contacts between the rotor and stator with which to supply current. Loadpoint Bearings Ltd were able to supply us with a custom made spindle that used brushes to make an electrical connection to the rotating shaft. The brushes would lift off at high speeds meaning that current could only be supplied at low rotation speed. I installed the new spindle during the course of the PhD with assistance from Lewis Carpenter and technical staff.

6.3.6 Linear air bearing and linear motors

For most applications it is desirable to have the smoothest motion possible in a stage system. Linear bearings achieve this by using compressed air to provide a cushion of gas between the moving parts of the slideway. This also reduces error in motion due to machining tolerances in the moving components as the air cushion acts to average out these some of these errors. They

ensure completely frictionless motion as the drive motor does not have a physical connection to axis. This is achieved using linear motors which also have the advantage of not introducing cyclic error which can occasionally be seen using rotating leadscrews.

6.3.7 Touch sensor for probing

The machine needs a way of knowing where the surface of the substrate is and the most accurate way to do this is to probe it on the machine. The sample mounting stage sits on top of a piezo sensor allowing touch sensing. Using a comparator circuit when the voltage from the piezo circuit rises above a reference level the position is recorded by the computer. The touch probe system and circuit was designed and built by Lewis Carpenter.

6.4 Initial trials

Initial trials of the WEDG process were conducted using a compressed air spindle as an air bearing spindle with electrical connection to the shaft was not available at this time. An electrical connection was made to the shaft via the eyelet. Figure 75 shows a photograph of the air driven spindle.

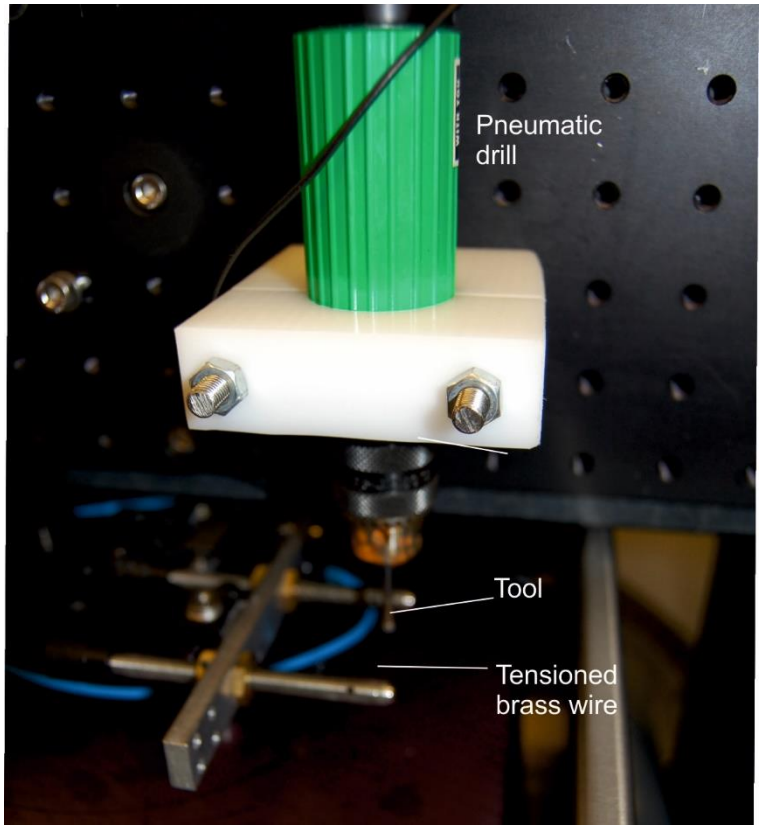

Figure 75. Picture of air driven spindle.

A Delrin clamp was used to fix the spindle to the backboard of the mill. The spindle speed was controlled directly by changing the air pressure supplied to it with a regulator. For the electrode a section of brass wire was used, held between two screws to apply tension. This was installed at an angle onto the machine so that translation in the x-axis used a fresh section of wire as well as bringing the wire slightly closer the tool bit to account for the reduction in diameter of the tool bit. A diamond coated drill was used as the workpiece in the first trials. Table 4 shows the parameters that were selected for the experiment.

Table 4. WEDG parameters used for initial trials.

Capacitance	6.8
Voltage	50 V
Wire	250 µm
Workpiece	Diamond coating on steel core
Dielectric	DI water

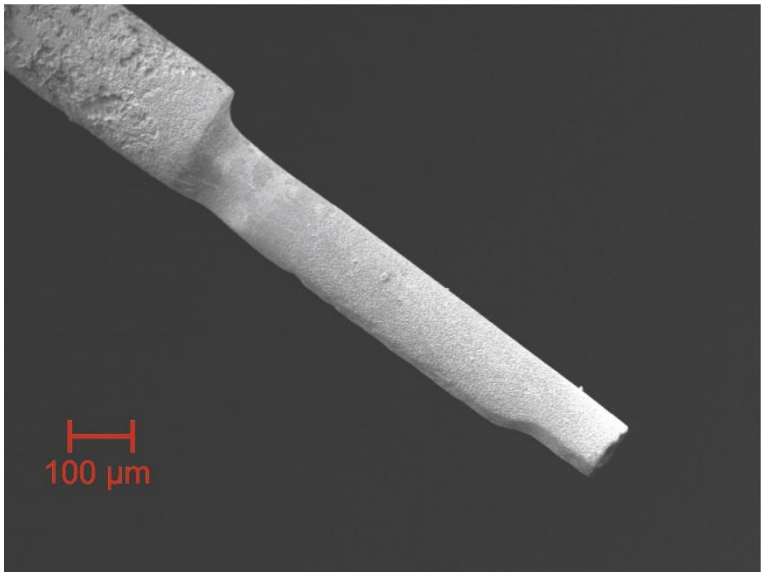

Figure 76. Steel shaft cut machined with EDM.

Figure 76 shows the result of the shaft machining. The offset is due to the mounting and the spindle axis and tool axis not being aligned. The newly machined section will be aligned to the spindle axis. One of the benefits of dressing tools on-machine is that they will be automatically aligned to the spindle axis. The EDM machining has stripped the shaft of the diamond coating leaving the steel core. This test confirmed the principle of material removal and that the WEDG process could be used to produce highly geometrically accurate concentric shafts.

Figure 77 shows data from the oscilloscope monitoring the voltage across the spark gap. The signal can provide information about how frequently discharges are occurring and whether open or short circuits are present.

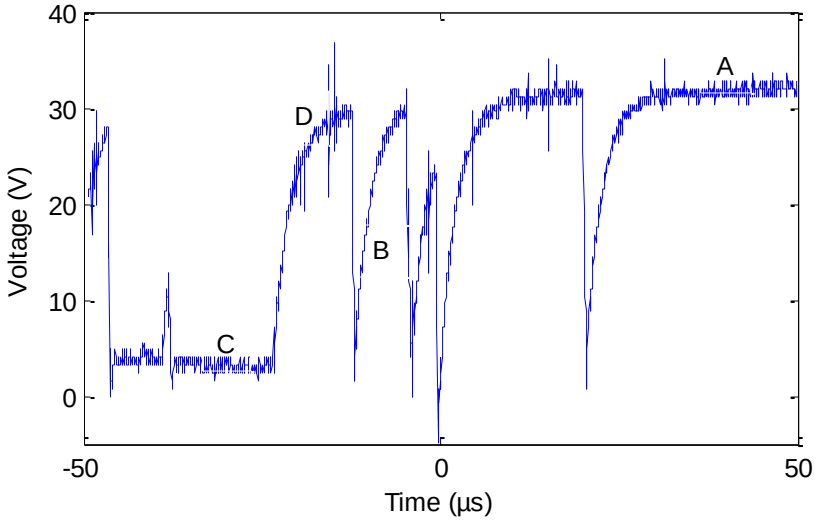

Figure 77. Oscilloscope measurement of discharge gap voltage. The letters correspond to different events.

A) Constant high voltage indicates that the tool and electrode are not close enough for sparking to initiate.
B) Discharge across the gap results in a sharp drop in voltage across the gap
C) A prolonged region of zero gap voltage indicates a short circuit were the tool and electrode are in contact
D) Slowly increasing voltage occurs when the circuit capacitor charges with a time constant = RC

The next stage was to attempt machining of PCD as this material is hard enough to form a shaped cutting tool. The previous experiment was repeated with the PCD blank. Figure 78 shows a photograph of the tool used which was supplied by Dave Richards Engineering Ltd .

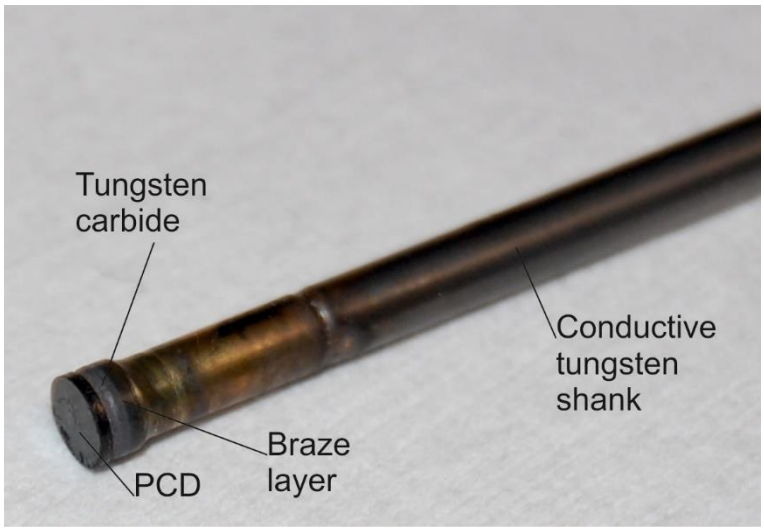

Figure 78. Photograph of PCD tool.

The tungsten carbide backed PCD discs are first cut from a wafer. The discs are then brazed onto a tungsten shank allowing mounting in a chuck. Initially discharges could be initiated by bringing the PCD close to wire, but eventually the discharges became impossible to sustain. This is believed to be due to cobalt depletion, whereby the cobalt binder which usually provides the electrical conduction becomes depleted in the surface region causing the discharges to cease [17].

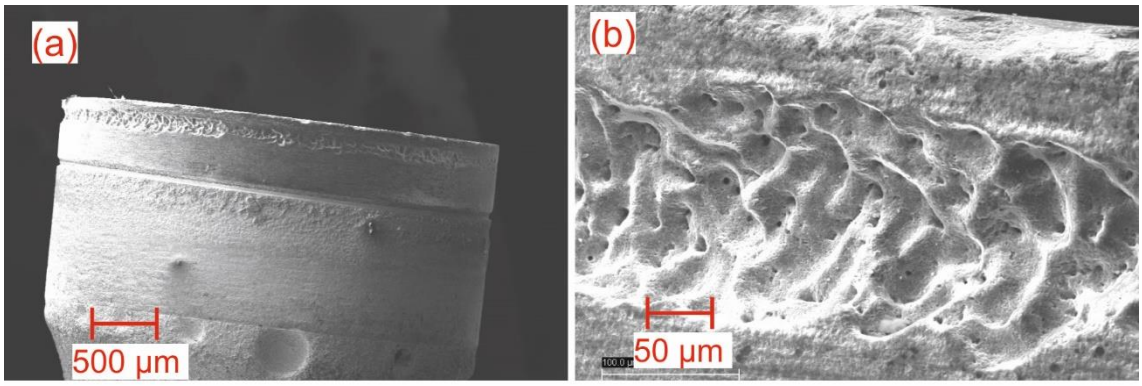

Figure 79. (a) PCD machined with DI water (b) shows a higher magnification section

Figure 79(b) shows the surface of the machined PCD. It can be seen that it has machined unevenly with pockets of the order 20 µm in size. It was thought that the issue could be related to the conductivity of the house deionized (DI) water. For this reason dielectric oil was chosen as this is custom made for EDM applications and should have lower conductivity. Commonwealth Oil 244 was chosen as the dielectric fluid as previous research had good results when used with PCD [18].

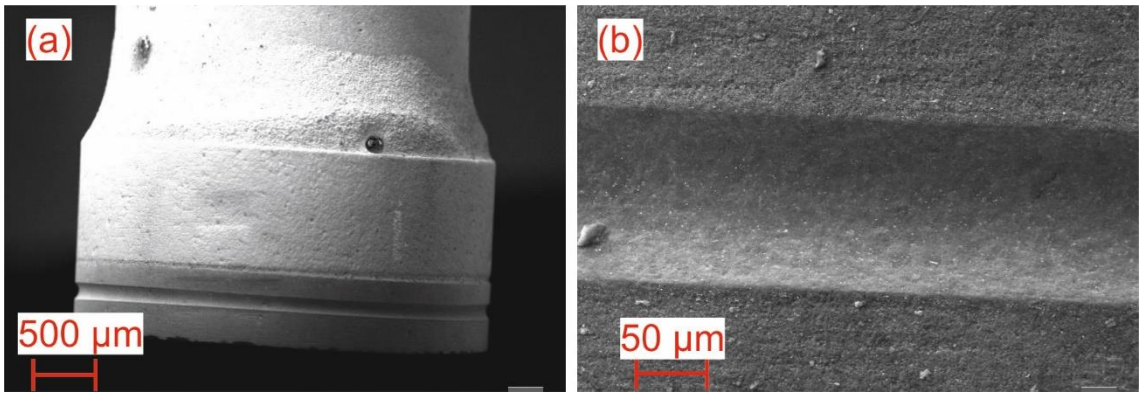

Figure 80. (a) Groove cut into PCD with dielectric oil (b) shows a zoomed section of PCD

With the dielectric fluid the discharges could be maintained indefinitely. From SEM images it can be seen that the surface is free of the irregular machining seen previously and the form is as expected from being cut with cylindrical wire.

Figure 81 shows a representative plot of the gap voltage during the EDM machining as measured with an oscilliscope.

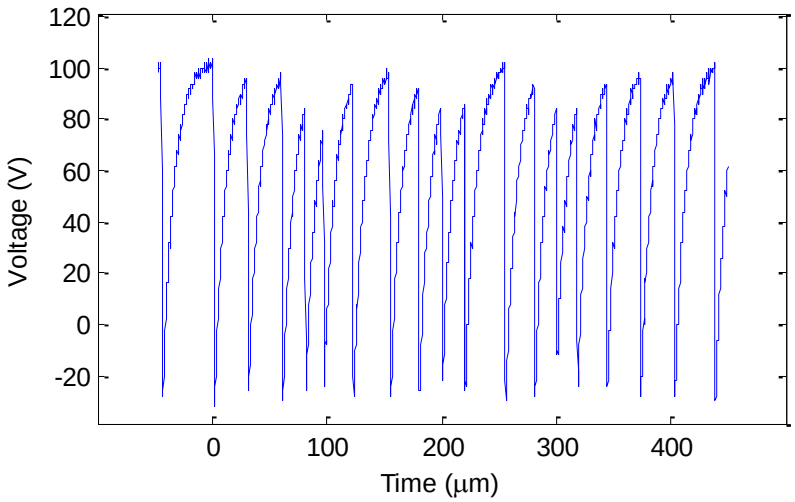

Figure 81. Oscilloscope measurement of discharges

The lack of short circuits or open circuits shows that the gap distance during this measurement was suitable for efficient machining.

6.5 EDX characterization

As the PCD is a composite material it was of interest what the microstructure of the surface was like as this can have an effect on the surfaces produced. As described in Chapter 3 EDX is an SEM tool for obtaining elemental composition. Figure 82 shows the secondary electron image of the region which was analysed using EDX.

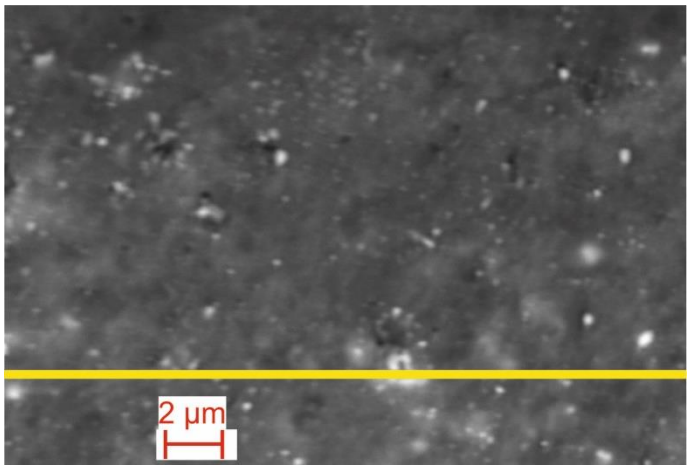

Figure 82. EDX Line scan position of PCD surface. Yellow line shows the linescan over which the EDX data is taken

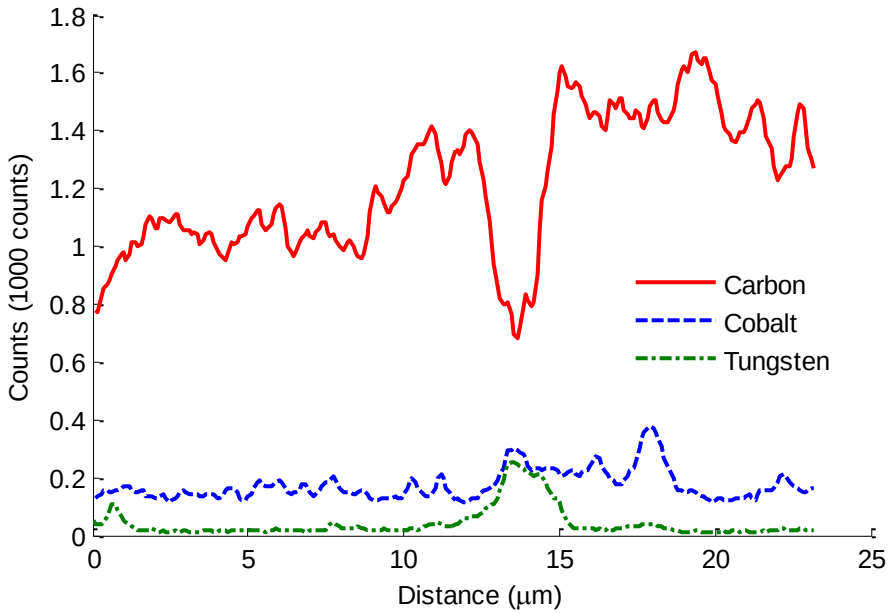

Figure 83. Elemental composition of PCD surface showing cobalt, carbon and tungsten content.

Figure 83 shows line maps of the elemental compositions determined by EDX to have the highest concentrations. This analysis shows whether the tool picks up material during the WEDG process. The data shows that the bulk of the material is carbon as expected. Cobalt is the second most prominent element as expected due to its role as a binder element in the PCD. Some tungsten is present which is believed to come from the shank used to hold the PCD. The variation in concentration is approximately 1 µm which is the approximate size of a diamond crystal. Figure 84 shows a Fast Fourier Transform (FFT) of the data which shows a periodic feature at 1.5 µm for carbon.

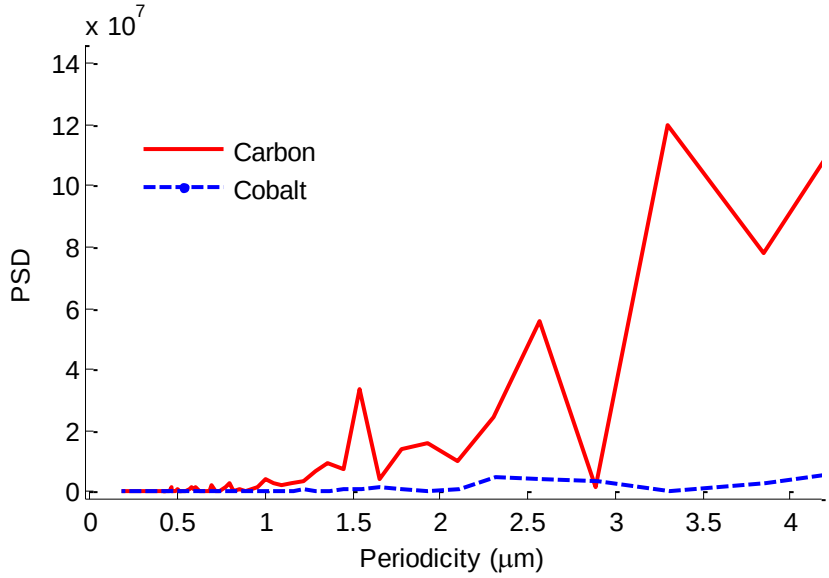

Figure 84. FFT of the spectra for carbon and cobalt.

6.6 Small tool fabrication with wire

It was necessary to design and fabricate a wire feed system for the machine as nothing commercial was readily available. A geared DC motor was used to drive a take-up spool of wire. A supply spool was fitted to a shaft with a nylon friction block to provide the tension in the wire. The wire was fed through two sapphire wire guides and around a brass post with a narrow groove in it. It was found that this design when used with the 250 µm brass wire could not 'straighten' the wire due to it passing round a radius that was too small. When the dielectric medium was changed from DI water to dielectric oil it was decided to conduct the machining in a small tank instead of having a recirculating system. This avoided having a construct a pump system compatible with the oil and also reduced the ignition risk. This required a redesign of the front elements of system to take the wire into the tank and out again. The redesigned system is shown in Figure 85. It was found that a big cause of wire jumping and breaking was from the respooling of the wire onto the smaller spools compatible with the unit. EDM grade wire is carefully spooled as wire breakage is a costly and time consuming event that effects production. As a respooling machine was not available it was decided to buy commercial wire on smaller spools and use these directly on the machine.

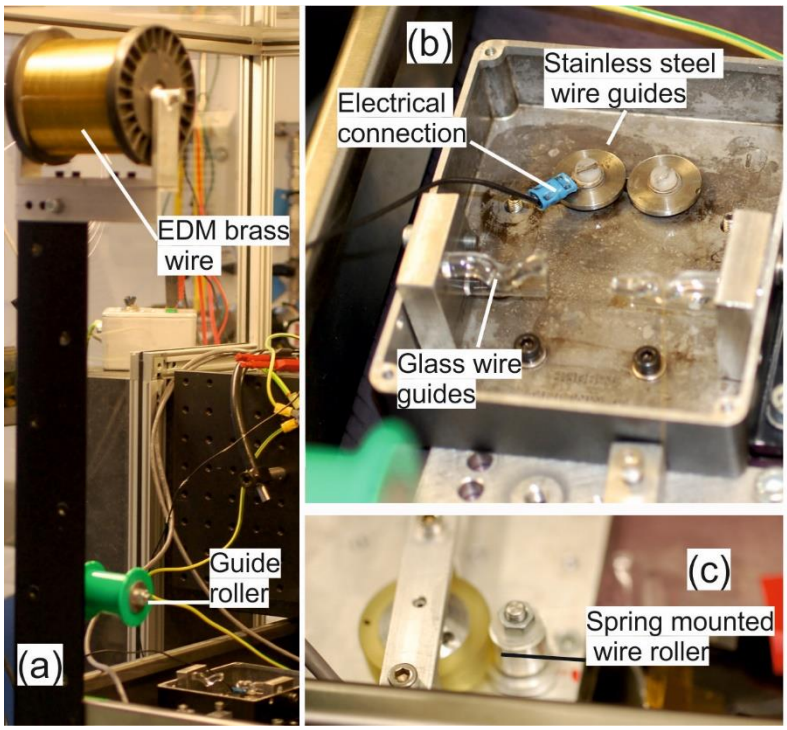

Figure 85. New wire feed system (a) The spool is mounted to the mill tray at a distance ensuring the pulling angle does not cause slippage (b) EDM machining is conducted in tray to allow use of dielectric fluid (c) Spring mounted roller arm to pull wire through

Once the feasibility of using WEDG to machine PCD tools was demonstrated an experiment was conducted to investigate what small tools could be made with the WEDG process. Initially it is required to find the position of the PCD blank relative to the wire. The position on the Y axis is found relative to the wire by contacting the wire with both sides of the rotating tool and finding the average. To make a 50 µm tool the stage is then moved to the radius of the tool plus the radius of the wire. This method is more accurate than contacting a single side of the tool, especially if the initial tool radius is not well known or there is run out present. To find the height of the blank it is touched on to the top of the wire.

Once the first wire unit was finished it was decided to investigate what small tools could be fabricated from the PCD material. The first tool fabricated was a D-shape cutter, which consists of a cylindrical cutter with a segment removed to aid swarf removal and improve coolant flow.

Figure 86 shows the schematic of the steps towards how the D-shaped cutter was formed.

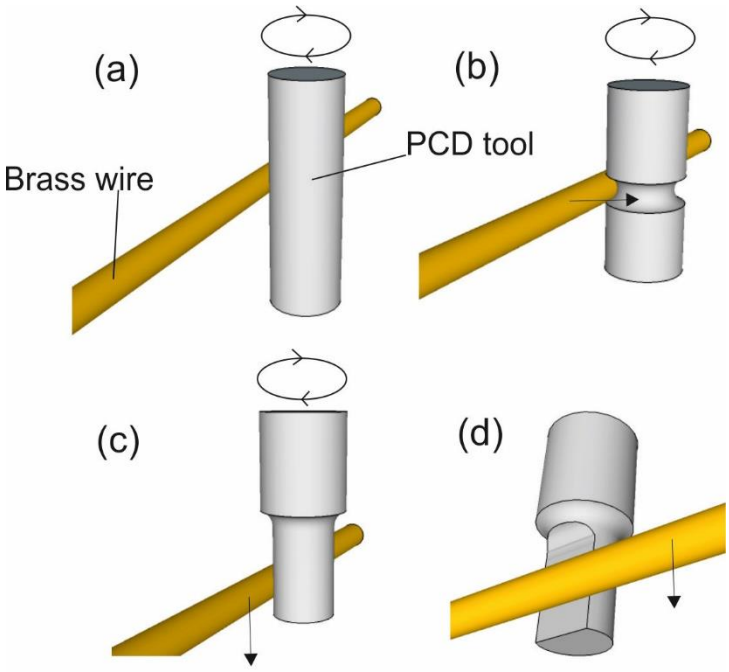

Figure 86. Schematic of tool fabrication. (a) Brass wire is aligned to tool (b) Wire is fed in horizontally to desired radius (c) Wire is fed vertically to create tool of desired lenghth (d) Tool is clamped and wire is fed vertically to create D-shape cutter.

For stages (a)-(c) the tool is rotating which ensures fabrication concentric to the spindle axis. For (d) the spindle is clamped and part of the side removed to leave a 'D' shaped tool. The position of the tool relative to the wire was found with the procedure described earlier. The toolpath was programmed to move the tool to 0.11 mm from the origin allowing 0.05 mm for the wire width, 0.05 mm for the tool radius and 0.01 mm to account for the spark gap. A SEM image of the finished tool is shown in Figure 87.

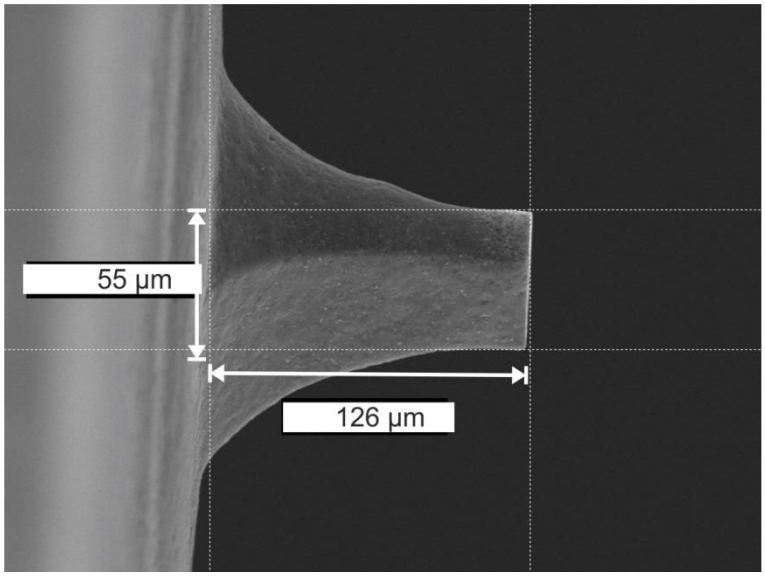

Figure 87. SEM image of tool following WEDG. The lighter area represents the flat face of the D-cutter.

The diameter is 55 µm and the length is 126 µm. The tool length is not a lot longer than the required depths of typical cuts which makes it more robust. The short length of the tool makes it less likely to break during machining than a longer commercial tool. The sidewalls are vertical over the end 20 µm.

6.7 Channel milling with small tool

The small PCD tool was then used to mill a sample of FHD glass. By milling grooves of various depths and including a sloping section it was hoped to find the expected transition from the ductile to brittle regime. The tool path used for milling channels in FHD silica is shown in Figure 88 The lead in section allows milling at a continuum of depths which helps when locating transitions in machining regimes that may occur abruptly.

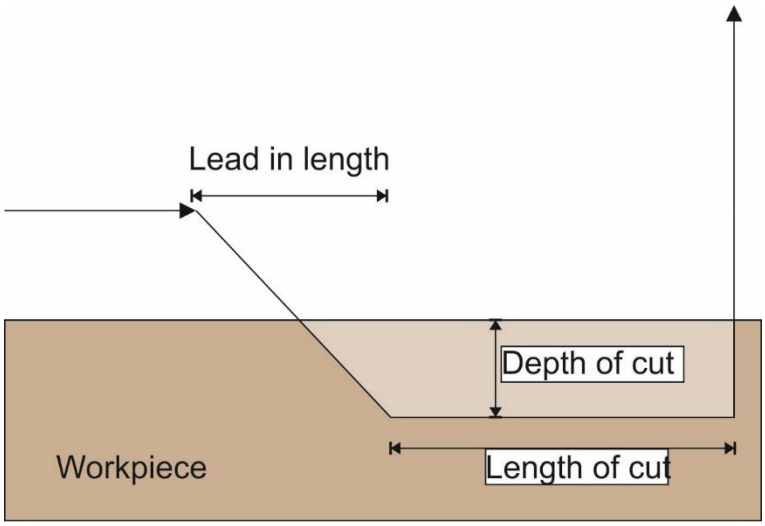

Figure 88. Schematic of toolpath.

The machining parameters are shown in Table 5. Three cuts at different depths were done to investigate the effect of depth of cut on machining types. These groove depths represent cuts that are on the scale of silica-on-silicon integrated optics. The choice of parameters is similar to that previously used in Chapter 4 however a higher spindle speed is used due to the tool having a smaller diameter with lower cutting speeds.

Table 5. Machining parameters for milling 3 grooves.

Spindle speed(krpm)	95
Feed (mm/min)	0.5
Depth of cut (µm)	15,20,25
Length of cut(mm)	0.5
Length of lead in (mm)	0.5

A composite microscope image of the three grooves is shown in Figure 89.

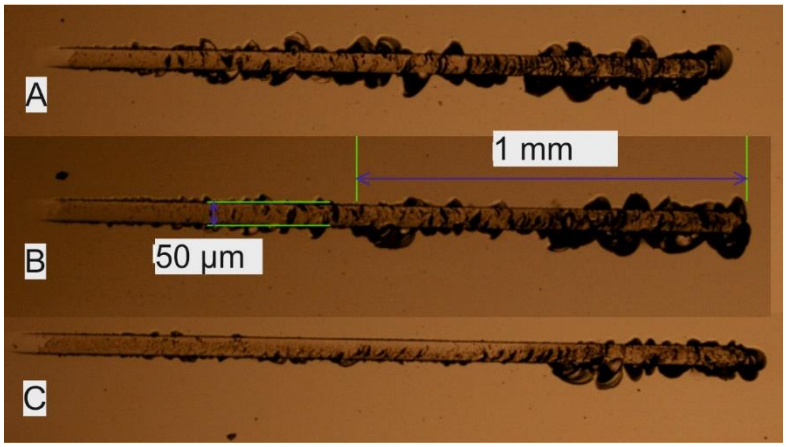

Figure 89. x5 microscope image of grooves.

A x20 microscope image of the groove is shown in Figure 90 and allows the detail in the groove to be better inspected.

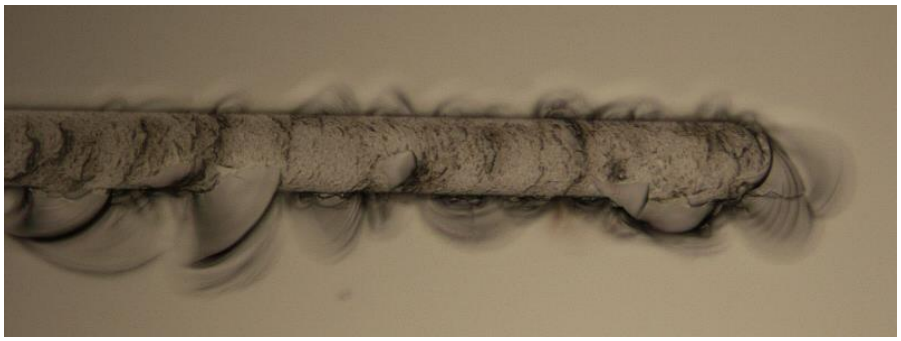

Figure 90. Microscope image of 50 µm wide groove.

It can be seen that there is multiple evidence of chipping along the length of the groove. Line scans measured using the Zescope showing the depths of the grooves are shown in Figure 91. They show that the first groove has reached the target depth of cut however the 2nd and 3rd are shallower than programmed.

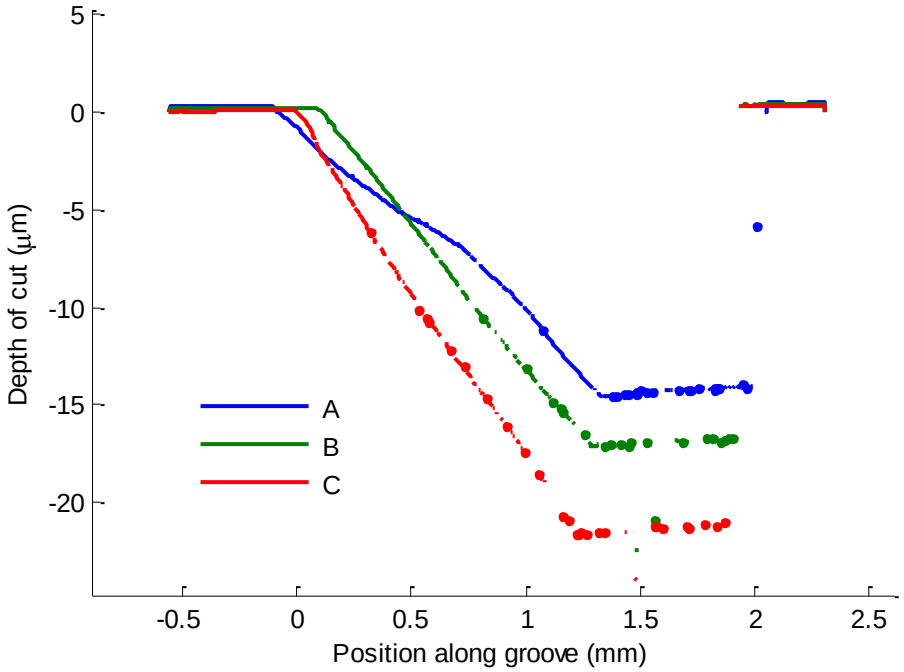

Figure 91. Depth profiles of the grooves obtained from Zescope data.

From the depth profiles it can be seen that the lead in section groove A is not straight which could either be an indicator of poor z-axis performance, thermal expansion of the mill bit or a variation in cutting regime affecting the force applied. As it is only visible on one groove inconsistency in z-axis performance is believed to be the cause of this.

The horizontal profile of groove A extracted from the Zescope data is shown in Figure 92.

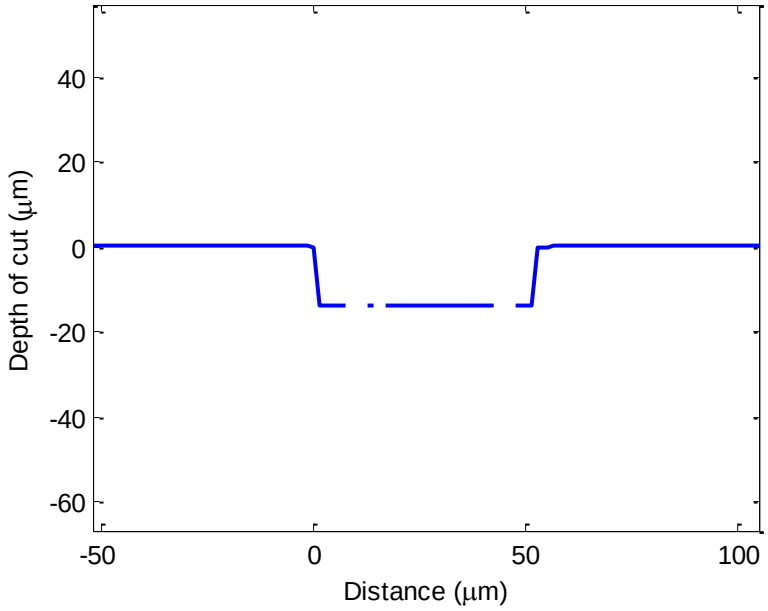

Figure 92. Horizontal profile of groove A.

Using the data points at the top and bottom of the groove the average angle of the sidewall is found to 85 °. This compared favourably with grooves milled with commercial diamond coated tungsten carbide milling tools [19].

One possible explanation for the chipping was lack of coolant reaching the cutting area. This could be due to the current tooling having a tiered profile making it difficult for coolant to reach the cutting zone. It was decided to attempt to machine a conical shape of tool. Figure 93 shows how the original tool can be modified to a conical shape to allow better access for coolant to the cutting zone.

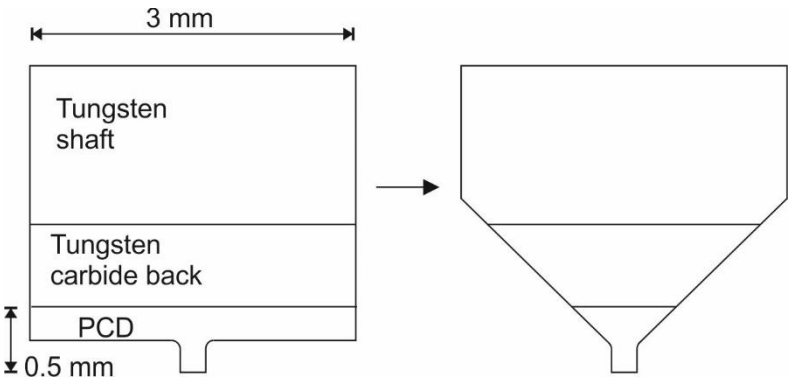

Figure 93. Conical tool fabrication.

To remove this volume of PCD material with the wire feed system proved slow as the wire experienced some vibration leading to short and open circuits when discharges could occur. David Richards Engineering Ltd was able to supply the tools ground to a cone with 90° included angle. This greatly reduced the volume of material that was required to be removed. The tool is not significantly weakened as the braze between the shaft and WC-backed PCD disc is not significantly reduced.

6.7.1 Probing tests

As the previous grooves had not reached the programmed depth of cut the probing system was tested by probing a polished silica optical flat from Comar with a specified flatness better than $\lambda/10$ across the optical surface. The method of mounting chips using wax was found to be very secure, however there was the possibility of an uneven wax layer adding some misalignment. With a rotating tool the optic is probed at 9 points in a 15mm x 30 mm grid to determine the height and tilt. During milling the tilt is compensated for in the CNC program however it is still advantageous to have the optic mounted as flat as possible so that the tool is close to perpendicular. Figure 94 shows the height measured at each position. From this errors of probing

over the grid can be calculated. Figure 94 shows the position of the 9 points probed over a 3×3 grid.

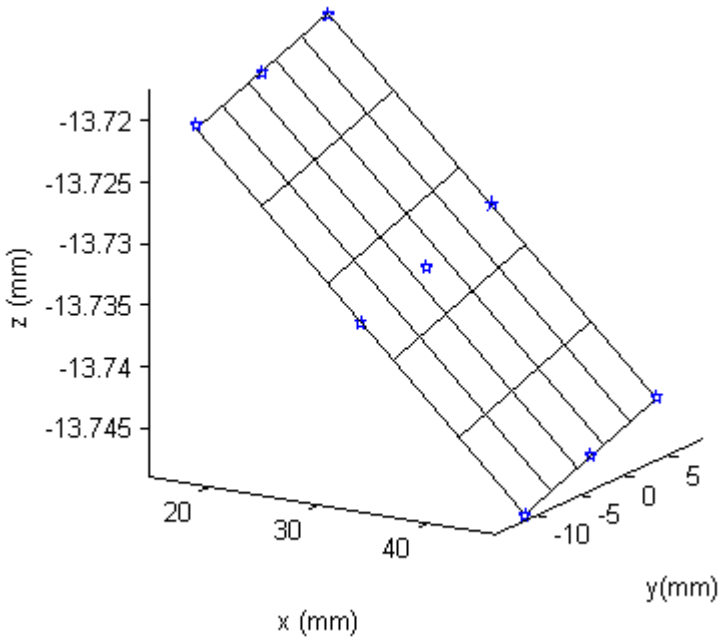

Figure 94. Probe positions for height sensing and tilt correction.

The maximum height deviation between a best fitting plane and data point was 0.606 µm while the RMS error was 0.187 µm. This suggests that the probing was accurate and the z axis stage maybe to blame for the undercutting. The z-axis also experienced a problem where repeated slow moves caused an overcurrent error. Advice from Aerotech Ltd was that this was caused by the distribution of grease in the bearings and could be solved with a long move to the top of the z-axis. While this allowed normal operation again, it is believed it may be indicative of a problem affecting the true position of the z-axis which can affect how accurately the mill cuts the targeted depth of cut.

With improved coolant flow the milling of narrow grooves was again attempted. Six grooves of varying depths were milled into FHD glass. These included more cuts at shallower depths to examine whether this would reduce chipping. Table 6. shows the parameters used for the 6 cuts. These were identical to the previous PCD diamond cutting experiment with the exception that 5 grooves were milled.

Spindle speed(krpm)	95
Feed (mm/min)	0.5
Depth of cut (µm)	1) 5 2) 10 3) 15 4) 20 5) 25
Length of cut(mm)	0.5
Length of lead in (mm)	0.5

Table 6. Parameters for the second small groove cutting experiment.

A microscope image of the grooves is shown in Figure 95.

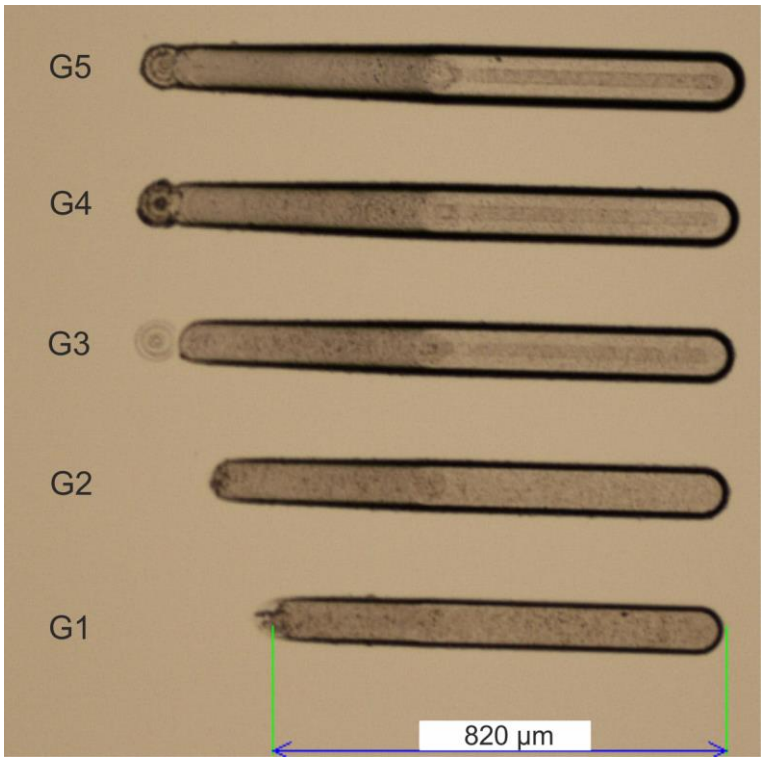

Figure 95. x5 microscope image of grooves milled with PCD tools.

To examine the groove base in more detail a x50 microscope image is shown in Figure 96.

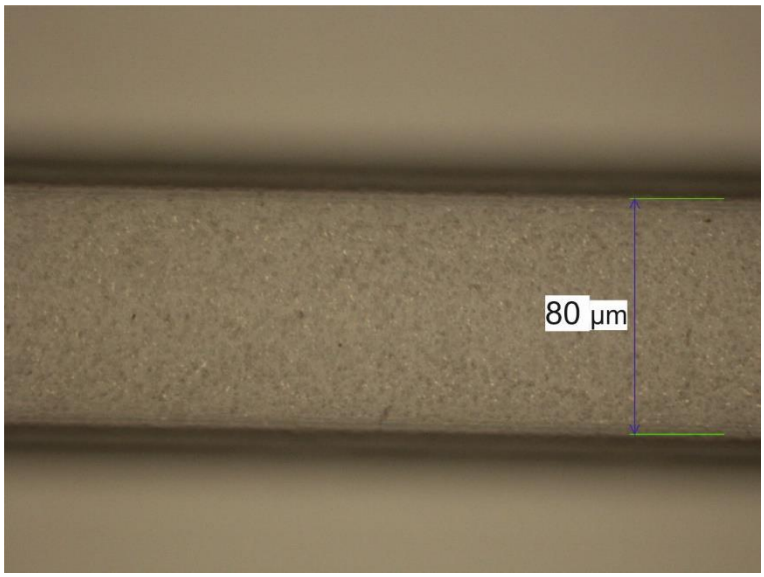

Figure 96. x50 microscope image of groove A.

It can be seen that irregular chipping has largely been eliminated supporting the theory that providing easy access to coolant to the cutting zone is important. With the chipping eliminated it becomes easier the analyse how the surface roughness of the grooves are affected by depth of cut. When the surface roughness of different depths of cut are looked at it is apparent that there is a transition between modes of machining. Considering the shallowest groove, the surface is evaluated along the length of the groove and plotted in Figure 97. It can be seen that there is a change in surface roughness that occurs at 1.2 µm.

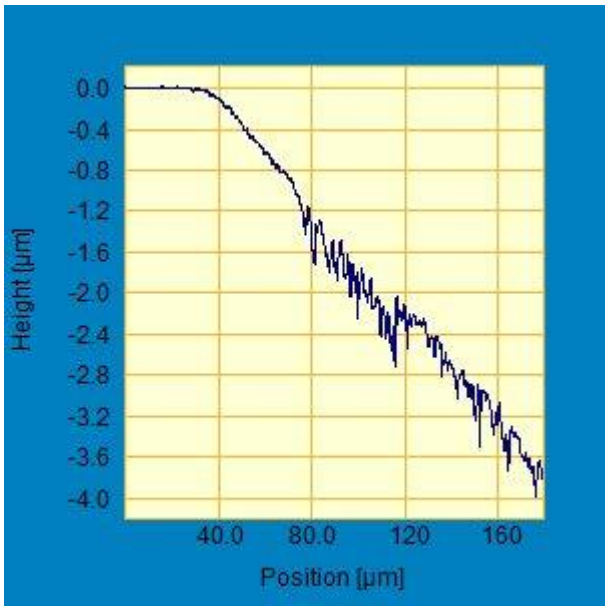

Figure 97. Profile of groove.

This suggests that milling with the PCD should feature a final finishing cut of less than 1 µm. This was difficult to achieve with the performance of the z stage.

The depth profiles of the grooves are shown in Figure 98. They indicate some that the grooves are slightly deeper than commanded. This may be due to poor z-axis performance.

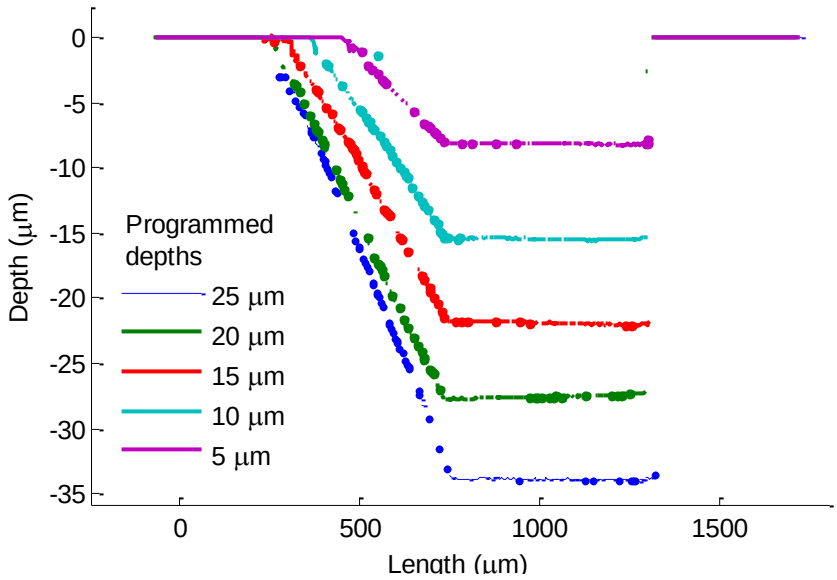

Figure 98. Depth profiles of 5 of the grooves.

Generally the depth uniformity is within 1 µm apart from the 4th groove where it is 2 µm. Surface roughness of Sa 64 nm was obtained for the shallowest groove. These grooves can be compared to deep etching in silica glass using other techniques. Nagarah *et al.* [20] deep etched fused silica with HF and achieved a surface roughness of 10 nm however defect patterns were visible and the isotropic nature of the etch means vertical sidewalls are not possible. Figure 99 shows cross sections across the width of the grooves fabricated by a WEDG produced tool.

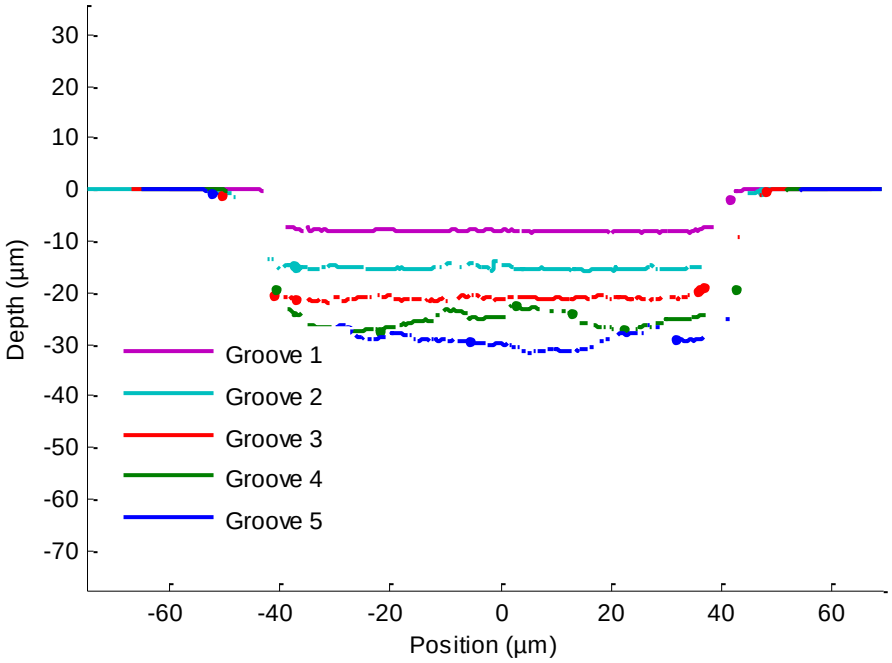

Figure 99. Cross sections of the 5 grooves.

The uniformity across the width is within 1 µm for groove 1 showing the optic was levelled to the spindle axis. It is not possible compensate for this tilt using corrections obtained from sample probing. Grooves 4-6 show deviation at the centre which is related to the poor surface quality of these grooves. Groove 6 features a depressed centre which maybe caused by uneven tool wear. As the centre of the tool has zero linear speed it tends to erode less material and wear slower leading to grooves with depressed centres. A tool with the centre point removed is one option to mitigate the problem of uneven tool wear and is discussed in the next section.

6.8 Small tool with cutting teeth

More complex tools can be fabricated than the cylindrical geometry as discussed above. As mentioned previously tools can experience uneven wear across their face. This can cause defects in milled surfaces as has been previously reported [19]. One way to avoid this is to remove the centre of the tool with WEDG system. This design is also beneficial for allowing better coolant flow to the cutting zone. It has the disadvantage that they cannot be used for vertical drilling. Also removing the centre weakens the tool. With the smallest available wire diameter of 0.1 mm it was not possible to make 50 µm diameter centreless tools. Making cross cuts is a simple way to use the wire to remove the centre of the tool. By clamping the tool to prevent rotation and indexing by 90° a tool with four teeth can be fabricated.

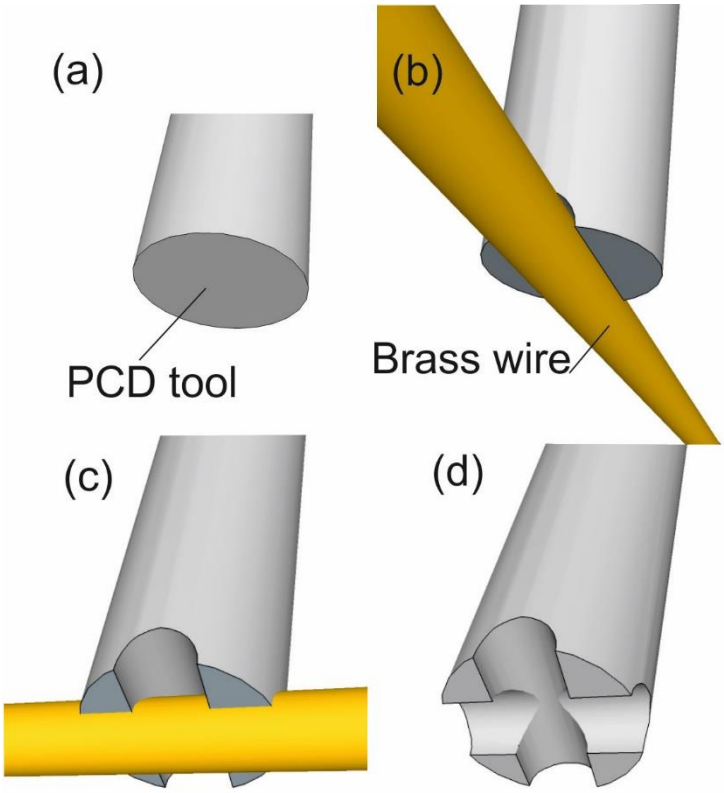

Figure 100. Schematic of fabrication of tool with teeth (a) Starting PCD small tool (b) First cut with tool stationary (c) Second cut with tool stationary (d) Finished tool

An SEM image of finished tool is shown in Figure 101.

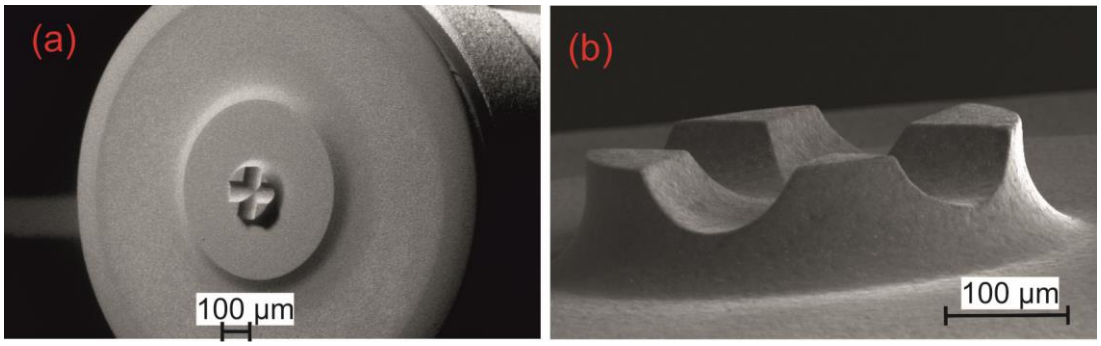

Figure 101. SEM images of tool.

6.9 Milling of optical fibre

The tool was used to demonstrate milling of an optical fibre. D-shaped fibre with the core exposed is useful for evanescent sensing and modulation of signals. The fibre is held rigidly to the silicon wafer using deposited FHD glass. This is a new patented fibre mounting alignment system developed by another member of the group, Chris Holmes [21][22] that offers a new platform for developing fibre-planar hybrid devices. This arrangement ensures that the fibre is held as flat as the silicon wafer and will have sufficient strength to survive the forces during machining. Using glass to fix the fibre also provides a more chemically robust device.

The milling parameters are shown in Table 7.

Spindle speed(krpm)	40
Feed (mm/min)	0.5
Depth of cut (µm)	30
Length of cut(mm)	3
Length of lead in (mm)	1

Table 7. Optical fibre milling parameters.

The spindle speed is reduced from that used in the bulk groove milling as the new tool is approximately half the diameter of the previous tool used and this keeps the maximum surface speed (found at the edge of the tool) constant.

Figure 102. shows a x50 microscope image of the cut surface.

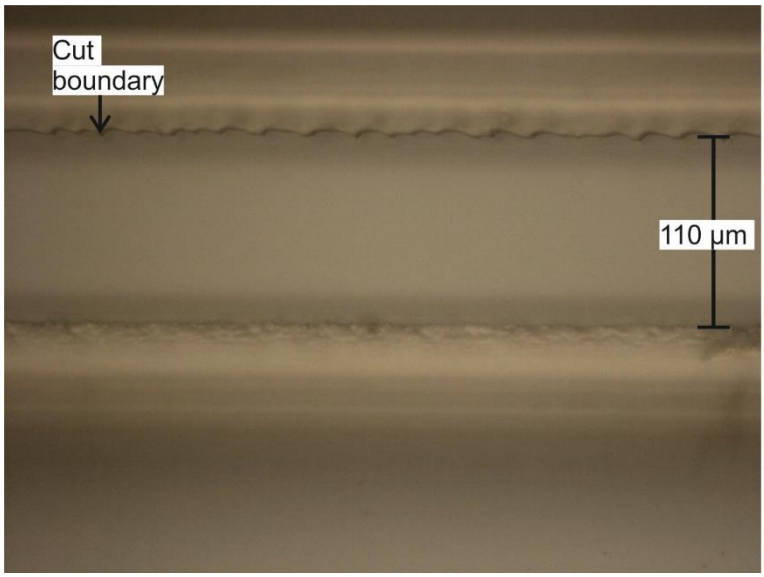

Figure 102. x50 microscope image of cut fibre showing milled region on top

The microscope image shows that the surface is free of chipping or cosmetic defects. A line slice shows how the depth profile varies along the cut. It can be seen that the surface is flat with a decrease in depth towards the end of the cut representing uniformity of 0.9 µm over the 3.2 mm cut length. This uniformity is better than seen for the milling in bulk samples suggesting the tool wear and load on the z axis are lower. The tapered lead is visible but shows some lost data due to the gradient being difficult for the Zescope to measure.

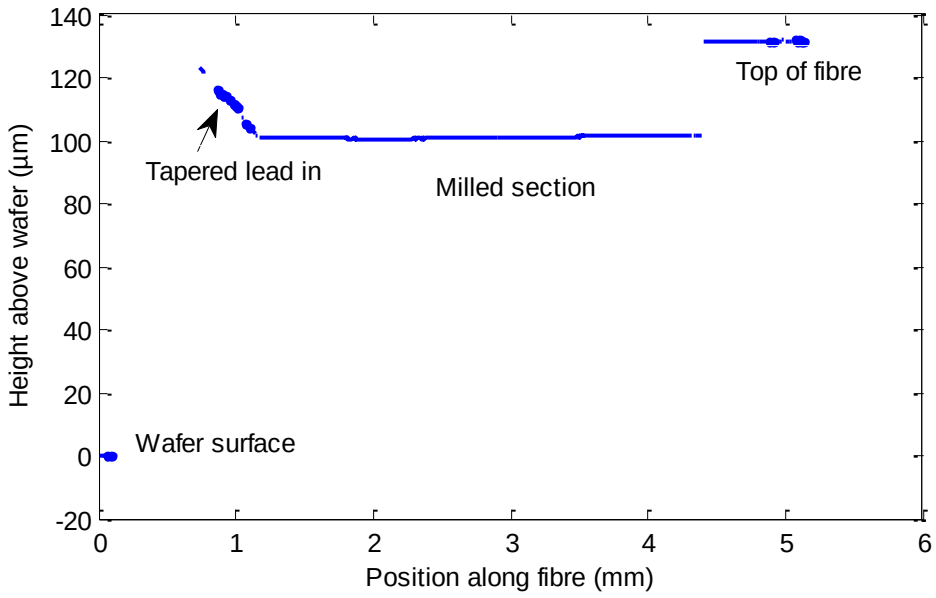

Figure 103. Line slice along length of fibre showing the depth of cut.

The roughness of the surface was evaluated with the Zescope and found to be Sa 17 nm. The surface roughness is found to be better than for the grooves in bulk silica. This may be due to

lower machining forces present during machining as the contact area is smaller and the new tool more effective in allowing coolant to reach the cutting zone.

The feathered edge along the fibre is due to the FHD glass not adhering uniformly to the fibre. Figure 104 shows a fibre before machining which shows the FHD on the left side of the fibre is rougher than the right.

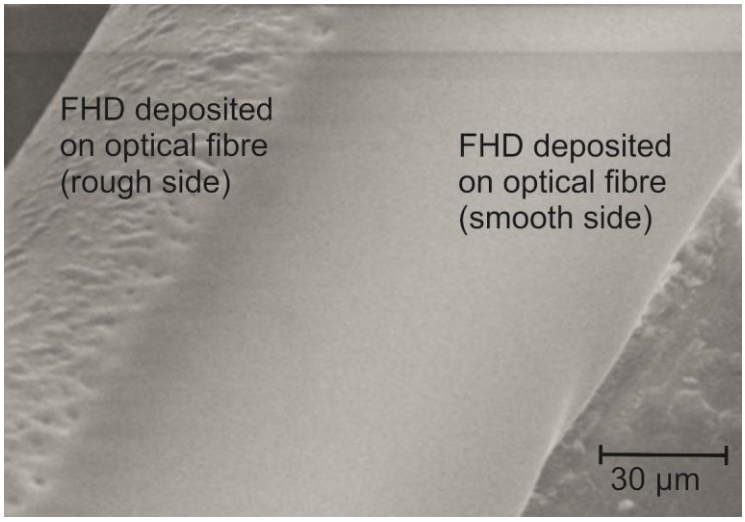

Figure 104. SEM of fibre-FHD composite before machining taken courtesy of Dr Chris Holmes.

When the top of the fibre is cut off this will cause the cut boundary not to be straight. Due to the directionality of the FHD deposition process the two sides of the fibre may have different thicknesses of FHD or different surface textures as seen in Figure 104. This explains the different appearances of the cut boundaries in Figure 102.

6.10 Ring tool fabrication

For the fabrication of circular structures including whispering gallery resonators a ring tool was fabricated. Physical machining is a technique for producing circular structures where deep depths of cut are required or when machining materials such as lithium niobate where the crystal structure or chemistry may make wet etching or ICP etching difficult. Single point diamond turning of glass has been shown to be extremely difficult and so a different design of tool was required that would enable machining in the ductile mode. Many works have cited the importance of hydrostatic pressure when machining in the ductile regime [23]. This is understood to lead to plastic flow which is condition of ductile mode machine. A ring tool has full contact between the cutting edge and workpiece and should give greater hydrostatic pressure. The fabrication of this tool will be covered in this chapter and its use to fabricate whispering gallery structures discussed in Chapter 7. To make the ring tool a combination of the wire system and straight electrodes are used. The straight electrodes are used to remove material at the centre of

the tool whilst the wire is used to machine the outside of the ring and add cross cuts to help with material removal. These are designed to aid material removal and improve coolant flow to cutting zone. This is illustrated in Figure 105.

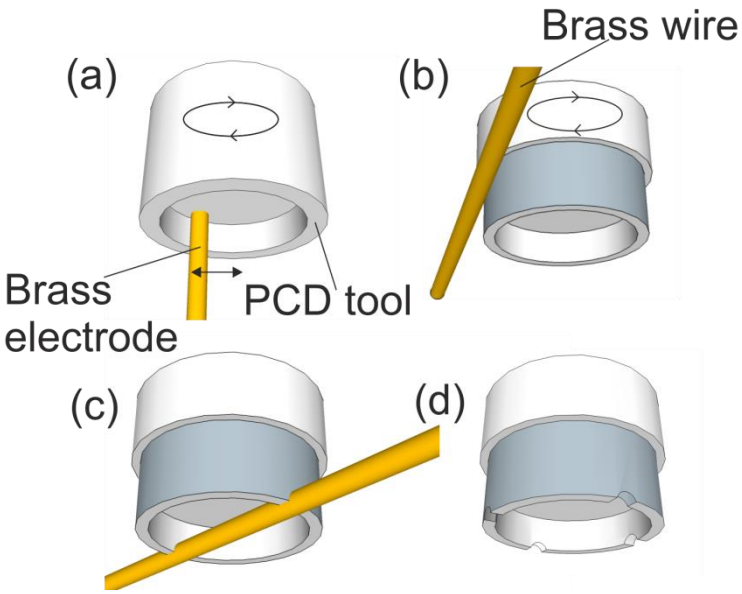

Figure 105. Fabrication steps for ring tool (a) Centre of tool is hollowed out with straight brass electrode (b) Wire is used to remove runout from outer edge (c) Wire is used to cut teeth into tool (d) Finished tool.

Due to the geometry of the wire, it is not possible to use it for material removal at the centre and a vertical brass electrode was used. This has the issue of wearing faster than the PCD is eroded. An SEM image of the finished tool is shown in Figure 106. There is some extra detail at the centre due to the removal of material at the centre being carried out in multiple steps. This area will not engage the workpiece so does not affect the function of the tool.

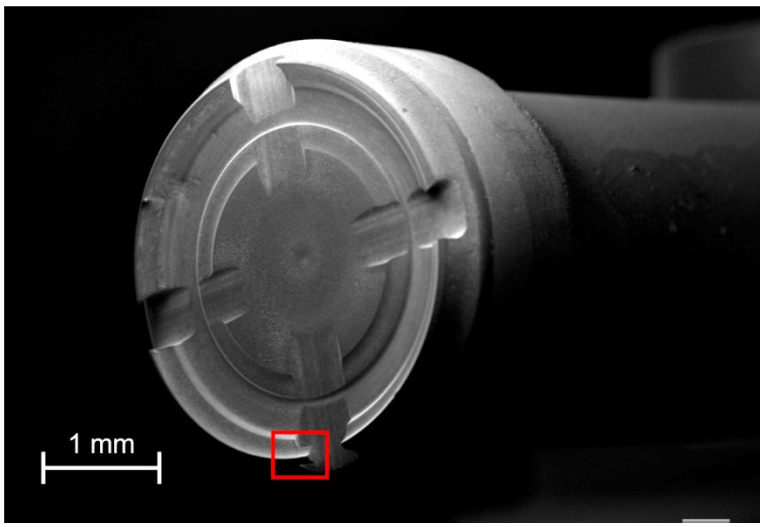

Figure 106. SEM image of finished tool. The area in the red box is shown in the next figure.

Figure 107 shows a close up of the cutting edge showing a the shape of the inner outer walls. The sloping cutting faces mean pressure will be applied to the final cut surface.

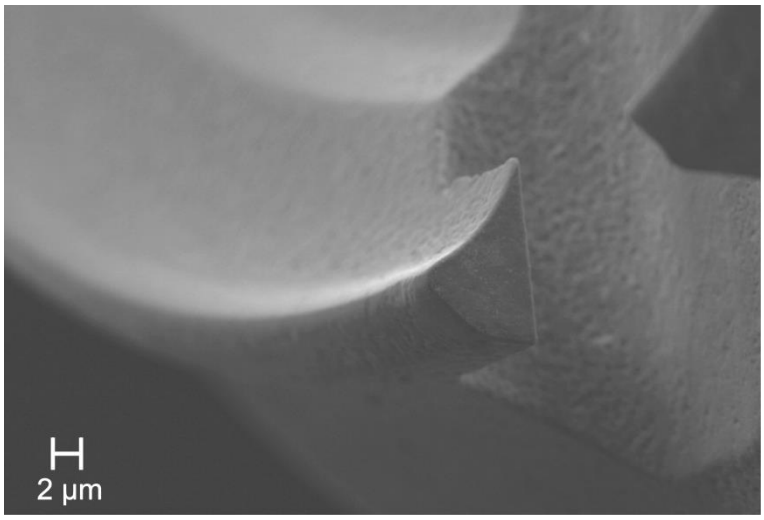

Figure 107. Close up of cutting edge.

This image shows the curved edges of the tool which are due to electrode wear. This could be improved by cutting deeper into the centre but as is shown in Chapter 7 shallow angles are shown to help with cutting in the ductile regime. The cut surface is very even due to the nonlinear nature of the WEDG process, which means high points are preferably eroded. This tool was used for machining the resonators in Chapter 7 and the structures generated are characterized in that chapter.

6.11 References

[1] T. Bifano, TG Dow and R. Scattergood, “Ductile-regime Grinding - A New Technology For Machining Brittle Materials,” *J. Eng. Ind. Asme*, vol. 113, no. 2, pp. 184–189, 1991.

[2] L. G. Carpenter, P. A. Cooper, C. Holmes, C. B. E. Gawith, J. C. Gates, and P. G. R. Smith, “Nanoscale roughness micromilled silica evanescent refractometer,” *Opt Express*, vol. 23, no. 2, pp. 1005-1014, Jan. 2015.

[3] J. A. McGeough, *Micromachining of Engineering Materials*, 1st ed. New York/Basel: CRC Press, 2002.

[4] P. N. Rao, *Manufacturing Technology*. McGraw Hill Education (India), 2013.

[5] E. C. Jameson, *Electrical Discharge Machining*. Society of Manufacturing Engineers, 2001.

[6] H. Kurafuji and T. Masuzawa, “Micro-EDM of Cemented Carbide Alloys,” *J. Japan Soc. Electr. Mach. Eng.*, pp. 1–16, 1968.

[7] J. Kozak, K. P. Rajurkar, and S. Z. Wang, “Material Removal in WEDM of PCD Blanks,” *J. Eng. Ind.*, vol. 116, no. 3, pp. 363-369, Aug. 1994.

[8] T. Masuzawa, K. Okajima, T. Taguchi, and M. Fujino, “EDM-Lathe for Micromachining,” *CIRP Ann. - Manuf. Technol.*, vol. 51, no. 1, pp. 355–358, Jan. 2002.

[9] C. J. Morgan, R. R. Vallance, and E. R. Marsh, “Micro-machining and micro-grinding with tools fabricated by micro electro-discharge machining,” *Int. J. Nanomanuf.*, vol. 1, no. 2, pp. 242–258, 2006.

[10] X. Cheng, Z. G. Wang, S. Kobayashi, K. Nakamoto, and K. Yamazaki, “Development of a six-axis wire electrical discharge machine for the fabrication of micro end mills,” *Proc. Inst. Mech. Eng. Part B J. Eng. Manuf.*, vol. 223, no. 2, pp. 121–131, Feb. 2009.

[11] A. Rees, “Micro electrical discharge machining: axis-symmetric component manufacture and surface integrity,” University of Wales, 2011.

[12] Y. Qin, *Micromanufacturing Engineering and Technology*. William Andrew, 2010.

[13] G. Bissacco, J. Valentincic, H. N. Hansen, and B. D. Wiwe, “Towards the effective tool wear control in micro-EDM milling,” *Int. J. Adv. Manuf. Technol.*, vol. 47, no. 1–4, pp. 3–9, May 2009.

[14] D. T. Pham, A. Ivanov, S. Bigot, K. Popov, and S. Dimov, “An investigation of tube and rod electrode wear in micro EDM drilling,” *Int. J. Adv. Manuf. Technol.*, vol. 33, no. 1–2, pp. 103–109, Jun. 2006.

[15] P. Fonda, K. Katahira, Y. Kobayashi, and K. Yamazaki, “WEDM condition parameter optimization for PCD microtool geometry fabrication process and quality improvement,” *Int. J. Adv. Manuf. Technol.*, Feb. 2012.

[16] Y. . Wong, M. Rahman, H. . Lim, H. Han, and N. Ravi, “Investigation of micro-EDM material removal characteristics using single RC-pulse discharges,” *J. Mater. Process. Technol.*, vol. 140, no. 1–3, pp. 303–307, Sep. 2003.

[17] R. Cox, “Conversation with Dave Richards Eng,” 2013.

[18] C. J. Morgan, “Microgrinding with polycrystalline diamond microtools to improve the precision of microscale features,” University of Kentucky, 2008.

[19] L. G. Carpenter, “Precision dicing and micromilling of silica for photonics,” 2013.

[20] J. M. Nagarah and D. A. Wagenaar, “Ultradeep fused silica glass etching with an HF-resistant photosensitive resist for optical imaging applications,” *J Micromech Microeng*, vol. 22, no. 3, p. 035011, Mar. 2012.

[21] C. Holmes, J. C. Gates, and P. G. R. Smith, “Planarised optical fiber composite using flame hydrolysis deposition demonstrating an integrated FBG anemometer.,” *Opt Express*, vol. 22, no. 26, pp. 32150–7, Dec. 2014.

[22] C. Holmes, “Fiber planar optical composite,” Patent Application, 2014.

[23] V. K. Jain, *Micromanufacturing Processes*. CRC Press, 2012.

Chapter 7: Towards a whispering gallery resonator

7.1 Introduction

The name 'whispering gallery' was coined by Lord Raleigh to describe the acoustic modes which make it possible for a listener to hear someone speaking from opposite sides of St Paul's Cathedral's dome. Optical whispering galleries guide light in a similar manner and allow extremely high field intensities to build up making them interesting when researching nonlinear optics [1]. Optical cavities play a crucial role in optics as components where the output spectrum of light can be shaped by the geometric properties of the resonator. Whispering gallery devices have been proposed for a variety of applications both for theoretical physics experiments and practical photonics. Fabry Perot (FP) cavities are currently commonly used for many applications when a resonator is required, however they can be difficult to miniaturize and suffer from vibration instabilities due to their size [2]. Whispering gallery resonators may offer a monolithic solution to applications where small sizes and stability are important.

This work will look at disc resonators fabricated from a planar chip platform. The aim is to produce structures with the correct geometry to support optical modes. Whispering gallery or micro disc resonators confine light with total internal reflection both at the curved perimeter and within the thickness of the disc [3]. The choice of material to use will be determined by both the material properties and by the ease of fabrication in that material. This work will look for the first time at fabrication processes for resonators in glasses deposited by flame hydrolysis deposition (FHD) which are known for their purity and ability to be deposited with a variety of compositions. FHD deposited germanophosophate on thick silica is first explored as a resonator material. A machining process using a WEDG manufactured ring tool is used to define the resonator. A flame polishing process is demonstrated to leave a very smooth germanophosphate layer but does not modify the underlying silica layer. FHD deposited germanium dioxide on pure silicon is also investigated. A xenon difluoride silicon etch is found to be an effective way of leaving a high aspect ratio glass lip which has the properties to act as a whispering gallery resonator. Furnace reannealing of the germanium dioxide is found to remove the machining signatures.

7.1.1 Basic physics of WG's

Whispering galleries are similar to other optical cavities in that geometry of the structure means certain wavelengths will be resonantly enhanced. If a wave has a wavelength that is some integer multiple of the resonator path length (in this case the circumference of the resonator) after every

round trip it will experience constructive interference [4]. Likewise destructive interference will occur for those wavelengths not at resonance with the structure. This feature is illustrated in Figure 108.

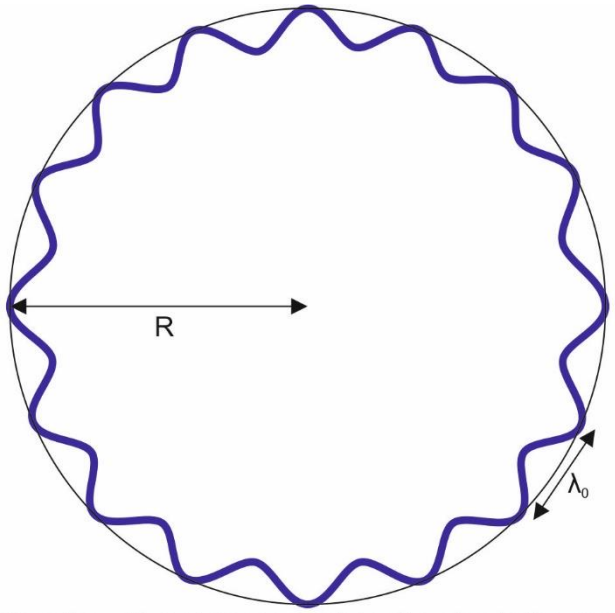

Figure 108. Constructive interference inside whispering gallery.

These modes differ from those in a Fabry-Perot cavity in that they are not standing waves. The spectra of the light inside the resonator will be a frequency comb with pronounced intensity at spaced intervals. Typically with cavities as the quality factor of the cavity improves the anti-resonance dips will become shallower and narrower. The comb spacing will generally not be uniform as material and modal dispersion will cause it to vary with wavelength [5]. Various schemes have been proposed for compensating for the dispersion, for example by having a graded index structure [6] or when this is not possible in a crystal structure by microstructuring the light guiding boundary [7]. The resonator guides light by total internal reflection (providing the resonator refractive index is higher than that of the outside space). The free spectral range of a resonator is the wavelength 'gap' between successive resonances and is given by equation (84) [8].

$$\Delta\lambda_{fsr} = \frac{\lambda^2}{n2\pi R} \tag{84}$$

The variables are as represented in Figure 108. Thus it can be seen as the resonator structure becomes larger the fringes will become more closely spaced.

Resonator loss can occur by a number of different mechanisms. Depending on the nature of the resonator some mechanisms will tend to dominate over others.

1) **Bend loss**: Any bent waveguide will experience some loss due to a light tunnelling effect. For a large structure with small curvature this effect is small. This effect sets a theoretical upper limit on the allowed Q factor and will usually be the dominant loss mechanism for small resonators of radius ~10 μm [9]
2) **Absorption loss**: Light will be absorbed by intrinsic and extrinsic material loss. Intrinsic loss is impossible to eradicate but extrinsic loss may be reduced by using purer materials. For pure materials measuring loss in a resonator can be an accurate method of determining the absorption loss of the material [10]. Certain glasses such as silica may be prone to absorb water moisture, leading to degradation of the device if losses become unacceptably high [11].
3) **Scattering loss**: Surface roughness and imperfections in the resonator's surface will scatter light and cause loss. This is expected to be the dominant mode of loss for machined resonators

The Q factor is a measure of how well the resonator structure contains light. When operating the resonator stores energy. It also loses energy due to the mechanisms described previously and this limits how much energy can be contained in the resonator. The Q factor can then be defined by

$$Q = 2\pi \frac{E_s}{E_d} \tag{85}$$

Here E_s is the energy stored and E_d is the energy that is dissipated per cycle [12].

It can also be understand as a measure of the average photon lifetime in the cavity [13].

$$Q = \omega_R \tau_p \tag{86}$$

A high Q affects the output spectrum by giving narrower resonance dips.

$$Q = \frac{\lambda_r}{\Delta\lambda} \tag{87}$$

$\Delta\lambda$ is the full-width-half-maximum (FWHM) of the resonance dip. High Q factors mean higher intensities of light in the resonator which is almost always desirable.

If there are multiple contributors to the Q-factor the total value Q_{total} can be determined from equation (88).

$$\frac{1}{Q_{total}} = \frac{1}{Q_1} + \frac{1}{Q_2} \ldots \tag{88}$$

7.1.2 Literature review

The field of whispering gallery resonators has attracted a lot of research attention and whispering gallery resonators have been fabricated for a range of applications and out of various optical materials.

The first evidence of resonator behaviour in spherical structures was in water droplets [14]. Although all circular resonators operate on similar principles there are a variety of different designs that will produce different optical outputs.

Silica has attracted much attention due to its wide transparency window and- as it has long been used for low-loss optical applications- the high purity of the available material. The highest Q factor for a resonator in an amorphous material of over 100 million was achieved by Vahalla *et al.* [15] with a silica micro toroid structure. This was achieved by minimizing surface scattering by using a thermal reflow process. For high Q resonators smooth surfaces are a prerequisite. For this reason thermal reflow methods are popular because they can yield surfaces close to being atomically smooth due to surface tension. One drawback is that they limit the controllable resonator shapes as surface tension will generally create spherical toroidal structures. Buffered HF etching is a process which can give extremely smooth surfaces and has been used in delay line generators [15]. With HF etching it is difficult to precisely control resonator shape although Vahala *et al.* have fabricated wedge shaped edges by controlling the lithographic machining.

Crystalline materials have properties that make them well suited in resonator applications. Generally crystals are more resistant to diffusion from moisture than amorphous materials as well as having low intrinsic loss. Crystalline materials have nonlinear properties that can give additional optical properties to resonators. Periodic poled single crystal lithium niobate was used to generate second harmonic generation by Ilchenko *et al.* [1]. As the period poling was in stripes the resonant light encountered a range of periods around the ring thus increasing the band width. Using a 400 nm thick single crystal lithium niobate (LN) on insulator substrate Wang *et al.* have demonstrated resonators with a Q factor of 10^5 and second harmonic generation efficiency of 0.109 W^{-1} [16].

Diamond machining has already been applied to whispering gallery resonators by Grunadin [17]. He used a diamond core drill to remove a cylindrical portion from single crystal magnesium fluoride. Diamond turning and polishing were used to form a raised lip around the cylinder which acts as the guiding structure. Thermal reflow is possible following physical machining for glasses and it is proposed to investigate both directly machined and reflowed resonators. For crystalline materials, melting is not an option as this will destroy the crystal structure. Ilchenko *et al*. showed

that polishing was another viable way of creating smooth edges for lithium niobate crystal resonators [1]. Whispering gallery resonators have found applications in quantum experiments [18] and they have been proposed as broadband optical filters for telecommunications [19].

7.1.3 Coupling

Coupling light into a resonator is not a simple problem; this is because as the Q factor increases and the rate of power loss decreases it becomes harder to get light in. A high Q factor resonator free space coupling with a focused Gaussian beam cannot couple appreciable power into the resonator. This has been one of the main technological difficulties in the adoption of whispering galleries.

Tapered fibre coupling is a method whereby a tapered fibre is brought close to the ring [9]. The tapered fibre has a small diameter that allows a fraction of the light energy to propagate outside of the fibre. The tapered fibre also has the advantage that the output light from the resonator can be collected and analysed at the other end of the fibre. Energy is coupled into the disc once the separation becomes less than the size of the evanescent field. Three types of coupling cases exist depending on the separation.

1) **Under-coupling**

When the fibre is far from the resonator very little of the evanescent field reaches the resonator and coupling in to the resonator is small

2) **Critical-coupling**

At an optimum distance from the cavity there can be almost 100% coupling of light from the fibre into the resonator

3) **Over-coupling**

If the separation is reduced still further the scattering from the fibre increases and the coupling decreases.

The main drawback of tapered fibre coupling is that it the tapered fibre is weak and will degrade over time meaning that it is not a good solution for packaged devices.

Coupled mode analysis can be used to derive these coupling conditions following the approach of Yariv [20]. The geometry of this is shown in Figure 109.

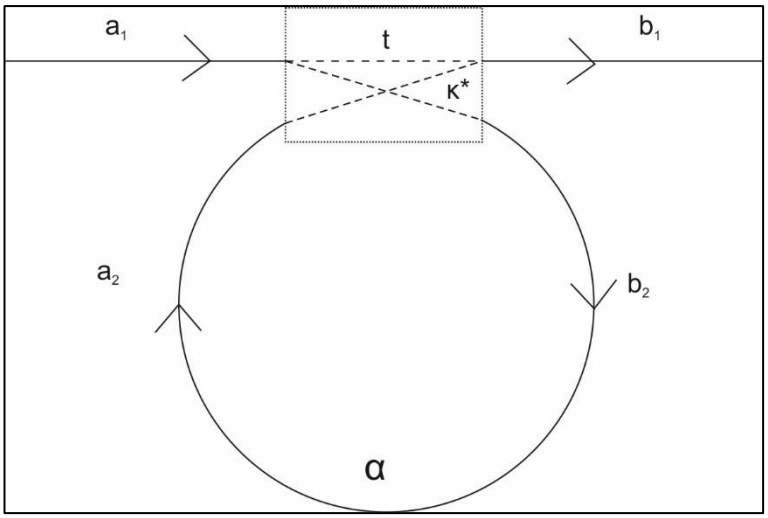

Figure 109. Schematic of coupling between a ring and straight waveguide.

If for simplicity we assume the waves only travel in one direction and no power is lost during the coupling we can relate b_1 and b_2 to a_1 and a_2 with a scattering matrix which includes constants κ, the coupling coefficient and t, the transmission coefficient.

$$\begin{vmatrix} b_1 \\ b_2 \end{vmatrix} = \begin{vmatrix} t & \kappa \\ \kappa^* & -t^* \end{vmatrix} \begin{vmatrix} a_1 \\ a_2 \end{vmatrix} \tag{89}$$

$$|t|^2 + |\kappa|^2 = 1 \tag{90}$$

In addition a_2 and b_2 are related by the circularity condition in the ring.

$$a_2 = b_2 \alpha e^{i\theta} \tag{91}$$

Where α is the loss in the ring and θ is the phase shift.

Solving these equations yields

$$\left|\frac{b_1}{a_1}\right|^2 = \frac{\alpha^2 + |t|^2 - 2\alpha|t|\cos\theta}{1 + \alpha^2|t|^2 - 2\alpha|t|\cos\theta} \tag{92}$$

At resonance $\theta = 2\pi m$. Taking the input power a_1 to be unity we have

$$|b_1|^2 = \frac{(\alpha - |t|)^2}{(1 - \alpha|t|)^2} \tag{93}$$

The output transmission goes to zero when $\alpha = t$. Figure 110 shows this plotted for two values of α.

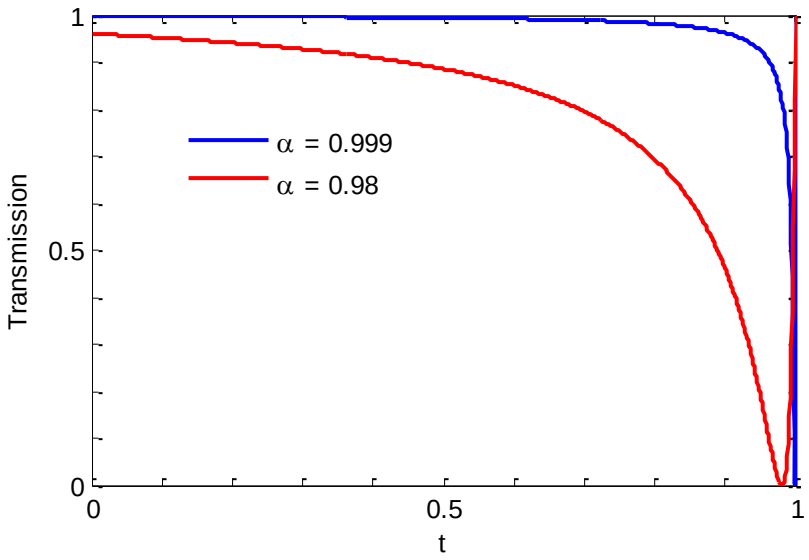

Figure 110. Transmission plotted versus t for two values of *α.*

This dip in these plots corresponds to the critical coupling situation where theoretically almost 100% of the input light can be coupled into the resonator. This can be controlled in practice by changing the tapered fibre to resonator distance. The coupling strength depends very strongly on ring-fibre separation thus this provides a significant technological challenge. As the absorption loss of the resonator decreases the coupling becomes even more sensitive to separation. The next chapter will describe the fabrication of a resonator from germanophosphate on thick thermal oxide.

7.2 Germanophosphate on thick thermal oxide

7.2.1 Milling of ring structures

Phosphogermanate is a silicon free glass which can be deposited using the FHD system. It represents a new material for the fabrication whispering gallery structures which has interesting properties such as the ability to hold higher densities of rare earth elements than silica. As this was the first example of an FHD deposited layer of phosphogermanate, characterization of a whispering gallery device would allow further information about the quality of the layer and its application in resonator devices. Due to chemical reactions with the silicon wafer it must be deposited onto a wafer with a thermally grown thick silicon oxide layer. The initial substrate was a 5 micron thick phosphogermanate layer on a 17 micron thick thermal oxide. The polycrystalline diamond ring tool whose fabrication was described in Chapter 6 was used to machine the resonator structure.

Cutter rotation speeds and feed rates are factors that have an effect on the type of machining and subsequent surface quality. A parameter space test was taken to determine the effect of these on the cut. Spindle speeds of 7 krpm, 12.5 krpm and 15 krpm were chosen. The feed rate was kept constant at 0.01 mm/min. The parameters used are shown in Table 8.

Table 8. Parameters for experiment on effect of spindle speed on edge quality.

Tool	PCD Diamond SX-850
Spindle speed	A) 7 krpm B) 10 krpm C) 13 krpm
Feed rate	0.01 mm/min
Coolant	Water

The SEM was used to take images of the sidewalls for comparison of the machined surfaces. Figure 111 shows a schematic of the close to horizontal angle at which this measurement was made. High magnification images of the resonator edges are shown in Figure 112.

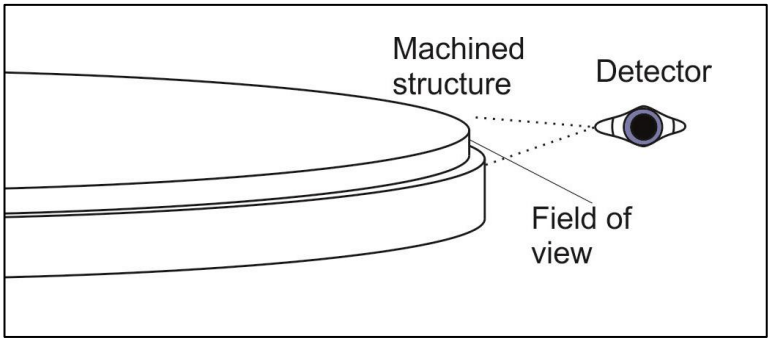

Figure 111. Position of sample when taking SEM images of sidewall.

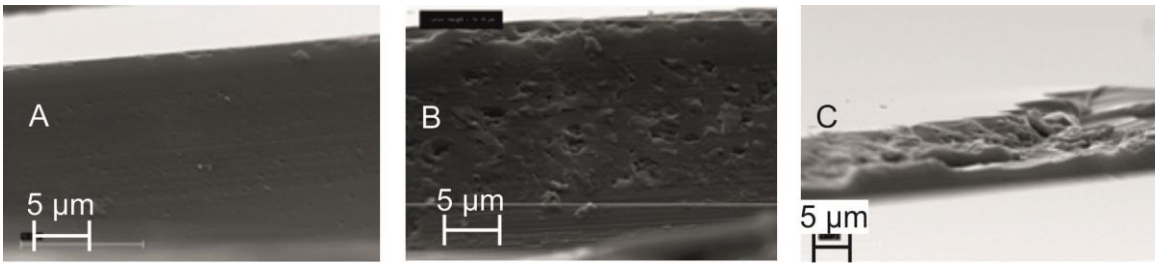

Figure 112. Effect of changing spindle speed on edge (a) 7 krpm (b) 10 krpm (c) 13 krpm.

From these images it is clear that 7 krpm gave the best edge quality, if other variables were kept constant. The effect of feed rate was also tested at 0.1, 0.05 and 0.01 mm/min keeping the

spindle speed at 10 krpm. The parameters used are shown in Table 9. The tool is made from Element 6 SX-850 PCD which is the grade with smallest diamond particle size available.

Table 9. Parameters for experiment to explore effect of feed rate on edge

Tool	PCD Diamond SX-850
Spindle speed	7 krpm
Feed rate	A) 0.1 mm/min B) 0.05 mm/min C) 0.01 mm/min
Coolant	Water

The effect of these is shown in the images in Figure 113.

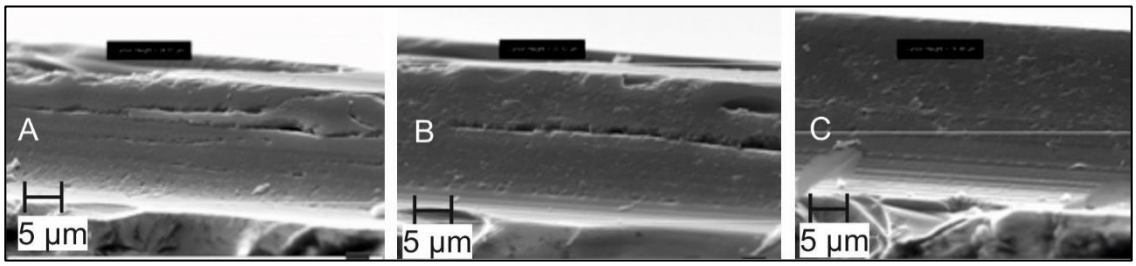

Figure 113. Effect of feed rate on edge (a) 0.1 mm/min (b) 0.05 mm/min (c) 0.01 mm/min.

These tests indicated the best results were obtained for S = 7 krpm and F = 0. 01 mm/min.

Table 10. shows the machining parameters used for the machining the first disc structures in phosphogermanate on thick silica on silicon substrates.

Table 10. Machining parameters used for phosphogermanate ring.

Tool	PCD Diamond SX-850
Spindle speed	7 krpm
Feed rate	0.01 mm/min
Coolant	Water

Figure 114 shows an SEM image of the full ring viewed from directly above. The dicing saw was used to dice next to the ring to allow better inspection of the sidewall.

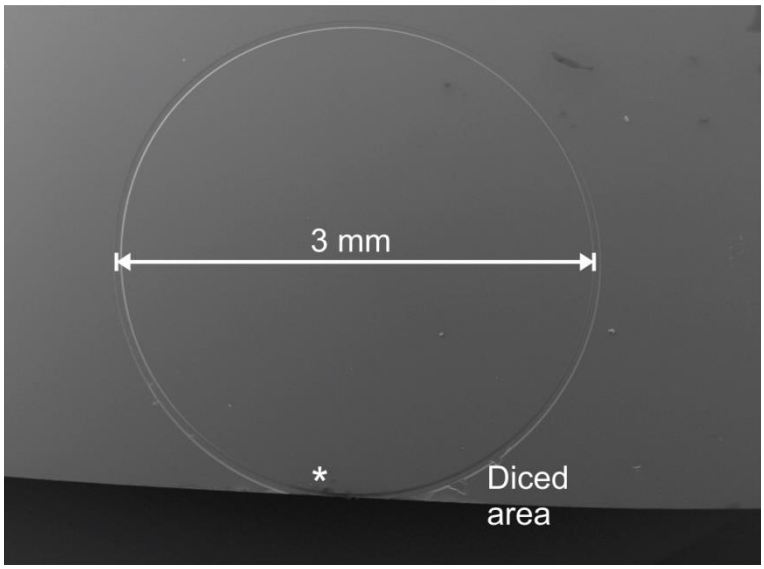

Figure 114. SEM image of full ring structure.

The area marked with '*' was viewed at close to horizontal to allow better inspection of the cut area. This is shown in Figure 115.

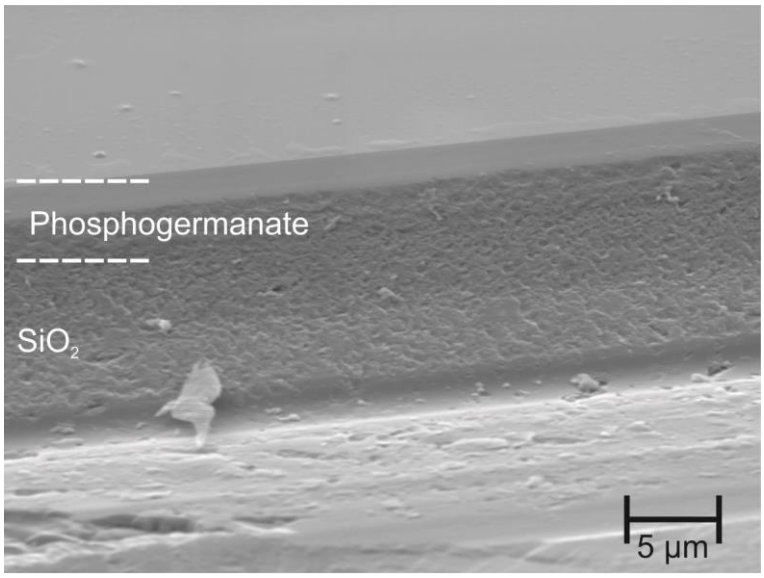

Figure 115. Side wall at position marked with '*' in Figure 114.

It can be seen there is a smooth region near the top of the cut with a shallower angle than the rest of cut which is closer to vertical. This was not seen during the parameter space experiment previously. This change in surface quality is not due to the interface between the phosphogermanate and silica as phosphogermanate is thicker than this region. One explanation for this discontinuity is that the smooth section is at a shallower angle and so experiences greater hydrostatic pressure during the machining. Pressure during machining has been proposed to help the transition to the ductile machining regime as it aids plastic shear deformation as explained in Chapter 2.

It was attempted to mill deeper to see whether this area could be extended to cover the whole phosphogermanate surface but the current required by the z axis went above the specified limit of 3.3 Amps which stopped the mill. Another way of improving the surface roughness of the phosphogermanate surface was required. Due to the lower melting point of phosphogermanate and relative higher thermal isolation of the edge it was decided to attempt flame polishing of this structure.

7.2.2 Flame polishing experiment in diced phosphogermanate

When a glass layer becomes molten it will pull itself into the shape with the lowest surface area to minimize its surface energy. This can be used to produce atomically smooth surfaces as chips and roughness are smoothed out. Flame polishing works on the principle that the surfaces and edges of a layer have higher thermal isolation than the bulk layer so can be reflowed without affecting the rest of the layer [21]. In this work flame polishing was first studied on diced grooves (in the same sample type) as it was quicker to generate multiple straight grooves than ring structures. As the curvature of the rings is not large they will behave similarly to straight grooves. Domestic methane gas used to make glassware for chemistry labs was used as the flame source. Once the grooves had been flame polished their facets were diced to allow inspection of the edges. 3 chips containing diced grooves were used with one groove left untouched to allow flame polished grooves to be compared to non-polished grooves.

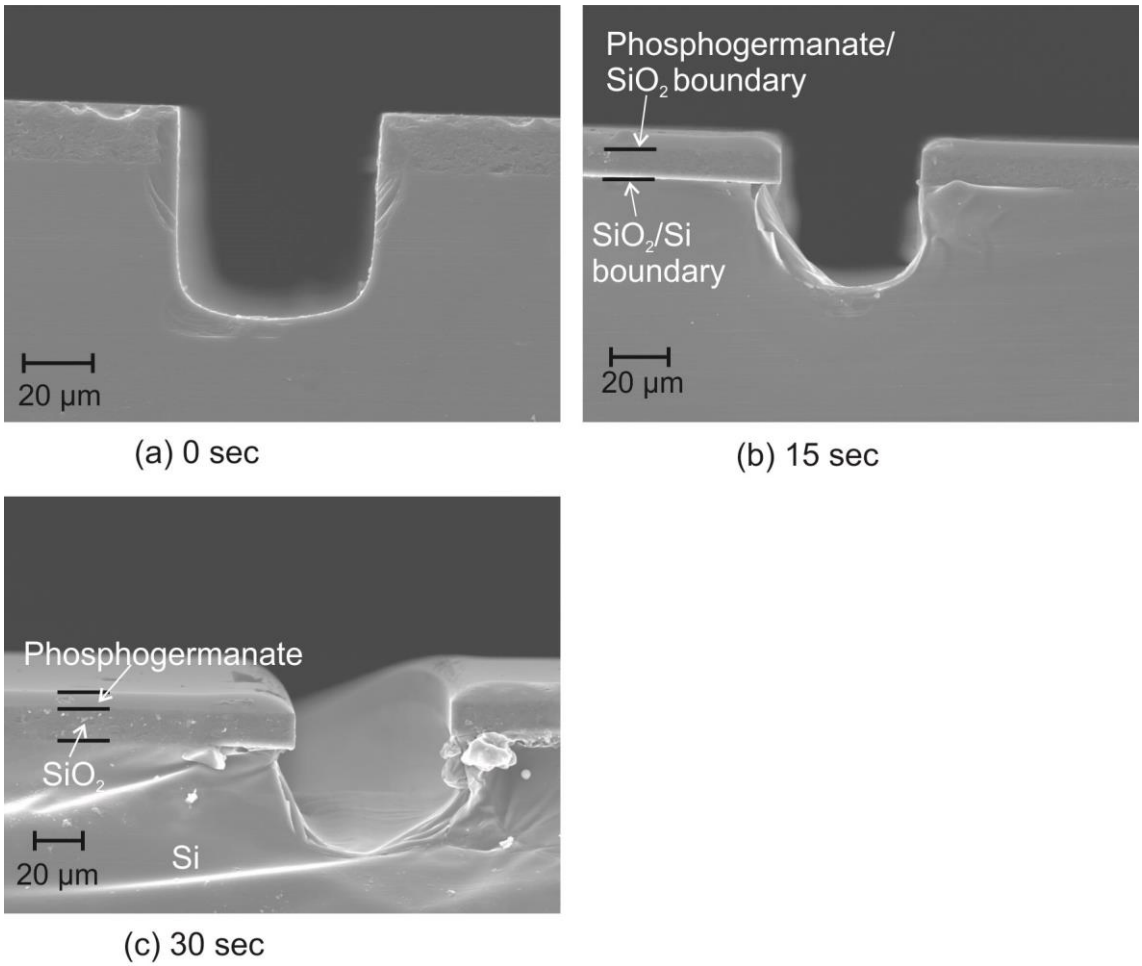

Figure 116. SEM edges of diced facets of flame polished grooves. (a) Groove with no flame polishing (b) 15 seconds of polishing (c) 30 seconds of polishing.

It can be seen the phosphogermanate layer on top of the thick thermal oxide undergoes reflow which is visible after 15 seconds of flame polishing. When molten, the surface area of the phosphogermanate will be minimised by assuming a shape with a curved cross section as can be seen in the SEM images. This shows that the final shape of the phosphogermanate edge will be independent of the initial shape even if the layer previously has highly vertical sidewalls (as commonly generated from dicing). After 30 seconds the facet image suggests that distortion of the substrate had occurred, suggesting that keeping every aspect of the polishing setup such as nozzle size and substrate-to-torch distance constant, 15 seconds of flame exposure would give reflow of the whispering gallery edges.

To investigate the surface features of the flame polished edges they were looked at higher magnification with the SEM from an angle facing the groove facet. These images are shown in Figure 117.

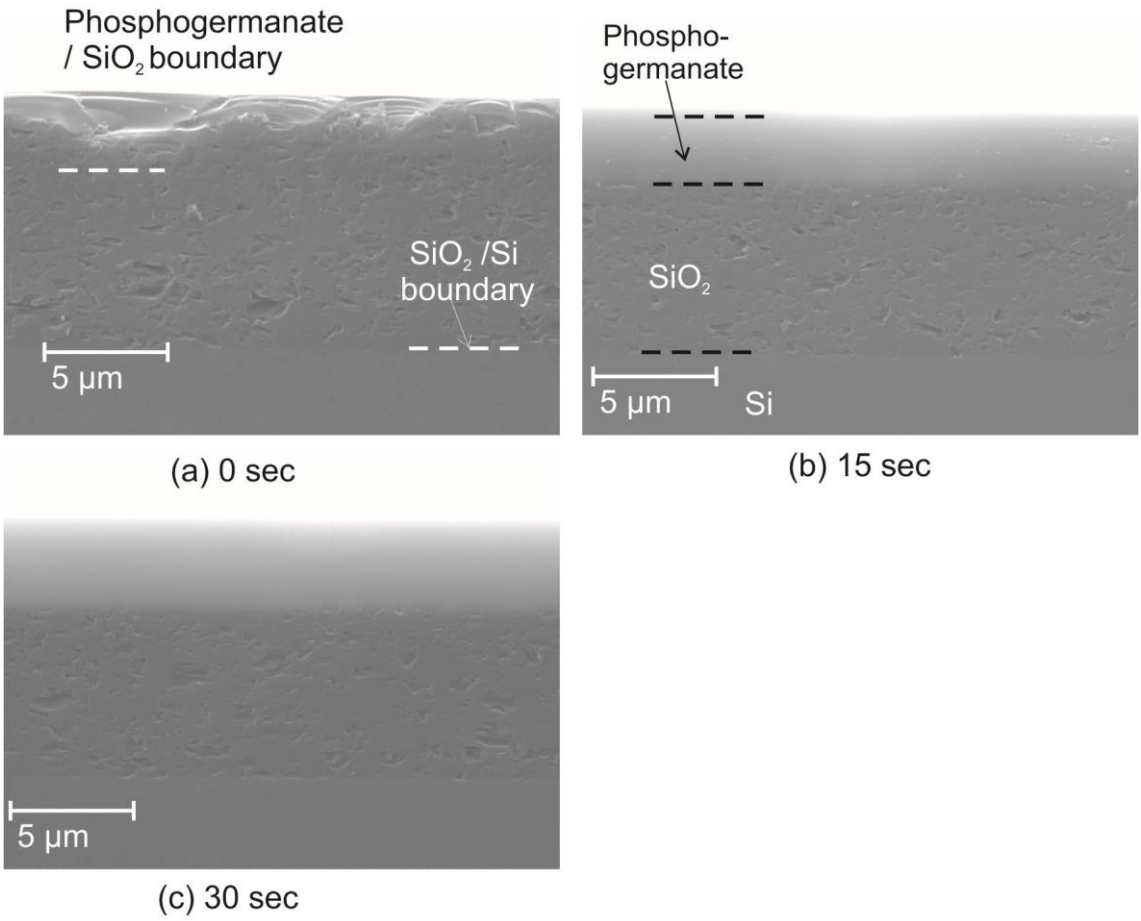

Figure 117. SEM images of groove sidewalls.

In Figure 117(a) it can be seen that with the secondary electron detector there is no discernible difference in surface morphology between the glass layers, although the topside chipping is clear. The layer boundary does not coincide with this chipping. The pure silicon substrate has been left with comparatively smooth surface following dicing. After 15 s of flame polishing the phosphogermanate layer has become smoother although there are still visible defects on the layer. After 30 s the phosphogermanate layer looks smooth with no visible defects. It is clear that the SiO_2 layer has not changed as the temperature did not reach the higher melting point. Although the phosphogermanate edge initially contained a high level of topside chipping this has been completely removed. This experiment suggested that flame polishing was a viable way of producing the extremely low surface roughness demanded by high Q factor whispering galleries.

7.2.3 Flame polishing of phosphogermanate ring

After the process of flame polishing had been tested on the diced grooves it was applied to the ring structure. The torch was circled round the ring for 15 seconds following the same process that was applied to the diced grooves. The SEM images of the resultant edges are shown in Figure 118.

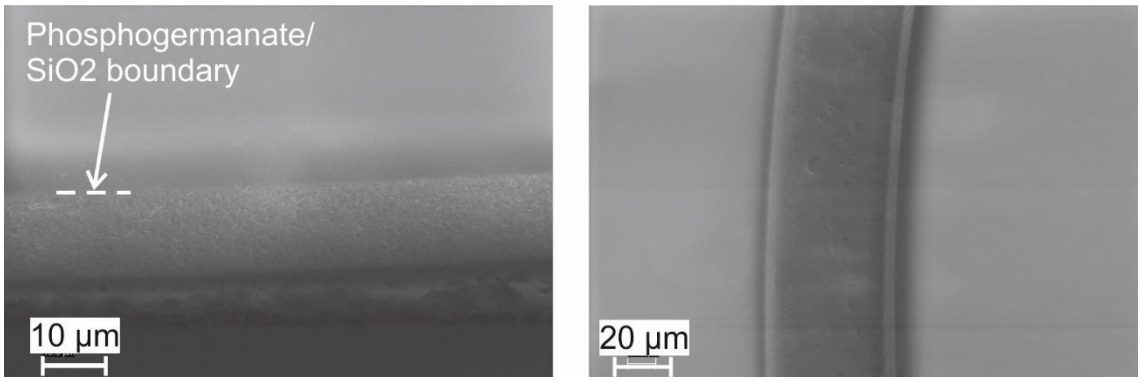

Figure 118. SEM images of ring structure following flame polishing.

When Figure 118(a) is compared with Figure 115 it can be seen that shape of the sidewall is lost during flame polishing. The flame polished area again shows good uniformity and few visible defects. Figure 118(b) shows this edge uniformity was maintained over a longer portion of the ring.

7.2.4 Characterization of phosphogermanate ring

As the phosphogermanate has a higher refractive index than the SiO_2 it was tested to see whether optical guidance could be sustained in the structure. The schematic in

Figure 119 shows how the tapered fibre was brought next to edge of the ring by viewing through a high magnification (x60) microscope.

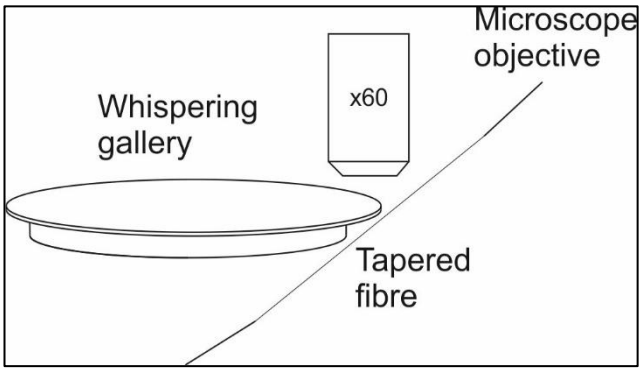

Figure 119. Schematic showing how the position of the tapered fibre is controlled relative to the resonator.

Figure 120 shows a camera image of the microfibre next to the ring.

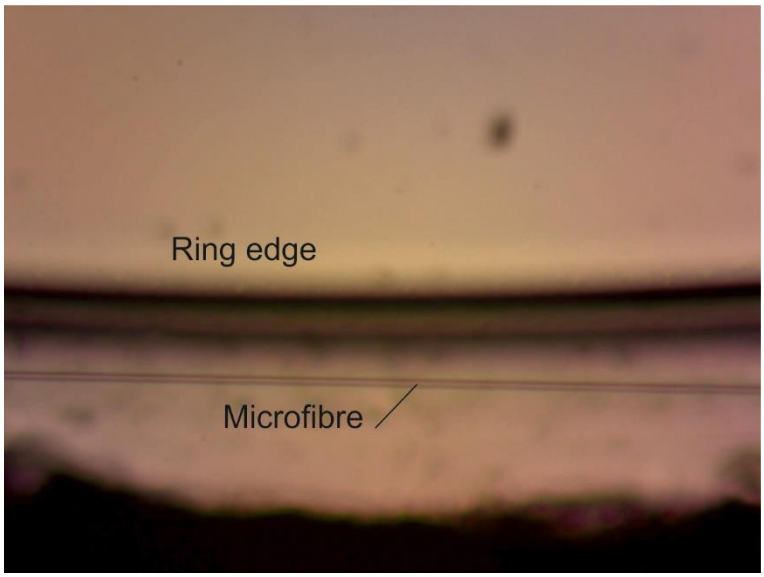

Figure 120. Camera image of microfibre close to ring (x5) objective.

Alignment is made by using the highest magnification objective lens (x60) and bringing the fibre and ring into the same focus. X and Y alignment is possible to ~1 µm with the resolution of the microscope.

To understand the effect the measuring system and the source have on the out spectrum, data was taken initially with the tapered fibre far from the whispering gallery. It was then brought close and the spectrum was measured. Data showing a comparison of these spectra are shown in Figure 121.

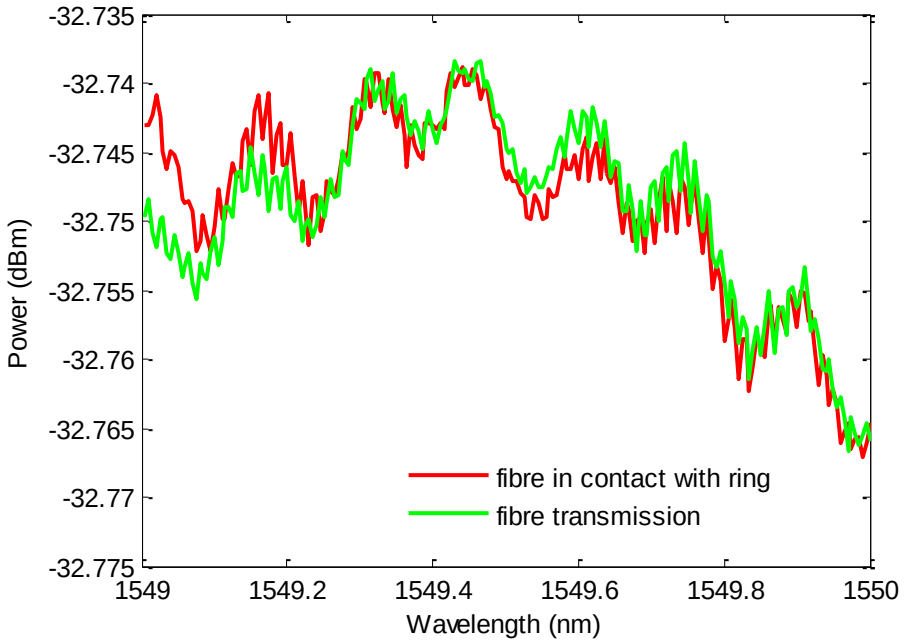

Figure 121. Green: Transmission spectrum through the microfibre. Red: With microfibre in contact with whispering gallery. There is no evidence of excitation of modes in the ring device.

To display better the periodic features in the data an FFT of the data was made and is shown in Figure 122.

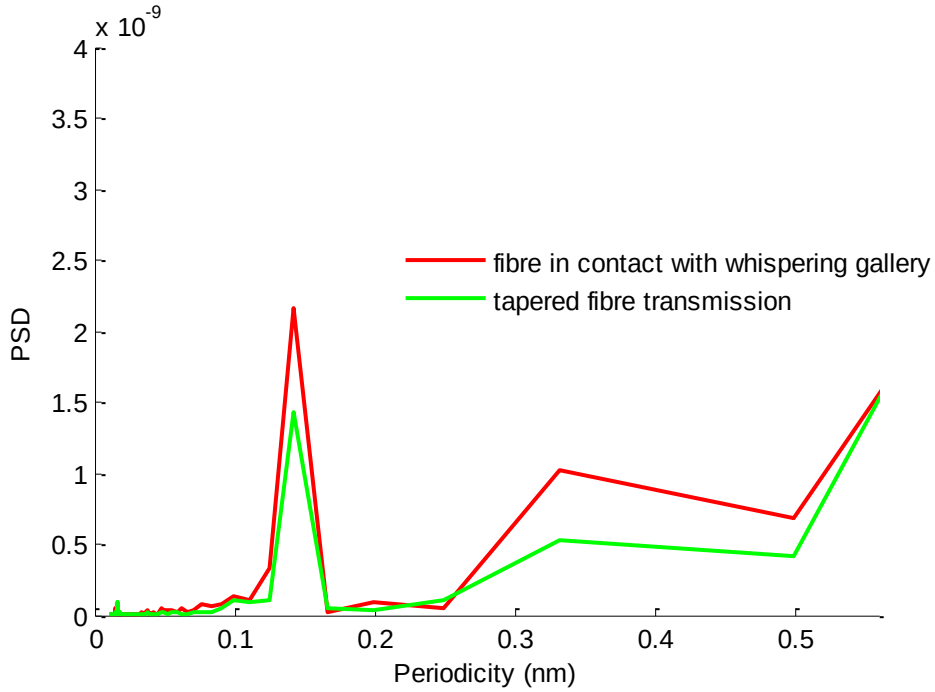

Figure 122. FFT of coupling experiment spectra.

The prominent peak at 0.14 nm is present in both the transmission through the tapered fibre and the coupling data. This means it is not caused by interaction between the fibre and resonator and

is caused either by the source or some other component in the characterization setup. There is no peak at the calculated free spectral range of 0.17 nm suggesting that this resonator could not support a mode. This believed to be due to the shallow angle of the phosphogermanate layer causing light to be guided in the SiO_2 layer which was very lossy as it had not been reflowed during the flame polishing.

7.2.5 HF etch of device

As a literature search returned no etchant with etch selectivity between phosphogermanate and SiO_2 an HF etch was attempted as it is a known etch for silica. 49 % HF solution was used as the etchant at room temperature. Figure 123 shows the result of this etch.

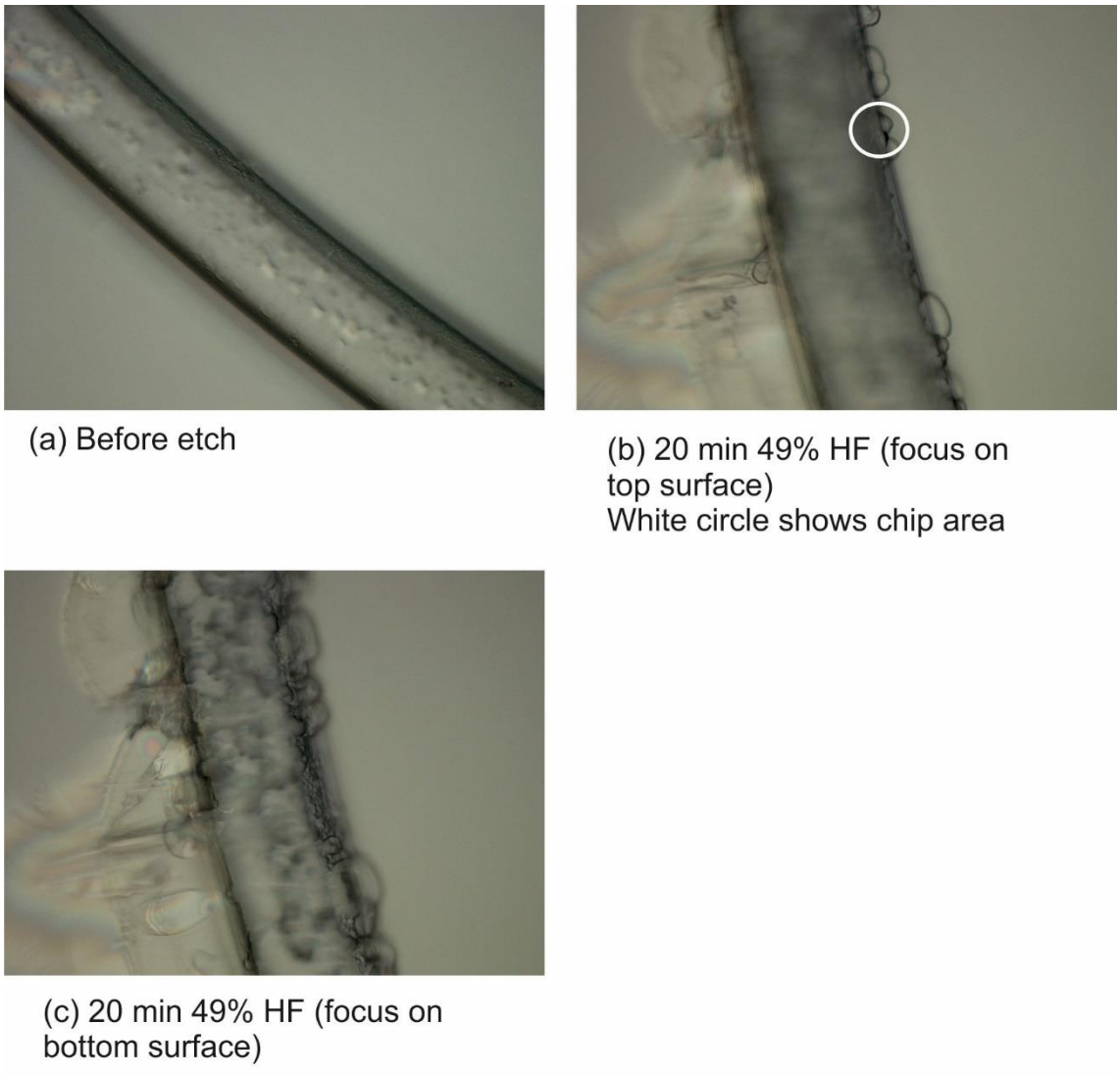

Figure 123. HF etch of phosphogermanate resonator.

From Figure 123(b) it can be seen that most of phosphogermanate layer on the disc appears to be intact and the silica has etched in an irregular way. The phosphogermanate layer on the other side

of the ring appears to have been damaged as seen by the cracking and interference fringes, although this area does not directly affect the function of the device. A chip was visible on the phosphogermanate layer and for this reason the HF undercut approach was not pursued further. This result suggests that phosphogermanate may have higher resistance to HF etch than silica but further work would be required to prove this.

7.3 Milled structures for FHD deposition

The objective of this experiment was to provide a platform to directly deposit FHD glass onto a milled structure to test whether FHD glass was able to bead around the pillar to form a resonator. With the beading of the FHD glass it may be feasible to create a resonator of higher index phosphogermanate around the thick silica layer.

While using the ring tool described previously is one way to fabricate whispering gallery structures it is also possible to use a conventional milling tool following a circular toolpath. Unlike with the ring machining described previously this process allowed considerable flexibility in the toolpath. For example the tool could be brought down in a helical spiral to the final depth or used to drill vertically to the final depth and then follow a constant depth circle. An experiment was carried out to study the effect of using two different commercially available tools and different toolpaths and the parameters are shown in Table 11. #1 to #4 follow helical toolpaths with changing pitch. #5 to #8 first ramp down to the target depth and then follow a circle at a constant depth.

Table 11. Parameters for the milled structures in silica on silicon. Boxes with multiple entries mean multiple revolutions were used with the final value being for the finish cut.

Structure Number	Feed rate (mm/min)	Programmed radius of cut (mm)	Spindle speed (rpm)	Depth of Cut (µm)	Tool
1	1/1/1/1/0.25	0.75/ 0.65	10	20/40/50/50/45	1mm tungsten carbide (WC)
2	1/1/1/1/0.25	0.75/ 0.65	15	20/40/50/50/45	1 mm WC
3	1/1/1/1/0.25	0.75/ 0.65	15	20/40/50/50/45	1 mm WC
4	0.1	0.5	60	25/50/50	1 mm WC
5	0.1	0.5	60	45° ramp then 80	0.5 mm Diamond coated UKAM
6	0.1	0.5	60	45° ramp then 80	0.5 mm Diamond coated UKAM
7	0.1	0.5	62	45° ramp then 80	0.5 mm Diamond coated UKAM
8	0.1	0.325	62	45° ramp then 80	0.5 mm Diamond coated UKAM

Following milling the structures were investigated under the microscope as shown in Figure 124.

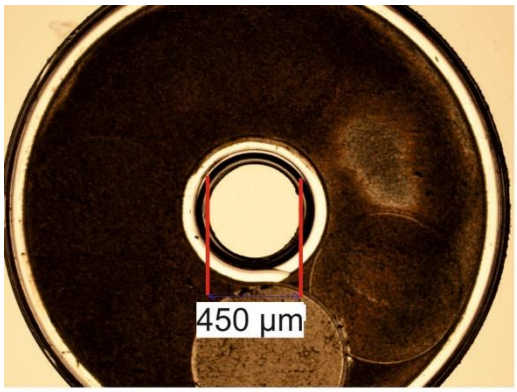

#1

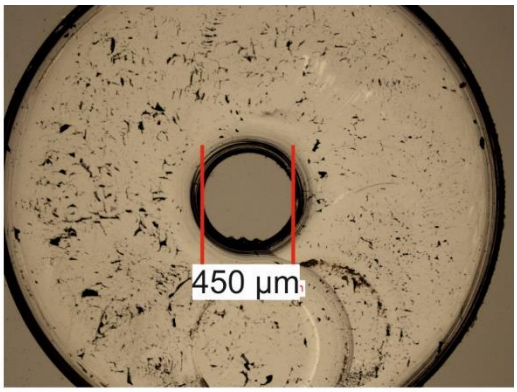

#2

#3

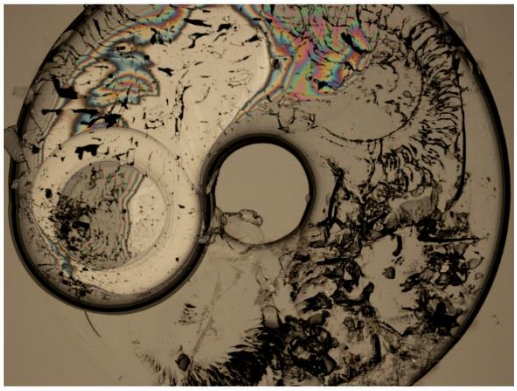

#4

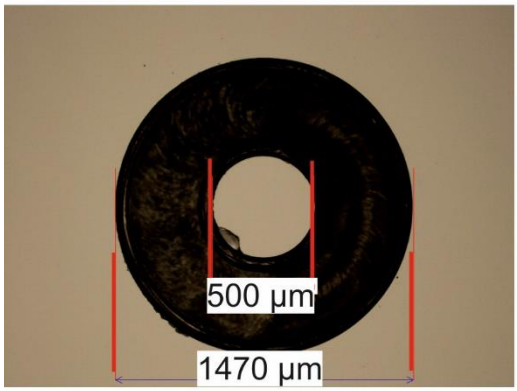

#5

#6

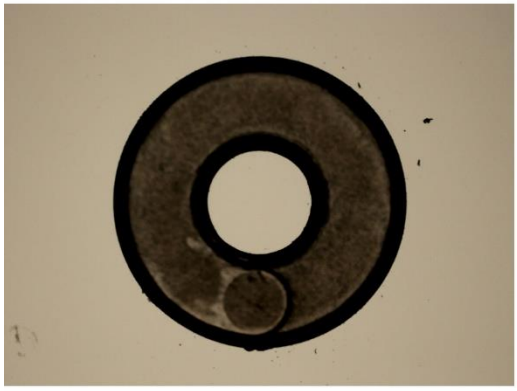

#7

#8

Figure 124. Microscope images of milled discs under x5 magnification.

From the microscope images it can be seen the 0.5 mm WC tungsten tool generated surfaces with more chipping around the central pillar. With this tool #1 had the least topside chipping suggesting slower spindle speed of 10 krpm was well chosen for this tool. The diamond coated tool generated pillars with low top side chipping as seen in #7 and #8.

The SEM was used to image structure #8 as shown in Figure 125.

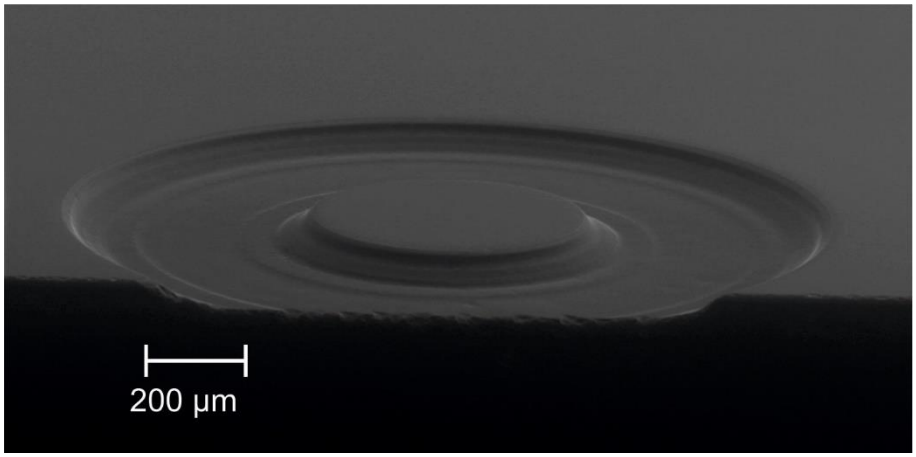

Figure 125. SEM image of structure #8.

This shows that the cut has sloping sidewalls. This is due to the commercial tooling used having a rounded base. Higher verticality in the sidewalls could be obtained by using deeper depths of cut to engage the straight portion of the tool.

With the assistance of another member of the group the FHD system was used to deposit a phosphogermanate layer onto the structure. The recipe and consolidation process followed was exactly the same as used in the devices used previously in 1.3. To understand how the deposited glass had adhered to the silica the device was diced in half and one half lapped and polished with the assistance of another member of the group, Miranda Turvey, to prepare a cross section facet for SEM analysis.

The facet was inspected with the SEM. The back scatter detector (BSD) on the SEM was found to give excellent distinction between layers. One edge of the facet of the pillar structure is shown in Figure 126.

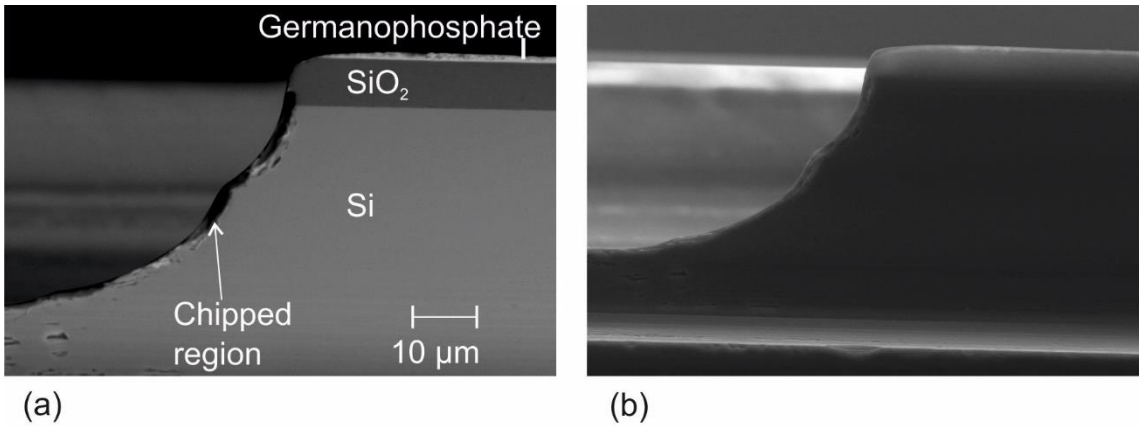

Figure 126. (a) BSD detector image of phosphogermanate deposited onto silica pillar (b) Secondary electron image from same area.

As the BSD intensity is strongly dependent on atomic number, the three materials present in the structure can be seen. The dependence on intensity with atomic number is only reliable when the surface is flat so chipping will give a false colour. This can be seen in a region near the edge which underwent chipping during the lapping and polishing. That this region corresponds to chipping and not a different material can be seen by comparing it with the SE image which shows surface features in the same area. Due to this it was decided that FHD deposited glass would be more likely to bead into a resonator shape if deposited on a structure with an undercut lip.

7.3.1 HNA etch

To create a lip the silicon under the silica must be etched away without etching the silica layer. One of the common etches used in the optical cleanroom is potassium hydroxide, as used in Chapter 4. This etch is anisotropic which makes it unsuitable for circular structures as there will be 4 points aligned to the silicon wafer crystalline axis where very little etching occurs. HNA etch consists of hydrofluoric acid, nitric acid and acetic acid and is capable of etching silicon. The etch selectivity to silica is not very high so etching of the silica layer would also occur. The half pillar previously used for the facet analysis was etched in HNA solution for 9 minutes at room temperature.

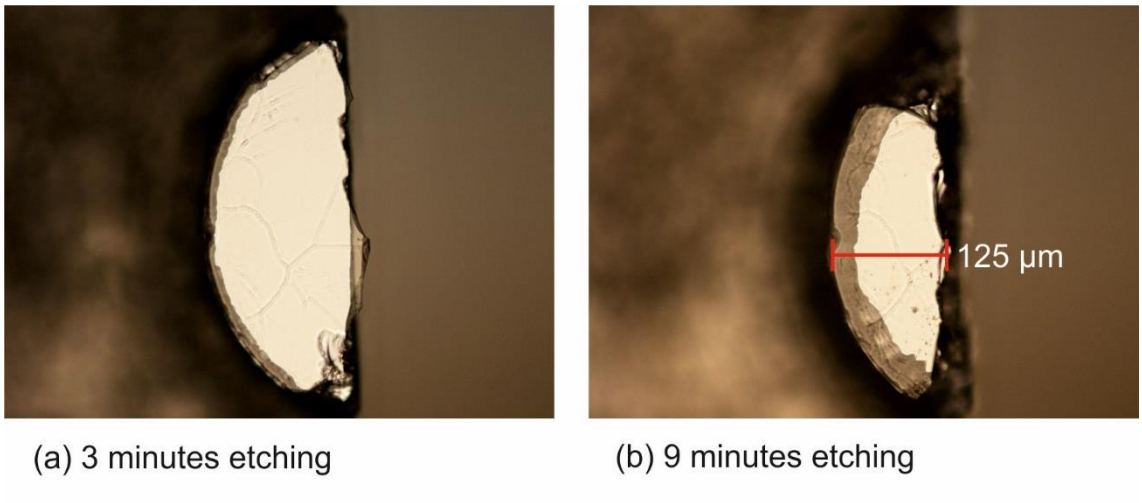

Figure 127. Germanophosphate on thick thick thermal silicon oxide on silicon during HNA etch.

It can be seen that although the etch has resulted in lip forming it has also caused cracks in the layer and has not left a lip of uniform width. Chips were also visible and for these reasons this approach was not continued.

7.4 Germanium oxide on silica

From the previous work it was decided to continue the research to form a resonator in a material that could be under etched with a selective etch. Silicon is known to have a variety of selective etch options compared to glass and so a material that could be grown on a bare silicon was sought. A thermally grown oxide was an option but would be difficult to flame polish as it has a higher melting point than that of silicon (~1400 °C). At this time other members of the group were experimenting with depositing the first germanium dioxide layers using an FHD process. This material was selected as it would be new material for optical whispering gallery devices.

7.4.1 Milling

The same PCD tool used previously was again used to mill the ring shape through the germania layer. The parameters used are shown in Table 12.

Table 12. Machining parameters chosen for whispering gallery.

Tool	PCD Diamond SX-850
Spindle speed	7 krpm
Translation speed	0.01 mm/min
Cut depth	15 µm

A microscope image part of the ring is shown in Figure 128.

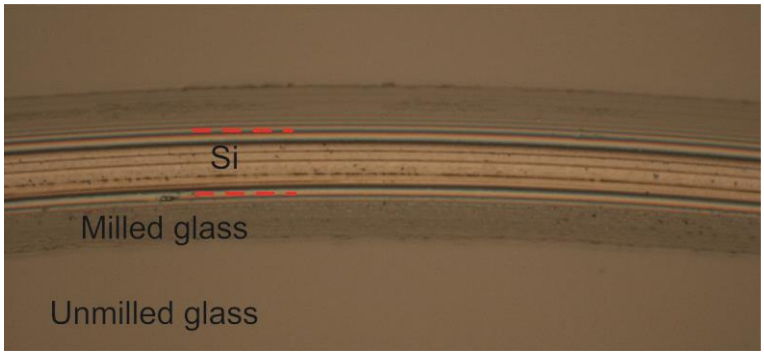

Figure 128. x50 microscope image of milled ring.

It can be seen that the inner surface of the disc is rougher than the rest of the substrate. The surface is consistent and large scale chips are not present.

7.4.2 Thermal reflow

As the milled surface was rough it was attempted to reflow the glass layer to see if a better quality surface could be produced. For a more repeatable and clean process it was decided to use a furnace reanneal to reflow the whole GeO_2 layer in a cleanroom environment. A furnace used for FHD consolidation was used as it was capable of reaching the required temperatures and allows a variety of purge gases. Due to surface tension it was expected that this would lead to a wedged cross section with a shallow wedge angle. As the furnace run would result in taking the chip to 1360 °C for 4 hours this would result in considerable thermal oxide growth on the silicon if done in the presence of oxygen. The furnace was first run with just a helium purge in an effort to avoid thermal oxide growth. The result of this was an obviously poor germania layer. This may have been caused by germanium monoxide leaving the surface as gas. The process was rerun with the oxygen purge present. Optical microscope images of the disk edge before and after thermal reflow are shown in Figure 129.

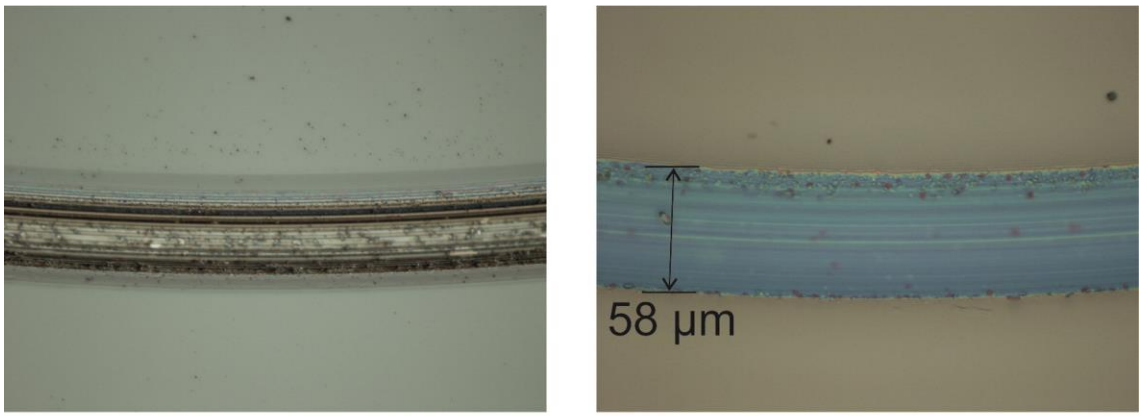

(a) Before furnace anneal (b) After furnace anneal

Figure 129. Sample of reflowed edge. The light blue colour on the silicon is indicative of the thermal oxide that has been grown during the furnace run.

It was estimated from growth rates for silica that approximately 750 nm of thermal oxide had been grown. Rough spots were visible on the silicon however the silica edge looked clean. Figure 130 shows the edge once the thermal oxide had been removed. On the inner cut face, where the silicon meets the silica it is believed that thermal growth may cause stress in the germania layer. This is a probable cause of the chips which become observable after the furnace anneal.

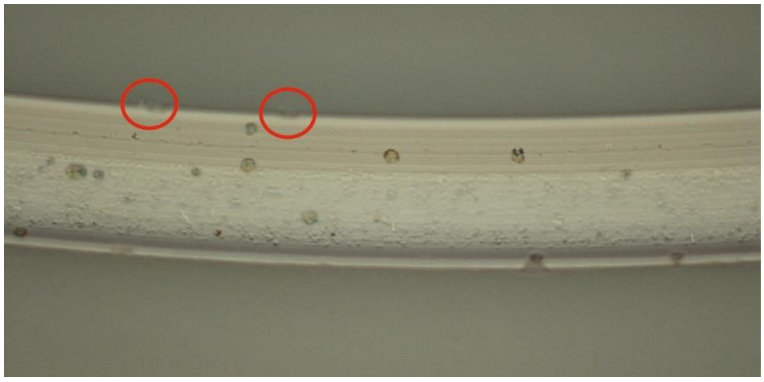

Figure 130. Edge following HF etch to remove unwanted thermal oxide. Circles show chipping.

7.4.3 Dicing for better access

As the whispering galleries are located on the chip it is necessary to find a way of coupling to the whispering gallery at a single point. Tapered fibre were fabricated by a member of the Optical Microfibre group in the ORC, Imran Khudus. The microfibre has a taper thickness 1.5 µm over a length of 5mm. Tapered fibres with a bend are possible to fabricate but it was found that greater stability to vibration was achieved with a straight fibre under tension. It was decided to cut away the edge of the whispering gallery to allow the fibre to be brought next to the ring. This is achieved by using the dicing saw and making the cuts as in Figure 131.

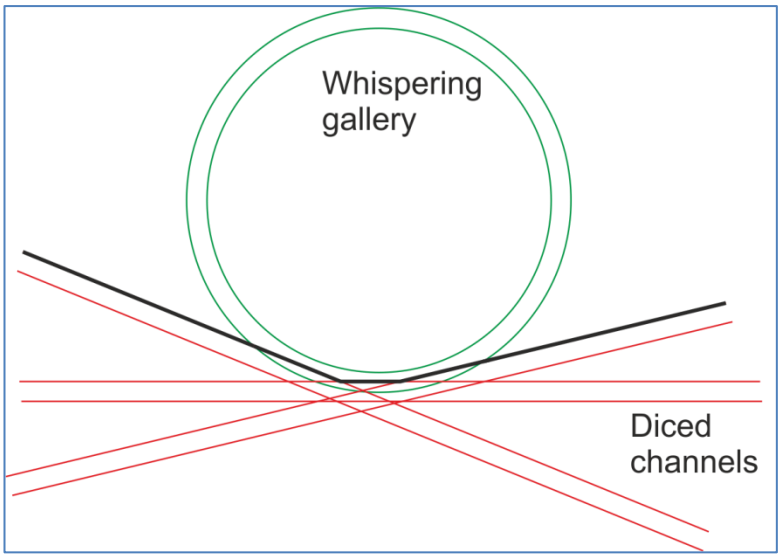

Figure 131. Diced grooves (red) to allow access to the whispering gallery resonator (green) Final edge shape after dicing (black).

This enables the tapered fibre to be positioned close to the whispering gallery edge without touching the substrate.

7.4.4 XeF_2 etch

As previous attempts at wet isotropic etching of silicon had not proved satisfactory another tool for selective etching was sought. The cleanroom contained a Xantix xenon difluoride (XeF_2) etcher. XeF_2 is one of the most selective silicon etchants known making it ideal for this situation where minimal etching of the silica was required. Prior to the etch a 30s HF acid dip is performed to remove native oxide growth which can be enough to hinder the etch. The etching details are shown in Table 13.

# of cycles	6
XeF2 pressure	2.4 Torr
Cycle time	30 s

Table 13. Etch parameters for XeF_2 etch.

The microscope image of the device after etching is shown in Figure 132. The undercut region is clearly visible due to its lower reflectivity. The undercut depth of almost 30 µm required only 3 minutes of total etch time due to the fast etch rate.

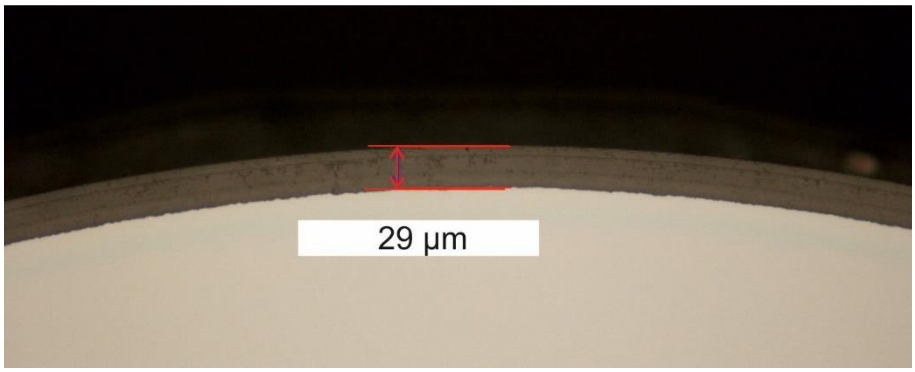

Figure 132. Following XeF2 etch the overhanging GeO_2 lip is visible.

The lip remained intact following the etching despite having a high aspect ratio; 3 µm thick and 30 µm long.

7.5 Characterization

7.5.1 Tapered fibre

Tapered fibre coupling into the resonator was attempted with the same setup as before. An Agilent tuneable laser (81950A) was used. A microscope was used to control the position of the fibre taper relative to the resonator. The spectrum was recorded using a wavelength sweep with the fibre close to the disc. This is shown in red in Figure 133 and can be compared to the transmission through the tapered fibre shown in green.

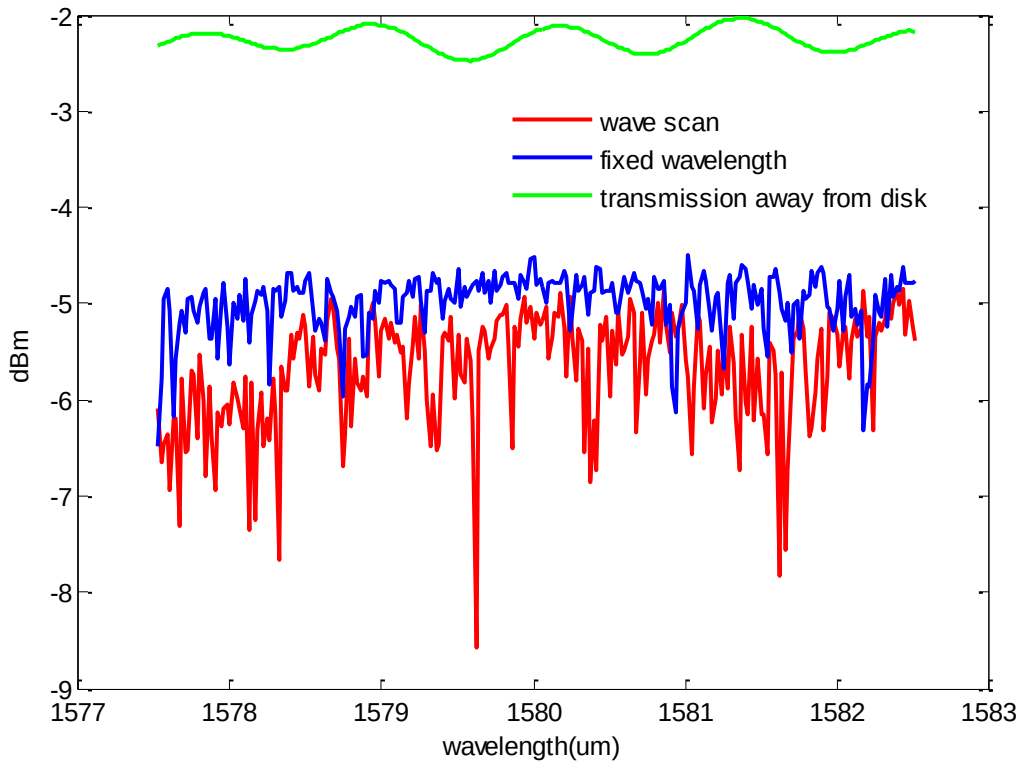

Figure 133. Spectrum of germanium oxide whispering gallery device. The resonances are too small to distinguish the mode.

The recorded scan contained peaks and troughs but the position of these was not repeatable after multiple scans. To better understand this, the program was rerun without stepping in wavelength but logging data at the same time interval of 1 s. This data appeared similar to the wavelength sweep suggesting the features seen in the wavelength sweep were not due to resonance. To understand this better the FFT spectra were taken and are shown in Figure 134.

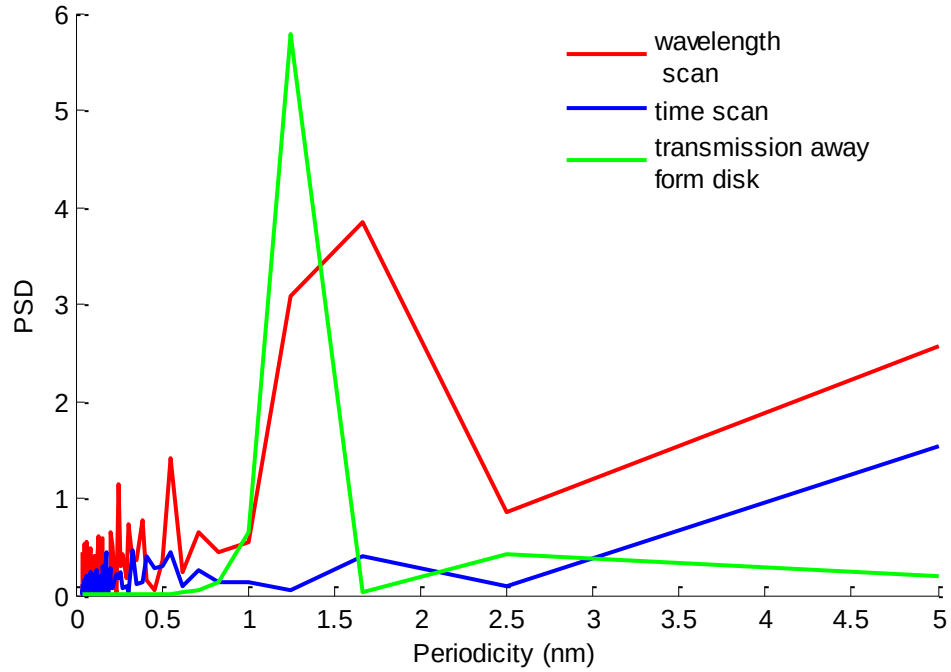

Figure 134. FFT of spectra.

The 1.25 nm period in the transmission data when the fibre is far from the ring is visible and this is believed to be due to a short cavity somewhere in the measurement setup. As the free spectral range is expected to be 0.17 nm a zoomed in portion from the high spatial frequencies is shown.

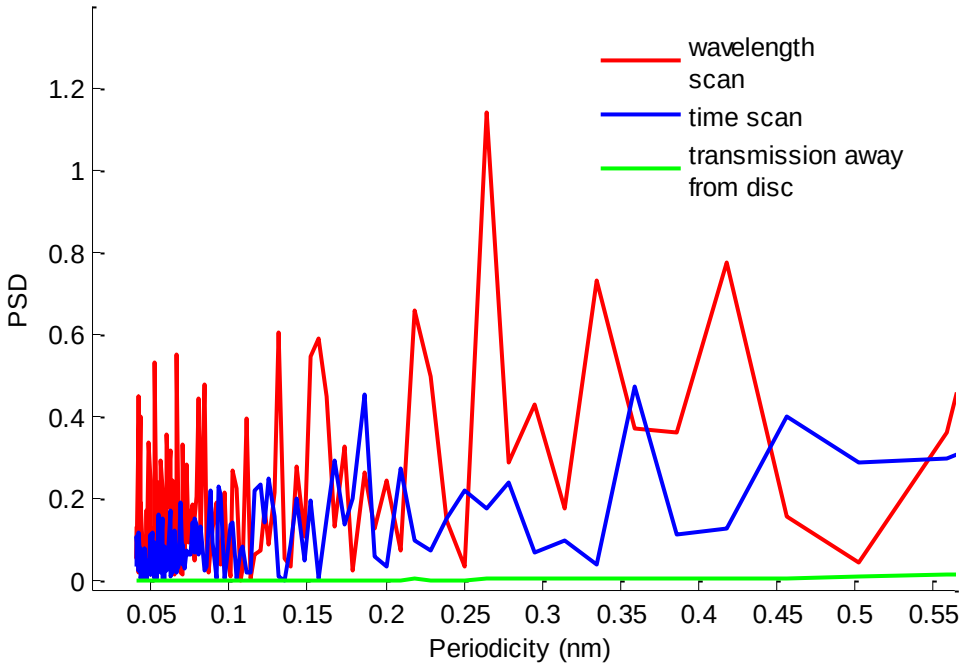

Figure 135. FFT data from higher spectral frequencies.

There is a period at 0.15 nm, however it is difficult to conclusively verify this is from resonance in the ring as other peaks have a similar PDS. The data from the fibre being close to the ring has

higher power in distinct wavelengths. The time scan at a single wavelength also has more power in certain wavelengths than the transmission meaning it is difficult to conclude that resonance is the primary reason for the peaks seen. Vibration of the tapered fibre is a possible explanation for the oscillations but as the fibre appeared to be held to the disc by Van der Waals forces it was unlikely to have this effect.

7.5.2 Commercial silica sphere

To test the tapered fibre coupling a 1 mm diameter polished silica sphere was purchased. With the specifications of the ball it was guaranteed to act as resonator providing a good test whether the coupling arrangement was working.

A periodic structure can be seen in the data. When the Fast Fourier Transform (FFT) of the data is taken it allows better visualization of the various periodic data. This data is first windowed using a Hamming function to reduce artefacts in the FFT from the finite data range. The tapered fibre was moved towards the sphere until contact was made. Van der Waals forces held the tapered fibre stationery against the sphere reducing vibration.

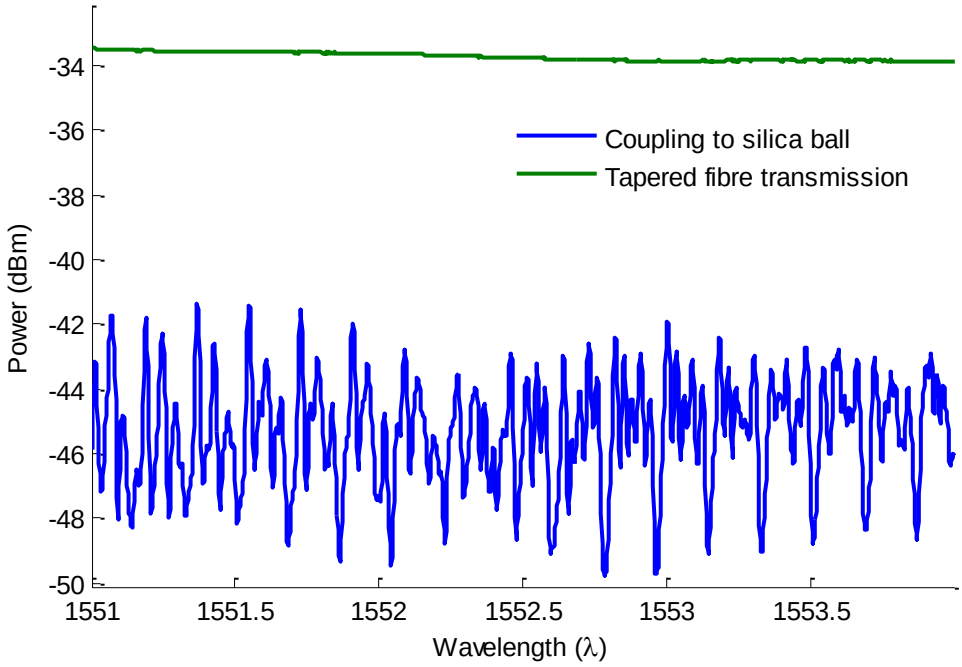

Figure 136. Green: Spectrum measured through tapered fibre when far from ball. Blue: Spectrum through tapered fibre when in contact with ball.

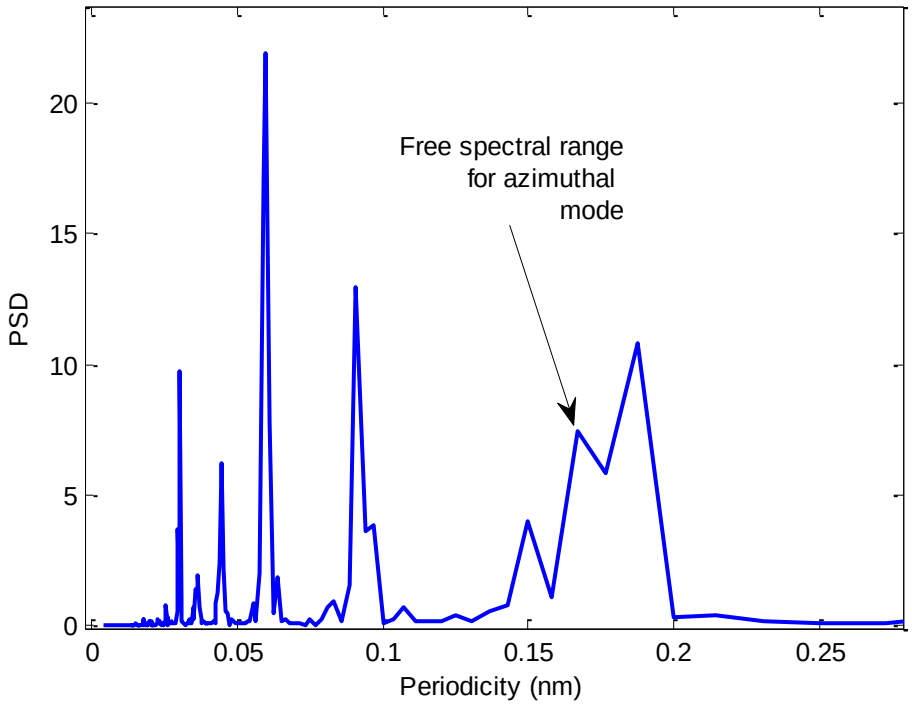

Figure 137. FFT of spectrum showing expected resonance peak. Power spectral density (PSD) is plotted on the y-axis.

The free spectral range for modes travelling around the azimuth of the sphere is 0.18 nm and this shows good agreement with a peak in the FFT data. This test shows that our method of optical measurement would likely have generated resonator fringes. Unfortunately this means the device still had too much chipping and other defects to be operational.

7.6 Germanium oxide on silica: Second device

7.6.1 Flame polishing

It is believed the difficulty of getting resonance in the previous structure was related to loss caused by defects introduced in the furnace anneal stage. For this reason it was decided to look for other options which would make this step unnecessary. Flame polishing is another thermal reflow process which involves exposing the glass to a hot enough flame. As there is not enough time for the whole substrate to reach thermal equilibrium parts of the substrate with higher thermal isolation will become hotter. Equipment used for fibre optic preform flame polishing was adapted to flame polish the chip. This was done in a cleanroom environment which reduced the level of atmospheric particles compared to the previous flame polishing work which was done in an unregulated environment. Figure 138 shows a photograph of the flame polishing.

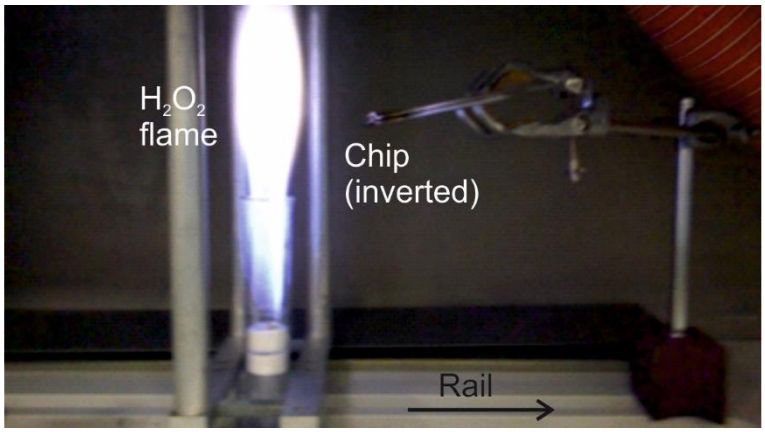

Figure 138. Diagram of OVD setup.

The OVD system has CNC control of the burner carriage. This was translated under the chip (which was mounted repeatedly) at a constant speed. The oxygen flow to the flame was kept high to ensure the reaction was oxygen saturated. Hydrogen flow rates to the torch were increased gradually. At low temperatures no change in the edge shape was seen. Once the H_2 flow rate was increased to 26 l/min a ripple effect was noticed in the glass layer.

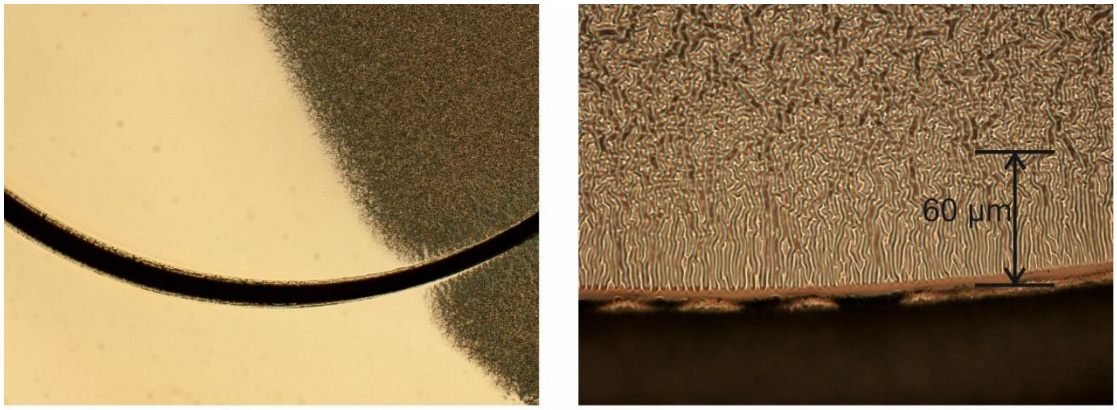

Figure 139. Ripple effect in glass layer.

It was initially expected that this is a phase separation effect producing regions with different germanium composition. The surface features initially form at right angles to the resonator edge and after a length of approximately 60 µm become random in orientation. To confirm whether ripple features were marked by surface deviations as opposed to refractive index changes the profiler was used to scan across the surface across the boundary between the distinct regions and the trace is shown in Figure 140.

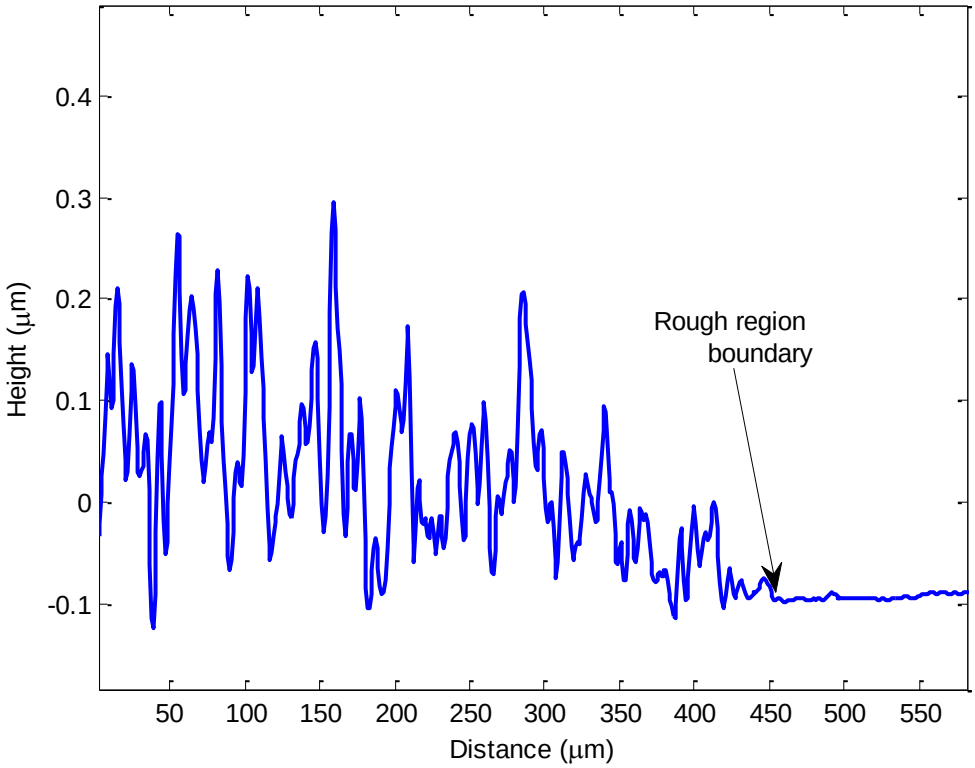

Figure 140. Profiler data from rippled surface.

The height of the ripples is found to be around 0.2 µm. It was found that by increasing the H_2 flow rate to 32 l/min this effect could be removed and the glass layer went back to being homogenous when viewed by the optical microscope.

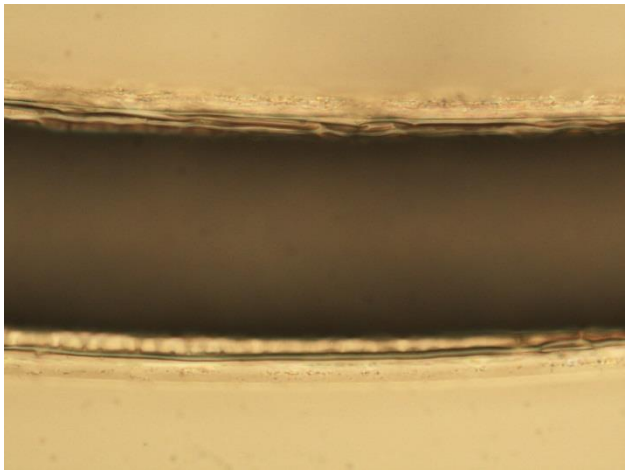

Figure 141. Edge following further flame polishing.

The edge quality following flame polishing was not very uniform. The SEM was used to get a better image of edge.

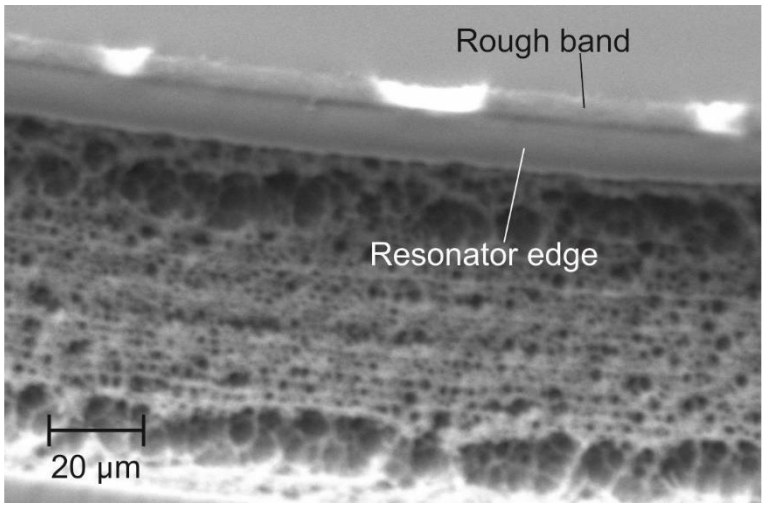

Figure 142. Edge viewed under SEM.

It can be seen that the direct edge is smooth but there is a band of rougher surface further back. The silicon substrate was also beginning to bow at the temperatures reached during this exposure. For this reason it was decided not to procede with flame polishing for thermal treatment.

7.6.2 Milling process development

Due to the defects present with the thermally treated structures it was decided to see whether directly machined structures would be capable of working as resonators. If possible this would reduce the number of processing steps required. Machining of resonators can also give more control of geometry as the cutter shape can be controlled. Previous cuts had shown a correlation between depth of cut and surface quality and so this was investigated by looking at two cuts of different depths. The depth of cut must be enough to reach the silicon but may be deeper. Programmed depths of 10 µm for cut A and 20 µm for cut B were tested and the resultant surfaces shown in Figure 143.

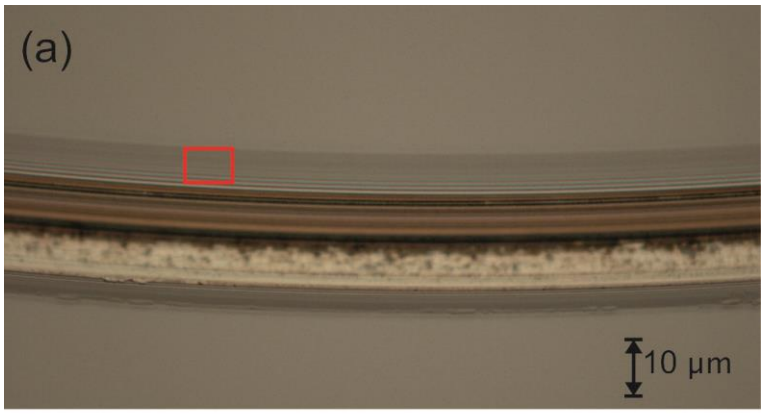

(a) 10 µm programmed deep cut

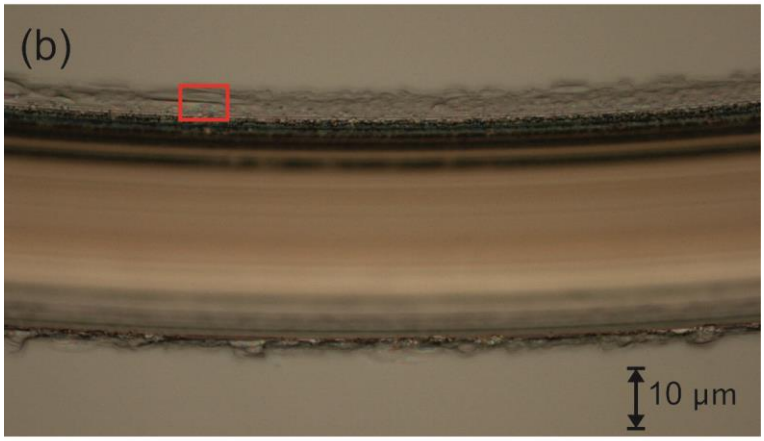

(b) 20 µm programmed deep cut

Figure 143. The feedrate was 0.01 mm/min and a spindle speed of 7 krpm was used which were previously found to be effective. Red squares show where the surface roughness was evaluated.

Note that the inner surface is smoother than the outer surface. This is possibly due to the angle of the cutting surface giving different machining pressures. As the outer surface does not form part of the whispering gallery chipping and roughness can be tolerated in this area.

Another factor which was found to improve the cutting was regular redressing using the WEDG system. When a tool had not been dressed for a while cutting performance suffered. After the dressing fresh diamond particles in the PCD material are exposed and the sharper cutting elements aid cutting.

The surface roughness of the edge of the resonator plays an important role in determining the Q factor of the device. Measuring this can be difficult with thin films due to ‘cross talk’ between the interfaces. To enable a measurement of the top surface, the chip was coated with a 10 µm gold layer which could later be removed with a gold etch. This made the surface close to 100% reflective. Figure 144 shows the a 3d Zescope measurement of the surface.

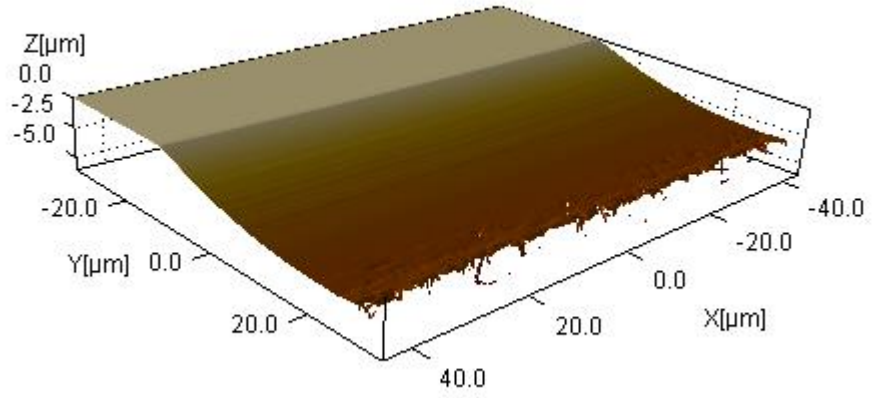

Figure 144. Zescope image of shallow ring edge.

The surface roughness for the machined area was Sa 4.9 nm and Sq 5.9 nm. This is compared to the roughness of Sa 0.28 nm and Sq 0.33 for the unmachined resonator top surface. This low level of surface impairment indicates that ductile regime machining is occurring. From the image it can be seen that the predominant texture is of lines concentric to the ring.

The Zescope is also used to measure the form of the groove and angles of the inner and outer surface. The angle of the inner surface was found to be 5.3° and that of the outer 12.4°. Since these surfaces experience the same cutting conditions it could be that a shallower cut angle allows greater pressure on the machined surface. The true depth of ring A was 6 µm which was lower than the programmed depth of 10 µm. Ring B was measured to be 10 µm when the programmed value was 20 µm. Undercutting was a consistent feature with this type of structure and is believed to be due to insufficient loop stiffness in the mill system. The most likely source of this is the z axis as it was operating near to the stage lift capacity. It is possible this slack in the system may improve the surface roughness generated by allowing a constant pressure to be exerted on the workpiece at the expense of precise depth control.

The deeper machined ring was also characterized by the Zescope and the edge image is shown in Figure 145. It can be seen there are regions of brittle machining and surface roughness of Sa 82 and Sq 117 nm confirm this.

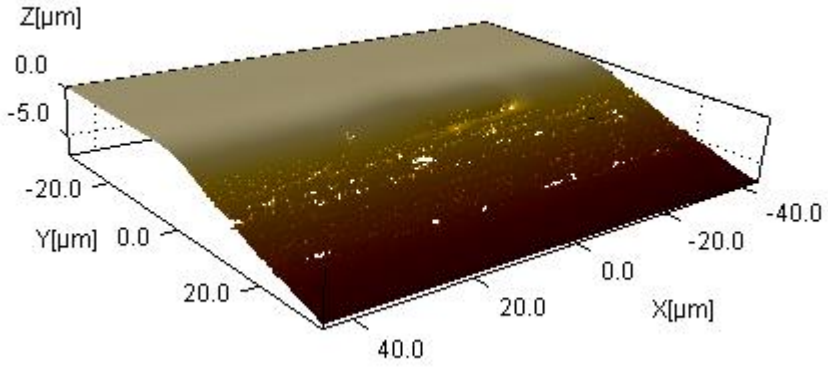

Figure 145. Zescope image of deep ring edge edge.

As described previously this device was under etched using the XeF2 etcher using the same parameters as in section 1.5. Figure 146 shows a microscope image of the etched device

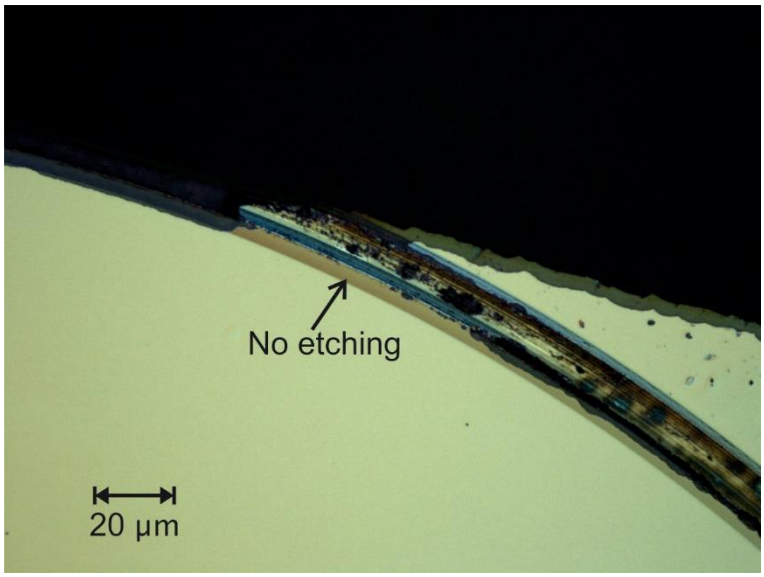

Figure 146. x50 microscope image of resonator edge following XeF_2 underetch.

During this run the silicon did not etch uniformly and there are areas seen which have not etched at all. It is possible that the chip was not dry enough prior to the etch. The area of unetched silicon draws out the light from the ring and prevents guidance occurring so it was not possible to test for resonance with this structure. Due to time constraints, the work on whispering galleries had to be finished at this stage.

7.7 Summary

The fabrication of structures with geometries appropriate for the creation of whispering gallery devices has been demonstrated. Using PCD tools, micro disc structures have been demonstrated

in phosphogermanate on thick silicon dioxide and in germanium oxide on silicon. Heat treatment processes including hydrogen flame polishing and furnace annealing have been tested and shown to be capable of reflowing the glass layer. Milling in the ductile regime has been shown to be able to give smooth surface of Sa 4.9 nm indicating ductile regime machining was occurring. Defects caused by milling and thermal treatment meant that resonance could not be sustained in the devices. XeF_2 was used to undercut the germanium oxide layer without damaging the glass layer.

7.8 References

[1] V. Ilchenko, A. Savchenkov, A. Matsko, and L. Maleki, "Nonlinear Optics and Crystalline Whispering Gallery Mode Cavities," *Phys. Rev. Lett.*, vol. 92, no. 4, p. 043903, Jan. 2004.

[2] M. Vaughan, *The Fabry-Perot Interferometer: History, Theory, Practice and Applications*. CRC Press, 1989.

[3] D. G. Rabus, *Integrated Ring Resonators: The Compendium*. Springer, 2007.

[4] E. Hecht, *Optics*. San Francisco: Addison Wesley, 2002.

[5] F. Träger, *Springer Handbook of Lasers and Optics*. Springer Science & Business Media, 2012.

[6] V. S. Ilchenko, A. A. Savchenkov, A. B. Matsko, and L. Maleki, "Dispersion compensation in whispering-gallery modes," *J. Opt. Soc. Am. A*, vol. 20, no. 1, pp. 157-162, Jan. 2003.

[7] I. S. Grudinin and N. Yu, "Dispersion engineering of crystalline resonators via microstructuring," *Optica*, vol. 2, no. 3, pp. 221-224, Mar. 2015.

[8] A. B. Matsko, *Practical Applications of Microresonators in Optics and Photonics*. CRC Press, 2009.

[9] K. Vahala, *Optical Microcavities*. World Scientific, 2004.

[10] M. Bukshtab, *Applied Photometry, Radiometry, and Measurements of Optical Losses*. Springer Science & Business Media, 2012.

[11] X. Fan, *Advanced Photonic Structures for Biological and Chemical Detection*. Springer Science & Business Media, 2009.

[12] K. Yallup and K. Iniewski, *Technologies for Smart Sensors and Sensor Fusion*. CRC Press, 2014.

[13] I. S. Grudinin, V. S. Ilchenko, and L. Maleki, “Ultrahigh optical Q factors of crystalline resonators in the linear regime,” *Phys. Rev. A*, vol. 74, no. 6, p. 063806, Dec. 2006.

[14] J. B. Snow, S.-X. Qian, and R. K. Chang, “Stimulated Raman scattering from individual water and ethanol droplets at morphology-dependent resonances,” *Opt Lett*, vol. 10, no. 1, pp. 37-39, Jan. 1985.

[15] D. K. Armani, T. J. Kippenberg, S. M. Spillane, and K. J. Vahala, “Ultra-high-Q toroid microcavity on a chip.,” *Nature*, vol. 421, no. 6926, pp. 925–8, Feb. 2003.

[16] C. Wang, M. J. Burek, Z. Lin, H. A. Atikian, V. Venkataraman, I.-C. Huang, P. Stark, and M. Lončar, “Integrated high quality factor lithium niobate microdisk resonators,” *Opt Express*, vol. 22, no. 25, p. 30924, Dec. 2014.

[17] I. S. Grudinin, “Crystalline Whispering Gallery Mode Resonators for Quantum and Nonlinear Optics,” California Institute of Technology, 2008.

[18] D. W. Vernooy, A. Furusawa, N. P. Georgiades, V. S. Ilchenko, and H. J. Kimble, “Cavity QED with high- Q whispering gallery modes,” *Phys. Rev. A*, vol. 57, no. 4, pp. R2293–R2296, Apr. 1998.

[19] A. A. Savchenkov, V. S. Ilchenko, A. B. Matsko, and L. Maleki, “Tunable filter based on whispering gallery modes,” *Electron. Lett.*, vol. 39, no. 4, p. 389, Feb. 2003.

[20] A. Yariv, “Coupled-mode theory for guided-wave optics,” *IEEE J. Quantum Electron.*, vol. 9, no. 9, pp. 919–933, Sep. 1973.

[21] Murata, *Handbook of Optical Fibers and Cables*, 2nd Ed. CRC Press, 1996.

Chapter 8: Conclusion and future work

8.1 Summary

The core aims of this project were to explore the application of physical machining to make optical prototypes of devices that would be difficult to fabricate by currently available methods. The key results of the work have been:

- Micromilling was used to fabricate a tuneable Bragg grating with a factor of 90 better tuning efficiency than a bulk chip device.
- A novel dual cantilever device was fabricated using dicing which can act as a sensor or actuator. The device was characterized and compared to a theoretical model.
- Wire electro discharge machining of polycrystalline diamond was investigated and used to fabricated 50 μm diameter small tools, centreless small tools and a ring tool.
- The ring tool was used to demonstrate ductile machining of a structure with application in optical ring resonators.

In future, the potential that physical machining has to offer could extend the fabrication toolbox for integrated optics. This could be achieved by both improvements in equipment and also in processing knowledge. Machine tools with hydraulic linear bearings would have higher loop stiffness which would improve the cutting performance and reduce roughness. In addition acoustic monitoring of the cutting would allow greater information to be extracted about the cutting process. The group has recently purchased a new Disco DAD322 dicing machining and is in the process of tendering for an improved milling machine. More accurate machines mean that processing knowledge will be easier to acquire and more reliable. Ultimately we aim to get to a situation where physical machining is repeatable and dependable and so it can be used as a fabrication tool by a researcher or operator not requiring specialist knowledge.

8.2 MOEM devices using physical machining

8.2.1 Tuneable Bragg grating microbeam device

In Chapter 4 a silica-on-silicon device that allows tuning of a Gaussian apodized Bragg grating has been demonstrated. Tuning efficiency is enhanced by incorporating the Bragg grating into a microbeam which gives greater thermal isolation and acts as a smaller thermal mass. A tuning efficiency of 45 pm/mW for the TM mode and 39 pm/mW for the TE mode has been achieved

which is a factor of 90 better than for a comparable bulk silica device. The device could find applications where highly efficient tuning and low thermal cross-talk is required. So far, tuning has been shown over a range of 0.4 nm corresponding to 50 GHz which is appropriate for telecomm dense wavelength division multiplexing (DWDM) applications. The 1.5 mm long microbeam buckled following the etch release step.

8.2.2 Microbeam devices: future work

In future, the device has the potential to create a bistable switch that would not require continuous power supply to tune between two states. The device described had a suitable geometry for 1 mm Bragg grating however some devices may require longer Bragg gratings [25]. The maximum length of microbeam that could be fabricated without breaking was found to be around 2 mm. If longer microbeams are required it may be necessary to produce structures with anchor points along the length. A Microbeam array might be another useful structure. Using a plunge cut mode with the dicing saw this structure has been been demonstrated without optical elements. Table 14 shows the machine parameters for the plunge cuts.

Spindle speed	20
Feed rate	0.01
Depth of cut	80 µm
Blade	90 µm nickel bonded

Table 14. Plunge cut parameters.

Plunge cutting is a much faster technique than milling with the only disadvantage of having unavoidable cut regions either end of the microbeam. Figure 147 shows an SEM of the microbeam array. Figure 147 shows an SEM image of the microbeam array.

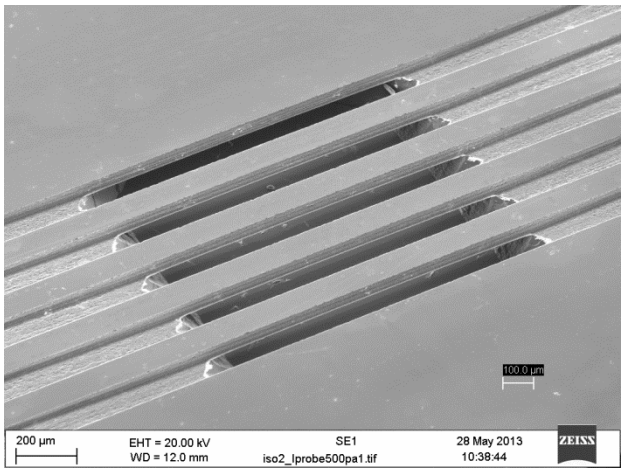

Figure 147. Microbeams produced using plunge cut mode.

One future application of this technology, would be if multiple microbeams have different widths, which would result in a range of structure with different resonant frequencies which could be used in resonant frequency based sensing. If devices could be made close to the buckling length it may be possible to actuate the buckling using heat. In this case a large jump in tuning could be gained for a small amount of power. If there is hysteresis then the device could stay in this state when the power is stopped giving a bistable switch. The difficulty in accurately fabricating the correct length means some another method of changing the stress such as mechanically may be required to trim the microbeam closer to the buckling point.

8.2.3 Dual cantilever device

The dual cantilever device contained an array of four dual-cantilevers, demonstrating potential for creating parallel arrays for switching or sensing applications. The signals from these arrays could be wavelength multiplexed with the use of Bragg gratings. The devices are shown to operate in a mode suitable for a displacement sensor or with the addition of an actuator, such as a piezo-electric, a MOEMS variable attenuator. By investigating the response of the device to actuation with an optical fibre we have shown that the mechanical-optical behavior of the device is well described by conventional fibre optic angular misalignment coupling theory.Each cantilever contained nine discrete Bragg gratings, so the overall device incorporates many integrated elements on a single chip. These devices offer potential for use in switching, optical attenuators, and optical trapping. Their greater stiffness makes them attractive for use in harsh environments, and they may be embedded in composite materials where the higher required actuation forces are readily achievable. Furthermore, as they are waveguide devices they avoid the alignment issues inherent in free space measured structures.

8.3 WEDG machining for optical structures

Wire electro discharge machining (WEDG) was reported in Chapter 6 as a method of fabricating novel tool geometries from polycrystalline diamond (PCD). A 50 µm tool was fabricated and used to demonstrate milling in FHD silica. A centreless tool was also fabricated to eliminate the problem of differential mill wear and used to create a D-shaped optical fibre with surface roughness of Sa 17 nm. A ring tool was fabricated using a combination of wire and straight electrodes.

This tool was used to demonstrate microdisc structures. As reported in Chapter 7 (7.2) phosphogermanate on a thick silica layer was the first material investigated for a whispering gallery device. This material was easily compatible with a flame polishing process to generate extremely smooth resonator edges, however it was not possible to find a selective etch to remove the underlying silica. With the angle of the sidewalls following flame polishing it was not possible to sustain modes in this device. The second approach described in section 7.3 was to use a starting substrate of germanium dioxide on silicon. By using physical machining and XeF_2 undercutting a resonator shape with a 3 µm lip was formed. This is the required geometry for a whispering gallery structure that can be readily coupled with a tapered fibre for light input and collection. Thermal treatment in a furnace was shown to be a repeatable and batch compatible method of improving the surface roughness following machining. It is believed defects were caused by the growth of thermal oxide during the thermal reanneal process and the nature and number of these meant it was not possible to sustain a mode in the device. Ductile mode machining was achieved in this material over the bulk of the cut surface suggesting it as a possible route to directly machined resonators. A tapered fibre coupling system was designed and validated by coupling to a commercially sourced 3 mm fused silica ball.

This next section describes some work in new resonator devices which has been started but not completed by the time the PhD finished.

8.3.1 Thinned lithium niobate

Recent work by the group had led to thinned lithium niobate on silicon being available. The lithium niobate is mechanically thinned using lapping and polishing processes from a single crystal wafer and thus has the high purity properties associated with the bulk material. Material is also available periodically poled. This material requires deeper cut depths that make physical machining with its high removal rates an attractive technique.

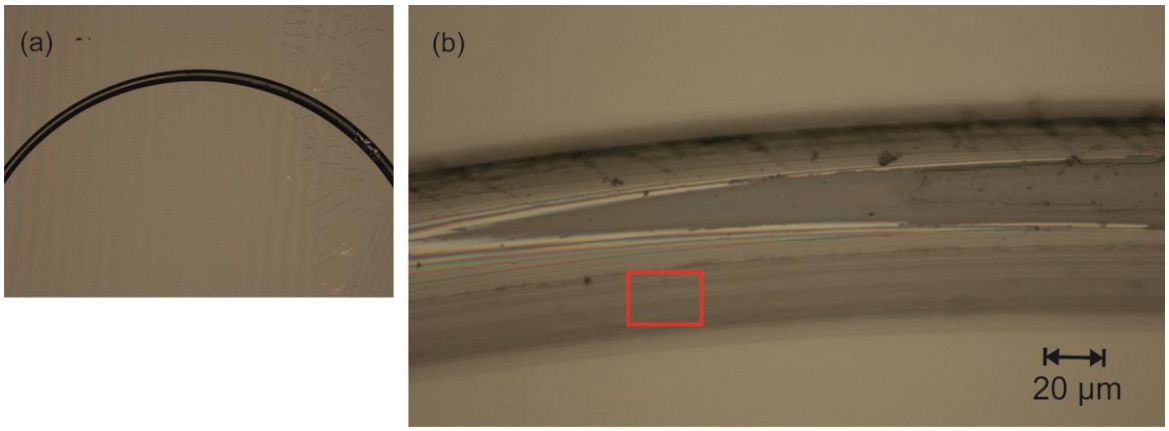

Figure 148. (a) Lithium niobate ring following machining. (b) Higher magnification image of same structure. Area measured for surface roughness is shown in the red box.

Following machining the surface roughness of the inner surface was measured with the Zescope to be Sa 29 nm. To improve this a manual polishing step was done using colloidal silica polishing solution. A cotton bud was used to polish around the machined area for 5 minutes. The edge after polishing is shown in Figure 149.

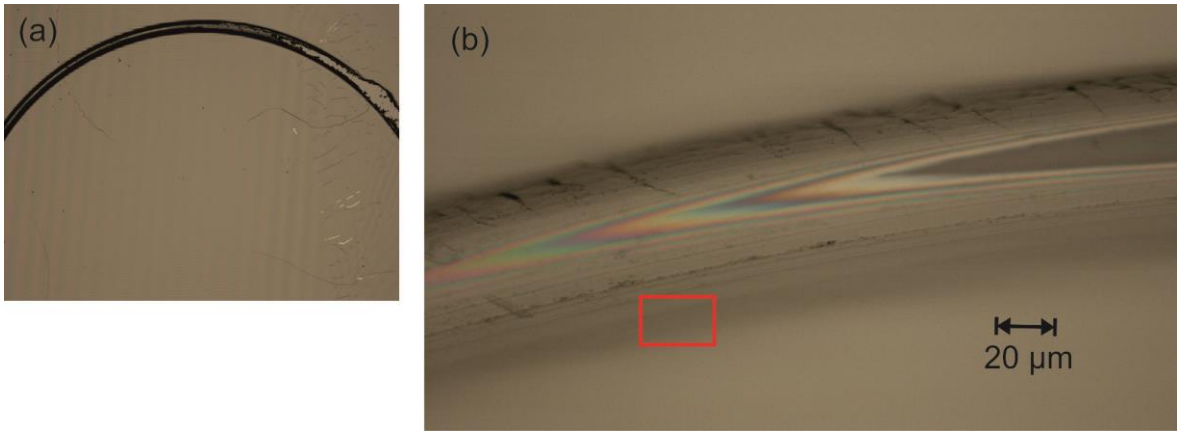

Figure 149. $LiNO_3$ ring following polishing. Area measured for surface roughness is shown in the red box.

The surface roughness of the same area after polishing was Sa 6.2 nm. This showed that the combination of machining and polishing could potentially be used to generate smooth resonators in lithium niobate. The next with this work would be to find an etch suitable for the epoxy, allowing for creation of layer waveguiding ring devices.

8.3.2 Damascene waveguide

Another type of resonator structure that has been initially explored in my work is named after the Damascene microprocessing technique first adopted for microelectronics [22]. Firstly a ring would be machined into a material. A higher index material would be then deposited and may overfill

the ring. A planarizing step would then be required to remove the overfill layer and this is often done through polishing.

One benefit of this method is that it could be easier to integrate the resonator with a coupling planar waveguide. If the damascene resonator is built into the core layer of the device then in principle a waveguide can be written close enough to give evanescent coupling. Figure 150 shows the fabrication steps that could be used to fabricate a Damascene resonator.

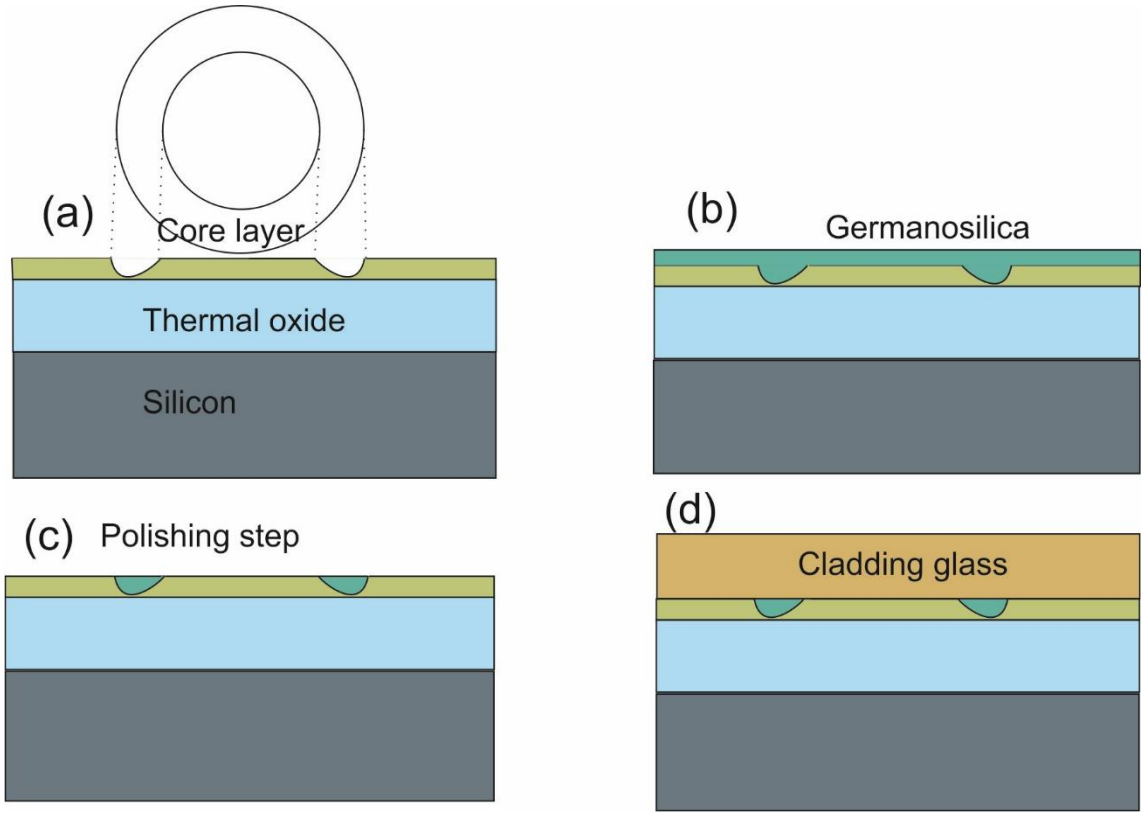

Figure 150. Diagram showing potential fabrications steps for Damscene resonator.

Attempts towards achieving the first step were undertaken. The starting substrate is a silicon wafer with a thermally grown oxide of 17 µm and a germanosilica core of 5 µm. The results of the milling are shown in Figure 151.

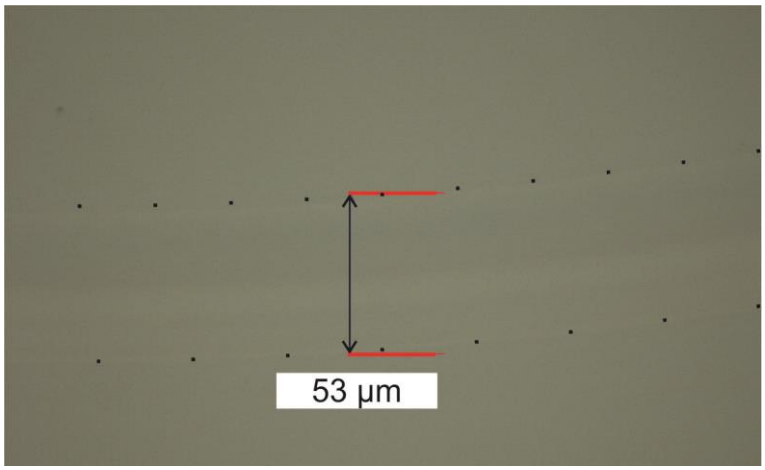

Figure 151. Microscope image of the milled structure. The black dots indicate the extent of the machined area which is difficult to see due to the smoothness of the cut

The surface roughness measured for this cut was Rs 5.7 nm. The cut surface is difficult to distinguish from the substrate which is an indicator of high smoothness. The depth of cut was measured using the Zescope and is shown in Figure 152.

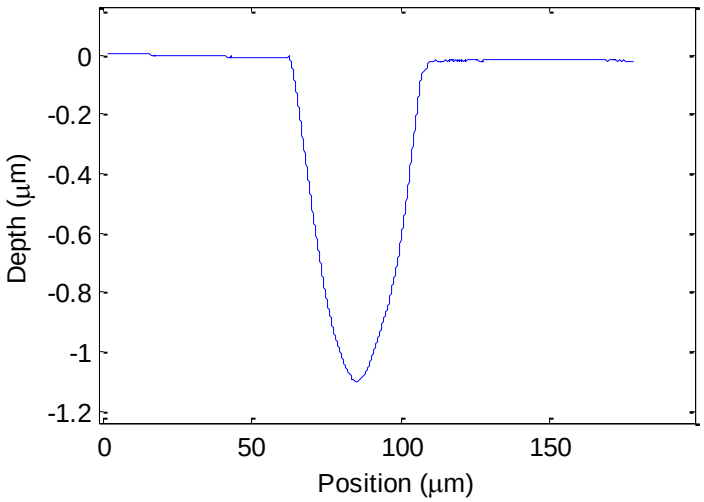

Figure 152. 2D profile from Zescope showing depth of cut.

The structure shows some tilt which is due to difficulty in ensuring that the tool is perpendicular over the full ring area.

The next stage in this work is to deposit a higher refractive index glass layer and then polish back the layer to leave glass only in the machined ring.

Appendix A Journal publications list

Journal Publications:

P.A. Cooper, L.G. Carpenter, C. Holmes, C. Sima, J.C. Gates, P.G.R. Smith

Power efficiency enhanced thermally tunable Bragg grating for silica-on-silicon photonics

IEEE Photonics Journal Vol 7 Issue 2. 2015

P.A. Cooper, L.G. Carpenter, P.L. Mennea, C. Holmes, J.C. Gates, P.G.R. Smith

Integrated optical dual-cantilever arrays in silica on silicon

Optics Express 2014 Vol.22(26) pp.31801–31813

L.G. Carpenter, **P.A. Cooper**, C. Holmes, C.B.E. Gawith, J.C. Gates, P.G.R. Smith

Nanoscale roughness micromilled silica evanescent refractometer

Optics Express 2015 Vol.23(2) pp.1005-1014

L.G. Carpenter, H.L. Rogers, **P.A. Cooper**, C. Holmes, J.C. Gates, P.G.R. Smith

Low optical-loss facet preparation for silica-on-silicon photonics using the ductile dicing regime

Journal of Physics D: Applied Physics 2013 Vol.46(47) pp.475103

Conference Publications:

P.A. Cooper, L.G. Carpenter, P.L. Mennea, C. Holmes, J.C. Gates, P.G.R. Smith

Optomechanical cantilever device for displacement sensing and variable attenuator

Photonics West 2014 San Francisco 1-6 Feb 2014

Appendix A

P.A. Cooper, C. Holmes, L. Carpenter, C. Sima, P. Mennea, J.C. Gates, P. Smith

Silica microbeams for tunable Bragg gratings

CLEO-Europe/IQEC 2013 Munich 12-16 May 2013

P.G.R.Smith, J.C.Gates, C.Holmes, C.B.E.Gawith, L.G.Carpenter, P.L.Mennea, M.T.Posner, **P.A.Cooper**, S.G.Lynch

Fabrication of silica-integrated waveguide circuits for quantum-enhanced sensing, quantum information processing, and number-resolving detection

SPIE Photonics West San Francisco 7-12 Feb 2015 (Invited)

L.G.Carpenter, **P.A.Cooper**, C.Holmes, C.B.E.Gawith, J.C.Gates, P.G.R.Smith

Micromilling with nanoscale roughness for silica photonics

SPIE Photonics West San Francisco 7-12 Feb 2015

L.G. Carpenter, C. Holmes, **P.A. Cooper**, J.C. Gates, P.G.R. Smith

Precision dicing of optical materials

SPIE Photonics West San Francisco 1-6 Feb 2014

J.C. Gates, S.G. Lynch, P.L. Mennea, **P.A. Cooper**, S. Ambran, H.L. Rogers, L.G. Carpenter, C. Sima, D.J. Wales, C. Holmes, P.G.R. Smith

UV written planar Bragg grating sensors - an overview of fabrication geometries and applications

Advanced Photonics 2013 Puerto Rico 14-17 Jul 2013 (Invited)

C. Holmes, L.G. Carpenter, **P.A. Cooper**, H.L. Rogers, J.C. Gates, P.G.R. Smith

Micro-mechanical integrated optical structures

European Conference on Integrated Optics (ECIO) Sitges Barcelona 18-20 Apr 2012

Appendix B Journal publication: Integrated optical dual-cantilever arrays in silica on silicon

Integrated optical dual-cantilever arrays in silica on silicon

Peter A. Cooper*, Lewis G. Carpenter, Paolo L. Mennea, Christopher Holmes, James C. Gates and Peter G.R. Smith

Optoelectronics Research Centre, University of Southampton, Highfield Campus, SO171BJ, UK

*pac1g11@soton.ac.uk

Abstract: A dual cantilever device has been demonstrated which can operate as a force sensor or variable attenuator. The device is fabricated using physical micromachining techniques that do not require cleanroom class facilities. The response of the device to mechanical actuation is measured, and shown to be well described by conventional fiber optic angular misalignment theory. The device has the potential to be utilized within integrated optical components for sensors or attenuators. An array of devices was fabricated with potential for parallel operation.

OCIS codes: (130.3120) Integrated optics devices; (220.1920) Diamond machining; (220.4000) Microstructure fabrication; (230.1480) Bragg reflectors; (120.4880) Optomechanics.

References and links

1. A. Boisen, S. Dohn, S. S. Keller, S. Schmid, and M. Tenje, "Cantilever-like micromechanical sensors," Rep. Prog. Phys. **74**, 036101 (2011).
2. E. Ollier, "Optical MEMS devices based on moving waveguides," IEEE J. Sel. Top. Quant **8.**, 155–162 (2002).
3. K. Park, J. Jang, D. Irimia, J. Sturgis, J. Lee, J. Robinson, M. Toner, and R. Bashir, ""Living cantilever arrays" for characterization of mass of single live cells in fluids.," Lab on Chip **8**, 1034–41 (2008).
4. T. Xu, M. Bachman, F-G. Zeng, and G-P. Li, "Polymeric micro-cantilever array for auditory front-end processing," Sens. Actuators. A Phys. **114**, 176–182 (2004).
5. K. Zinoviev, C. Dominguez, J. A. Plaza, V. J. C. Busto, and L. M. Lechuga, "A novel optical waveguide microcantilever sensor for the detection of nanomechanical forces," J. Lightwave Technol. **24**, 2132–2138 (2006).
6. L. G. Carpenter, C. Holmes, H. L. Rogers, P. G. R. Smith, and J. C. Gates, "Integrated optic glass microcantilevers with Bragg grating interrogation.," Opt. Express **18**, 23296–301 (2010).
7. B. Barber, C. R. Giles, V. Askyuk, R. Ruel, L. Stulz, and D. Bishop, "A fiber connectorized MEMS variable optical attenuator," IEEE Photon. Technol. L. **10**, 1262–1264 (1998).

8. J. E. Ford, J. A. Walker, D. S. Greywall, and K. W. Goossen, "Micromechanical fiber-optic attenuator with 3 μs response," J. Lightwave Technol. **16**, 1663–1670 (1998).
9. A. Constable, J. Kim, J. Mervis, F. Zarinetchi, and M. Prentiss, "Demonstration of a fiber-optical light-force trap," Opt. Lett. **18**, 1867 (1993).
10. B. J. Black and S. K. Mohanty, "Fiber-optic spanner," Opt. Lett. **37**, 5030–5032 (2012).
11. M. Succo, "An Integrated Optical-Waveguide Chip for Measurement of Cold-Atom Clouds," Ph.D. Thesis, Imperial College London (2011).
12. T. Brown, "Harsh military environments and microelectromechanical (MEMS) devices," Proceedings of IEEE **2,** Sensors, 2003. 753–760 (2003).
13. N. Courjal, B. Guichardaz, G. Ulliac, J-Y. Rauch, B. Sadani, H-H. Lu, and M-P. Bernal, "High aspect ratio lithium niobate ridge waveguides fabricated by optical grade dicing," J. Phys. D (Appl Phys) **44**, 305101 (2011).
14. Y. Jia, C. E. Rueter, S. Akhmadaliev, S. Zhou, F. Chen, and D. Kip, "Ridge waveguide lasers in Nd:YAG crystals produced by combining swift heavy ion irradiation and precise diamond blade dicing," Opt. Mater. Express **3**, 433–438 (2013).
15. L. G. Carpenter, H. L. Rogers, P. A. Cooper, C. Holmes, J. C. Gates, and P. G. R. Smith, "Low optical-loss facet preparation for silica-on-silicon photonics using the ductile dicing regime," J. Phys. D (Appl Phys) **46**, 475103 (2013).
16. G. D. Emmerson, S. P. Watts, C. B. E. Gawith, V. Albanis, M. Ibsen, R. B. Williams, and P. G. R. Smith, "Fabrication of directly UV-written channel waveguides with simultaneously defined integral Bragg gratings," Electron. Lett. **38**, 1531–1532 (2002).
17. R. M. Parker, "Optofluidic Bragg Grating Sensors For Chemical Detection," Ph.D. Thesis, University of Southampton (2010).
18. R. M. Parker, J. C. Gates, M. C. Grossel, and P. G. R. Smith, "A temperature-insensitive Bragg grating sensor-Using orthogonal polarisation modes for in situ temperature compensation," Sensor Actuat. B Chem. **145**, 428–432 (2010).
19. C. Holmes, L. G. Carpenter, H. L. Rogers, J. C. Gates, and P. G. R. Smith, "Quantifying the optical sensitivity of planar Bragg gratings in glass micro-cantilevers to physical deflection," J. Micromech. Microeng. **21**, 035014 (2011).
20. B. G. Aitken and R. E. Youngman, "Borophosphosilicate glasses: properties and structure," Phys. Chem. Glasses **47**, 381–387 (2006).
21. H. L. Rogers, S. Ambran, C. Holmes, P. G. R. Smith, and J. C. Gates, "In situ loss measurement of direct UV-written waveguides using integrated Bragg gratings," Opt. Lett. **35**, 2849–2851 (2010).
22. A. Ghatak and K. Thyagarajan, *An Introduction to Fiber Optics* (CUP, 1998), p. 154.

1. Introduction

The use of Micro-Opto-Electro-Mechanical Systems (MOEMs) in integrated optics promises devices with improved performance, compactness and greater functionality. The cantilever is a common element within microstructures with mechanical properties that make it especially well-suited to function as a sensor or actuator [1]. MOEM devices using a single cantilever have been demonstrated previously, for example, where a moveable waveguide is displaced relative to a fixed waveguide. Ollier *et al.* fabricated an optical switch based on silica-on-silicon technology that used electrostatic switching to function as a switch between channel waveguides [2]. While single cantilevers provide a way to create devices, the use of dual cantilevers has been pioneered by Park *et al.* as a way of attracting cells to adhere to a cantilever, whereon they can be cultured and weighed using a resonance frequency method [3]. In another example of this geometry Xu *et al.* fabricated dual cantilevers in polymer, which also served as waveguides, in a device that functioned as an acoustic sensor [4].

Various schemes are well known for transducing mechanical motion onto an optical signal. For example, a small mirror mounted on the cantilever will deflect a laser beam, an approach widely

deployed together with quadrant detectors in atomic force microscopy. However, all free space optics are susceptible to their local environment, for example temperature, airflow, vibration, shock, *etc.*, and a well-known advantage of integrated optics, beyond the simple factor of compactness, is robustness and reduced cross-sensitivity. Thus, if the components for optical sensing can be integrated into the cantilever then this can have benefits for the performance and compactness of the device. The integration of optical components into a glass cantilever for force sensing has already been demonstrated by Zinoviev *et al.* [5]. Carpenter *et al.* [6] incorporated two Bragg reflectors into a glass cantilever to create a cavity. In that work deflection of the cantilever caused a change in the optical path length of the cavity thereby modifying the optical spectrum which was used to determine the deformation.

Beyond sensing, fiber based variable optical attenuators have been demonstrated by Barber *et al.* [7]. They used a voltage-controlled moving mirror MEMS device to achieve up to 50dB of attenuation. Ford *et al.* fabricated a MEMS device which used a silicon nitride quarter wave plate to realize a variable reflective mirror [8]. Their device exhibited 25 dB of dynamic range with an insertion loss of 3 dB. Another area where the dual-cantilever geometry is employed is in the domain of particle trapping. Constable *et al.* first demonstrated an optical light trap configuration comprising of only two optical fibers avoiding the use of any other optical elements [9]. They indicated that angular displacement of the fibers allows the trap position to be moved. Black *et al.* [10] further showed that translational displacement could be used to give controlled rotation of smooth muscle cells. As well as applications in biological science, Succo *et al.* demonstrated a monolithic implantation of a cold atom trap [11] using dual waveguides. A dual-cantilever version of this device could be used to provide better physical access for probing of the atom, and offers potential for microscopic adjustment of trap parameters. In this report, we describe a dual-cantilever device, fabricated and characterized for the first time in silica-on-silicon. The new devices in this work are larger in cross-section than conventional MEMS leading to greater bending stiffness and high resonant frequencies. While high stiffness requires greater force to actuate, it can be advantageous in providing better immunity to acoustic noise or vibration and thus can be desirable for attenuator, switching or trapping applications. Furthermore, in some MEMs applications in harsh environments, e.g. projectiles, accelerations of up 100,000g occur and more robust MEMs structures may have advantages [12]. The lack of free space optics combined with the potential for multiplexed sensing could make possible the use of this type of device in field applications.

Currently photolithographic techniques dominate in the fabrication of MOEM devices. While this fabrication approach has many benefits including parallel processing and small feature size, it requires access to cleanroom facilities, and such access to appropriate equipment can be expensive and be energy intensive. An alternative to lithography for fabrication is based on physical machining, and is developing rapidly as tools and systems become available. Mechanical dicing

has been demonstrated in a range of materials and formats such as lithium niobate [13] and Nd:YAG [14]. In the dual-cantilever work in this study, we used the physical dicing technique which can give optical-quality surface-roughness with low processing times. The surface quality of the machining technique has been previously demonstrated in silica-on-silicon photonics using the ductile dicing regime [15].

2. Design and experimental realization

Fig. 1. Shows a 3D visualization showing the concept of dual opposing cantilevers machined into silica-on-silicon. Each cantilever contains an optical waveguide. The cantilevers are produced using dicing technology and etching away silicon to release the silica structures.

The dual cantilever arrangement shown in Fig. 1 consists of a neighboring pair of cantilevers with each cantilever containing a waveguide. The devices are fabricated in silica-on-silicon and the details of the fabrication will be described in detail later. When both cantilevers are deflected, this changes the relative angle between them and hence the coupling of light between the launching waveguide and the receiving waveguide. This section will describe the fabrication steps, as well as design considerations that affect the performance of the device. The underlying substrate is a silicon wafer of <100> orientation of 1mm thickness, providing a robust starting platform. The key techniques in the fabrication of the cantilevers are a micromachining process using a dicing approach and wet etch with potassium hydroxide. The optical glass is deposited onto the silicon substrate via Flame Hydrolysis Deposition (FHD). A thermally grown layer of oxide on the silicon wafer acts as an underclad layer and has a thickness of 15 µm. On top of this layer a core layer of silica glass is deposited using FHD and is doped with germanium and boron to promote photosensitivity. A cladding layer is then deposited which is doped with phosphorous and boron to provide a lower consolidation temperature relative to the core. After each layer is deposited it is consolidated in a furnace at temperatures between ~1200° C and ~1360° C. The channel waveguide will be later formed in the core planar layer. Although high temperatures are required

during the fabrication of the substrate, other devices, such as MEMS, could be integrated upon the substrate but only post consolidation. The high processing temperatures result in a very physically and chemically robust platform.

To create the cantilevers a Loadpoint Microace dicing saw was used to define 7 grooves through the silica and into the silicon. A nickel-bonded blade with a width of 100 µm impregnated with 4000 grit diamond abrasive was used (ZH05-SD4000-N1-50 KK). A plunge-cut mode was used which consists of the blade coming vertically downwards onto the workpiece without any translation. Fig. 2(a) shows the structure after the dicing steps. As plunge-cutting is more susceptible to blade breakage and top-edge chipping, optimization was required to avoid these issues. A plunge speed of 5 µm/s and spindle speed of 20 krpm were found to reduce chipping to an acceptable level. Due to the circular blade shape, the resultant grooves are crescent shaped with the silicon only being exposed at the center where the grooves are deepest. As seen in the image the exposed silicon at the center shows higher reflectivity than the exposed silica due to lower surface roughness and increased Fresnel reflection. This is illustrated by the graphic in Fig. 2a.

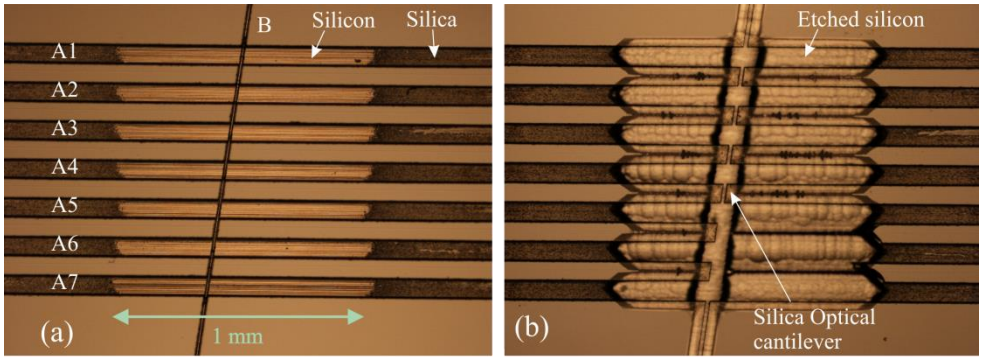

Fig. 2a. The image shows an optical microscope (top-side) image of the glass cantilevers before etching. 7 parallel grooves are diced using a plunge method technique (labelled as A1-A7 on the image). The silicon substrate is observed in the middle of the grooves and highlights the crescent shape. A second channel (B) is diced at an angle of 8° from perpendicular to the previous grooves which was in a conventional non-plunge mode. Fig 2b shows the glass cantilevers after etching. The regions of exposed silicon are removed by the KOH etchant, resulting in the lighter coloured central regions. The overlaying optical cantilevers are essentially transparent but can be seen most clearly in the region of the central channel.

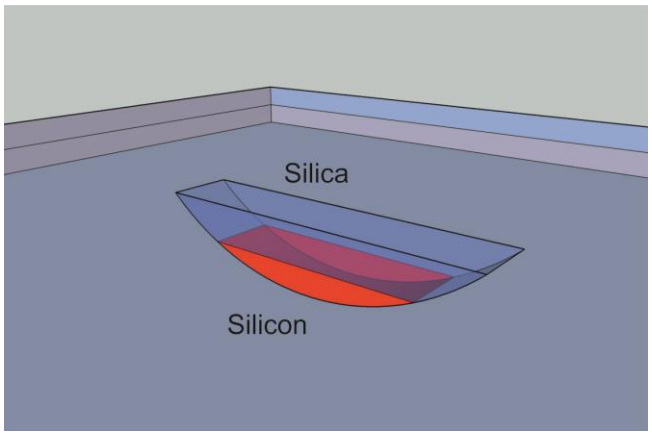

Fig. 3. Image shows a 3D visualization of the crescent shaped plunge-cut illustrating that the silicon becomes exposed only in the central region of each cut. This is important as the silicon etches much faster with KOH, so it is this exposed region that undercuts the overlying adjacent silica to create the cantilevers.

To create the dual cantilevers a second groove (B) is diced with a 15 µm width blade at an angle of 8 degrees from perpendicular to the previous grooves. Having the end facets of the cantilevers at this angle ensures that the reflected light exceeds the numerical aperture of the guide, which could lead to fringes in the measured spectrum. The previously reported direct UV writing process [16] is used to simultaneously define the waveguides and Bragg gratings. 9 Bragg gratings are written along the waveguide with various periods which will be used for characterization. The waveguides were written after the dicing but before the wet-etch described in the next section. Using the UV fluorescence from the sample, the waveguides and Bragg gratings were precisely aligned to the diced grooves. The thickness of the core FHD layer was measured using a Metricon prism coupling system to be 5.4 µm. This defines the vertical dimension of the waveguide core. The horizontal dimension is controlled by the UV writing spot size and the applied fluence. These parameters have been adjusted to match the mode size to standard single mode optical fiber and hence the mode field diameter at 1550nm is ~10um in the vertical and horizontal directions. The resulting waveguide is single mode which is confirmed by the single Bragg peaks observed during spectral characterization. This data also confirms that the waveguides have little birefringence and indicates that the two polarization modes have similar modal dimensions. This is also confirmed by modelling with a commercial modelling program Fimmwave (Photon Design Ltd). More details of this modelling and optical mode measurements can be found elsewhere [17,18]. The dimensions of the cantilevers were designed such that the core mode was more than 17 µm away from any lateral surfaces to ensure that the mode was not affected by the external environment. Finally, the chip was wet-etched in 25% potassium hydroxide solution at 75°C for 5 hours to preferentially remove the silicon and release the glass cantilevers from the substrate. A comparison of the device pre and post etching can be seen in Fig. 2.

The cross-sectional area of the cantilever is 100µm × 40µm. The channel waveguide runs through

the cantilever such that it is centered about the vertical and horizontal neutral axis. This minimizes strain induced refractive index and physical length variations upon actuation [19].

Fig. 4 shows a Scanning Electron Microscope (SEM) image of the released cantilevers after etching. At the stage of wafer fabrication the glass layers are all under compressive stress due to the lower coefficient of thermal expansion of the glass compared to the silicon. In addition, stress in each layer of the glass differs due to the different doping levels and also their consolidation temperatures. For example the thermal expansion coefficients vary between ~$5.5x10^{-7}$ K^{-1} for pure silica, representative of thermal oxide, and up to $4.3x10^{-6}$ K^{-1} for borophosphosilicate [20]. This differential is evident in Fig. 4 where upon release the micro-cantilevers deflect out of plane. Thus cantilever curvature can be controlled through a combination of layer thicknesses, cross-sectional form, or directly manipulating stress in the layers through changing dopant concentrations and consolidation temperature of the FHD process.

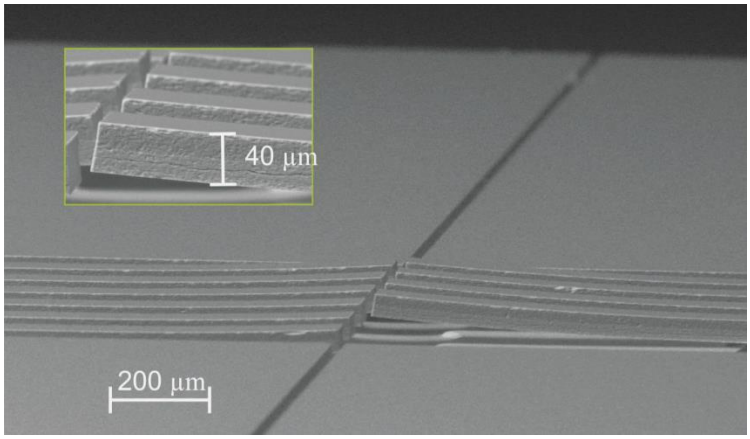

Fig. 4. SEM image of the etched cantilever device. Note that first two cantilevers at the right side of the image sustained damage during the etching / drying process, however, this enables a clear visualization of the side walls of the third cantilever (shown in the inset image). The deflection out of the plane occurs because of stress inherent in the layers due to their high consolidation temperature.

The inset of Fig. 4 shows a side wall image of one of the cantilevers. The device was further characterized with a Zemetrics Zescope optical profiler and results are shown in Fig. 5. These measurements show that the form of the intrinsic displacement was essentially the same for each cantilever. For the set of cantilevers the resultant intrinsic displacement after fabrication ranged from 5µm to 17µm for the shortest and longest devices respectively. Due to the 8º crosscut used to form the dual cantilevers, the cantilever pairs have varying levels of length mismatch. The main cause of variation in the form, is due to the position of the root which is affected by the KOH etching conditions. The limiting factors for the size of cantilever that could be produced by this method are the lateral positional accuracy of the dicing saw used and the physical strength of the

machined ridge. Were the width of the cantilever to become too narrow the interaction between the optical mode and the sides of the cantilever would increase, risking additional loss.

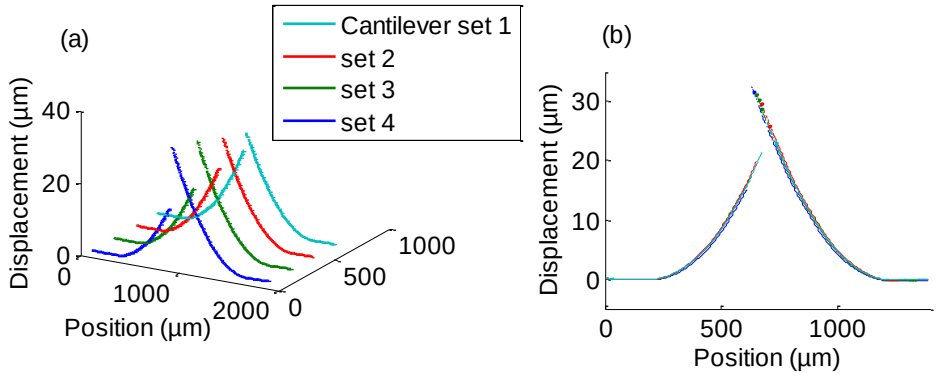

Fig. 5. Profiles of cantilevers showing out-of-plane displacement without load (due to the release of intrinsic stress) Fig. 5a shows deflection of each cantilever measured with the Zescope optical profiler. The length mismatch results in differing maximum displacements. Fig. 5b shows the same data but with the curves overlapped, effectively an isometric view of Fig. 5a. The shapes are very consistent with only a difference in final height between the curves.

A finite element simulation (FEM) model was run using COMSOL Multiphysics software. A three stage model was built that first simulates the thermal oxide and FHD glass depositions to simulate the thermal stresses that are built up once the consolidated glass layers are cooled to room temperature. The 3rd stage was to model the out of plane deflections once the cantilevers are freed from the silicon substrate. The following values were used for the thermal expansion coefficients. Silicon: 2.5×10^{-6}. Thermal oxide silica: 0.55×10^{-6} K^{-1}. Cladding layer glass (borophosphosilicate): 4.3×10^{-6} K^{-1}. The results from the COMSOL simulation are shown in Fig. 6.

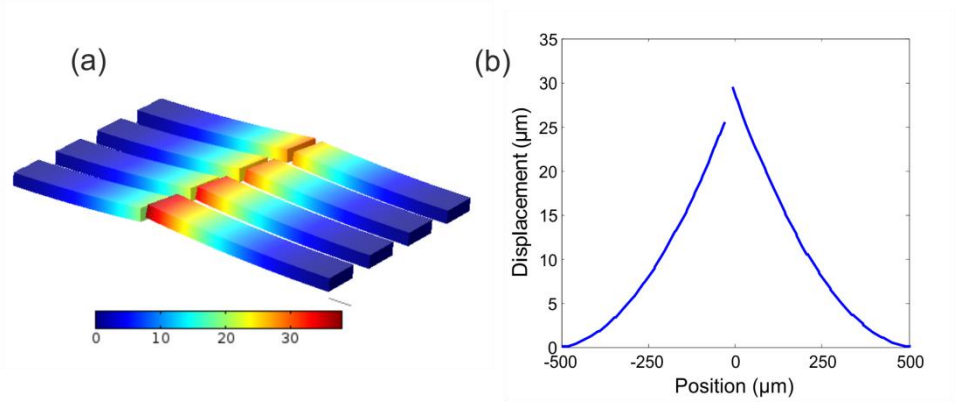

Fig. 6a. Comsol simulation showing out-of-plane displacement following etch release (in microns). 6b The displacement cross-section through the pair of cantilevers most equal in length. The parameters of the simulation are listed in the text.

To compare the model with the experimental data the out-of-plane deflection of cantilevers forming set 1 was studied. The model predicted 25 and 29 µm for the two cantilevers, while for the real device the deflections were 19 and 26 µm. It is believed that this difference is because the true coefficient of thermal expansion of the cladding layer is not known with high accuracy. However the reasonable accuracy of the model suggests that the biggest contribution to the bending is the higher thermal coefficient of expansion of the FHD cladding glass compared to the thermal oxide.

3. Results and discussion

Having fabricated the dual cantilever containing waveguides and Bragg gratings, the loss was measured using an approximation of the grating based method [21]. The location and wavelengths of the Bragg gratings are shown in Fig. 7.

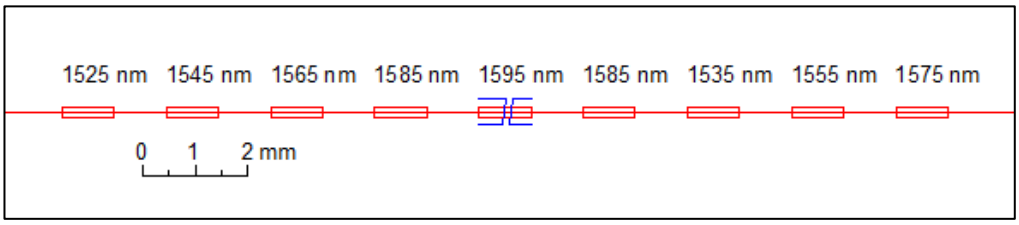

Fig. 7. A schematic showing the locations of the waveguide and Bragg gratings in relation to the cantilevers. Red: Bragg gratings and waveguide. Blue: Cantilevers. The gratings are 1mm in length and separated by 1mm. The total cantilever section length is also approximately 1mm and only affects the 1595 nm grating. The total device size is 10mm × 20mm.

The optical spectrum of the device was measured in reflection using a broadband source and Optical Spectrum Analyzer (OSA) as shown in Fig. 8.

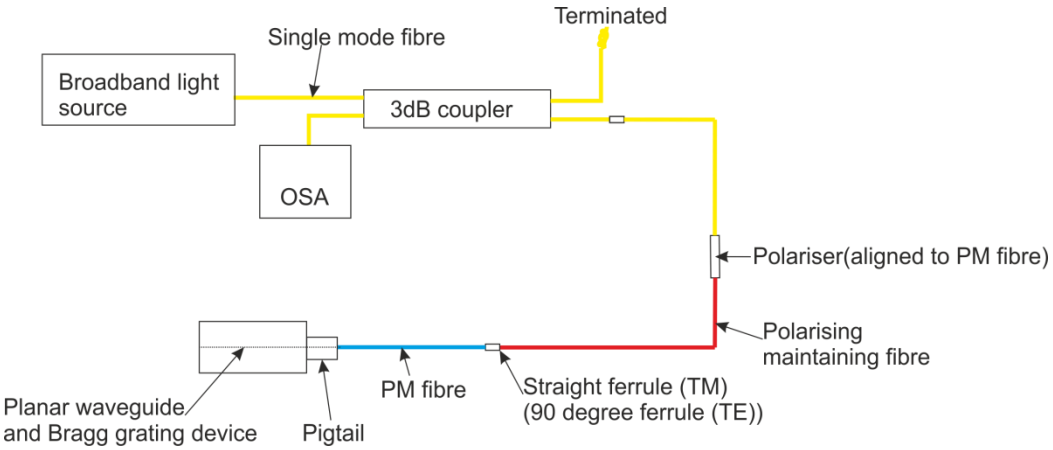

Fig. 8. Optical setup used to characterize the reflection properties of the devices. A polariser aligned to a PM fiber ensures spectrally independent polarised source.

Polarization maintaining optical fiber components and a polarizer are used so that the two orthogonal polarization modes can be measured separately. Fig. 9 shows the spectra for the TE and TM modes. The reflectivity is normalized to the source power and includes the coupling loss due to the fiber-optic pigtailing. There is a loss between the cantilevers due to the Fresnel reflections at the two interfaces (calculated to be ~0.3dB). There is also loss from the lateral misalignment caused by the 8º interface and is calculated to be ~0.6 dB. The two gratings at 1585nm form a Fabry-Pérot cavity. The fringes from this are clearly visible in Fig. 9 but will not be used in this work. The effective indexes of the TE and TM modes at 1550 nm are 1.44823 and 1.44847 respectively. This birefringence is due to in-plane thin film stress caused by the mismatch in thermal expansion coefficients between the silica and silicon. This corresponds to birefringence of 2.36×10^{-4}. This effect is due to the stress-optic effect creating anisotropic refractive index, with the TM mode exhibiting a higher refractive index.

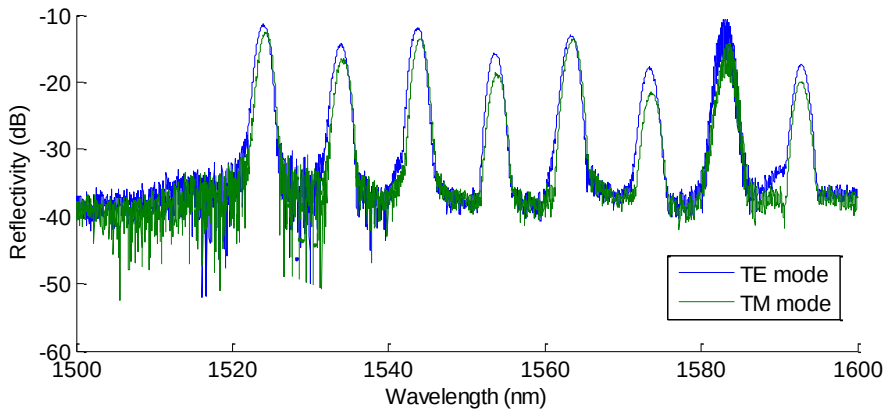

Fig. 9. Reflection spectra taken after dicing but before etching. The data shows the absolute reflectivity calibrated against a known fiber end reflection. Analysis of the peaks shows a wavelength shift due to birefringence of 0.28 nm.

After etching the cantilevers are released, without load the misalignment becomes large and effectively zero signal is seen from the gratings beyond the diced groove. This is to be expected as the dual cantilevers were all asymmetric in length and so without load sit at different heights. The robustness of the cantilevers allows them to be deflected using an external load thereby bringing the waveguides into alignment. In the next section measurements will be presented demonstrating this operation.

To test the optical response of the cantilevers to actuation, an optical fiber was used to deflect the cantilevers as it could be easily cleaved to give a perpendicular end facet, as well as benefitting from having a small diameter which restricts the contact area to be close to the ends of the cantilevers. The device was mounted on a flexure translation stage (Thorlabs 3-Axis NanoMax Stage) which allowed X, Y and Z positioning with sub-micron precision. Two modes of actuation are possible: to push both cantilevers simultaneously or to only deflect one as shown in

Fig. 10(a) & (b) respectively. In this paper a positive displacement corresponds to the cantilevers being pushed into the plane of the device. Fig. 11 shows camera images of the device taken during the experiment.

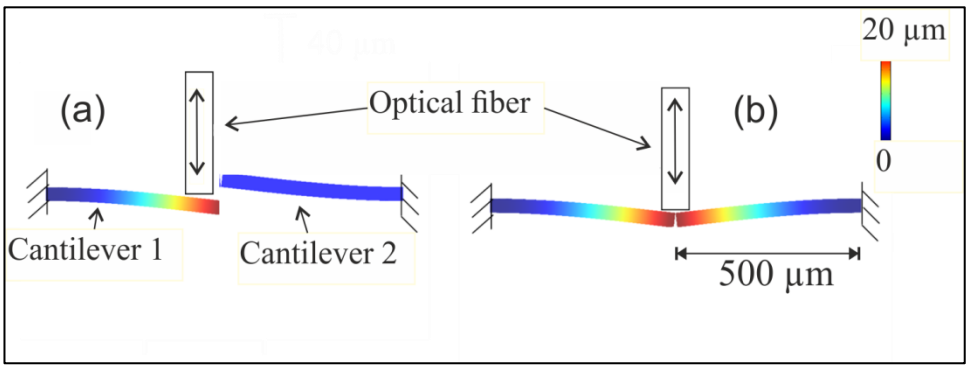

Fig. 10. Showing the two possible types of actuation. The colour maps calculated in Comsol indicate the displacement of the cantilever from its rest state. The colour bar shows the displacement in microns.

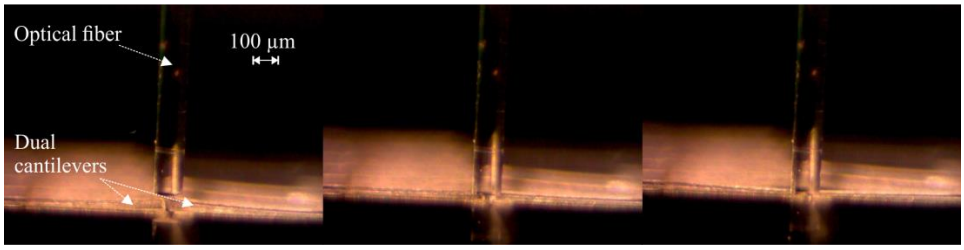

Fig. 11. Camera images showing physical actuation of the cantilevers with an optical fiber pushing down on the cantilever with different heights of actuation. An optical fiber was used as it is only 125 micron and provides a stiff small cross-section rod.

Fig. 12 shows a comparison of the TE spectra for the actuated and rest states. Upon actuation the two cantilevers can be aligned, such that light couples between them. This is observed in as upon actuation the Bragg reflections from both cantilevers can be seen. Those marked with the label ‘A’ are on the side of the device coupled to the optical fiber while those labeled ‘B’ are on the other side. The peak labeled ‘C’ is from the Fabry-Perot cavity whilst the grating giving peak ‘D’ is located in the cantilevers. There is also an increase of approximately 10 dB in the background level due to increased broadband Fresnel reflection from the facet of the second cantilever.

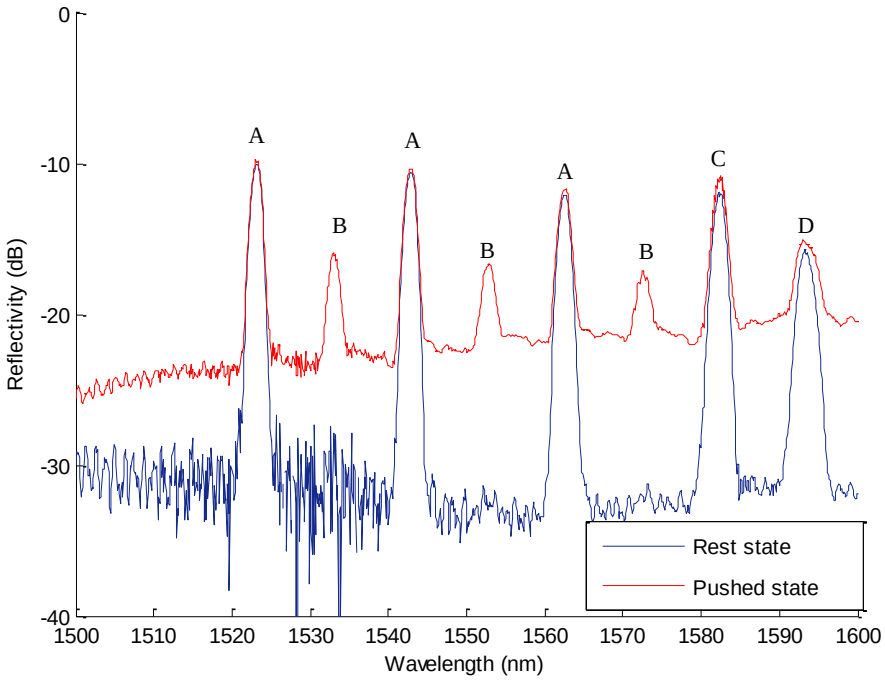

Fig. 12. The measured TE spectra of the device in the rest state (blue), and a deflected state (red). Actuating the devices increases the reflectivity of Bragg gratings opposite to the coupling side. As can be seen it also increases the background level by approximately 10dB. The Bragg gratings labelled with 'A' are on the side of the device coupled to the optical fiber while those labelled 'B' are on the other side.

The optical coupling between the cantilevers is determined by the angle between them. By measuring the transmitted intensity it is possible to measure the coupling. However by using the reflectivities of the Bragg gratings it is also possible to measure them in a way which is insensitive to fluctuations in source power and requires only coupling to one waveguide facet. Peak intensities are fitted to Gaussian apodized Bragg gratings (1555nm and 1565nm) on each side of the central cavity and used to give a relative reflectivity which is only dependent on the optical coupling between the cantilevers. The insertion loss at the maximum coupling point can be obtained by measuring the spectrum from both ends of the device. [21]. The measured minimum coupling losses were 2.4±0.1 dB for the TM mode and 2.8±0.2 dB for the TE mode. The data suggests that there may be a greater loss for the TE mode, but as the difference is only 1.7σ this may not be statistically significant. The slightly greater numerical aperture of the TM mode, due to birefringence, may contribute to this difference.

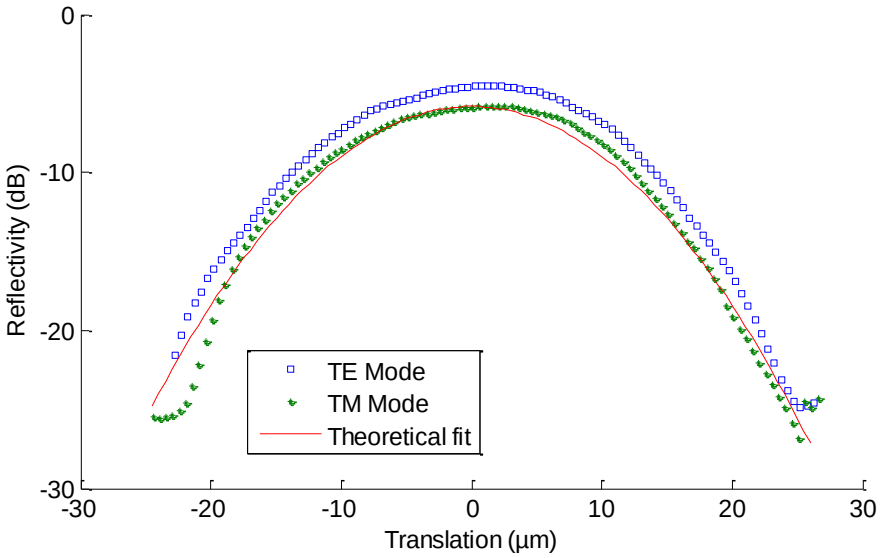

Fig. 13. Plot showing the ratio of reflectivity from Bragg gratings on opposing sides of the dual cantilevers (relative reflectivity) versus the displacement of both cantilevers. The theoretical fit makes use of equation (1).

Fig. 13 shows the coupling as both cantilevers are pushed simultaneously. The zero value for translation is obtained by fitting the quadratic misalignment loss curve after the experiment. It can be seen that the optical coupling goes through a maximum which occurs for a certain angle between the cantilevers. This is expected to be 0º, however error in the angle of the facets from the fabrication processes may give an offset. The geometry is related to the problem of loss due to angular misalignment between two fibers [22]. Here the misalignment angle is taken to be twice the angle of rotation of a single cantilever. The loss in dB is given by eq (1).

$$\alpha_a\left(dB\right) = 4.34\left(\frac{\pi n_l w\theta}{\lambda_0}\right)^2 \qquad (1)$$

Here α_a is the loss in decibels, n_l is the refractive index of the medium between the fiber ends, θ is the angle of misalignment, λ_0 is free space wavelength and w is the spot size of the mode. This loss figure (given in dB) is derived from the overlap integral of the mode exiting a first fiber being coupled into the input mode of a second fiber. The mode size w of the UV written waveguide, is approximated as 5 µm which is similar to SMF28 single mode optical fiber.

Actuating a single cantilever was also accomplished, and similarly, shows a coupling peak as seen in Fig. 14. The peak is asymmetric once the actuated cantilever moves below the second cantilever, which suggests coupling from cladding modes back into the core mode. This is thought to be as a result of the curvature of the cantilevers and the angled interface of the receiving cantilever which remains deflected due to the intrinsic stress. Once the deflected cantilever is below the receiving cantilever coupling is still possible due to refraction and scattering resulting in an asymmetric peak. The sensitivity of relative reflectivity to translation over the central 10 µm of the fitted model is 0.16 dB/µm.

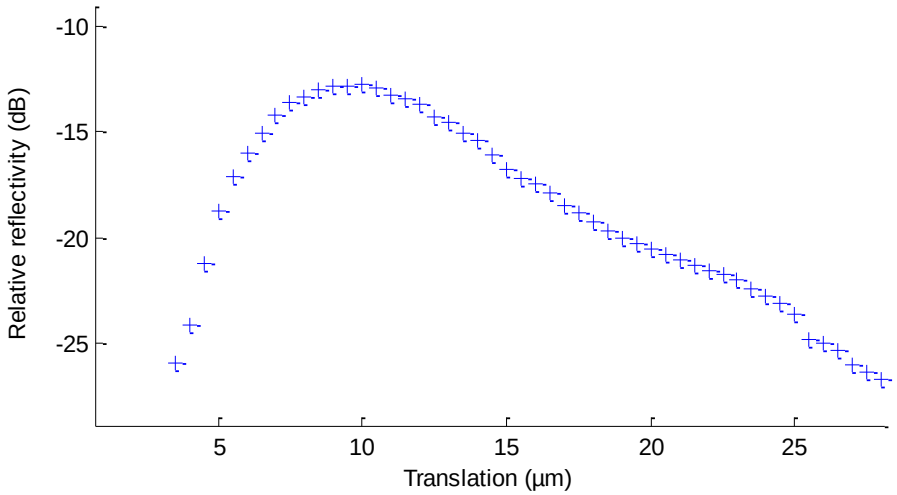

Fig. 14. The relative reflectivity response of a single cantilever translation also showing a point of maximum coupling for the TE mode. It is however less symmetric which suggests that there is coupling to the fundamental mode through cladding modes and due to the lack of verticality of the receiving cantilever end facet. Scatter may also contribute to this asymmetry.

The experiment was also carried out using the transmitted intensity. For this experiment the device was pigtailed with optical fibers at both ends of the waveguide using UV curing glue. The spectra are shown in Fig. 15 and again show good agreement to the theoretical coupling efficiency. This experiment was then repeated with the device covered with refractive index oil of n = 1.46. This modifies the gap refractive index and shows the expected change of making the peak narrower with a higher transmission (1.13 dB) as the Fresnel reflection is reduced. Furthermore, diffraction is reduced in the higher index oil leading to a narrower width. In addition the higher refractive index of the oil will tend to strip cladding modes reducing excitations at larger displacement. The deviation of the experimental data from the model is observed at larger displacements corresponding to lower light levels at 15 dB below the peak transmitted signal due to both background scatter and excitation of cladding modes. This effect was not observed in the reflection data of Fig. 13 due to the high return loss of the device.

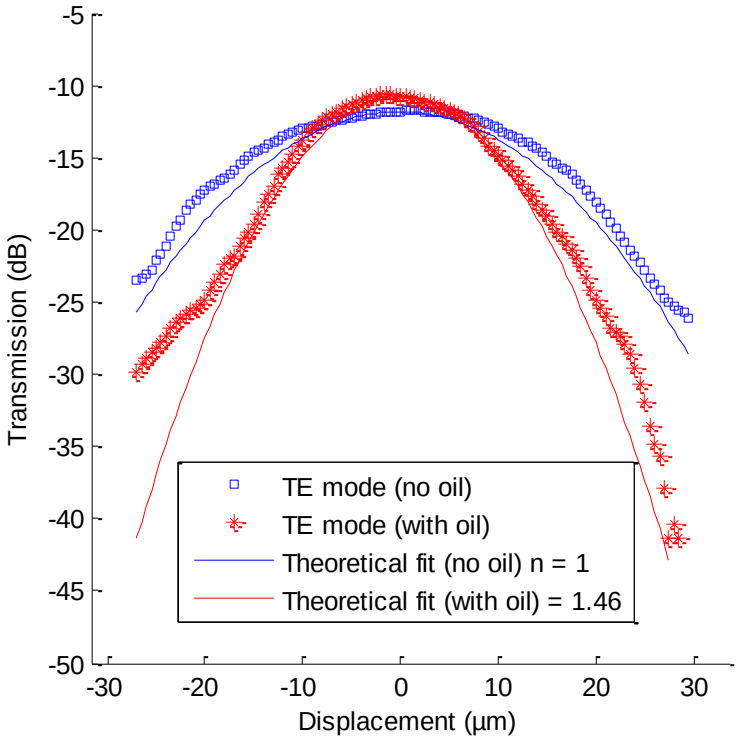

Fig. 15. Transmission during double push actuation showing effect of immersion in oil n = 1.46. The total transmission is improved with oil as would be expected from reducing off scatter and Fresnel loss. The peak narrows because the output beam does not diffract as rapidly so the receiving fiber position becomes more critical.

4. Conclusion

A new approach of fabricating dual cantilever devices has been demonstrated, utilizing precision dicing technology, direct UV writing and selective wet etching. The approach makes use of physical micromachining techniques that do not require cleanroom class lithographic and etch facilities. The devices are shown to operate in a mode suitable for a displacement sensor or with the addition of an actuator, such as a piezo-electric, a MOEMS variable attenuator. By investigating the response of the device to actuation with an optical fiber we have shown that the mechanical-optical behavior of the device is well described by conventional fiber optic angular misalignment coupling theory.

The device contained an array of four dual-cantilevers, demonstrating potential for creating parallel arrays for switching or sensing applications. The signals from these arrays could be wavelength multiplexed with the use of Bragg gratings. Each cantilever contained nine discrete Bragg gratings, so the overall device incorporates many integrated elements on a single chip. These devices offer potential for use in switching, optical attenuators, and optical trapping. Their greater stiffness makes them attractive for use in harsh environments, and they may be embedded in composite materials where the higher required actuation forces are readily achievable. Furthermore, as they

are waveguide devices they avoid the alignment issues inherent in free space measured structures.

Acknowledgments

We would like to acknowledge the support of the Engineering and Physical Sciences Research Council (EPSRC) for supporting this work.

Appendix C: Journal publication: Power efficiency enhanced thermally tunable Bragg grating for silica-on-silicon photonics

Power efficiency enhanced thermally tunable Bragg grating for silica-on-silicon photonics

P.A. Cooper[1], L.G. Carpenter[1], C. Holmes[1], C. Sima[2], J.C. Gates[1], P.G.R. Smith[1]

[1]Optoelectronics Research Centre, University of Southampton, Highfield Campus, SO17 1BJ, UK
[2]Next Generation Internet Access National Engineering Laboratory, Huazhong University of Science and Technology, Wuhan, 430074, P.R. China

Abstract: A thermally tuneable Bragg grating device has been fabricated in a silica-on-silicon integrated optical chip, incorporating a suspended microbeam improving power efficiency. A waveguide and Bragg grating are defined through the middle of the microbeam via direct UV writing. A tuning range of 0.4nm (50 GHz) is demonstrated at the telecoms wavelength of 1550 nm. Power consumption during wavelength tuning is measured at 45 pm/mW, which is a factor of 90 better than reported values for similar bulk thermally tuned silica-on-silicon planar devices. The response time to a step change in heating is longer by a similar factor as expected for a highly power efficient device. The fabrication procedure involves a deep micro-milling process as well as wet etching and metal deposition. With this response the device would be suitable for trimming applications and wherever low modulation frequencies were acceptable. A 4-point-probe based temperature measurement was also done to ascertain the temperature reached during tuning and found an average volume temperature of 48 ºC corresponding to 0.4 nm of tuning. The role of stress induced buckling in device fabrication is included.

Index Terms: Bragg grating, thermal tuning, microbeam, power efficiency.

1. Introduction

Microbeams are a common structure in Micro-Opto-Electro-Mechanical (MOEM) devices. In their most basic form they consist of a beam clamped at both ends suspended over a substrate. A variety of applications that take advantage of the special properties of microbeams can be found in the literature; Guckel *et al*[1] fabricated microbeams to measure the stress in a deposited polysilicon film. A thermally driven microvalve was fabricated by Lisec *et al*[2]. Joe *et al* used the resonant frequency behaviour of microbeams for gas sensing applications[3]. Optical applications include a bridge suspended thermo-optic phase shifter[4] in silica-on-silicon and a tuneable Bragg grating in a silicon waveguide[5].

Bragg gratings in silica waveguides have already been proven in fields such as telecoms, sensing and quantum information experiments[6]. The ability to control either the reflected wavelength or the spectral shape of the Bragg grating can lead to new types of device. Wavelength tuning can be used in add/drop multiplexers for Dense Wavelength Division Multiplexing (DWDM)[7]. Tuning the chirp or non-linearity of a grating has applications in active dispersion control for communications systems[8].

The approach of undercutting a laser written microstructure has been used previously to demonstrate microcantilevers, clamped only at a single end [9], and membranes [10]. This new device allows for transmission operation and simplifies the placement of the heating element.

The microbeam geometry is expected to give enhanced thermal tuning efficiency performance due to its thermal isolation from the environment and the extremely low heat capacity of the microbeam. As the silicon substrate is an excellent conductor of heat, it efficiently sinks heat away from the waveguide, thereby increasing the thermal load and decreasing the energy efficiency when tuning in a bulk substrate. In a microbeam device the air gap around the microbeam provides effective thermal isolation. The current interest in fabricating optical waveguide chips for quantum information processing requires large numbers of heating elements for optical phase tuning,

resulting in the chip having to dissipate large amounts of power to remain at stable temperature[11]. Incorporating microbeam structures at heating points could drastically reduce the amount of bulk heating and cross-talk between phase shifters.
Various methods of optical tuning have been reported in the literature for integrated planar devices; piezoelectric actuation was used in a phase shifting device by Donati *et al* [12] and liquid crystal tuning was demonstrated by Adikan *et al* [13]. The ideal method of tuning will depend on different factors including device format, tuning range required and response time. Thermal tuning is a proven method of tuning for integrated optics and was selected for this work due to the reliability and relative simplicity of fabrication.

2. Thermal tuning theory

In our device we thermo-optically tune a Bragg grating, located in a microbeam, and also demonstrate control of the optical path length of a Fabry-Pérot cavity defined across the microbeam. The graphic in Fig. 1 shows how the structure of the microbeam is created through a combination of micromilling and wet etching as well as the location of the optical elements in relation to the physical structure.

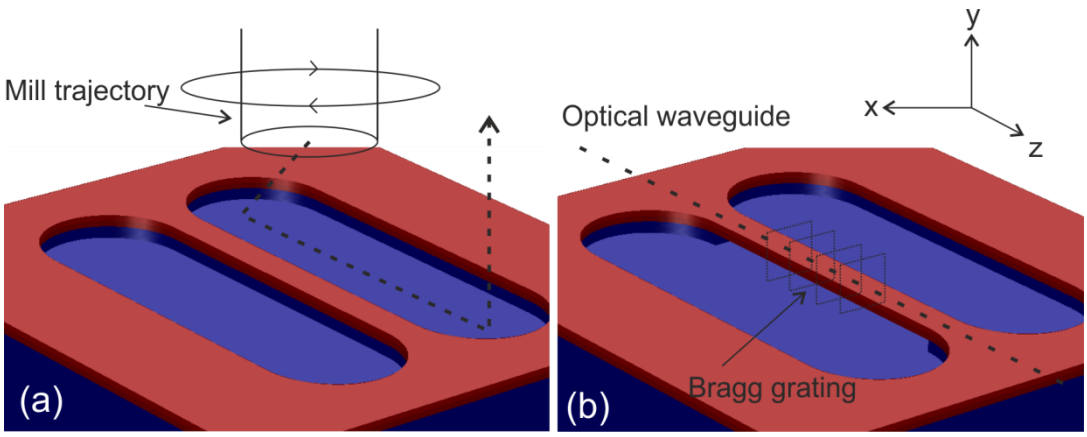

Fig. 1. (a) Structure geometry following milling. The glass layers are shown in red while the silicon is coloured blue. The trajectory of the milling cutter is shown. (b) Structure after KOH wet etching showing how the silicon underneath the microbeam has been removed. The locations of the optical waveguide and Bragg grating are also shown with dotted lines. For simplicity the 'run-up' section described later are not included in this schematic diagram.

A Bragg grating is a region of periodically modulated refractive index that reflects light resonantly at wavelengths given by the Bragg condition. The Bragg condition gives the centre wavelength λ_B reflected by a Bragg grating and is given by equation (1).

$$\lambda_B = 2n_{eff}\Lambda \qquad (1)$$

where Λ is the pitch of the Bragg grating and n_{eff} is the effective refractive index of the waveguide mode. A simple mathematical model can be developed to model the efficiency of thermal tuning by considering how the variables in equation (1) are affected by temperature and the associated changes in the waveguide. Thermal tuning can change the Bragg condition in three ways; firstly via thermo-optic effect, secondly through stress-optic and thirdly by grating pitch expansion, which in our device is modified due to the mechanical anchoring at either end of the beam. The shift in Bragg peak wavelength can be expressed by the change in refractive index with equation (2).

$$\Delta\lambda_B = \frac{\Delta n}{n_{eff}}\lambda \qquad (2)$$

Firstly, due to the thermo-optic effect in most materials *n* is a function of temperature. For small temperature changes the relationship is linear, given by equation(3).

$$\Delta n = \xi \Delta T \qquad (3)$$

Here ξ is the thermo-optic coefficient and has a value of 1×10^{-5} K^{-1} for pure silica glass[14].

For our device, we know that the modal refractive index $n_{eff} = 1.448$ for wavelengths around 1550 nm. By combining equations (2) and (3) the theoretical tuning sensitivity of the device due to the

thermo-optic effect is 10.7 pm/°C and this is consistent with the values of standard non-MEM's type devices[15].
Secondly, the stress-optic effect, also referred to as photoelasticity, describes the effect of stress on the refractive index. In a constrained system heating will lead to thermal stress developing as the material is not free to expand. As stress is a tensor it is necessary to consider the change in refractive index along three orthogonal axis. The three components of refractive index are given by equations (4)-(6). The coordinate system used is as shown in Fig. 1.

$$n_x = n - pS_x - q\left(S_y + S_z\right) \quad (4)$$

$$n_y = n - pS_y - q\left(S_x + S_z\right) \quad (5)$$

$$n_z = n - pS_z - q\left(S_x + S_y\right) \quad (6)$$

Where S_x, S_y and S_z are the normal components of the stress tensor and the stress optic coefficients p = 6.5×10^{-13} Pa^{-1} and q = 4.2×10^{-12} Pa^{-1} for pure silica glass[16]. If a normal stress is applied along the microbeam axis, this causes stresses in the orthogonal directions with a magnitude determined by Poisson's ratio.

$$S_x = -\nu S_z \quad (7)$$

$$S_y = -\nu S_z \quad (8)$$

Here ν is Poisson's ratio with a value of 0.17 for silica glass[17]. When equations (7)-(8) are substituted into equation (4), the refractive index change as a function of S_z is obtained.

$$\Delta n_{x,y} = S_z\left(p\nu - q\left(1-\nu\right)\right) \quad (9)$$

If the stress is caused by constrained thermal expansion it will be proportional to the temperature change.

$$S_z = E\alpha\Delta T \quad (10)$$

Here E is the Young's modulus of silica, taken to be 73.1 GPa. α is the coefficient of thermal expansion which was taken to be 0.55 x 10^{-7}[17]. This results in a negative tuning sensitivity due to the stress-optic effect of -0.12 pm/°C. This simple analysis is not capable of distinguishing any potential birefringence caused by the stress-optic effect.

Thirdly in addition to the stress induced by thermal changes, the microbeam will also tend to expand, altering the period of the grating. In an unconstrained system thermal expansion will cause an increase in the pitch of the Bragg grating.

$$\Delta\Lambda = \alpha\Delta T\Lambda \quad (11)$$

$\Delta\Lambda$ is the increase in pitch of the Bragg grating. For the device described the thermo-optic effect will always be contributing during the tuning. A further complication is that a stressed beam can undergo buckling to release stress which will affect how subsequent strains develop. If a microbeam is in the buckled state thermal strain will be only partially constrained and some grating pitch expansion will occur. If it is unbuckled, thermal stresses will occur but the grating pitch will not change appreciably.

As mentioned, it is possible for an axially stressed beam to undergo buckling if its length exceeds a critical length. Buckling is a sudden, discontinuous change of beam shape in a response to a critical applied axial load in a beam. In a symmetric beam with uniform load there is a bifurcation and buckling in any direction is possible. However if the beam has shape imperfections or cross-sectionally varying stresses these may help to define the preferred buckling direction. A slightly bent beam under increasing stress will deflect continuously however it will not buckle until the critical load level is reached. The buckled beam has a characteristic shape known as the buckled mode and will generally have its maximum displacement at the centre of the beam. The stress, S, required to cause buckling in a beam with length L_c is given by the Euler-Bernoulli equation[18].

$$S = \frac{\pi^2 E h^2}{3L_c^2} \quad (12)$$

L_c is the critical length of the microbeam beyond which buckling occurs. *h* is the thickness of beam. Fig. 2 illustrates how an initially straight microbeam buckles to a lower energy configuration with the characteristic shape of the 1st buckling mode.

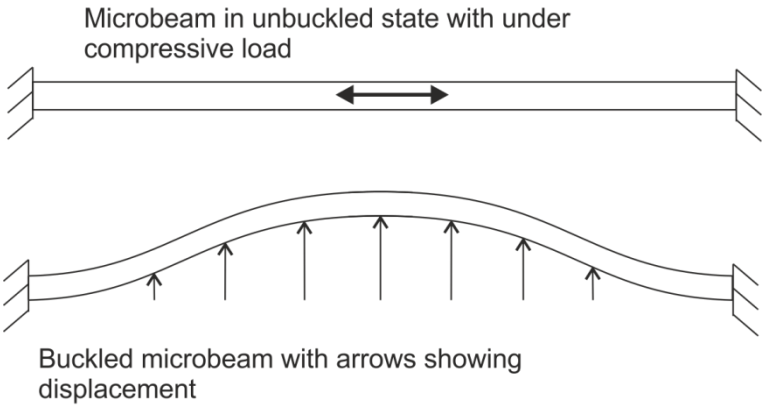

Fig. 2. Graphic showing how a microbeam will eventually buckle to relieve compressive stress when mechanically anchored at both ends.

3. Fabrication

The fabrication process for our tunable Bragg grating device includes physical micromachining, wet etching and metal deposition. The initial substrate consists of 2 layers of Flame Hydrolysis Deposition glass on a silicon wafer with a 15 µm thermally grown layer to act as an underclad. The core layer is doped with germanium to increase photosensitivity. The wafer is diced with a commercial dicing saw to produce device sized chips or die. In this work microbeams of two lengths were fabricated. A 1 mm long microbeam contained optical elements and was characterized both optically and mechanically whilst a 1.5 mm microbeam was characterized mechanically.

For the wet etch to fully undercut the microbeam, two deep trenches must be machined through the silica exposing the silicon. The grooves must be sufficiently deep to prevent premature formation of slow etching <100> etch planes, which drastically reduce the etch rate. Reactive ion etching (RIE) and inductively coupled etching (ICP) would have required very long process times to reach this depth of groove. For this reason physical micromachining was selected as the machining time was shorter and fabrication of lithographic masks was not required, and in addition is capable of yielding very smooth surfaces[19]. A micro-mill was used to fabricate two grooves to a depth of 80 µm. The micro-mill has a Loadpoint Bearings air-bearing spindle with dynamic runout better than 1 µm. The workpiece is translated on an air-bearing Aerotech X,Y translation stage with nanometer level resolution. Table 1 shows the processing parameters used during the milling operation.

Tool diameter	0.5 mm
Mill type	UKAM 500 µm diameter diamond microdrill
Spindle speed	60,000 rpm
Linear feed rate	0.1 mm/min

Table 1 Machining parameters used for micromilling of grooves

It was essential to minimise edge chipping and cracks in the silica as these could cause failure of the microbeam at the etch stage. Fig. 3 shows two milled grooves after optimisation and demonstrates that the edge chipping has been kept to a low level.
During development of the milling process it was found that top edge chipping occurred more frequently at the start and end of grooves where the tool was either engaging or disengaging the surface. For this reason, 'run-up' sections at 90º to the main grooves were introduced and can be seen in Fig. 3. These kept initial edge chipping out the way without affecting the function of the device. Each 'run-up' was 0.5mm in length and the tool took a linear descent to the cut-depth of 80 microns.

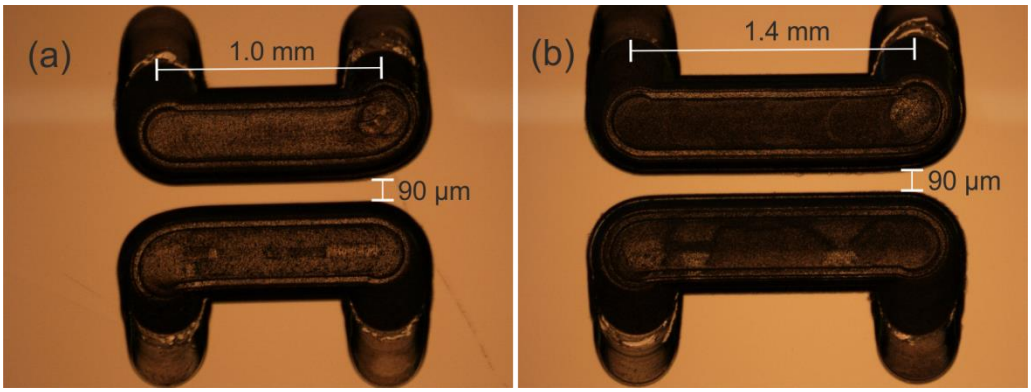

Fig. 3. Optical microscope images of milled grooves prior to UV writing and etching. (a) 1mm (b) 1.5mm

The chip is loaded under high-pressure hydrogen to allow diffusion into the core, increasing photosensitivity. Single mode waveguides and Bragg gratings are written into the glass layer using the direct UV writing process[20]. Fig. 4 shows the layout of the optical elements in the device. A Gaussian apodized Bragg grating with central reflection wavelength of 1565 nm is located in the microbeam whilst two Bragg gratings with a peak reflection wavelength of 1550 nm are written either side to form a Fabry-Pérot cavity. As the Fabry-Pérot cavity is formed with two Gaussian apodized Bragg gratings, spectrally it consists of sharp fringes with periodicity determined by the cavity length with a Gaussian function envelope. The cavity was used to determine the response time of the microbeam to applied heating due to sensitivity of fringe position to changes in the optical path length.

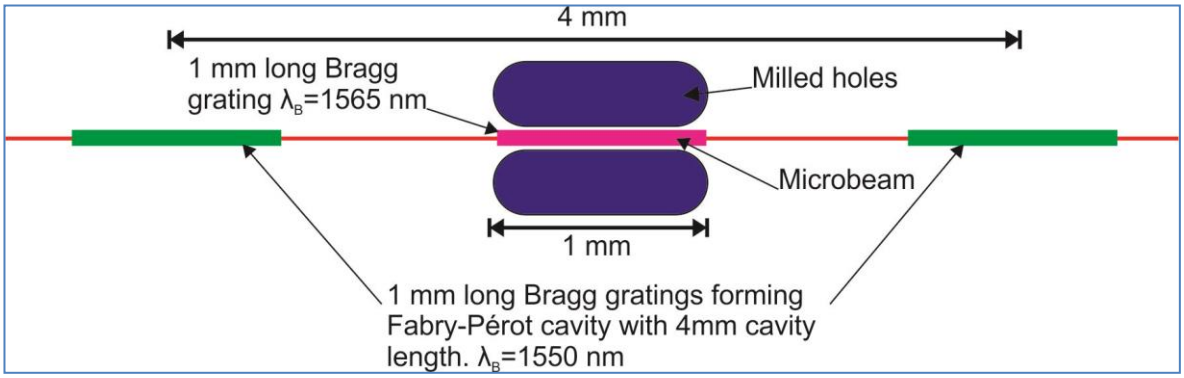

Fig. 4. Schematic showing layout of microbeam and Bragg gratings

A potassium hydroxide wet etch was used to remove the exposed silicon releasing the microbeam. The chip was immersed in 4.5 mol/l solution at 75 ºC for 5 hours. Fig. 5 shows microscope images of the released microbeams. The glass microbeam is almost transparent but can be seen above the silicon floor in the microscope image. The irregular silicon etch features are a result of anisotropic etching of the groove bases due to the crystalline planes of the <100> substrate.

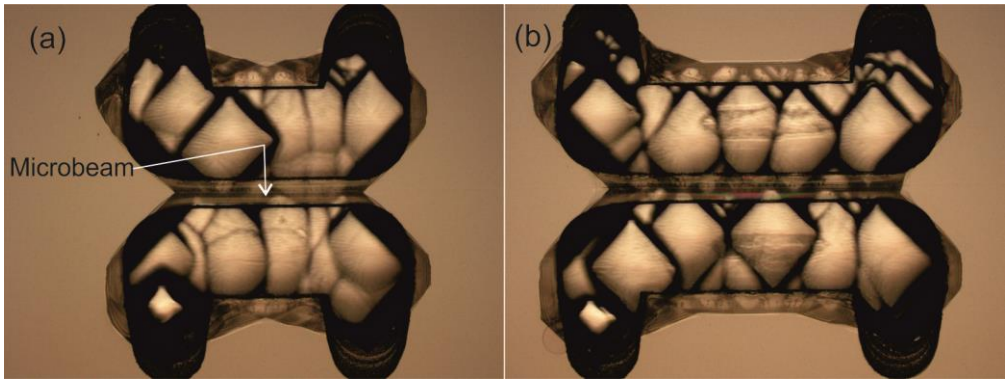

Fig. 5. Microscope images of the microbeams following KOH wet etch (a) 1mm (b) 1.5mm. The arrow locates the glass microbeam separated from the underlying silicon floor.

The reflection spectrum of the device was characterized optically before and after etching. *Fig. 6* shows a comparison of the spectra before and after etching. The Bragg grating in the microbeam is shown at around 1566 nm whilst the Fabry-Pérot cavity peak location is at approximately 1552 nm. A zoomed-in section of the spectra is plotted to show the Fabry-Pérot fringes more clearly.

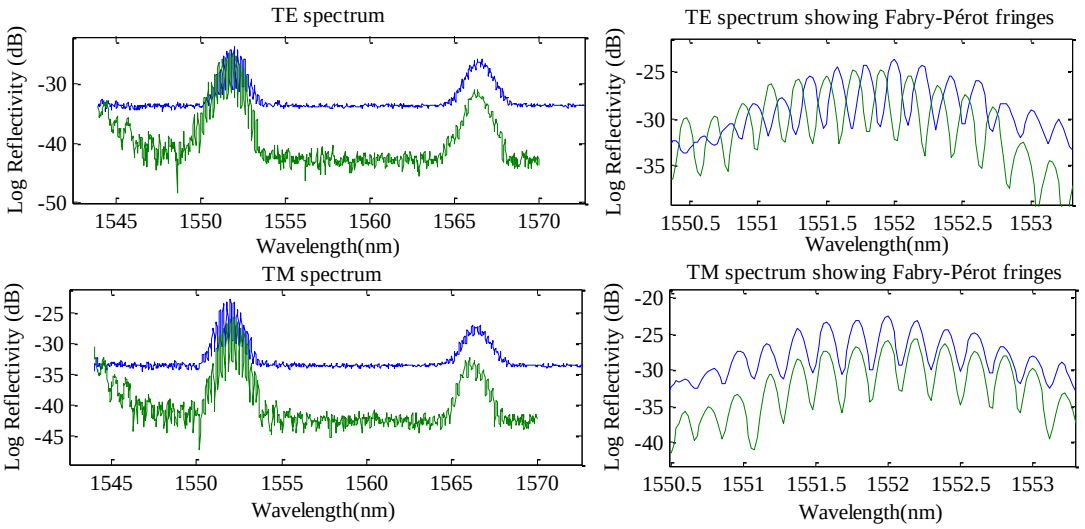

Fig. 6. Comparison of spectra before (blue line) and after etching (green line) for the TE and TM modes.

A gold heating strip is deposited using evaporative deposition. A 5 nm seed layer of chromium is first deposited to improve adhesion between the gold and silica glass. Polyimide tape was used as a rough mask for the heating strip. A microscope image following this step is shown in Fig. 7. The reduction in width across the microbeam ensures that the majority of Joule heating will occur in this region. The metallic heater element is separated by 17 microns of cladding glass from the core of the waveguide, thus ensuring that the optical field does not suffer attenuation due to the metal. Using a grating based method[21]. we can estimate that there is negligible additional loss from the microbeam fabrication beyond the ~0.2 dB/cm intrinsic loss of the waveguides themselves.

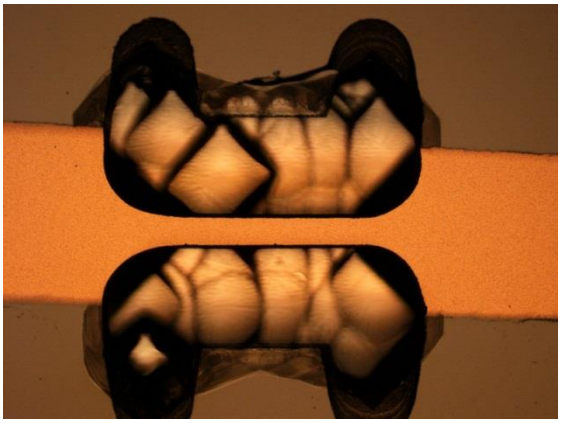

Fig. 7. Optical microscope image of microbeam following the Cr+Au deposition

A scanning electron microscope was used to image the device to confirm it had been fully undercut. Fig. 8 shows two shows SEM images for two different lengths of microbeam.

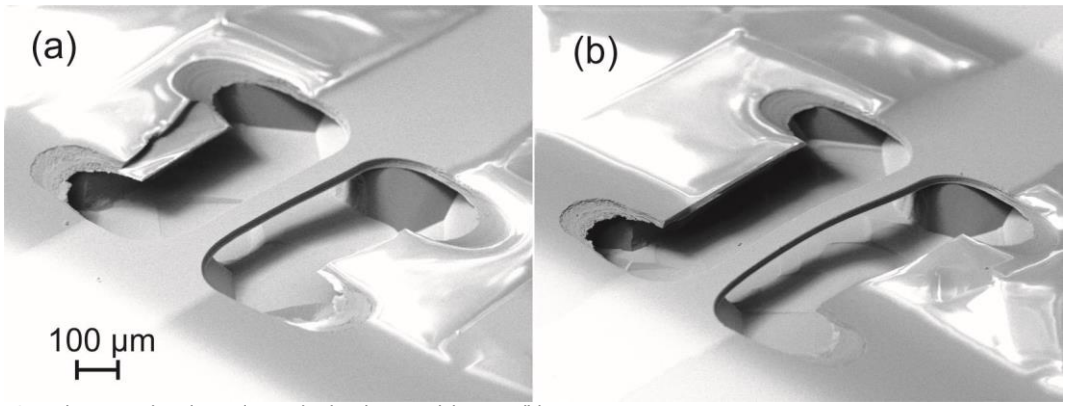

Fig. 8. SEM images showing released microbeams.(a) 1mm (b) 1.5mm.

4. Characterisation

Thermo-optical characterization: With the heating element deposited the tuning of each Bragg grating's reflection wavelength with heating power was studied. An Optical Spectrum Analyser (OSA) was used to measure the reflection spectrum of the device for a range of heating powers. Gaussian fitting to the Bragg peak allows the peak Bragg wavelength to be plotted as a function of heating power. The optical setup includes a polariser which allows the TM and TE modes to be studied independently. Fig. 9 shows the shift in central Bragg peak wavelength with electrical heating power. Also shown is the average temperature of the microbeam during tuning. This was measured using a 4-point-probe method which will be described later in the report.

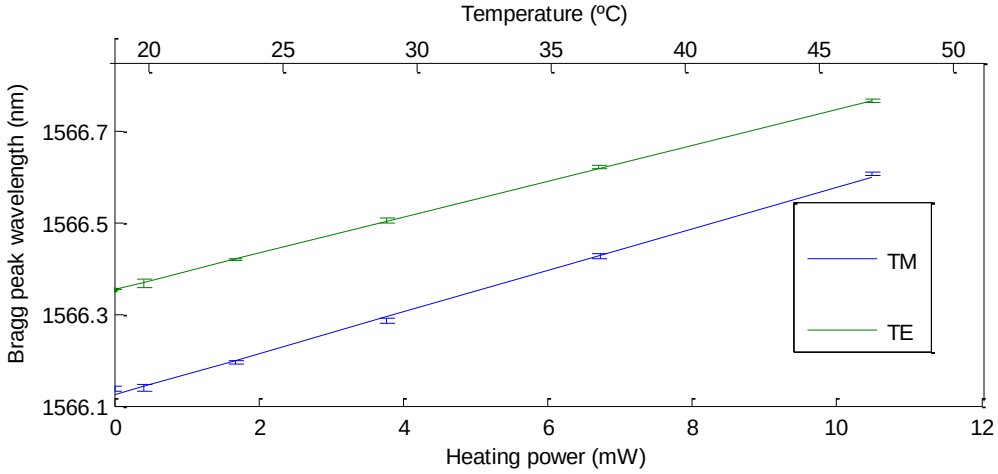

Fig. 9. Shift in central Bragg peak wavelength with electrical heating power. The top axis also shows the temperature reached by the microbeam as measureed by a 4-point-probe technique.

It can be seen that the tuning efficiency is slightly higher for TM 45±2 pm/mW vs 39±1 pm/mW for TE. This is believed to be due to the inherent in-plane fabrication stress in the silica which means the material behaves anisotropically when heated. The Bragg peak shift is linear in power for both modes. For a tuneable reflector device it is desirable that the spectral shape of the Bragg peak is maintained during tuning. Fig. 10 shows that this is the case over the tuning range studied. The fringes in Fig. 10 result from interference between the Bragg grating response and imperfectly terminated end-facets and this is confirmed by the period of the fringes. The gratings in this device were Gaussian apodised, but can in principle, be designed to offer more advanced functionality as commonly used in laser written Bragg gratings [22].

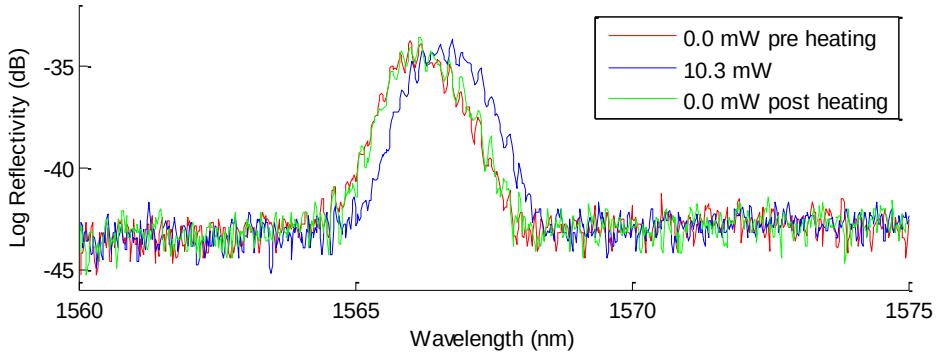

Fig. 10. Spectra showing Bragg peak during tuning.The spectrum at maximum heating is shown in blue and indicates that the spectral shape and height are preserved during tuning.

Fig. 11 shows a photograph of the completed device which has a footprint of 10 mm x 20 mm and a height of 3mm.

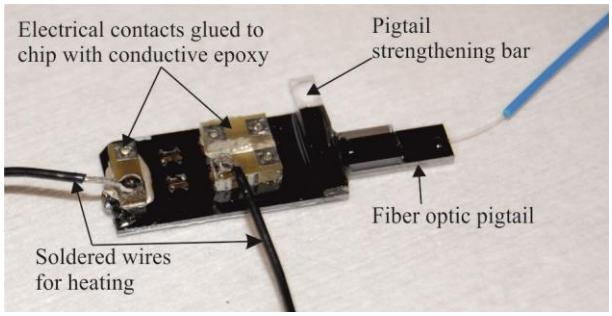

Fig. 11. Photograph of completed device showing location of microbeam, fiber optic pigtail and electrical contacts.

A four-point probe measurement was conducted to find the temperature reached by the microbeam. During tuning the current supplied to the heating element was measured using an Agilent U1253A multimeter and the voltage drop across the element was measured using a Keithley 2100 multimeter. From these data the I-V relationship for the thin film heating element was established. The temperature dependent coefficient of resistance was determined by bulk heating of the device and performing the 4-point probe measurement at low current to reduce extra heating. The experimentally determined temperature coefficient of resistance was determined to be 0.00230(6) $^{o}C^{-1}$. It has previously been reported that in thin metallic gold films this value is lower than for the bulk material [23]. The data in Fig. 9 includes the inferred temperatures reached during Bragg peak tuning. It can be seen an average temperature of 47 ^{o}C is reached at the maximum of the tuning. The tuning efficiency of this device is approximately a factor of 90 better than a thermally tuneable Bragg grating in a bulk silica device[15]. The limiting factor to the tuning range is expected to be either the erasure of the Bragg grating at high temperatures or the additional mechanical stress during tuning.

5. Thermo-mechanical characterization

Following the optical characterisation the mechanical behaviour of the microbeam during tuning/heating was also investigated. Localised heating causes a thermal deformation of the microbeam. The microbeams were characterized mechanically using a Zemetrics Zescope optical profiler. The Zescope records 3 dimensional surface plots from which line slices of height can extracted. Fig. 12 shows the measured microbeam profiles without any applied heating. The sign convention is with positive deflection being out of the plane of the device.

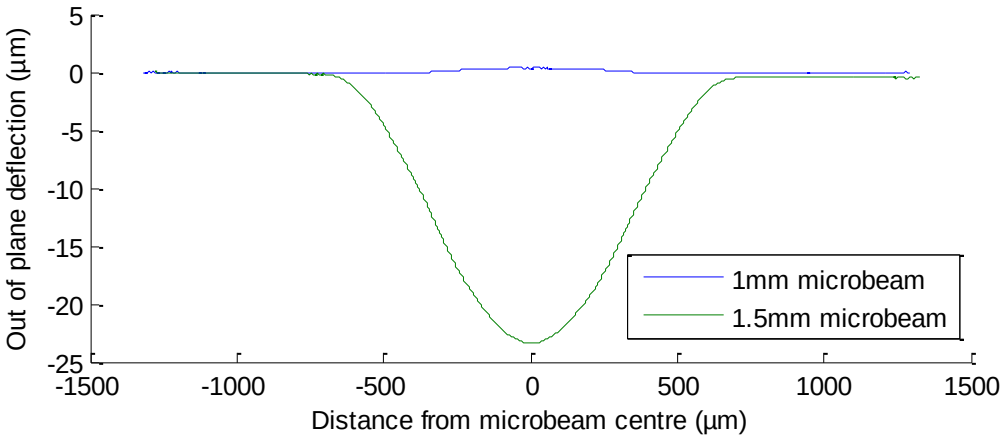

Fig. 12. Deflection of microbeams following etch release. The shorter microbeam shows slight out-of-plane deflection whilst the longer 1.5 mm microbeam has undergone buckling.

It can be seen that for the 1 mm long microbeam there is a small positive deflection of 0.4 µm. The 1.5 mm microbeam has deflected downwards by 23.3 µm. This strongly suggests only the 1.5 mm microbeam has buckled. The direction of buckling is downwards, towards the silicon substrate. This direction offers greater strain relief to the thermal oxide underclad, which has higher initial compressive stress than the FHD overclad. An upwardly buckled microbeam may also be locally stable and further work would be possible to determine the repeatability and the effect of etching conditions on the buckling direction. The effect of heating on the deflection was also investigated for both the buckled and unbuckled microbeams. Fig. 13 shows how the centre points of the microbeams moved under increasing heating.

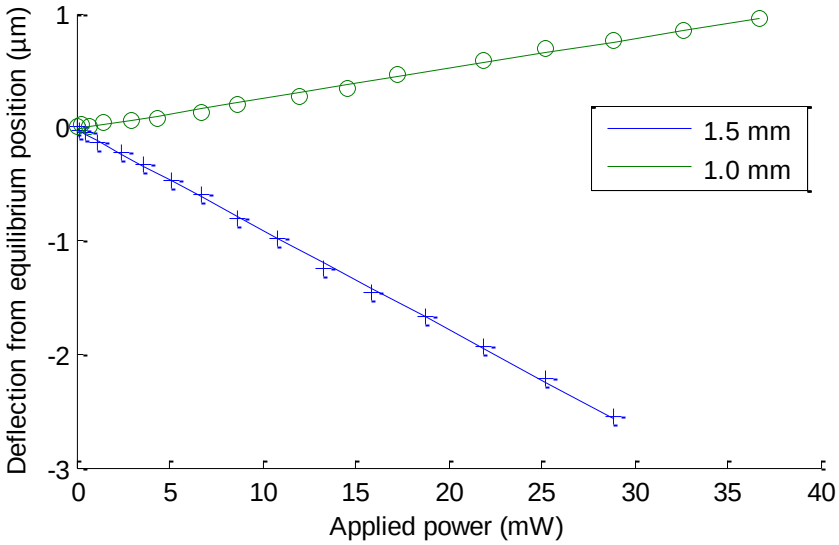

Fig. 13. Effect of heating on microbeam deflection. The buckled microbeam shows greater out-of-plane growth for the same applied heating power than the unbuckled microbeam.

This data shows that the buckled microbeam deflects further out of the plane for a given heating power than the unbuckled microbeam. This is expected as the buckled microbeam is less constrained to deflect out of plane. The direction of the heating induced deflections follow the direction of initial movement following etch release.

6. Response time

The increased energy efficiency of this device comes at penalty of a slower time response. The response time to a switch-on voltage of 0.5 V was measured using an optical setup consisting of a tuneable laser tuned to wavelength which coincides with a spectrally narrow Fabry-Pérot fringe. From the tuning efficiency results obtained this is equivalent to a peak shift of 0.43 nm for the TM mode.

The tunable laser was tuned to 1552.13 nm which was found to be between a maxima and minima on the Fabry-Pérot pattern. When heated the optical path length of the microbeam increased changing the cavity length of the Fabry-Pérot cavity. The heating power used only increased the cavity length by a fraction of one wavelength and so the response from the photodiode was approximated to be linear with heating. For the switch-on a 1/e time of 44±3 ms was obtained and for the switch-off 50±1 ms was measured. This is a factor of ~50 slower than the tuning response times reported for Bragg gratings in bulk silica substrates and confirms that the trade-off for the device is between greater power efficiency and response time [15]. For applications in data-center switching or dispersion compensation our response times are sufficient, while for other applications devices with greater power consumption and high switching speeds may be preferable.

7. Conclusion

A silica-on-silicon device that allows tuning of a Gaussian apodized Bragg grating has been demonstrated. Tuning efficiency is enhanced by incorporating the Bragg grating into a microbeam which gives greater thermal isolation and acts as a smaller thermal mass. Tuning efficiency of 45 pm/mW for the TM mode and 39 pm/mW for the TE mode has been achieved which is a factor of 90 better than for a bulk silica device. The device could find applications where highly efficient tuning and low thermal cross-talk is required. Tuning has been shown over a range of 0.4 nm corresponding to 50 GHz which is appropriate for telecomm DWDM applications. The 1.5 mm long microbeam buckled following the etch release step. This feature has the potential to create a bistable switch that would not require continuous power supply to tune between two states.

Acknowledgments

The authors would like thank EPSRC for funding the work. Grant number: EP/I003835/1

References

[1] H. Guckel, T. Randazzo, and D. W. Burns, “A simple technique for the determination of mechanical strain in thin films with applications to polysilicon,” *J. Appl. Phys*., vol. 57, no. 5, p. 1671, Nov. 1984.

[2] T. Lisec, S. Hoerschelmann, H. J. Quenzer, B. Wagner, and W. Benecke, “Thermally driven microvalve with buckling behaviour for pneumatic applications,” in *Proc. IEEE Micro Electro Mechanical Systems An Investigation of Micro Structures, Sensors, Actuators, Machines and Robotic Systems*, 1994, pp. 13–17.

[3] D. J. Joe, Y. Linzon, V. P. Adiga, R. a. Barton, M. Kim, B. Ilic, S. Krylov, J. M. Parpia, and H. G. Craighead, “Stress-based resonant volatile gas microsensor operated near the critically buckled state,” *J. Appl. Phys*., vol. 111, no. 10, p. 104517, May 2012.

[4] A. Sugita, “Bridge-suspended silica-waveguide thermo-optic phase shifter and its application to Mach-Zehnder type optical switch,” in *International Conference on Integrated Optics and Optical Fiber Communication*, 1990, pp. 105–109.

[5] C. R. Raum, R. N. Tait, and R. C. Gauthier, “Fabrication and characterization of a thermo-mechanically tunable grating-assisted suspended waveguide filter,” in *Proc. SPIE Silicon Photonics III*, 2008, vol. 6898.

[6] B. Calkins, P. L. Mennea, A. E. Lita, B. J. Metcalf, W. S. Kolthammer, A. Lamas-Linares, J. B. Spring, P. C. Humphreys, R. P. Mirin, J. C. Gates, P. G. R. Smith, I. A. Walmsley, T. Gerrits, and S. W. Nam, “High quantum-efficiency photon-number-resolving detector for photonic on-chip information processing.,” *Opt Express*, vol. 21, no. 19, pp. 22657–70, Sep. 2013.

[7] A. Iocco, H. G. Limberger, R. P. Salathe, L. A. Everall, K. E. Chisholm, J. A. R. Williams, and I. Bennion, “Bragg grating fast tunable filter for wavelength division multiplexing,” *J Lightwave Technol*, vol. 17, no. 7, pp. 1217–1221, Jul. 1999.

[8] B. J. Eggleton, A. Ahuja, P. S. Westbrook, J. A. Rogers, P. Kuo, T. N. Nielsen, and B. Mikkelsen, “Integrated Tunable Fiber Gratings for Dispersion Management in High-Bit Rate Systems,” *J Lightwave Technol*, vol. 18, no. 10, pp. 1418–1432, Oct. 2000.

[9] L. G. Carpenter, C. Holmes, H. L. Rogers, P. G. R. Smith, and J. C. Gates, “Integrated optic glass microcantilevers with Bragg grating interrogation.,” *Opt Express*, vol. 18, no. 22, pp. 23296–23301, Oct. 2010.

[10] C. Holmes, L. G. Carpenter, J. C. Gates, and P. G. R. Smith, “Miniaturization of Bragg-multiplexed membrane transducers,” *J Micromech Microeng*, vol. 22, no. 2, p. 025017, Feb. 2012.

[11] B. J. Metcalf, J. B. Spring, P. C. Humphreys, N. Thomas-Peter, M. Barbieri, W. S. Kolthammer, X.-M. Jin, N. K. Langford, D. Kundys, J. C. Gates, B. J. Smith, P. G. R. Smith, and I. A. Walmsley, “Quantum teleportation on a photonic chip,” *Nat. Photonics*, vol. 8, no. 10, pp. 770–774, Sep. 2014.

[12] S. Donati and S. . B. Donati, “Piezoelectric actuation of silica-on-silicon waveguide devices,” *IEEE Photonic Tech Lett*, vol. 10, no. 10, pp. 1428 – 1430, Oct. 1998.

[13] F. R. Mahamd Adikan, J. C. Gates, A. Dyadyusha, H. E. Major, C. B. E. Gawith, I. J. G. Sparrow, G. D. Emmerson, M. Kaczmarek, and P. G. R. Smith, “Demonstration of 100 GHz electrically tunable liquid-crystal Bragg gratings for application in dynamic optical networks,” *Opt Lett*, vol. 32, no. 11, p. 1542, Jun. 2007.

[14] J. H. Wray and J. T. Neu, “Refractive Index of Several Glasses as a Function of Wavelength and Temperature,” *J. Opt. Soc. Am*., vol. 59, no. 6, p. 774, Jun. 1969.

[15] C. Holmes, D. O. Kundys, and J. C. Gates, “150 GHz of thermo-optic tuning in direct UV written silica-on-silicon planar Bragg grating,” *Electron. Lett*., vol. 45, no. 18, pp. 954–955, Aug. 2009.

[16] P. C. Humphreys, B. J. Metcalf, J. B. Spring, M. Moore, P. S. Salter, M. J. Booth, W. Steven Kolthammer, and I. A. Walmsley, “Strain-optic active control for quantum integrated photonics.,” *Opt Express*, vol. 22, no. 18, pp. 21719–26, Sep. 2014.
[17] B. G. Aitken and R. E. Youngman, “Borophosphosilicate glasses: properties and structure,” *Phys Chem Glasses*, vol. 47, no. 4, pp. 381–387, Aug. 2006.
[18] J. M. Gere and S. P. Timoshenko, *Mechanics of Materials*, 4th ed. Cheltenham, Glos, UK: Stanley Thornes, 1999.
[19] L. G. Carpenter, P. A. Cooper, C. Holmes, C. B. E. Gawith, J. C. Gates, and P. G. R. Smith, “Nanoscale roughness micromilled silica evanescent refractometer,” *Opt Express*, vol. 23, no. 2, p. 1005, Jan. 2015.
[20] G. D. Emmerson, S. P. Watts, C. B. E. Gawith, V. Albanis, M. Ibsen, R. B. Williams, and P. G. R. Smith, “Fabrication of directly UV-written channel waveguides with simultaneously defined integral Bragg gratings,” *Electron. Lett.*, vol. 38, no. 24, pp. 1531–1532, Nov. 2002.
[21] H. L. Rogers, S. Ambran, C. Holmes, P. G. R. Smith, and J. C. Gates, “In situ loss measurement of direct UV-written waveguides using integrated Bragg gratings,” *Opt Lett*, vol. 35, no. 17, pp. 2849–2851, 2010.
[22] R. Kashyap, *Fiber Bragg Gratings*. San Diego, CA, USA: Academic Press, 1999.
[23] F. Avilés, O. Ceh, and A. I. Oliva, “Physical Properties Of Au And Al Thin Films Measured By Resistive Heating,” *Surf. Rev. Lett.*, vol. 12, no. 1, pp. 101–106, Jan. 2005.